



HAL
open science

Quantification of the transposition error for CFD computations of the heat transfer coefficient.

Viken Khayiguian

► **To cite this version:**

Viken Khayiguian. Quantification of the transposition error for CFD computations of the heat transfer coefficient.. Fluid mechanics [physics.class-ph]. Institut National Polytechnique de Toulouse - INPT, 2021. English. NNT : 2021INPT0095 . tel-04186478

HAL Id: tel-04186478

<https://theses.hal.science/tel-04186478>

Submitted on 23 Aug 2023

HAL is a multi-disciplinary open access archive for the deposit and dissemination of scientific research documents, whether they are published or not. The documents may come from teaching and research institutions in France or abroad, or from public or private research centers.

L'archive ouverte pluridisciplinaire **HAL**, est destinée au dépôt et à la diffusion de documents scientifiques de niveau recherche, publiés ou non, émanant des établissements d'enseignement et de recherche français ou étrangers, des laboratoires publics ou privés.



Université
de Toulouse

THÈSE

En vue de l'obtention du

DOCTORAT DE L'UNIVERSITÉ DE TOULOUSE

Délivré par :

Institut National Polytechnique de Toulouse (Toulouse INP)

Discipline ou spécialité :

Energétique et Transferts

Présentée et soutenue par :

M. VIKEN KHAYIGUIAN

le lundi 15 novembre 2021

Titre :

Quantification of the transposition error for CFD computations of the heat transfer coefficient

Ecole doctorale :

Mécanique, Energétique, Génie civil, Procédés (MEGeP)

Unité de recherche :

Institut de Mécanique des Fluides de Toulouse (IMFT)

Directeur de Thèse :

M. CHRISTOPHE AIRIAU

Rapporteurs :

M. LAURENT CORDIER, UNIVERSITE DE POITIERS

MME BERENGERE PODVIN, LIMSI

Membres du jury :

MME CATHY CASTELAIN, UNIVERSITE DE NANTES, Présidente

M. CHRISTOPHE AIRIAU, UNIVERSITE TOULOUSE 3, Membre

M. DIDIER SAURY, ENSMA POITIERS, Membre

M. MAMADOU CISSE, FRAMATOME, Membre

M. NICOLAS GOREAUD, FRAMATOME, Invité

M. VALÉRY BOTTON, INSA LYON, Membre

Remerciements

En tout premier lieu, je tiens à remercier les membres du jury de la thèse, le président du jury, Cathy Castelain, les rapporteurs, Bérengère Podvin et Laurent Cordier qui ont acceptés de relire mon manuscrit de thèse et dont les observations ont permis d'améliorer le manuscrit.

Je tiens ensuite à remercier Nicolas Goreaud qui s'est occupé de l'encadrement industriel et qui m'a fait confiance en me choisissant comme doctorant pour réaliser cette thèse. Son suivi et son soutien ont permis à cette thèse d'arriver à son terme et ont rendu le travail agréable. Je remercie aussi David Lo Jacono qui fut mon encadrant la première année. J'ai pu découvrir avec lui l'IMFT et le monde de la recherche. Enfin je remercie Christophe Airiau qui a repris le flambeau les deux années suivantes et qui a été très disponible malgré la distance Lyon-Toulouse. Ses observations et son soutien tout au long de cette thèse ont été essentielles à l'obtention des travaux présentés dans le document et à la production du manuscrit.

J'ai bénéficié tout au long de ces trois années d'un suivi mensuel par un comité comprenant les encadrants de thèse, Mamadou Cissé, Jérémy Galpin, Phillipe Martinez et Alejandro Mourgues que je souhaite remercier. Les points d'avancements qui ont été effectués avec eux et les différentes discussions que j'ai pu avoir avec chacun d'eux ont menés à des échanges très intéressants et très constructifs.

Je remercie également les personnels du Centre Technique Framatome Le Creusot qui m'ont aidé et ont contribué de manière importante lors des phases d'essais expérimentaux sur maquette. Je remercie en particulier Julien Lonjaret qui a été très disponible pour mener les essais, Bastien Jampy pour les conseils et l'aide sur l'altimètre laser, Mario Seixas qui a été très disponible quand j'en avais besoin que ce soit pour des plans ou pour mes moules de plâtre. Je remercie aussi tous les autres pour la bienveillance dont ils ont fait part envers moi et leur aide lorsque j'en avais besoin.

Je tiens à remercier également Alexandre Chea qui m'a aidé sur Fluent durant toute la thèse et qui a été très disponible pour me donner des conseils sur le logiciel et pour vérifier mes simulations. Côté STAR-CCM+, je remercie Keerthanan Kandeepan qui s'est occupé de vérifier les calculs avec son œil vigilant.

Je remercie également la section DTIPL-T de Framatome au sein de laquelle j'ai effectué la grande majorité de la thèse pour le soutien que ses membres m'ont apporté, les moments de convivialité, et la disponibilité que beaucoup ont eu tout au long de cette thèse lorsque je les sollicitais. Je remercie les habitués des soirées dégustations Arthur et Yves-Louis qui ne m'oublient jamais pour bien manger, à mon tuteur Olivier qui m'a donné envie de faire la CFD au point d'en faire une thèse, et tous les autres dont la bienveillance et la sympathie a rendu le quotidien facile et agréable.

Je remercie aussi ma copine Salma et mon ami Oualid, dont la patience a été mise à rude épreuve lors des derniers mois de thèse et qui ont été un soutien important.

Je remercie enfin ma famille pour leur soutien inconditionnel au cours de ma scolarité dont cette thèse est l'aboutissement.

Abstract

This dissertation deals with the use of RANS CFD commercial solvers for heat transfer computations of nuclear reactor components. The validation of two codes has been previously performed on reduced scale mock-ups at smaller Reynolds number scale in experimental facilities. The objective of this work has been to verify if the accuracy of calculation of the heat transfer coefficient with CFD evolves when approaching the real reactor scale Reynolds number. Experiments and CFD computations have been conducted for this purpose. The first step has been to lay down the basics of CFD and uncertainty quantification. The latter subject provides a working environment which consolidates the validation approach, as the comparisons are given by taking into consideration the different sources of uncertainty in heat transfer simulations and experiments. An important aspect of this work has been to develop a measurement methodology to retrieve heat transfer coefficient maps for water exchanging with a heated smooth wall with reasonable uncertainty. The method that has been chosen is based on the gypsum dissolution and the heat and mass transfer analogy. The measured mass transfer coefficient has been transposed to smooth wall heat transfer coefficient by considering the roughness of the gypsum surface after dissolution and the difference of heat and mass diffusion in water. The values of the heat transfer coefficient obtained have been compared to literature for Reynolds number in the range $[10^4, 10^5]$ on the well documented case of heat exchange in a rectangular channel for turbulent flow, showing good agreement. Then, two commercial softwares were tested for computations of the heat transfer coefficient by reproducing the experiments. In the rectangular channel, the boundary conditions uncertainty during the experiments were propagated through the CFD simulations with two different methods: the deterministic sampling which uses a limited number of sigma points to propagate the covariance of the inputs and Monte Carlo method which relies on the estimation of large samples of the boundary conditions with a surrogate model based on gaussian process. These two methods have been found to yield identic results indicating that the boundary conditions uncertainty is negligible in comparison to the experimental uncertainty. Finally, the comparison between CFD and experiments has been done and combined to the experimental uncertainty to estimate the model error which has been found to decrease for increasing Reynolds numbers. The process has then been reproduced for comparisons of CFD and experiments in a 1/5th reduced scale mock-up of a steam generator water box. The measurement methodology has been adapted and combined both heat and mass transfer measurements. The 2D mass transfer data has been processed with the Proper Orthogonal Decomposition and the heat transfer measurements were used to measure the transposition factor. Heat and mass transfer data showed consistent values indicating good confidence on the heat and mass transfer analogy. The heat and mass transfer measurements were then combined to proceed to the uncertainty quantification of CFD on the Reynolds number range $[10^5, 10^6]$. The numerical error has been

estimated with a grid convergence method (GCM) using Richardson extrapolation and was shown to be negligible. The same conclusion was drawn for the boundary conditions uncertainty which has been estimated with Monte-Carlo method. Finally, the comparison between CFD and experiments has been found to depend on the turbulence model, depend on near wall meshing and depend on software. It has also been concluded that the type of cells had an impact on simulations of the steam generator mock-up flow where tetrahedral cells yielded higher Nusselt number. The overall comparison between CFD computations and experiments finally showed the non-evolution of the model error with increasing Reynolds number.

Résumé

Le travail présenté dans ce document porte sur l'utilisation de la mécanique des fluides numérique ou, abrégé en anglais, CFD, pour des calculs de transferts thermique dans un réacteur nucléaire à l'aide de modèle de turbulence RANS. L'utilisation de ces codes dans l'industrie nucléaire nécessite une phase de validation qui permet de déterminer la précision des résultats calculés. Cette validation se fait sur maquette à une échelle géométrique réduite en laboratoire. La plupart du temps, la similitude du régime de turbulence basée sur la conservation du nombre de Reynolds entre l'échelle maquette et l'échelle réacteur ne peut être assuré en raison de la difficulté de reproduire expérimentalement les conditions réacteurs. Les résultats de la validation sont donc en général transposés à l'échelle réacteur en faisant l'hypothèse que la validité des modèles n'est pas remise en cause lors de l'approche de l'échelle réacteur. Un des objectifs de cette thèse a été de vérifier cette hypothèse en étudiant l'évolution de l'erreur de modèle avec le nombre de Reynolds.

L'estimation de l'erreur de modèle décrivant le biais et la variance sur les résultats induits par le modèle, repose sur l'existence de données expérimentales. La première étape a donc été de générer des données de transfert de chaleur en vue de la validation des codes STAR-CCM+ et Fluent. Une méthode de mesure basée sur l'analogie entre le transfert de masse et de chaleur a été développée à cet effet. Cette méthode utilise un mur soluble de gypse qui exposé à l'eau se dissout. L'usure mesurée permet ensuite de remonter au nombre de Sherwood sur la surface. La méthode a d'abord été testée pour des mesures de coefficient d'échange dans un canal rectangulaire pour des nombres de Reynolds dans la gamme $[10^4, 10^5]$. Un facteur de transposition entre le nombre de Sherwood calculé et le nombre de Nusselt pour une paroi à température fixée et lisse a été proposé. Ce facteur prend en compte la rugosité de la surface de gypse après dissolution et la différence de propriété diffusives du transport de masse et de chaleur. Le nombre de Nusselt ainsi obtenu a été comparé aux données de la littérature et a montré un bon accord. La méthode a ensuite été adaptée pour des mesures dans une reproduction à l'échelle géométrique 1/5 d'une boîte à eau de générateur de vapeur d'un réacteur nucléaire. Quatre emplacements de mesures ont été couverts en face d'un jet impactant et ont permis d'effectuer des mesures de coefficient de transfert de masse et de chaleur. Les expériences de transfert de masses ont été effectuée avec la dissolution du gypse permettant de calculer des cartes de Sherwood. Ces champs de Sherwood ont été traités à l'aide de la décomposition orthogonale aux valeurs propres (POD en anglais). D'autre part, les mesures de transfert de chaleur ont permis de mesurer deux valeurs moyennes du nombre de Nusselt sur les parties supérieurs et inférieurs des emplacements de mesure. Ces mesures ont permis le calcul du facteur de transposition entre le nombre de Sherwood obtenu par dissolution gypse et le nombre de Nusselt calculé depuis les mesures de coefficient d'échange thermique dans l'eau. De plus, l'effet de la rugosité sur la mesure de gypse a pu être étudié, son impact est cohérent avec les éléments trouvés dans littérature.

La quantification de l'erreur de modèle nécessite aussi de quantifier les sources d'erreur et d'incertitude lors de calculs CFD. Parmi elles, l'incertitude des conditions limites pendant les essais a été propagée à travers le calcul du coefficient d'échange à l'aide de deux méthodes: le « Deterministic Sampling » (DS), qui permet d'évaluer les moments statistiques des résultats des calculs à l'aide d'un échantillon contenant un faible nombre de points, et la méthode de Monte Carlo qui consiste à effectuer un nombre important de tirages aléatoires des conditions limites et d'estimer la réponse des calculs CFD pour chacune des réalisations. Cette dernière méthode repose sur la création d'un métamodèle avec les processus gaussiens, qui permet de reproduire la réponse des calculs CFD en un temps négligeable. Ces deux méthodes ont montré des résultats similaires pour des calculs avec un paramètre incertain, et il a été montré que cette incertitude est négligeable devant l'incertitude expérimentale pour les calculs dans le canal rectangulaire et la maquette de boîte à eau de générateur de vapeur. L'évaluation de l'erreur numérique due à la discrétisation du domaine a été faite à l'aide d'une méthode de convergence du maillage pour un des modèles de turbulence testé. Il a été montré que cette erreur est négligeable pour les maillages utilisés. Enfin, l'erreur entre la CFD et l'expérience a été évaluée pour plusieurs modèles de turbulence et il a été montré que les résultats en sont fortement dépendant. De plus, le maillage proche paroi semble aussi impacter le calcul et une des perspectives de la thèse serait d'en quantifier l'effet. Enfin, l'erreur de modèle a pu être reconstruite à partir des différentes sources d'erreur et d'incertitudes, et il a été montré que celle-ci n'augmente pas lorsque le Reynolds augmente.

Contents

Contents	viii
List of Figures	xi
List of Tables	xxi
Nomenclature	xxiii
Introduction.....	1
Chapter 1 Uncertainty quantification applied to Computational Fluid Dynamics	1
1.1 CFD Computations of heat transfer coefficient	2
1.1.1 Conservation equations	2
1.1.2 Non dimensional numbers	5
1.1.3 Modelling of turbulence.....	7
1.1.4 Conclusion	17
1.2 Uncertainty quantification.....	18
1.2.1 Definition and nomenclature in the UQ frame	18
1.2.2 Statistical concepts.....	21
1.2.3 Surrogate modelling.....	25
1.2.4 Numerical methods for UQ.....	31
1.3 Conclusion.....	39
Chapter 2 Mass transfer measurements in a rectangular channel and heat transfer analogy	41
2.1 Introduction	41
2.2 Transposition of the mass transfer coefficient	42
2.2.1 Heat and mass transfer analogy	42
2.2.2 State of the art	43
2.2.3 Roughness effect on the flow.....	46
2.3 Experimental setup and configuration.....	48
2.4 Methodology	49
2.5 Results and analysis	54
2.5.1 Evolution of the operating conditions.....	54
2.5.2 Evolution of the Sherwood number on the experimental range	57
2.6 Conclusion.....	60
Chapter 3 Uncertainty quantification on the rectangular channel	63

3.1	Presentation of the CFD model	63
3.1.1	Geometry.....	63
3.1.2	Grid	64
3.1.3	Boundary conditions and physical properties	67
3.1.4	Data processing.....	67
3.2	Investigation of the Nusselt number along the heated wall	69
3.2.1	Results of the CFD simulations	69
3.2.2	Comparison to experiments	73
3.3	Determination of the uncertainty $U_{inputs,exp}$	76
3.3.1	Introduction.....	76
3.3.2	Method 1: Surrogate model and Monte-Carlo method	77
3.3.3	Method 2: Deterministic Sampling.....	80
3.3.4	Summary of performed computations	82
3.3.5	Results of the propagation	82
3.4	Estimation of the model error E_{model}	89
3.5	Conclusion.....	93
Chapter 4	Heat and mass transfer measurements in a steam generator mock-up.....	95
4.1	Introduction	95
4.2	Experimental setup.....	96
4.2.1	Presentation of the mock-up	96
4.2.2	Heat and mass transfer for an impinging jet	99
4.2.3	Data reduction.....	103
4.3	Heat and mass transfer measurements on the partition plate	109
4.3.1	Mass transfer measurements	109
4.3.2	Heat transfer measurements	124
4.4	Transposition of mass transfer data with the heat and mass transfer analogy	128
4.4.1	Data processing.....	128
4.4.2	Surface distribution.....	130
4.4.3	Transposition factor	132
4.4.4	Discussion.....	135
4.5	Conclusion.....	136
Chapter 5	CFD simulations on the steam generator mock-up.....	139
5.1	Introduction	139
5.2	CFD model.....	139
5.2.1	Geometry.....	139

5.2.2	Grid	140
5.2.3	Physical model	142
5.2.4	Boundary conditions and physical properties	143
5.3	Data reduction	144
5.4	Surrogate models	145
5.5	Results	147
5.5.1	Introduction	147
5.5.2	Influence of the grid	149
5.5.3	Surface distribution of the Nusselt number	154
5.6	Conclusion	166
Chapter 6	Uncertainty quantification on the steam generator	167
6.1	Introduction	167
6.2	Experimental uncertainty	168
6.3	Numerical error	175
6.4	Propagation of the uncertainty of the simulation inputs	178
6.5	Error between the computations and the experiments	180
6.5.1	Realizable $k - \epsilon$	183
6.5.2	$k - \omega$ SST and Scale Adaptive Simulation	189
6.5.3	Conclusion	194
6.6	Model error	195
6.7	Conclusion	198
	Conclusion and perspectives	201
	References	205

List of Figures

Figure 1.1: evolution of the turbulent Prandtl number as a function of the molecular Prandtl number from different experiments and calibrated model. From (Jischa & Rieke, 1979). 14

Figure 1.2 :from (Wei & Willmarth, 1989) : Non dimensional mean velocity profiles, for $Re = 2970$ (\odot), $Re = 14\,914$ (\square), $Re = 22\,776$ (Δ), and $Re = 39\,582$ (∇). The viscous layer (1), the buffer layer (2) and the log layer (3) are indicated..... 16

Figure 1.3– calculation of a 95% confidence interval from the computed Nusselt number Nu_{CFD} and the error between CFD and reality $E_{CFD/realty}$21

Figure 1.4 - Example of realizations of a 2D joint distribution: With diagonal covariance matrix (left) and non-diagonal covariance matrix (right)25

Figure 1.5 – from (Loyd, et al., 2014): Example of linear regression using a gaussian process of mean μ , kernel Σ and Bayesian statistics. The realization points $\mathbf{X} = (x_i, y_i)_{i \leq N}$ are denoted with black points. The quantiles of the predictive density $p(f(x)|\mathbf{X}, \mu, \Sigma)$ at each input locations are given with shades of red. Left: the predictive density is estimated from 3 realizations $(x_i, y_i)_{i \leq N}$, right: estimation from 15 realizations.28

Figure 1.6 – From (Duvenaud, 2014). Examples of kernel for GP (solid black line) and impact on the type of curves (blue and red) that can be found.30

Figure 1.7 - Example of regression of a function f using a GP model with a squared exponential kernel – Red crosses correspond to measured points used in order to fit the true signal in solid black line. The black dashed curve corresponds to the prediction calculated after conditioning the GP with the data points. The shades of grey represent quantiles of the predictive density at each input location.....31

Figure 1.8: Process of propagating a random variable (Gaussian for instance) through a code36

Figure 1.9: Propagation with Deterministic Sampling of the uncertainty of an input following a normal distribution $\mathcal{N}(5, 0.5)$ through the function f . Three sigma points having each a weight representative of the input parameter PDF (left). The evaluation is shown on the middle plot with estimations of the resulting mean value and standard deviation. The output PDF is then shown on the right plot with the calculated mean (in blue) and a 2 sigma interval (red).....38

Figure 2.1 comparison of the radial distribution of the Sherwood number and Nusselt number around a cylinder in cross flow obtained with gypsum dissolution, naphthalene sublimation and heat transfer measurements. The Sherwood number is scaled by $Re^{1/2}Sc^{1/3}$ and the Nusselt number by $Re^{1/2}Sc^{1/3}$. From (Chang, et al., 2013).45

Figure 2.2: relation between the friction factor f used to calculate the pressure drop per unit of length for given relative roughness e/R and Reynolds number Re . From (Nikuradse, 1950).	47
Figure 2.3: evolution of the roughness enhancement of the Sherwood number with the dimensionless roughness height (peak to valley). From (Wang & Ewing, 2017).	48
Figure 2.4: schematic view of the experimental loop.	49
Figure 2.5: view of the rectangular test section. The flow goes from right to left.	49
Figure 2.6: metallic holder with the gypsum samples molded in 3D printed cast.	49
Figure 2.7: evolution of the heat transfer coefficient for a developing boundary layer.	52
Figure 2.8: evolution of the local Sherwood number profiles at different steps of the normalization process. The gray zone in figure (a) gives the 2σ interval calculated when averaging in the transverse direction. The abscissa $x = 0$ corresponds to the leading edge of the gypsum lining.	53
Figure 2.9: evolution of the Reynolds number during the experiment at $Re \approx 28\,400$. (a) random fluctuations of the Reynolds number and (b) comparison of the sample histogram to the normal distribution defined from the mean and standard deviation μ_{Re} and σ_{Re} of the Reynolds number during the experiment.	55
Figure 2.10: evolution of the Reynolds number with respect to time during an experiment where the temperature is not established (a) and approximate probability density function (b).	56
Figure 2.11: estimation of the probability density function for an experiment at $Re \approx 19\,200$. The realizations of the Reynolds and Schmidt numbers during the experiment are shown on (a) and contours of the estimated probability density function is shown on (b).	56
Figure 2.12: Effect of the Pearson coefficient on the shape of the joint probability distribution isocontours. High values of the probability density function are given in yellow and low values in blue.	57
Figure 2.9: comparison of the asymptotic Sherwood number transposed to $Sc = 10$ with the transposition factors $F1$ and $F2$	58
Figure 2.10: roughness measurements: on the right, the red line corresponds to an observed critical value of the roughness height e^+ (Wang & Ewing, 2017) from which the hydraulically smooth wall condition ends. In grey, the region for which the influence of the roughness is non-negligible for the conducted experiments.	59
Figure 2.11: correlation on the asymptotic Sherwood number extracted from the data points and uncertainty calculated on the correlation ($\mu_{Sh} \pm 2\sigma_{Sh}$ interval in grey).	59
Figure 2.12: comparison of correlation obtained with gypsum to different correlations indicated on Table 2.1. The grey zone corresponds to the $\pm 2\sigma_{Sh}$ interval.	59
Figure 2.13: ratio between the maximum and asymptotic value of the Sherwood number along the gypsum surface. Mean value over the experiments is indicated with the horizontal line while the grey zone gives the $\mu \pm 2\sigma$ interval zone.	60
Figure 3.1: view of the geometry for simulations in the rectangular duct. Inlet in beige, adiabatic wall in grey, outlet in orange. The location of the gypsum sample during the experiment is given in red.	64

Figure 3.2: view of a section of the channel near the fixed temperature wall for the different meshing strategies: grid 1S (a) and grid 2S(b). For grid 2S, different refinement levels are depicted.	65
Figure 3.3: mesh1F and 2F: view of a section of the channel at the inlet near the fixed temperature wall for the different meshing strategies. (a) Grid 1F with near wall refinement and (b) 2F without.....	66
Figure 3.4: view from the top of the mesh in the refinement region near the gypsum measurement location: (a) grid 2S for a high flowrate situation and (b) grid 2Fa.....	66
Figure 3.5: evaluation of the parameters describing the Nusselt profile for simulations at $Re = 104$ and $Pr = 2$. The exponential fit is given in red and the CFD values of Nu_x on the grid is black circles. (a) extraction of the fit parameters Nu_{max} and Nu_a for the simulation on Grid 1S and (b) extraction of Nu_0 and Nu_{2D} on Grid 2S.....	68
Figure 3.6: comparison of the Nusselt profile along the heated wall for the different CFD models for $Re = 100\ 000$ and $Pr = 10$. Computations with Fluent (green) and STAR-CCM+ (black).	69
Figure 3.7: asymptotic Nusselt number calculated with Grid 1F ((a) and (b)) and Grid 1S ((c) and (d)). The Nusselt is divided by Pr^c with $c= 0.39$ for 1F (b) and $c= 0.34$ for 1S (d).....	70
Figure 3.8: comparison of the different correlations given for the asymptotic Nusselt number for the different software and grids.....	71
Figure 3.9: comparison of the entrance effect for the different computations. (a) Maximum Nusselt number on the profile as a function of the Reynolds number for all computations. (b) Comparison for Grid 1S and 1F of the ratio Nu_{max}/Nu_a	72
Figure 3.10: evolution of the characteristic length of the exponential fit for Grid 1S and Grid 1F.	72
Figure 3.11: comparison of the asymptotic Nusselt number obtained from experimental correlations and numerical correlations for the different grids. The grey zone corresponds to the interval $Nu_{a,exp} \pm 2 \sigma_{exp}$ of the gypsum dissolution experiments correlation.	73
Figure 3.12 : relative bias on the calculation of the asymptotic Nusselt number compared to gypsum dissolution experimental data.....	74
Figure 3.13 : relative bias on the calculation of the asymptotic Nusselt number compared to Gnielinski correlation.....	75
Figure 3.14: levels of the Reynolds and Prandtl number for the uniform design $U_{50}(10^1 \times 5^1)$	78
Figure 3.15: data generated from a GP with a SE kernel and test points indicated with red crosses. The predictive mean is indicated with dashed line, the real function with a solid black line. The length scale l of the SE kernel is fixed with (a) $l = 0.3$. and (b) $l = 3$. Shades of grey indicate quantiles of the predictive distribution.	79
Figure 3.16: design of experiment used for the CFD runs for the propagation of five uncertain Reynolds numbers through the calculation of the Nusselt number with Deterministic Sampling.	81
Figure 3.17 :construction of the surrogate model for the established boundary layer Nusselt for Grid 2S. (a) Example of training (\circ) – evaluation (\square) separation of the data for one of the	

NS surrogate model created. (b) Resulting surrogate model mean and (c) standard deviation.	84
Figure 3.18 : <i>BIAS</i> and <i>STD</i> for the different computations	85
Figure 3.19: example of the resulting standard deviation of the Nu_{2D} for $Re = 100\ 000$. The CFD runs values are given with the symbols (\circ). The mean and standard deviation of Nu_{2D} are respectively given by the black cross and error bar. The total error bar length is 4σ	87
Figure 3.20: results of the uncertainty quantification with Deterministic Sampling for Grid 2S. The bias is close to zero and is indicated with text for each estimation point. The standard deviation is given with error bars.....	88
Figure 3.21 : comparison of the bias and standard deviation of $U_{inputs,exp}$ between method 1 and method 2 (in % of the CFD simulation prediction).....	88
Figure 3.22 : evolution of the model error mean and standard deviation for Prandtl number equal to 2 and 10 for grid 1S and 2S. The model error is estimated with gypsum data on (a) and (c), and with Gnielinski correlation (b) and (d). Cross symbols indicate the bias relatively to Nu_{CFD} and the error bar gives a $\pm \sigma_{E_{model}}$ interval.....	91
Figure 3.23 : evolution of the model error mean and standard deviation for Prandtl number equal to 2 and 10 for grid 1F and 2F. The model error is estimated with gypsum data on (a) and (c), and with Gnielinski correlation (b) and (d). Cross symbols indicate the bias relatively to Nu_{CFD} and the error bar gives a $\pm \sigma_{E_{model}}$ interval.....	92
Figure 4.1: Framatome's technical center facility – Steam generator water box mock-up.	96
Figure 4.2: Framatome's technical center facility – Steam generator water box mock up. (a) Partition plate with the four measurements location and the approximative location of the stagnation zone in red. (b) Inlet nozzle of the mock-up, the direction of the flow is indicated with the red arrow.	97
Figure 4.3: schematic view of the experimental setup.....	97
Figure 4.4: view of the measurement device for the partition plate: (a) Mass transfer measurement device (b) Heat transfer measurement device.....	98
Figure 4.5: flow zones in an impinging jet – zone 1, initial mixing zone ; zone 2, established jet ; zone 3, deflection zone ; zone 4, wall jet. From (Jambunathan, et al., 1992).....	100
Figure 4.6: effect of the nozzle/plate non dimensional distance on the radial variation of the heat transfer coefficient centered around the stagnation point. In red, the case $Z/D_H = 2$ corresponding to the mock-up situation is highlighted. From (Jambunathan, et al., 1992)...	101
Figure 4.7: radial distribution of the Nusselt number on a plate for an oblique circular jet impinging with an incidence angle $\theta = 45^\circ$. From (Ma, et al., 1997)	102
Figure 4.8: transversal velocity vector field downstream a 90° bend pipe and amplitude of the velocity indicated with a heat map. W_b is the bulk speed. From (Kalpakli & Örlü, 2013)...	102
Figure 4.9: evolution of the exponent a with the radial displacement from the stagnation point for the empirical law $Nu \propto Re^a$. From (Jambunathan, et al., 1992).....	103
Figure 4.10: evolution of the boundary conditions during dissolution for an experiment at $Re = 7.5 \cdot 10^5$ and $Sc = 1.2 \cdot 10^3$	104

Figure 4.11: example of the treatment of surface data obtained for an experiment on location 2: (a) raw wear Δh_r , (b) filtered wear Δh_f and (c) roughness matrix e	106
Figure 4.12: steps for the extraction of e_{pv} and l_{str} for $Re \approx 106$ and $Sc \approx 6 \cdot 10^2$ (a) division of the original surface in windows of $1\text{ cm} \times 1\text{ cm}$ and extraction of profiles for a given range of angles. (b) Example of profile inclined of $\theta \approx 30^\circ$ from the horizontal line and (c) associated height from which e_{pv} and l_{str} are extracted.	106
Figure 4.13: view of the measurement device with a computer aided design software. The iso-contours of temperature are given on a section of the model.	108
Figure 4.14: Reynolds and Schmidt numbers covered for the experiments on the partition plate on (a) location 1, (b) 2, (c) 3 and (d) 4. The given value corresponds to the average value during the dissolution.	109
Figure 4.15: evolution of the standard deviations of the operating conditions during the dissolution for all experiments (a) Reynolds number, (b) Schmidt number.	110
Figure 4.16: evolution of the surface average Sherwood number as a function of the Reynolds number on (a) location 1, (b) 2, (c) 3 and (d) 4. The different colors data obtained at $Sc = 6 \cdot 10^2$ (black) and $Sc = 1.2 \cdot 10^3$ (red),.....	111
Figure 4.17: evolution of $Sh_{mean}/Sc^{0.44}$ as a function of the Reynolds number at the different locations	112
Figure 4.18: evolution of the local Sherwood number over the gypsum sample for all locations at $Re \approx 4 \cdot 10^5$, $Sc \approx 1200$. The local value of the Sherwood number is indicated with a heat map (low Sherwood in blue and large values in red). The view is from the back of the partition plate which is given in a schematic way in (e). The estimated flow direction and stagnation region are indicated respectively with red arrows and dotted line circle.	113
Figure 4.19: relative information content (RIC) of the modes calculated from the POD for all the locations.	114
Figure 4.20: first three modes ϕ_1, ϕ_2, ϕ_3 of the POD on location 1 and associated components a_1, a_2, a_3 plotted as function of the Reynolds number during the dissolution.	116
Figure 4.21: Surface average truncation error with $N_{POD} = 1$ for the different experiments on location 1 (a) RMSE and (b) MAE.	117
Figure 4.22: correlation for a_1 as a function of the Reynolds number for location 1. The experimental points are depicted with circles, the fit is given with the purple dotted line....	117
Figure 4.23: first three modes of the POD on location 2 and associated components plotted as function of the Reynolds number during the dissolution.....	118
Figure 4.24: calculated bias between the reconstructed map and the original map when using one mode. (a) RMSE and (b) MAE for the different experiment on location 2.....	118
Figure 4.25: correlation for a_1 as a function of the Reynolds number for location 2. The experimental points are depicted with circles, the fit is given with the purple dotted line....	119
Figure 4.26: first three modes of the POD on location 3 and associated components plotted as function of the Reynolds number during the dissolution.	120
Figure 4.27: calculated bias between the reconstructed map and the original map when using one mode. (a) RMSE and (b) MAE for the different experiment on location 3	120

Figure 4.28: correlation for a_1 as a function of the Reynolds number for location 3. The experimental points are depicted with circles, the fit is given with the purple dotted line....	121
Figure 4.29: first three modes of the POD on location 4 and associated components plotted as function of the Reynolds number during the dissolution.....	122
Figure 4.30: calculated bias between the reconstructed map and the original map when using one mode. (a) RMSE and (b) MAE for the different experiment on location 4.....	122
Figure 4.31: correlation for a_1 as a function of the Reynolds number for location 4. The experimental points are depicted with circles, the fit is given with the purple dotted line....	123
Figure 4.32: boundary conditions Re, Pr swept for the different locations.....	125
Figure 4.33: evolution of the Nusselt number as a function of the Reynolds number at location 1. (a) evolution of Nu_U and Nu_D with the Reynolds number (fit plotted with solid line).....	126
Figure 4.34: comparison of the mean Nusselt number over the surface Nu_m at the different locations on the experimental range. Nu_D and Nu_U are given in purple dotted line for location 4.....	127
Figure 4.35: ratio Nu_U / Nu_D as a function of the Reynolds number for the different location on the partition plate. ($Pr = 4 : \nabla$, $Pr = 6 : \circ$, $Pr = 8 : \blacksquare$).	127
Figure 4.36: extraction of mass transfer data for transposition factor calculations (a) original Sherwood number distribution with extractions zones indicated inside the dotted lined circles. (b) Extracted zones U and D on which the surface average Sherwood numbers Sh_U and Sh_D are calculated.	129
Figure 4.37: ratio Nu_U / Nu_D as a function of the Reynolds number for the different location on the partition plate compared to Sh_U / Sh_D . The ratio is calculated from the original maps and the truncated POD of the Sherwood number Sh_1, Sh_2, Sh_3 calculated respectively with 1, 2 and 3 modes (blue, red and green).	131
Figure 4.38: evaluation of the transposition factor (a) F_1 , (b) F_2 and (c) F_3 for locations 1 (red), 2 (blue), 3 (green) and 4 (purple). Experimental points obtained at $Sc \approx 600$ (\circ) and $Sc \approx 1200$ (\square). Data obtained on zones U and D is given respectively with unfilled and filled symbol.....	133
Figure 4.39: effect of the roughness on the transposition factor. (a) Evolution of the transposition factor at $Sc = Pr = 1$ as a function of e_{pv}^+ on location 1 (red), 2 (blue), 3 (green) and 4 (purple) on U (\circ) and D (\square). (b) Evolution of the calculated e_{pv}^+ on U (\circ) and D (\square) as a function of the Reynolds number.....	134
Figure 4.40: comparison of the rough Sherwood number $Sh/Sc^{0.33}$ (black) to transposed Sherwood numbers Sh/F with $F = F_3$ (blue) and $F = F_W$ (red) (Wang & Ewing, 2017). The values estimated on position U are denoted with squares and D with triangles.	135
Figure 5.1: CAD model of the SGWB mock-up.....	140
Figure 5.2: view of the grid LREPOLY near the zone of interest: (a) in the water box (b) in the pipe upstream the water box.	141
Figure 5.3: view of the grid LRETET near the zone of interest: (a) in the water box (b) in the pipe upstream the water box.	142

Figure 5.4: design of experiment of the computations for grids LRE (blue) and HRE (red). 144	
Figure 5.5: heat transfer coefficient surface distribution calculated with CFD at $Re = 10^6$ and $Pr = 6$. Rear view of the partition plate.....	145
Figure 5.6: view of the vertical plane section including the jet axis on which the velocity field and turbulence is investigated.....	145
Figure 5.7: Example of prediction of the Nusselt number on the partition plate from the surrogate models a_1 , a_2 , a_3 and a_4 and the modes ϕ_1 , ϕ_2 , ϕ_3 and ϕ_4 for $Re = 8 \cdot 10^5$ and $Pr = 2$. The values of the surrogate models with respect to the Reynolds and Prandtl numbers and the surface distribution of the modes are indicated on a heat map with low values in blue and high values in red. The predicted Nusselt number is indicated on the right side of the figure.	146
Figure 5.8: view of the velocity on a plane section of the geometry. The magnitude Vn is given with a heat map.	148
Figure 5.9: comparison of Nusselt number calculated with STAR-CCM+ and Fluent on grid HRETET and HREPOLY. The comparison is done with the RKE model at $Re = 10^6$ and $Pr = 6$. The blue cross corresponds to the stagnation point.	150
Figure 5.10: surface distribution of ΔNu_{GRID} and $\Delta Nu_{SOFTWARE}$ on the partition plate.....	150
Figure 5.11: comparison of the turbulent kinetic energy computed with (a) STAR-CCM+ on HREPOLY, (b) Fluent and (c) STAR-CCM+ on HRETET at $Re = 10^6$	151
Figure 5.12: velocity on the first cell next to the partition plate. Computations with the polyhedral mesh for $Re \approx 5 \cdot 10^5$ and $Pr \approx 4$	153
Figure 5.13: ΔV_{GRID} for the different computations at $Re = 5 \cdot 10^5$ and $Pr = 4$ obtained on the polyhedral mesh	154
Figure 5.14: surface distribution of the Nusselt number on the partition plate at $Re \approx 5.5 \cdot 10^5$ $Pr \approx 4$ for the different turbulence models on grids LRETET and HRETET.	155
Figure 5.15: surface distribution of the Nusselt number on the partition plate at $Re \approx 4.8 \cdot 10^5$ $Pr \approx 4$ for the different turbulence models on grids LRES and HRES.	156
Figure 5.16: evolution of the Nusselt number amplitude on the different locations of the partition plate for the different turbulence models. a) Nu_1 , b) Nu_2 , c) Nu_3 and d) Nu_4 . ..	158
Figure 5.17: evolution of the surface distribution between $Re = 5 \cdot 10^5$ and $Re = 10^6$ at $Pr = 6$. The scale has been adapted by dividing the Nusselt by its maximum value.	160
Figure 5.18: modes calculated with the snapshots of the Nusselt number with the RKE model on grid LREPOLY	162
Figure 5.19: modes calculated with the snapshots of the Nusselt number obtained with the RKE model on grid HREPOLY	162
Figure 5.20: predictions of the components associated to the modes obtained with the RKE model on grids LREPOLY and HREPOLY. The predicted values are given with a heat map.	163
Figure 5.21: evolution of $\mu_{\Delta Nu_{Surrogate}}$ on the partition plate for the different models.	165
Figure 6.1: Overview of the measurements on the steam generator mock-up. (a) measurement locations on the partition plate. (b) View of the measurement device and	

evolution of the Nusselt number with the Reynolds number on position U and D . (c) View of the gypsum sample and examples of measured surface distribution on location 1 and 2.	171
Figure 6.3: Surface distribution of $MAE(x, y)$ and $RMSE(x, y)$ for the different location. The contour corresponds to the iso-values 3.75%, 7.5%, 11.25%, 15%.	173
Figure 6.4: Standard deviation of the experimental uncertainty on the Nusselt number for the different locations.	174
Figure 6.5: Examples of evolution of the mean Nusselt number over the partition plate with $1/N^3$ at $Re = 5.5 \cdot 10^5$ (LRETET and HRETET) and $Re = 4.6 \cdot 10^5$ (LREPOLY and HREPOLY). μ_{ENUM} is calculated from the difference between Nu_{exact} and $Nu(1/N^3)$ given in dashed lines. The standard deviation is calculated by averaging the error between the fit regression and the data (black filled circles).	176
Figure 6.6: Local values of μ_{ENUM} and σ_{ENUM} on the partition plate at $Re = 5 \cdot 10^5$	177
Figure 6.7: Example of surface distribution $\sigma_{U_{inputs}}$ on the partition plate at $Re = 2.5 \cdot 10^5$ and $Pr = 6$	180
Figure 6.8: (a) Measurement locations and (b) example of surface distribution of the Nusselt number obtained with the different models	181
Figure 6.9: Example of the extraction of the RMSE between the experimental Nusselt number Nu_{EXP} and the CFD Nusselt number extracted on a window around the experimental location. The Nusselt number distribution Nu_{BEST} is extracted from the partition plate by translating the location as indicated on (a) The RMSE is calculated from comparison windows translated in the square dashed window. The original comparison window is given in black solid lines. The minimum RMSE location on which Nu_{BEST} is extracted is given in red. The comparison is shown on (b).	182
Figure 6.10: Average over the range $Re \in [10^5, 10^6]$ of the local relative error between Nu_{RKES} , Nu_{RKEF} and Nu_{EXP}	184
Figure 6.11: Evolution of the deviation between Nu_{CFD} and Nu_{EXP} . The MAE is given in black solid line, the min and max value of the absolute error over the surface are given in dotted line respectively in blue and red. The RMSE is given with solid dashed line.	185
Figure 6.12: Example of minimum RMSE extraction on location 4 for $RKES$	186
Figure 6.13: Comparison of ΔNu on location 3 for the original location and the moved window.	186
Figure 6.14: Evolution of the deviation between Nu_{CFD} and Nu_{EXP} with the windowed approach. The evolution of the minimum RMSE over the window is given in red. Its mean value in solid black line.	187
Figure 6.15: Average over the range $Re \in [10^5, 10^6]$ of the local relative error between Nu_{KOSST} , Nu_{SAS} and Nu_{EXP}	190
Figure 6.16: Evolution of the deviation between Nu_{CFD} and Nu_{EXP} for the KOSST and SAS models. The MAE is given in black solid line, the min and max value of the absolute error over the surface are given in dotted line respectively in blue and red. The RMSE is given with solid dashed line.	191
Figure 6.17: Example of displacement of the comparison with the SAS model for $Re = 4.5 \cdot 10^5$ and $Re = 5.5 \cdot 10^5$	192

Figure 6.18: Evolution of the deviation between Nu_{CFD} and Nu_{EXP} for the KOSST and SAS models with the windowed approach. The evolution of the minimum RMSE over the window is given in red. Its mean value in solid black line, while a $\mu \pm 2\sigma$ interval is given in grey.	193
Figure 6.19: evolution of the mean value and standard deviation of the model error E_{model} of the RKE model relatively to the mean value over the partition plate. The model error is calculated on location 1 (red), 2 (blue), 3 (green) and 4 (purple). The computations with STAR-CCM+ are given in solid lines while the dashed lines are obtained from Fluent computations	197
Figure 6.20: evolution of the mean value and standard deviation of the model error E_{model} of the SAS (dashed lines) and KOSST (solid lines) models relatively to the mean value over the partition plate. The model error is calculated on location 1 (red), 2 (blue), 3 (green) and 4 (purple)	197
Figure A.1: ensembles of two parameters without any covariance (left) with positive covariance (right)	A-2
Figure B.1: example of steps for the extraction of the ridges angle	B-1
Figure B.2: example of non-connected elements. The element (a) is filtered due to a too important aspect ratio while element (b) combines an acceptable aspect ratio in regard to the maximum length and a low enough fractal dimension	B-2
Figure B.3: Example of the calculation of the mean value and standard deviation of the flow direction with the algorithm presented on a sample exposed to the flow on location 2. On the left side, the mean value μ is given with blue filled circles while the standard deviation σ is given with the error bar indicating $\mu \pm 2\sigma$ intervals. On the right side, the heat map indicates the amplitude of the wear with red values relating to maximum values and blue to minimum values. The black arrows give the mean direction of the flow, and the red arrows give $\mu \pm 2\sigma$ intervals on the flow direction	B-3
Figure C.1: surface distribution of the four first POD modes ϕ_1, ϕ_2, ϕ_3 and ϕ_4 obtained with snapshots of the Nusselt number calculated with the KOSST model on LREPOLY	D-2
Figure C.2: surface distribution of the four first POD modes ϕ_1, ϕ_2, ϕ_3 and ϕ_4 obtained with snapshots of the Nusselt number calculated with the KOSST model on HREPOLY	D-2
Figure C.3: surface distribution of the four first POD modes ϕ_1, ϕ_2, ϕ_3 and ϕ_4 obtained with snapshots of the Nusselt number calculated with the SAS model on LREPOLY	D-3
Figure C.4: surface distribution of the four first POD modes ϕ_1, ϕ_2, ϕ_3 and ϕ_4 obtained with snapshots of the Nusselt number calculated with the SAS model on HREPOLY	D-3
Figure C.5: surface distribution of the four first POD modes ϕ_1, ϕ_2, ϕ_3 and ϕ_4 obtained with snapshots of the Nusselt number calculated with the RKE model on LRETET	D-4
Figure C.6: surface distribution of the four first POD modes ϕ_1, ϕ_2, ϕ_3 and ϕ_4 obtained with snapshots of the Nusselt number calculated with the RKE model on HRETET	D-4
Figure C.7: MAE calculated between the truncated POD and the original snapshots with four modes	D-6
Figure C.8: predictions of the components associated to the modes obtained with the KOSST model on grids LREPOLY and HREPOLY. The predicted values are given with a heat map	D-8

Figure C.9: predictions of the components associated to the modes obtained with the KOSST model on grids LREPOLY and HREPOLY. The predicted values are given with a heat map. .D-9

Figure C.10: predictions of the components associated to the modes obtained with the RKE model on grids LRETET and HRETET. The predicted values are given with a heat map...D-10

List of Tables

Table 1.1: from (Shih, et al., 1995): model coefficient for RKE turbulence model.....	10
Table 1.2: from (Menter, 1994)-: model coefficient for KOSST turbulence model.....	11
Table 1.3: near wall velocity in the different region of the boundary layer	16
Table 2.1 : correlation from literature.....	58
Table 3.1: dimensions of the rectangular channel.	63
Table 3.2 : approximate number of cells for the different grids.	65
Table 3.3 : physical properties of Water.....	67
Table 3.5 : coefficient of the fitted power law fit on Nu_{2D} (3.5)	71
Table 3.4 : approaches used for uncertainty propagation through RANS simulations with the different grids.....	82
Table 4.1 : correlation from literature.....	102
Table 4.2 : coefficient a, b of the power law fitted on the experimental data	126
Table 5.1 : number of cells in the different grids.....	141
Table 5.2: summary of the physical model for the CFD simulations	143
Table 5.3: physical properties of the fluid	143
Table 5.4: statistics on the field $ \mathbf{Vn} $ for the different computations.....	154
Table 6.1: σ_ϕ/ϕ mean and maximum values, estimated with the MAE and RMSE	172
Table 6.2: σ_ϕ/ϕ on U and D	172
Table 6.3: Number of cells of the different grids. The reference grids are given with bold characters.	176
Table 6.4: μ_{ENUM} and σ_{ENUM} averaged over the partition plate	177
Table 6.5: μ_{ENUM} and σ_{ENUM} averaged over the partition plate.....	183

Nomenclature

CFD and experiments

Symbol	Signification
Greek letters	
α	Thermal diffusion coefficient
α_t	Turbulent thermal diffusion coefficient
ϵ	Turbulent dissipation rate
δ_{ij}	Kronecker delta function
κ	Von Karman constant
λ	Thermal conductivity
λ	Head loss coefficient (§2.2.3)
μ	Dynamic viscosity
ν	Kinematic viscosity
ν_t	Turbulent kinematic viscosity
ϕ	Non dimensional concentration
ϕ_k	Mode obtained with the proper orthogonal decomposition
ρ	Density
$\underline{\sigma}$	Stress tensor.
$\tau, \underline{\tau}$	Shear stress, shear stress tensor
θ	Non dimensional temperature
Roman letters	
a_k	Coefficient of the proper orthogonal decomposition
c	Concentration
C_p	Specific heat coefficient
D_H	Hydraulic diameter
D_m	Mass diffusion coefficient
e	Roughness height
e_{pv}	Peak to valley height roughness
e^+	Non dimensional roughness height $e^+ = eu^*/\nu$
g	Gravity acceleration

h_{conv}	Convective heat transfer coefficient
k	Turbulent kinetic energy
K_c	Mass transfer coefficient
L	Characteristic length
l_{str}	Streamwise spacing of roughness elements
P	Pressure
q, q_w	Heat flux, wall heat flux
R	Radius
$\underline{\mathbf{R}}$	Reynolds stress tensor
$\underline{\mathbf{S}}$	Strain rate tensor
t	Time
T	Temperature
T^+	Non dimensional temperature $T^+ = \frac{\rho C_p u^* (T - T_w)}{q_w}$
\mathbf{u}	Velocity
u^*	Friction velocity
u^+	Non dimensional velocity $u^+ = u/u^*$
U	Characteristic velocity of a flow configuration
\mathbf{V}_n	Non dimensional velocity $\mathbf{V}_n = \mathbf{u}/U$
\mathbf{x}	Position
y^+	Non dimensional wall distance $y^+ = yu^*/\nu$

Non dimensional numbers

C_f	Skin friction drag $C_f = \frac{\tau_w}{\frac{1}{2}\rho u^2}$
f	Darcy friction coefficient
Nu	Nusselt number $Nu = \frac{hL}{\lambda}$
Pr	Prandtl number $Pr = \frac{\mu C_p}{\lambda}$
Re	Reynolds number $Re = \frac{UL}{\nu}$
Sc	Schmidt number $Sc = \frac{\nu}{D_m}$
Sh	Sherwood number $Sh = \frac{K_c L}{D_m}$
St_h, St_m	Stanton number for heat and mass transfer $St_h = \frac{Nu}{RePr}$, $St_m = \frac{Sh}{ReSc}$

Punctuation

X_t	Turbulent quantity
X_w	Wall quantity
X^+	Quantity non dimensionalized by turbulent length or time scale
$\langle X \rangle_t, \bar{X}$	Time average of quantity X

Uncertainty quantification

Symbol	Signification
Greek letters	
δ_X	Realization of the random variable X
δX	Centered random variable associated to the random variable X
μ_X	Mean value of the random variable X
ρ	Pearson correlation coefficient
σ_X	Standard deviation of the random variable X
Roman letters	
$Cov(X_i, X_j)$	Covariance between the random variables X_i and X_j
$E_{CFD/EXP}$	Random variable related to the error between CFD and experiment
E_{NUM}	Random variable related to the numerical error
E_{model}	Random variable related to the model error
f_X	Probability density function of the random variable X
Punctuation	
$\langle X^n \rangle$	Statistical moment of order n of the random variable X
$\langle \delta X^n \rangle$	Statistical centered moment of order n of the random variable X

Introduction

The knowledge of the flow behavior and of the heat transfers taking place in a nuclear reactor is essential to ensure the safety of the nuclear plant, whether it is in operating conditions, or incidental and accidental situations. From the thermal hydraulic aspect, the design of the primary circuit must take in considerations the thermal shocks than can occur in accidental situations in order to guarantee its physical integrity and the confinement of radioactivity. The thermal shocks are estimated from the convective heat transfer coefficient near solid boundaries, which is measured experimentally or obtained from numerical simulations.

In the last decades, the boost of the computational power in industry resulted in the progressive replacement of the experimental approach by a numerical approach using Computational Fluid Dynamics (CFD) softwares. Their use in the nuclear industry requires a prior step of validation and verification (V&V). On one hand, the verification relates to the numerical implementation of the equations in the code (solver) and will not be covered in this document. On the other hand, the validation concerns the physical validity of the model used for the calculations which is partly investigated in this dissertation.

In the nuclear industry, the validation process of CFD for heat transfer coefficient calculation is done according to the guidelines suggested by the American Society of Mechanical Engineers (ASME) (Coleman & Members, 2009). The results of simulations are compared to experimental measurements, and the different sources of uncertainty which affect the comparison are considered in order to increase the reliability of the validation process. This validation has been performed in the past with experimental data obtained on reduced scale mock-ups. The Reynolds number obtained in these experiments are lower than in a nuclear reactor. The validation on these experiments were found to yield results with a good agreement between CFD and experiments. The motivation of this work is to verify that the accuracy of CFD calculations of the heat transfer coefficient does not evolve between the validation scale on reduced scale mock-ups and the reactor scale. More precisely, the model error, relating to the accuracy of the turbulence modelling with CFD, has been investigated for Reynolds number approaching the reactor scale. In this context, the transposition error is defined from the evolution of the model error between the mock-up and the reactor scale and is investigated in this dissertation.

For this purpose, experimental measurements of the heat transfer coefficient were retrieved at different turbulence regimes, and numerical simulations were launched for comparisons.

Therefore, this work combined experimental, numerical and theoretical aspects which will be discussed in this dissertation. The experimental aspect of this work is certainly the most important one, as the reliability of the uncertainty quantification process is mainly affected by the reliability of the measurements taken as reference.

The first chapter focuses on the physical models underlying the calculation of heat transfer coefficient with CFD in industry and gives a short introduction to the uncertainty quantification process and to methods used for the evaluation of different sources of uncertainty.

The second step of this work has been to develop a methodology to generate heat transfer data from gypsum dissolution measurements through the lens of the analogy between heat and mass transfer. Preliminary tests have been conducted in a rectangular channel which is a well-documented flow configuration in literature. It has been observed that the surface aspect of the gypsum sample evolves during the experiments. The surface presents initially a smooth aspect, which is roughened as the gypsum dissolves in water. Therefore, the methodology had to consider this surface aspect for the comparison to smooth wall data. The methodology and the measurements for Reynolds number in the range $[10^4, 10^5]$ are presented in Chapter 2.

Then, CFD simulations were launched in order to estimate the accuracy of the calculated heat transfer coefficient in comparison to the experiments in the rectangular channel. Moreover, two uncertainty propagation technique were compared in this case. The Chapter 3 includes the presentation of the CFD model, the comparison to experiments and the results of a partial uncertainty quantification process as all the sources of error or uncertainties have not been quantified. This preliminary study also gives a first insight on the evolution of the model error on the experimental range.

The validation approach presented in Chapter 2 and Chapter 3 has then been adapted for the case of a $1/5^{\text{th}}$ scale mock-up of a steam generator water box. The quantity of interest is the heat transfer coefficient on a plate impinged by a jet. A heat transfer coefficient measurement device has been designed in order to include additional heat transfer data. Crossed measurements of heat and mass transfer coefficient were carried out to verify experimentally the heat and mass transfer analogy and to obtain estimations of the transposition factor. Moreover, the proper orthogonal decomposition has been introduced during these experiments in order to process the surface distribution of the mass transfer coefficient more efficiently. The experiments and their analysis are presented in Chapter 4. Moreover, this chapter includes a short bibliography on impinging jets.

The experiments were then reproduced with CFD simulations with different turbulence models, grids and software in Chapter 5. In this chapter, the effect of the turbulence model, grid and

near wall meshing on the calculation of the Nusselt number is investigated. Moreover, surrogate models were designed based on the computations that were performed.

Finally, the quantification of the different sources of error and uncertainty leading to the calculation of the model error are presented in Chapter 6. The evolution with respect to the Reynolds number is depicted in order to verify that the accuracy of the simulations is not impaired when reaching the reactor scale.

Chapter 1 Uncertainty quantification applied to Computational Fluid Dynamics

The increase of computational power in the last decades has boosted the use of *Computational Fluid Dynamics* (CFD) for the modelling of turbulent flows in the industry. CFD became an essential tool making easier the design, being in aeronautics, spatial applications, nuclear industry and many others sector. Moreover, the reliability of the models has increased with time as authors in the scientific literature studied and calibrated them.

In the nuclear industry, CFD has been used in order to develop new designs and improve the safety of nuclear plants. Their use requires a V&V (*Validation and Verification*) process in order to determine the reliability of the calculation for safety or design. This validation is carried out in the frame of uncertainty quantification (UQ), which consists in the identification of the different sources of uncertainty when comparing experiments and CFD simulations. The ASME (*American Society of Mechanical Engineers*) gave guidelines in (Coleman & Members, 2009) for the validation and verification of CFD codes for heat transfer computations which have been adopted by the industrials. On one hand, the verification step concerns the numerical implementations of the solver and will not be covered in this dissertation. On the other hand, the validation aims to determine the deviation between computations and real-life situations. This validation relies on experimental data that is essential to have a reliable assessment of the accuracy of the codes. In nuclear plants, the obtention of heat transfer data in operating conditions is hardly conceivable due to the technical feasibility of measurements, thus, validation is done on reduced scale mock-ups in experimental facilities (Dolleans, et al., 2008; Goreaud, et al., 2004; Barbier, et al., 2009) for the different applications. Elements on the validation of RANS CFD simulations for the hydraulic behavior prediction in a nuclear plant are given in (Martinez & Galpin, 2014). An overall good agreement has been found between the experimental measurements and the CFD simulations.

Most of the time, it is assumed that the accuracy of the CFD models is Reynolds number independent. The error between simulations and experiments is quantified on the reduced scale mock-up and transposed to the reactor scale. This assumption seems to be corroborated by elements in literature (Mannini, et al., 2010; Patel, et al., 1985), indicating that RANS simulations are more adapted to high turbulence regime, as the hydraulic behavior gets more regular, hence more predictive.

The main objective of this dissertation is to study the evolution of the accuracy of CFD simulations when the Reynolds number increases to verify the transposability assumption. In this section, the principles for the modelling of turbulent flows and heat transfer with CFD codes are first presented. Then, the nomenclature given by the ASME for uncertainty quantification will be given, in addition to basics on statistics used for UQ.

1.1 CFD Computations of heat transfer coefficient

1.1.1 Conservation equations

The computation of the heat transfer coefficient relies on the modelling and resolution of the flow field for a given flow configuration and set of boundary conditions. The fluid flow evolves according to the three following principles:

- Conservation of mass
- Conservation of momentum
- Conservation of energy

These three conservation principles lead to the general equations of mass, momentum and energy conservation, which can be applied to simulate the flow field and the heat exchanges.

The equations are written in Cartesian coordinates with the notation (x_1, x_2, x_3) , the velocity is written $\mathbf{u} = (u_1, u_2, u_3)$, its component in the x_i -direction is written u_i . In general, the x_i component of a vector is called by adding the index i to its original notation. The time dependency is depicted by the time variable t . The tensor notation and Einstein notation is used with Cartesian coordinates system in the following section. The other variables included in the modelling of turbulent flow and heat transfer are, the density ρ , the pressure P , temperature T , total energy E , specific heat coefficient C_p , dynamic viscosity μ , thermal conductivity λ , the gravitational acceleration constant g .

Continuity equation:

The continuity equation calculated from the mass conservation is given by the following equation:

$$\frac{\partial \rho}{\partial t} + \frac{\partial(\rho u_j)}{\partial x_j} = 0 \quad (1.1)$$

Momentum equations:

The conservation of momentum leads to three equations for each spatial direction. The equation in the x_i direction is given by:

$$\frac{\partial}{\partial t}(\rho u_i) + \frac{\partial}{\partial x_j}(\rho u_i u_j) = \frac{\partial}{\partial x_j}(\sigma_{ji}) + \rho g_i \quad (1.2)$$

Here, $\underline{\sigma} = (\sigma_{ij})_{i,j \in [1,3]^2}$ is the stress tensor.

The convective term on the left side of the equation can be re-expressed by using the mass conservation equation (1.1) :

$$\frac{\partial}{\partial t}(\rho u_i) + \frac{\partial}{\partial x_j}(\rho u_i u_j) = \rho \left[\frac{\partial u_i}{\partial t} + u_j \frac{\partial}{\partial x_j} u_i \right] + u_i \left[\frac{\partial \rho u_j}{\partial x_j} + \frac{\partial \rho}{\partial t} \right] = \rho \left[\frac{\partial u_i}{\partial t} + u_j \frac{\partial}{\partial x_j} u_i \right]$$

which leads to the following formulation:

$$\rho \left[\frac{\partial u_i}{\partial t} + u_j \frac{\partial}{\partial x_j} u_i \right] = \rho \frac{Du_i}{Dt} = \frac{\partial}{\partial x_j}(\sigma_{ji}) + \rho g_i$$

The operator $\frac{D}{Dt}$ represents the “*material derivative*”

Energy equation

The conservation of energy for a single species without heat source can be written for the total energy E as following with the material derivative:

$$\rho \frac{DE}{Dt} = -\frac{\partial}{\partial x_j} q_j + \frac{\partial}{\partial x_j} (u_i \sigma_{ji}) + u_i \rho g_i \quad (1.3)$$

Here, $\mathbf{q} = (q_j)_{j \in [1,3]}$ represents the heat flux.

Simplification of the equations

Hypotheses are given to simplify the equation and express the unknown quantities:

- Newtonian fluid: the viscous stress field is linearly proportional to the strain rate field
- Stokes hypothesis: the change of volume does not involve viscosity.
- Fourier conduction law for heat transfer with constant thermal conductivity λ
- Incompressible flow
- Constant density
- Constant viscosity
- No volumetric heat sources

For an incompressible flow, the continuity equation (1.1) is reduced to:

$$\frac{\partial u_j}{\partial x_j} = 0 \quad (1.4)$$

For a Newtonian fluid, the stress tensor can be expressed as following:

$$\sigma_{ij} = -P\delta_{ij} + \tau_{ij}$$

δ_{ij} is Kroenecker symbol which can be seen in this case as the identity matrix or the unitary tensor, τ_{ij} is the viscous stress tensor.

The strain rate tensor S_{ij} related to the deformation of the fluid is defined by:

$$S_{ij} = \frac{1}{2} \left(\frac{\partial u_i}{\partial x_j} + \frac{\partial u_j}{\partial x_i} \right)$$

By assuming the previously enounced hypotheses, the viscous stress tensor can be expressed as following:

$$\tau_{ij} = 2\mu S_{ij} - \frac{2}{3}\mu S_{kk}\delta_{ij}$$

leading to,

$$\sigma_{ij} = -P\delta_{ij} + 2\mu S_{ij} - \frac{2}{3}\mu S_{kk}\delta_{ij}$$

and, by reinjecting the expression of σ_{ij} in (1.2):

$$\frac{\partial}{\partial t}(\rho u_i) + \frac{\partial}{\partial x_j}(\rho u_i u_j) = -\frac{\partial P}{\partial x_i} + \frac{\partial}{\partial x_i} \left(2\mu S_{ij} - \frac{2}{3}\mu S_{kk}\delta_{ij} \right) + \rho g_i$$

For constant dynamic viscosity and incompressible flow, it is possible to simplify further this equation:

$$\frac{Du_i}{Dt} = -\frac{1}{\rho} \frac{\partial P}{\partial x_i} + \nu \frac{\partial^2 u_i}{\partial x_i^2} + g_i \quad (1.5)$$

with, $\nu = \mu/\rho$ the kinematic viscosity.

For the energy conservation equation, an alternative equation can be written for the internal energy. An equation is obtained for the mechanical energy by multiplying the momentum conservation equation (1.2) by \mathbf{u} . By subtracting the total energy equation (1.3) by the mechanical energy equation, the following equation without heat sources for the internal energy e_i can be written:

$$E = e_i + \frac{1}{2}u_i^2$$

$$\frac{De_i}{Dt} = -P \frac{\partial u_j}{\partial x_j} - \frac{\partial q_j}{\partial x_j} + \frac{\partial}{\partial x_j} (u_i \tau_{ji})$$

The term $\frac{\partial}{\partial x_j} (u_i \tau_{ji})$ and $-P \frac{\partial u_j}{\partial x_j}$ relate respectively to the power of the viscous forces and to the power of the pressure force. The conduction heat flux is given by Fourier heat conduction law:

$$q_j = -\lambda \frac{\partial T}{\partial x_j}$$

Another formulation can be obtained by introducing the static enthalpy defined by:

$$h_s = e_i + \frac{P}{\rho}$$

It can be shown that the energy equation can be expressed as following (Bejan, 2013) without volumetric source of energy:

$$\rho \frac{Dh_s}{Dt} = \frac{\partial}{\partial x_j} \left(\lambda \frac{\partial T}{\partial x_j} \right) + \frac{DP}{Dt} + \frac{\partial}{\partial x_j} (u_i \tau_{ji})$$

Finally, by introducing the specific heat and the thermal expansion coefficient of the fluid:

$$C_p = \left(\frac{\partial h_s}{\partial T} \right)_p, \quad \beta = -\frac{1}{\rho} \left(\frac{\partial \rho}{\partial T} \right)_p$$

it is possible to rewrite the left-hand side as following (Bejan, 2013):

$$\rho \frac{Dh_s}{Dt} = \rho \left[\frac{\partial h_s}{\partial t} + u_j \frac{\partial h_s}{\partial x_j} \right] = \rho C_p \frac{DT}{Dt} + (1 - \beta T) \frac{DP}{Dt}$$

This leads to the temperature formulation of the energy conservation equation:

$$\rho C_p \frac{DT}{Dt} = \frac{\partial}{\partial x_j} \left(\lambda \frac{\partial T}{\partial x_j} \right) + \beta T \frac{DP}{Dt} + \frac{\partial}{\partial x_j} (u_i \tau_{ji})$$

In the case of low Mach number, the term relating to the viscous stress can be neglected, moreover, for incompressible liquids, $\beta = 0$, leading to the simplified equation:

$$\rho C_p \frac{DT}{Dt} = \frac{\partial}{\partial x_j} \left(\lambda \frac{\partial T}{\partial x_j} \right) \quad (1.6)$$

For constant thermal conductivity, the equation can be simplified to:

$$\frac{DT}{Dt} = \alpha \frac{\partial^2 T}{\partial x_j^2} \quad (1.7)$$

with, $\alpha = \lambda / (\rho C_p)$ the thermal diffusivity in the fluid.

In monophasic thermal hydraulic studies, the energy equation is used most of the time in the form (1.6) or (1.7). A similar equation can be given for the transport of a single species in solution without mass sources. The equation can be written for the concentration c as following:

$$\frac{Dc}{Dt} = D_m \frac{\partial^2 c}{\partial x_j^2} \quad (1.8)$$

where D_m is Fick's law diffusion coefficient which is assumed to be constant.

1.1.2 Non dimensional numbers

The conservation equations include different fluxes and forces, which can be expressed with non-dimensional quantities.

The Reynolds number gives the ratio between inertial forces and viscous forces:

$$Re = \frac{UL}{\nu}$$

where U is a characteristic velocity of the fluid, L is a characteristic length which definition depends on the configuration of the flow. For instance, in pipe flow, $L = D_H$ the hydraulic diameter of the pipe, for impinging jet, D_H is the diameter of the nozzle. The characteristics of the flow turbulence depends on this Reynolds number. For instance, in pipes, distinct behaviors are observed around a critical Reynolds number $Re_c \approx 1000$: for $Re \ll Re_c$, the viscosity effects are dominant, and the effect of shear stress due to the velocity gradients are limited. In this case called laminar flow, the solution of the equation is deterministic. For higher Reynolds numbers, the regime is turbulent. In these regimes, random fluctuations and chaotic behaviors are observed. This regime of flow involves higher rates of mixing leading to increased heat and mass transfer rates near boundaries and in the bulk. In a nuclear reactor, this particular property of turbulence is of interest because it leads to a more efficient cooling of the core of the reactor.

The Prandtl number gives the ratio between the momentum diffusion coefficient and the heat transfer diffusion coefficient:

$$Pr = \frac{\nu}{\alpha} = \frac{\mu C_p}{\lambda}$$

where α and ν are respectively the heat diffusion coefficient and the kinematic viscosity of the fluid. In heat transfer studies, the value of the Prandtl number is of importance and affects the behavior of the heat fluxes near walls:

- for low Prandtl numbers ($Pr \ll 1$), the thermal diffusivity dominates, and the heat conduction is more significant than the convection. This is the case for liquid metals such as liquid sodium, or mercury.
- for intermediate Prandtl numbers ($Pr \sim 1$), the heat and momentum are dissipated equally, the heat transfer is thus a combination of convection and conduction. This is the case for a lot of gases.
- for large Prandtl numbers ($Pr \gg 1$), the momentum is much more dissipated and heat transfers are mainly driven by convection. This is the case of oils since they have low thermal conductivity.

The Schmidt number is analogous to the Prandtl number for mass transfer and is defined by:

$$Sc = \frac{\nu}{D_m}$$

with, D_m the mass diffusion coefficient of the species in solution in the flow.

The heat/mass transfer at the fluid/wall interface can be described with the Nusselt/Sherwood number being defined respectively by:

$$Nu = \frac{h_{conv} D_H}{\lambda}, \quad Sh = \frac{K_C D_H}{D_m}$$

where, h_{conv} and K_C are respectively the convective heat transfer coefficient and the mass transfer coefficient. D_H is a characteristic length defined as in the Reynolds number.

1.1.3 Modelling of turbulence

1.1.3.1 Introduction

Turbulent flows are by nature unsteady and chaotic. The resolution of the conservation equations (1.4), (1.5) and (1.7) written earlier for this regime is more challenging than for laminar flow. As explained in §1.1.3.2 one of the particularities of turbulent flow is the random fluctuations of the velocity. In these flows, the presence of eddies affects importantly the mixing and the heat and mass transfers near walls. Elements on the theoretical study of turbulent flows and their modelling can be found in (Pope, 2000). The equations given previously are complete in the sense that they do not require additional variables/equations in order to reproduce turbulent flow. Nevertheless, computing these equations requires an adequate time and space discretization in order to capture all the physical phenomenon, from the smaller eddy to the larger one. This approach is called *Direct Numerical Simulation* (DNS) and elements can be found in §9 of (Pope, 2000). The limiting aspect of this approach is the computing power required. In fact, the different scales (time, length) of the smaller eddies decrease with respect to the Reynolds number, such as the time required to compute industrial flow grows sharply to non-affordable CPU costs (see for instance §8.2 in (Pope, 2000)).

Thus, alternative strategies are used. These methods rely on additional equations to model the eddies that are not captured by the mesh and their impact on the flow. Most of the time, RANS (Reynolds Averaged Navier Stokes) methodologies are used to model the impact of turbulence for an affordable cost. This approach is compatible with the use of grids with cells larger than the smallest eddies and represents only the largest ones. The smaller eddies characteristics are often described by turbulent quantities (turbulent kinetic energy, dissipation, viscosity, length ...) which are transported in the flow.

Large Eddy Simulation (LES) is another approach which is between the most complicated RANS model and DNS simulation in term of computational cost. In this methodology, the larger turbulent structures are represented; and the smaller structures lower than to the grid size are modelled with a sub grid model. An introduction is given in §13 in reference (Pope, 2000).

1.1.3.2 Reynolds Average of Navier Stokes Equations

The RANS methodology is based on the decomposition of all the physical quantities as the sum of a steady contribution and a fluctuating term. This idea has been given the first time by Osborn Reynolds (Reynolds, 1895) from which the non-dimensional number is named. This proposal is based on experimental observations of the fluctuations associated to turbulence flow.

The RANS decomposition can be written for a physical quantity ϕ as following:

$$\phi = \bar{\phi} + \phi', \quad \overline{\phi'} = 0, \quad \overline{\bar{\phi}} = \bar{\phi}$$

where, $\bar{\phi}$ corresponds to the time average value of the quantity ϕ , ϕ' is the fluctuating part which time average value is zero. The instantaneous equations (1.4) (1.5) and (1.7) are then averaged regarding time in order to obtain for an incompressible flow with constant density and viscosity, the following RANS equations (Pope, 2000):

$$\begin{aligned} \frac{\partial \bar{u}_j}{\partial x_j} &= 0 \\ \frac{D\bar{u}_i}{Dt} &= -\frac{1}{\rho} \frac{\partial \bar{P}}{\partial x_i} + \frac{\partial}{\partial x_j} \left(\nu \frac{\partial \bar{u}_i}{\partial x_j} - \overline{u'_i u'_j} \right) + g_i \\ \frac{D\bar{T}}{Dt} &= \frac{\partial}{\partial x_j} \left(\alpha \frac{\partial \bar{T}}{\partial x_j} - \overline{u'_j T'} \right) \end{aligned}$$

It is noticeable that the RANS modelling of turbulence involves the same equations as (1.4) (1.5) and (1.7) for the mean quantities with an additional term due to the turbulent fluctuations. For the momentum equations, the appearing term is named Reynolds's stress tensor and is defined as following:

$$R_{ij} = \overline{u'_i u'_j}$$

In the energy equation, the additional term due to the turbulent fluctuations is:

$$q_{j,turb} = \rho C_p \overline{u'_j T'}$$

An analogous equation can be given for the transport equation of a single species in solution based on equation (1.8). The Reynolds decomposition for concentration c is applied yielding the following equation:

$$\frac{D\bar{c}}{Dt} = \frac{\partial}{\partial x_j} \left(D_m \frac{\partial \bar{c}}{\partial x_j} - \overline{u'_j c'} \right)$$

The RANS equations provided are still insufficient to solve the problem. Additional equations are required in order to solve the Reynolds stress tensor and the turbulent heat and mass fluxes. The eddy viscosity model is a simple approach to model turbulence. It relies on the calculation of an eddy viscosity with additional equations, which is then used to express the Reynolds stress tensor and the turbulent heat flux from the mean flow quantities. Most of the computations carried out in industry are based on this approach, as the computational cost and performance make it attractive.

1.1.3.3 Eddy viscosity model

1.1.3.3.1 Introduction

Eddy viscosity modelling of turbulence relies on the existence of an *eddy viscosity* ν_t from which the Reynolds stress tensor is expressed in combination to the mean strain rate tensor. This relation is written (Pope, 2000):

$$R_{ij} = \overline{u'_i u'_j} = \frac{2}{3} k \delta_{ij} - 2\nu_t \overline{S_{ij}}$$

with, k the turbulent kinetic energy and $\overline{S_{ij}}$ the mean strain rate tensor defined as:

$$\overline{S_{ij}} = \frac{1}{2} \left(\frac{\partial \overline{u_i}}{\partial x_j} + \frac{\partial \overline{u_j}}{\partial x_i} \right)$$

In this case, the Reynolds stress is calculated from the mean flow, at the condition that additional equations are given to compute ν_t . Different models can be used for the calculation of ν_t :

- algebraic models based on a mixing length: see the models given in (Baldwin & Lomax, 1978) or in (Smith & Cebeci, 1967). These simple zero-equation models are used to express the turbulent viscosity as a function of the boundary layer velocity profile.
- one-equation models: such as Prandtl model (Prandtl & Weighardt, 1945) where a mixing length l_m is still specified with an additional transport equation for the turbulent kinetic energy k enabling the computation of ν_t .
- two-equation models: transport equations are solved for two turbulent quantities which can be combined in order to extract all the other turbulent quantities of interest (turbulent length scale, turbulent timescale, eddy viscosity). Most of the models used in industry are from this class of models.
- nonlinear eddy viscosity models

The following sections will present two models that will be used in order to compute the heat transfer coefficient in the present work.

1.1.3.3.2 Realizable $k - \epsilon$ model

The $k - \epsilon$ model relies on the computations of the turbulent kinetic energy k relating to the energy of the velocity fluctuations and the turbulent dissipation rate ϵ which relates to their dissipation. Two transport equations are given for their calculation. In its standard version, the eddy viscosity is then calculated such as:

$$\nu_t = \frac{C_\mu k^2}{\epsilon}$$

with, C_μ a model constant. The standard $k - \epsilon$ (SKE) model has been suggested in (Jones & Launder, 1972) and the model calibration is given in (Lauder & Sharma, 1974).

The Realizable $k - \epsilon$ (RKE) model (Shih, et al., 1995) which is a more recent model implemented in CFD softwares is derived from the SKE model. This model introduces a new equation for ϵ and a functional relation of C_μ to the turbulent quantities, yielding more accurate computations. C_μ can be written:

$$C_\mu = \frac{1}{A_0 + A_s U^* \frac{k}{\epsilon}} \quad (1.9)$$

with, A_0 a calibration coefficient, A_s and U^* quantities derived from the mean strain rate tensor $\overline{S_{ij}}$ and the mean vorticity tensor $\overline{\Omega_{ij}}$:

$$\overline{\Omega_{ij}} = \frac{1}{2} \left(\frac{\partial \overline{u_i}}{\partial x_j} - \frac{\partial \overline{u_j}}{\partial x_i} \right)$$

$$A_s = \sqrt{6} \cos(\phi), \quad \phi = \frac{1}{3} \arccos(\sqrt{6} W), \quad W = \frac{\overline{S_{ij} S_{ik} S_{kj}}}{S^3}$$

Table 1.1: from (Shih, et al., 1995): model coefficient for RKE turbulence model

A_0	σ_k	σ_ϵ	C_1	C_2	C_μ
4	1	1.2	Equation (1.10)	1.9	Equation (1.9)

S is the modulus of the mean strain rate tensor defined as $S = \sqrt{\overline{S_{ij} S_{ij}}}$. U^* is given by:

$$U^* = \sqrt{\overline{S_{ij} S_{ij}} + \overline{\Omega_{ij} \Omega_{ij}}}$$

The equations for k and ϵ of the RKE model are written as following:

$$\frac{Dk}{Dt} = \frac{\partial}{\partial x_j} \left[\left(\nu + \frac{\nu_t}{\sigma_k} \right) \frac{\partial k}{\partial x_j} \right] - \overline{u'_i u'_j} \frac{\partial \overline{u_i}}{\partial x_j} - \epsilon$$

$$\frac{D\epsilon}{Dt} = \frac{\partial}{\partial x_j} \left[\left(\nu + \frac{\nu_t}{\sigma_\epsilon} \right) \frac{\partial \epsilon}{\partial x_j} \right] + C_1 S \epsilon - \frac{C_2 \epsilon^2}{k + \sqrt{\nu \epsilon}}$$

The model coefficient $\sigma_k, \sigma_\epsilon, C_1, C_2, C_\mu$ are given in Table 1.1. C_1 is calculated with:

$$C_1 = \max \left(0.43, \frac{\eta}{5 + \eta} \right), \quad \eta = \frac{Sk}{\epsilon} \quad (1.10)$$

The coefficient A_0 value has been obtained by calibration, $A_0 = 4$ is chosen in order to reproduce the log law for boundary layer flow. C_2 is obtained by calibrating the decay of turbulence downstream a grid. C_1 is calibrated with experimental data obtained for homogeneous shear flow and boundary layer flow. σ_ϵ is obtained from the log law of velocity in the inertial sublayer.

1.1.3.3 $k - \omega$ SST model

The $k - \omega$ SST (KOSST) model (Menter, 1994) is another two-equation turbulence model which provides the eddy viscosity. This model is based on the $k - \omega$ model formulated by Wilcox (Wilcox, 1988) and on a reformulation of the $k - \epsilon$ model for the turbulent dissipation rate ω in the outer part of the boundary layer. This formulation aims to take advantage of Wilcox $k - \omega$ model in near wall region which calculates better the boundary layers with adverse pressure gradients. This model does not use damping function near the wall (on the contrary of $k - \epsilon$ models) which increases the numerical stability of the computation. In the outer part of the boundary layer, the dissipation rate of Wilcox model is very sensitive to the freestream values of turbulent dissipation rate, thus the model is switched to the $k - \epsilon$ reformulation which is more reliable in this zone. A blending function F_1 is introduced in order to differentiate the treatment in the log region and further from the wall in the outer region.

Table 1.2: from (Menter, 1994)-: model coefficient for KOSST turbulence model

a_1	β^*	σ_{k1}	σ_{k2}	$\sigma_{\omega 1}$	$\sigma_{\omega 2}$	γ_1	γ_2
0.31	0.09	0.85	1.0	0.5	0.856	$\frac{\beta_1}{\beta^*} - \frac{\sigma_{\omega 1} \kappa^2}{\sqrt{\beta^*}}$	$\frac{\beta_2}{\beta^*} - \frac{\sigma_{\omega 2} \kappa^2}{\sqrt{\beta^*}}$

The set of equations for the $k - \omega$ SST model (Menter, 1994) can be written as following for constant density flows:

$$\begin{aligned} \frac{Dk}{Dt} &= \frac{\partial}{\partial x_j} \left[(v + \sigma_k v_t) \frac{\partial k}{\partial x_j} \right] - \overline{u'_i u'_j} \frac{\partial \overline{u}_i}{\partial x_j} - \beta^* \omega k \\ \frac{D\omega}{Dt} &= \frac{\partial}{\partial x_j} \left[(v + \sigma_\omega v_t) \frac{\partial \omega}{\partial x_j} \right] - \frac{\gamma}{v_t} \overline{u'_i u'_j} \frac{\partial \overline{u}_i}{\partial x_j} - \beta \omega^2 + 2(1 - F_1) \sigma_{\omega 2} \frac{1}{\omega} \frac{\partial k}{\partial x_j} \frac{\partial \omega}{\partial x_j} \end{aligned}$$

with, F_1 the blending factor given by:

$$F_1 = \tanh(\chi^4)$$

$$\chi = \min \left[\max \left(\frac{\sqrt{k}}{0.09\omega y}; \frac{500\nu}{y^2\omega} \right), \frac{4\rho\sigma_{\omega 2}k}{CD_{k\omega}y^2} \right], \quad CD_{k\omega} = \max \left(2\rho\sigma_{\omega 2} \frac{1}{\omega} \frac{\partial k}{\partial x_j} \frac{\partial \omega}{\partial x_j}, 10^{-20} \right)$$

where, y is the distance from the wall. The eddy viscosity is then obtained with,

$$v_t = \frac{a_1 k}{\max(a_1 \omega; \Omega F_2)}$$

with Ω the absolute value of the vorticity and F_2 is given by:

$$F_2 = \tanh(\xi^2), \quad \xi = \max \left(2 \frac{\sqrt{k}}{0.09\omega y}; \frac{500\nu}{y^2\omega} \right)$$

Any model coefficient ϕ in $\sigma_k, \sigma_\omega, \beta, \gamma$ are calculated from $\sigma_{k1}, \sigma_{k2}, \sigma_{\omega 1}, \sigma_{\omega 2}, \beta_1, \beta_2, \gamma_1, \gamma_2$ as following:

$$\phi = F_1 \phi_1 + (1 - F_1) \phi_2$$

The model coefficients are given in Table 1.2.

1.1.3.3.4 Improvement of eddy viscosity models

In the previous sections, two eddy viscosity models which are classically used in commercial CFD softwares have been presented. During their development, many authors added corrections enhancing their versatility. A **curvature correction** (Arolla & Durbin, 2013) can be added for both models when the flow presents curved boundaries which increases their accuracy. A correction can also be added on k and ϵ (Spalart & Rumsey, 2007) in presence of ambient turbulence in order to obtain **effective turbulent quantities**. In compressible flows, an **additional term** is given (Sarkar & Balakrishnan, 1990). Another improvement implemented in most of the softwares is the **two-layer approach** (Rodi, 1991), which allows to solve k and ϵ in the viscous layer differently. In this region, the transport equation for k is solved and ϵ is given in regard of its distance from the wall with wall functions. The eddy viscosity calculated from this method is blended with the one obtained by the original formulation of the RKE by using a proximity indicator. This additional model is interesting from an industrial point of view since the boundary layer are not necessarily resolved in these cases where wall-functions can be used. The near wall meshing in these cases are unrefined which contributes to lower the cost of the computations. The treatment of the near wall region with wall functions will be presented in §1.1.3.5. For the KOSST model, an additional **realizability constraint** is given by Durbin (Durbin, 1996) in order to ameliorate the behavior of the model near stagnation points. An anomaly near stagnation point has been observed with two equations models where the turbulent dissipation is too small allowing high rates of turbulent kinetic energy. This constraint is in the form of a maximum on the turbulent time scale.

1.1.3.3.5 SAS model

Another approach which will be used is the Scale Adaptive Simulation (SAS) model presented in (Menter & Egorov, 2005; Menter, et al., 2004). This model has been developed to give an alternative to URANS modelling of transient flows. URANS are the transformation of the RANS equations from steady flow to unsteady flow. The averaging operation filters all the spectrum of the turbulent frequencies which in results fail to reproduce the turbulent structures of the flow. Their influence on the flow is modelled with additional equations and turbulent quantities such as the turbulent kinetic energy or dissipation rate. This approach is often insufficient when different physical phenomena interfere with the turbulence. The SAS model has been developed to reproduce RANS abilities in flows when the grid spacing is larger than the turbulent length scale and switch to LES when the turbulent length scale is larger than the grid. This behavior is possible due to similar formalism between LES and RANS approaches to model turbulence that will not be covered in this dissertation. The SAS model is based on a

two-equations eddy viscosity model for the turbulent kinetic energy k and an integral length scale $\Phi = \sqrt{k}L$ derived from Rotta initial formulation (Rotta, 1972). This formulation leads to the presence of a term with a length dimension in the dissipation equation which can be used to estimate the length of the turbulence structures. This method has been generalized to the KOSST model in (Menter & Egorov, 2005) which will be used in computations in this work. The model equations, model coefficient and calibration can be found in (Menter & Egorov, 2005).

1.1.3.4 Turbulent heat and mass transfer

The **Simple Gradient Diffusion Hypothesis** (SGDH) is often given as a closure equation for the turbulent heat and mass fluxes' terms. For heat and mass transfer, this closure equation is written:

$$\overline{u_j T'} = -\alpha_t \frac{\partial \bar{T}}{\partial x_j}, \quad \overline{u_j c'} = -D_{m,t} \frac{\partial \bar{c}}{\partial x_j}$$

where α_t and $D_{m,t}$ are respectively the turbulent heat diffusion coefficient and turbulent mass diffusion coefficient. The SGDH assumes that the turbulence results in an enhancement of the thermal diffusivity (or mass diffusivity) which is represented by α_t (respectively $D_{m,t}$).

These turbulent quantities are expressed from the turbulent Prandtl number Pr_t , Schmidt number Sc_t and eddy viscosity ν_t as following:

$$Pr_t = \frac{\nu_t}{\alpha_t}, \quad Sc_t = \frac{\nu_t}{D_{m,t}}$$

The closure equations can be written:

$$\overline{u_j T'} = -\frac{\nu_t}{Pr_t} \frac{\partial \bar{T}}{\partial x_j}, \quad \overline{u_j c'} = -\frac{\nu_t}{Sc_t} \frac{\partial \bar{c}}{\partial x_j}$$

For eddy viscosity model, ν_t is computed from the turbulent quantities. Different methods are used in order to get the turbulent Prandtl or Schmidt number with experiments or numerically. Indications on their estimation can be found in (Jischa & Rieke, 1979), (Kays, 1994). In general, getting accurate data on the turbulent Prandtl number is difficult as it requires to measure on a local point the fluctuating quantities as well as the mean shear stress. Thus, DNS simulation are used in most of the case in order to deduce the Prandtl number from temperature profiles which is then used when the turbulent scales are not resolved. For high molecular Prandtl number ($Pr \gg 1$), the turbulent Prandtl number is stable and is often set to constant. Figure 1.1 shows the evolution of the turbulent Prandtl number according to the molecular Prandtl number. It is visible that the variation of the turbulent Prandtl number increases for low molecular Prandtl number which in this case cannot be set constant. For such fluids, a model must be implemented in order to get the good turbulent Prandtl number.

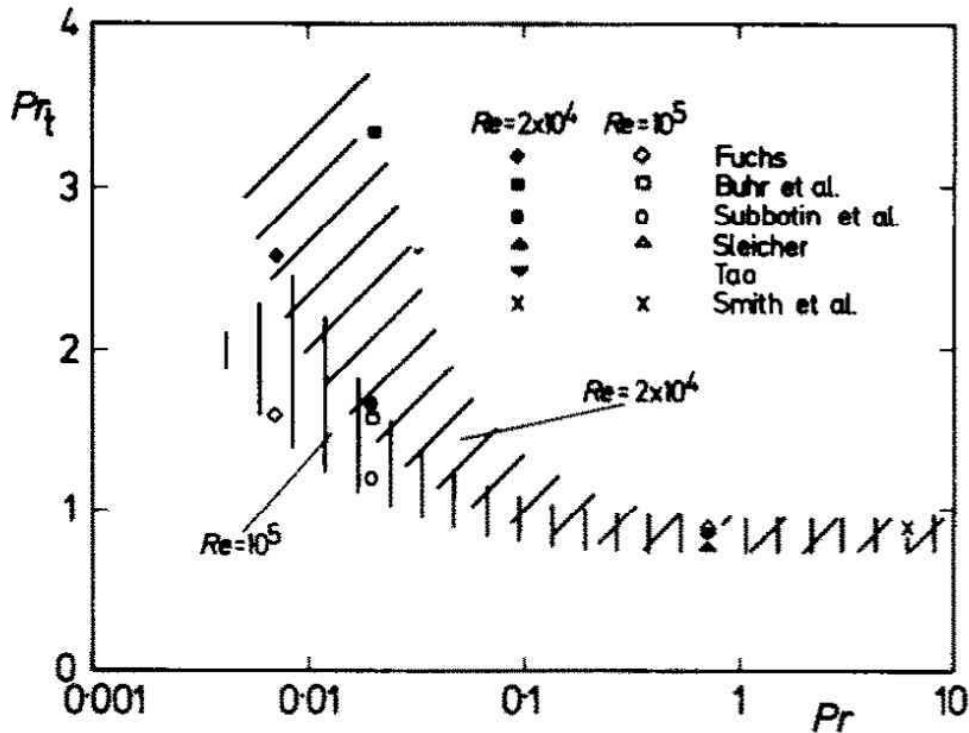


Figure 1.1: evolution of the turbulent Prandtl number as a function of the molecular Prandtl number from different experiments and calibrated model. From (Jischa & Rieke, 1979).

Nevertheless, some studies show the variability of the Prandtl number with the non-dimensional wall distance, and indication are given in (Kays, 1994). The turbulent Prandtl number is found to be a function of the Peclet number $Pe = Pr Re$ and stabilizes for high values. Pr_t is also found to differ in the log region and the sublayer of the boundary layer. This variation with height is also found in (Koeltzsch, 2000) for the turbulent Schmidt number Sc_t .

1.1.3.5 Wall treatment

Most of the flow are bounded by walls. In turbulent flow, walls have an important impact as the shear stress increases at their vicinity due to the important decrease of the velocity from the external region to the wall surface where it reaches zero. In numerical simulations, the treatment of the walls consists of generating coherent boundary conditions for temperature, velocity, and the turbulent quantities. The behavior of these quantities near the wall have been studied and general equations have been given based on the similarity of wall bounded flows. First, the non-dimensional wall quantities will be presented, then, the wall functions which are used to predict the different quantities will be given.

1.1.3.5.1 Scaling of the near wall quantities

In wall bounded flows with no slip conditions ($u = 0$ on the wall), the evolution of temperature, velocity or turbulence depends on the distance to the wall. The boundary layer is composed of three regions visible on Figure 1.2.

The velocity and distance to the wall are nondimensionalized by wall quantities that are given further in this paragraph:

- The **viscous sublayer** corresponds to the region in the direct vicinity of the wall. The velocity is low and viscous forces are preponderant. In this region, the non-dimensional velocity is a linear function of the wall distance
- The **log layer** is further from the wall and corresponds to a region where the viscous forces are negligible in front of the turbulent viscosity. The velocity follows in this case a logarithmic law with respect to the wall distance.
- The **buffer layer** is the zone between the viscous sublayer and the log layer.

In CFD, the boundary conditions will thus be different regarding the height of the cell adjacent to the wall. When the adjacent cell is in the viscous boundary layer, the velocity and temperature profiles are easily calculated as they evolve linearly in this region. When the wall mesh is coarser and the adjacent cell centroid lies in the buffer layer or log layer, algebraic relations are given for the temperature, velocity and turbulent dissipation rate. These relations are made general by transforming the physical quantities into non dimensional ones. This operation is achieved by extracting the friction velocity u^* representative of the flow in the near wall region. In the viscous sublayer, buffer layer, or log layer of the boundary layer, the expression of this velocity differs. The different expressions of u^* in the viscous layer and log layer are given in Table 1.3.

In the viscous sublayer, the friction velocity u^* is calculated from the modulus of the tangential velocity, the viscosity and the wall distance. In the log region, this velocity is estimated from C_μ the model coefficient given for the RKE and KOSST in §1.1.3.3 and k the turbulent kinetic energy. A blended approach can be used in order to have a general function applicable in the two layers and approximate the buffer layer temperature and velocity profile. A wall proximity function γ is used in this case in order to make a smooth transition from the viscous sublayer to the log layer wall function:

$$\gamma = \exp\left(-\frac{Re_y}{11}\right), \quad Re_y = \frac{\sqrt{k}y}{\nu}$$

The definition of this velocity allows to define the non-dimensional wall distance y^+ , the non-dimensional velocity u^+ , and non-dimensional temperature T^+ :

$$y^+ = \frac{yu^*}{\nu}, \quad u^+ = \frac{u}{u^*}, \quad T^+ = \frac{\rho C_p u^* (T - T_w)}{q_w}$$

With, q_w the wall heat flux.

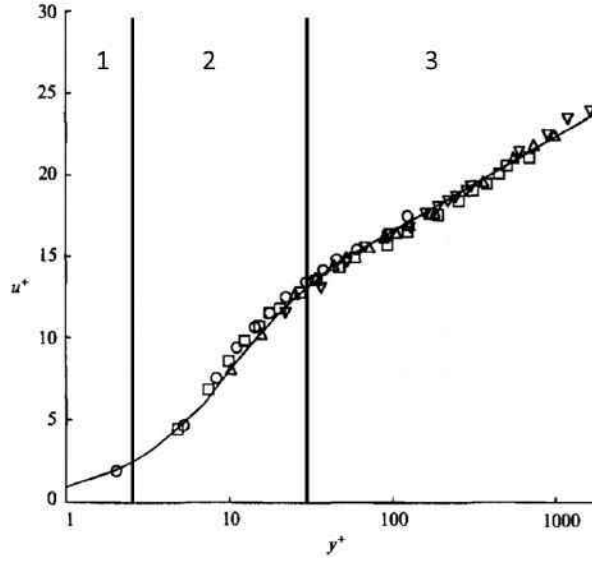


Figure 1.2: from (Wei & Willmarth, 1989) : Non dimensional mean velocity profiles, for $Re = 2970$ (\circ), $Re = 14914$ (\square), $Re = 22776$ (Δ), and $Re = 39582$ (∇). The viscous layer (1), the buffer layer (2) and the log layer (3) are indicated.

Table 1.3: near wall velocity in the different region of the boundary layer

Sublayer	Standard Wall function	Blended Wall function
Viscous sublayer	$u^* = \frac{v \mathbf{v}_{\text{tangential}} }{y}$	$u^* = \gamma \frac{v \mathbf{v}_{\text{tangential}} }{y} + (1 - \gamma) C_{\mu}^{\frac{1}{4}} k^{\frac{1}{2}}$
Buffer layer		
Log layer	$u^* = C_{\mu}^{\frac{1}{4}} k^{\frac{1}{2}}$	

1.1.3.5.2 Wall functions

The wall function for velocity is given by Reichardt blended wall function (Reichardt, 1951) which is valid for the viscous sublayer, buffer layer and log layer.

$$u^+ = \frac{1}{\kappa} \ln(1 + \kappa y^+) + C \left(1 - \exp\left(-\frac{y^+}{y_m^+}\right) - \frac{y^+}{y_m^+} \exp(-by^+) \right)$$

with, κ the von Karman constant calibrated on experiments, and C , y_m^+ and b defined as following:

$$C = \frac{1}{\kappa} \ln\left(\frac{E'}{\kappa}\right), \quad y_m^+ = \max[3, 267(2.64 - 3.9\kappa)E'^{0.0125}] - 0.987, \quad b = \frac{1}{2} \left(y_m^+ \frac{\kappa}{C} + \frac{1}{y_m^+} \right)$$

where $E' = \frac{E}{f}$, E and f being respectively the log law offset and a roughness function. For smooth wall, $f = 1$.

For details on the impact of roughness on the wall functions, see (Jayatilleke, 1966).

For temperature, a blended wall function is also used according to Kader's formulation (Kader, 1981) which gave satisfactory results for Prandtl numbers in the range $[6 \cdot 10^{-3}, 40 \cdot 10^3]$.

$$T^+ = \exp(-\Gamma) Pr y^+ + \exp\left(-\frac{1}{\Gamma}\right) Pr_t \left[\frac{1}{k} \ln(E' y^+) + P\right]$$

with,

$$\Gamma = \frac{0.01c(Pr y^+)^4}{1 + \frac{5}{c} Pr^3 y^+}, \quad c = \exp(f - 1)$$

P is obtained from (Jayatilleke, 1966):

$$P = 9.24 \left[\left(\frac{Pr}{Pr_t} \right)^{\frac{3}{4}} - 1 \right] \left[1 + 0.28 \exp\left(-0.007 \frac{Pr}{Pr_t}\right) \right]$$

This temperature allows the computation of the turbulent wall heat flux:

$$q_w = \rho C_p u^* \frac{T_c - T_w}{T_c^+}$$

where, T_c is the evaluation of the temperature using Kader law and T_w is the wall temperature. Wall conditions depending on the turbulence model are imposed for turbulent quantities and will not be covered here. A difference in the wall treatment should still be noted for 2-layer equation models, where the dissipation rate is imposed with an additional model leading to the computation of the dissipation rate and eddy viscosity (see for instance (Wolfshtein, 1969)).

1.1.4 Conclusion

Forced turbulent flows are of interest for industrials due to their peculiar behavior regarding mixing, which enhances heat transfer. However, their modelling can be challenging due to their chaotic behavior. Different approaches exist to simulate turbulent flow, including DNS, LES and RANS models. The two former approaches yield more accurate results, but their computational costs can quickly become prohibitive for industrial applications. Thus, RANS models are used most of the time to compromise cost and efficiency. Furthermore, the two-layer approach which involves the use of wall functions is chosen most of the time in order to limit the number of cells in CFD grids for high Reynolds number applications. Most of these models are calibrated on specific canonical cases which might not be relevant for industrial flow configurations. One of the objectives of this dissertation is to verify the accuracy of these models' implementations in commercial CFD softwares for heat transfer coefficient computations. The simulations that must be qualified are at the reactor scale involving very high Reynolds number in massive geometries. Different models described in this section will be investigated in the frame of Uncertainty quantification (UQ) in order to estimate confidence intervals on their calculations of heat transfer.

1.2 Uncertainty quantification

The uncertainty quantification (UQ) process applied to predictive science can be seen as using probabilities and statistics to assess the reliability on the calculation of a quantity of interest. In fact, most of real-life situations include uncertainty due to the randomness of some physical phenomenon. In addition, the models that are used include most of the time uncertainty due to their inaccuracy. For instance, when making risk analysis, the consequence arising from this variability must be considered to insure the reliability of the decisions. In the nuclear industry, UQ is required to ensure the safety of a nuclear plant. More specifically, when CFD computations are used to predict heat transfer coefficient, confidence intervals must be given to take margins for safety. The estimation of these confidence intervals relies on the identification of the different sources of uncertainty. The impact of considering different sources of uncertainty in the conclusions of risk analysis can be found for launch accident scenario in (Frank, 1999), or for flood in (Merz & Thieken, 2005). The first step before proceeding to the uncertainty quantification is to identify the different sources of uncertainty, leading to the differentiation of two types of uncertainties:

- Aleatory or natural uncertainty, which arises from phenomena presenting randomness. For instance, the evolution in time of a flow velocity will show some variability in turbulent flows. This type of uncertainty cannot be reduced by means of knowledge or more precise measurements.
- Epistemic uncertainties, which are due to incomplete knowledge, but which can be reduced. For instance, the use of a turbulence model to represent turbulent flows with CFD induces an error due to the non-completeness of the model. In this case, the uncertainty can be reduced by supplementing the models with additional knowledge.

In this section, statistical concepts will be reminded, then, the nomenclature and definitions provided by the ASME guide for the validation and verification of CFD codes used in the nuclear industry (Coleman & Members, 2009) will be given. Finally, the different sources of uncertainty and methods to assess their values will be presented.

1.2.1 Definition and nomenclature in the UQ frame

In order to standardize the notations used in the UQ frame, the definitions and notations that will be used have been taken from ASME (American Society of Mechanical Engineers) guide for the validation and verification of CFD codes (Coleman & Members, 2009):

- **Error** is a recognizable deficiency in any phase or activity of modeling and simulation that is not due to lack of knowledge. In literature, this error is called **epistemic uncertainty**.
- **Uncertainty** is a potential deficiency in any phase or activity of the modeling process that is due to lack of knowledge. This uncertainty is also known as **aleatory uncertainty** or **natural uncertainty** in literature.

The main idea behind the distinction of errors and uncertainties, is that errors can be reduced by employing more advanced models or more accurate numerical methods, or measurements. In contrast, uncertainties are related to unknown elements which by nature are unreducible. In this work, the Nusselt number (Nu) is investigated. The Nusselt number, related to the wall heat transfer coefficient, is an important parameter for safety analysis, which is either calculated from measurements or directly computed. In both cases, it is not possible to get its value with absolute certainty. In fact, the experimental measurements leading to its calculation are by nature uncertain due to the limitations of the measurement devices and due in this work to the turbulent behavior of the flow which adds fluctuations to the occurring heat transfer. Numerically, for a set of boundary conditions, the computed Nusselt number is determined, nevertheless, real physical situations present some randomness, especially the experimental flow configuration which is an input of the simulations. Thus, the use of Nusselt number data for safety analysis must include statistics, sensibility analysis for the estimation of confidence intervals. The Nusselt number is calculated from the wall heat transfer coefficient h_{conv} as follows:

$$Nu = \frac{h_{conv} L}{\lambda}$$

as defined in §1.1.2.

The convective heat transfer coefficient h_{conv} is defined for a reference temperature T_{ref} by the following formula:

$$h_{conv} = \frac{q_w}{T_{ref} - T_{wall}}$$

where, q_w is the wall heat flux and T_{wall} is the wall temperature. In experiments, the measure on q_w , T_{ref} and T_{wall} can include uncertainty or error that affect the calculation. The Nusselt number is then calculated with:

For a realization the Nusselt number δ_{Nu} depicted by the random variable Nu calculated with CFD codes, and when experimental data is available, the deviation between CFD computation and reality is decomposed as the sum of independent RV:

$$\delta_{E_{CFD/reality}} = \delta_{E_{CFD/exp}} + \delta_{U_{exp/reality}}$$

where,

- $\delta_{E_{CFD/reality}} = \delta_{Nu_{CFD}} - \delta_{Nu_{reality}}$: a realization of the **error between the computation and the reality $E_{CFD/reality}$** .
- $\delta_{E_{CFD/exp}} = \delta_{Nu_{CFD}} - \delta_{Nu_{exp}}$: a realization of the **error between the computation and an experimental measurement $E_{CFD/exp}$** .
- $\delta_{U_{exp/reality}} = \delta_{U_{exp}} = \delta_{Nu_{exp}} - \delta_{Nu_{reality}}$: is a realization of the **uncertainty on the measure U_{exp}** .

Moreover, if one has a prior knowledge of the models that are used for the calculation of a quantity with CFD codes, the error between a calculation and the reality can be expressed as:

$$\delta_{E_{CFD/reality}} = \delta_{E_{model}} + \delta_{U_{BC}} + \delta_{E_{num}}$$

- $\delta_{U_{inputs,exp}}$: a realization of the uncertainty $U_{inputs,exp}$ on the calculation due to **the uncertainty of the simulation inputs** that have been propagated through the calculation. This term can be obtained with different methods which can be intrusive, meaning the propagation of the uncertain parameter is done by the solver which makes the calculation, or non-intrusive with methods relying on evaluation of the CFD calculation on specific points.
- $\delta_{E_{num}}$: a realization of the **numerical error**. This error is done by the solver and exists because CFD computations are performed by discretizing a volume domain and the temporal domain in a finite number of elements instead of a solving in continuous domain.
- $\delta_{E_{model}}$: a realization of the **model error** E_{model} that is related to the inaccuracies of the models that are used such as turbulence model and wall treatment. Evaluating this term requires ultimately a comparison of computations and experiment as it will be done in this document.

In practice, the mean value μ and standard deviation σ of E_{model} , E_{num} , and $U_{inputs,exp}$ are combined to estimate the mean value and standard deviation of $E_{CFD/exp}$. These quantities are then used to estimate a confidence interval on the calculation of the heat transfer coefficient with CFD, as depicted on the illustration Figure 1.3. Most of the time, a $\pm 2\sigma_{E_{CFD/exp}}$ interval is given around the mean value in order to have the 95% confidence interval corresponding approximatively to the case of a random variable following a normal distribution. (see §1.2.2 for definitions). For other distributions, a $\pm k \times \sigma_{E_{CFD/exp}}$ interval can be given with k depending on the distributions.

The estimation of the model error can be done when experimental and numerical data are available. The two different ways to express the error between CFD and reality allows to calculate the model error as following:

$$\delta_{E_{model}} = \delta_{E_{CFD/exp}} + \delta_{U_{exp}} - \delta_{U_{inputs,exp}} - \delta_{E_{num}}$$

For independent random variables following normal distributions, the mean and the standard deviation are given by:

$$\mu_{E_{model}} = \mu_{E_{CFD/exp}} + \mu_{U_{exp}} - \mu_{U_{inputs,exp}} - \mu_{E_{num}} \quad (1.11)$$

$$\sigma_{E_{model}} = \sqrt{\sigma_{E_{CFD/exp}}^2 + \sigma_{U_{exp}}^2 + \sigma_{U_{inputs,exp}}^2 + \sigma_{E_{num}}^2} \quad (1.12)$$



Figure 1.3– calculation of a 95% confidence interval from the computed Nusselt number Nu_{CFD} and the error between CFD and reality $E_{CFD/reality}$

In the nuclear industry, the model error bias $\mu_{E_{model}}$ and standard deviation $\sigma_{E_{model}}$ are evaluated most of the time with experimental data obtained in reduced scale mock-ups. For instance, the validation of hydraulic calculations in the lower and upper plenum of an EPR (European Pressurized Reactor) has been done in a 1/5th scaled mock-up in (Dolleans, et al., 2008; Goreaud, et al., 2004; Barbier, et al., 2009) for Reynolds number smaller than in the reactor. When dealing with UQ at the reactor scale, the evaluated modelling error at the mock-up scale must be transposed, which could lead to the occurrence of a transposition error of the modelling error. The objective of this thesis is to evaluate the model error and its evolution when approaching the reactor scale in order to estimate the error due to the transposition. In this context, experimental measurements and computations of the heat transfer coefficient will be generated with the aim of quantifying the sources of error and uncertainty.

1.2.2 Statistical concepts

In this work, the studied data consist of series of numerical quantities, such as the time variation of the flowrate during an experiment or the surface variation of height on a non-flat surface. When measuring this data, random fluctuations are observed, resulting in uncertainties on the measured quantities. This section summarizes some definitions and concepts of the field of statistics used in order to quantify confidence intervals on these quantities. These elements can be found for example in (Ross, 1976).

The definitions will be given for unidimensional random variables X which realizations are in the space of real numbers. In this document, the following nomenclature is used:

- Capital letters are related to random variables.
- Small letter x or Greek letter δ_x are realizations of the random variable X .
- A p dimension vector quantity $\mathbf{X} = (X_1, \dots, X_p)$ will be written with bold fonts while a scalar quantity X will be written with normal fonts.

The probability density function (PDF) f of a continuous random variable X is used in order to calculate the probability with which X takes its value in a given interval $[a, b]$. This probability is obtained by integrating f on this interval. The probability $p(X \in [a, b])$ is written as following:

$$p(X \in [a, b]) = \int_a^b f(X) dX$$

The quantiles of the PDF f are the values that partition the total space covered by the random variable X in intervals of equal probability. For instance, if we divide the range $[a, b]$ covered by X in quantiles of 5%, the probability of realizations of X on each interval is 5% (i.e. the area under f on each of these intervals is constant). The first quantile $q_{5\%}$ corresponds to the 5% smallest realization of X $[a, q_{5\%}]$ while the last quantile would be the interval of the 5% highest realizations $[q_{95\%}, b]$.

The Expectation value or Mean value of a random variable is a way to measure the average value a random variable will take for many realizations. In this dissertation, two notations are used $\langle X \rangle$ and μ_X . This quantity is calculated as following:

$$\langle X \rangle = \mu_X = \int_{-\infty}^{+\infty} xf(x)dx$$

When the random variable takes discrete values x_1, x_2, \dots, x_N , the mean is calculated with:

$$\mu_X = \frac{1}{N} \sum_{n=1}^N x_n p(X = x_n)$$

The variance $\sigma^2 = Var(X) = \langle (X - \mu_X)^2 \rangle$ of a random variable is a way to measure how much the realization is expected to differ from the mean value. For a continuous random variable, this quantity is calculated with:

$$\sigma_X^2 = \int_{-\infty}^{+\infty} (x - \mu_X)^2 f(x) dX$$

σ_X is called the **standard deviation** of the random variable X . In the following, the centered random variable $X - \mu$ is denoted with the symbol δX .

When the RV takes discrete values x_1, x_2, \dots, x_N , the variance is given by:

$$\sigma_X^2 = \sum_{n=1}^N (x_n - \mu_X)^2 p(X = x_n)$$

Note that these ways to calculate the mean value and variance requires to know the probability function. When a random sample is a sequence of independent and identically distributed random variables from a distribution of expected mean value μ_X and variance σ_X^2 , it has been shown with the **Central Limit Theorem** that their distribution tends to fit a normal distribution, meaning that the sample mean, and variance converge to the expected values as the size of the sample grows:

$$\mu_X = \lim_{N \rightarrow \infty} \frac{1}{N} \sum_{n=1}^N x_n$$

$$\sigma_X^2 = \lim_{N \rightarrow \infty} \frac{1}{N-1} \sum_{n=1}^N (x_i - \mu_X)^2$$

Estimations of μ_X , and σ_X with samples of N elements are denoted with the symbols $\widetilde{\mu}_X$ and $\widetilde{\sigma}_X$

Comment: In the following sections, it is assumed that the random samples are drawn independently and follow the same distribution allowing the use of the Central Limit Theorem. This assumption is often valid for measurements of physical quantities presenting fluctuations in time, nevertheless, in some cases, the signal can present correlated variations, as for instance sinusoidal oscillations, refuting the assumption of similarly distributed random variables. In these cases, the mean value and the variance of the sample can still be calculated, nevertheless, the PDF remains unknown. These values still give a good indication of the distribution of the data and can be used in order to generate confidence intervals for the realization of the supposed random variable.

A random variable following the **Normal distribution**, or **Gaussian distribution** of mean μ and standard deviation σ is written $X \sim \mathcal{N}(\mu, \sigma)$. The PDF is as following:

$$f_X(x) = \frac{1}{\sqrt{2\pi\sigma^2}} e^{-\frac{(x-\mu)^2}{2\sigma^2}}$$

The previous concepts can be generalized to multidimensional realization spaces. A multidimensional random variable $\mathbf{X} = (X_1, \dots, X_p)$ can be seen as a set of unidimensional random variables following a multidimensional PDF f which realization space is of dimension p . Each element of the set can be dependent or independent of each other. A way to characterize how pairwise elements of the set of unidimensional random variables vary in relation to each other is to calculate the covariance for these two variables:

$$Cov(X_i, X_j) = \int (x_i - \mu_{X_i})(x_j - \mu_{X_j}) f(x_1, \dots, x_p) dx_1 \dots dx_p$$

Comment: $Cov(X, X) = Var(X)$ and $Cov(X_1, X_2) = Cov(X_2, X_1)$

The covariance can be extended to random vectors with inter-dependent components, as for example with three components:

$$Cov(\mathbf{X}) = \begin{pmatrix} Var(X_1) & Cov(X_1, X_2) & Cov(X_1, X_3) \\ Cov(X_1, X_2) & Var(X_2) & Cov(X_2, X_3) \\ Cov(X_1, X_3) & Cov(X_2, X_3) & Var(X_3) \end{pmatrix}$$

If the vector has 3 independent variables, the matrix will be diagonal with the variance elements on the diagonal.

The covariance matrix can also be evaluated for a sample of a continuous random variable with a finite number of elements sufficiently high enough: for a sample $(\mathbf{X}_n)_{n \in [1, N]} = (X_{1,n}, \dots, X_{p,n})_{n \in [1, N]}$ with p the number of random variables and N the size of the sample:

$$\text{Cov}(X_i, X_j) = \lim_{N \rightarrow \infty} \frac{1}{N-1} \sum_{n=1}^N (X_{i,n} - \tilde{\mu}_{X_i})(X_{j,n} - \tilde{\mu}_{X_j})$$

The generalization of the univariate normal distribution to the multidimensional case can be done: the covariance matrix is given in the place of the standard deviation. This generalization is named the **multivariate normal distribution** or **joint normal distribution**.

A random variable $\mathbf{X} = (X_1, \dots, X_p)$ follows a joint normal distribution of mean $\boldsymbol{\mu}$ and covariance $\boldsymbol{\Sigma}$, i.e., $\mathbf{X} \sim \mathcal{N}(\boldsymbol{\mu}, \boldsymbol{\Sigma})$, if its PDF can be written as following:

$$f_{\mathbf{X}}(x_1, \dots, x_p) = \frac{1}{(2\pi)^{\frac{p}{2}} \sqrt{\det \boldsymbol{\Sigma}}} \exp\left(-\frac{1}{2}(\mathbf{x} - \boldsymbol{\mu})^T \boldsymbol{\Sigma}^{-1}(\mathbf{x} - \boldsymbol{\mu})\right)$$

with $\boldsymbol{\mu} = (\mu_1, \dots, \mu_p)^T$, and $\det \boldsymbol{\Sigma}$ the determinant of $\boldsymbol{\Sigma}$ the covariance matrix.

An example of how the covariance affects the shape of a multivariate distribution can be seen in the case of a couple of two random variables (X_1, X_2) of mean $(0,0)$ on Figure 1.4. The covariance matrix is in this case given by:

$$C = \begin{pmatrix} 0.05^2 & a \\ a & 0.05^2 \end{pmatrix}$$

The diagonal case $a = 0$ corresponds to no covariance between X_1 and X_2 and is visible on Figure 1.4.a. The non-diagonal case is given on Figure 1.4.b where $a = 0.05^2 \times (-0.9)$. It is noticeable, that in the case of non-diagonal covariance matrix, the correlation between the parameters is nonzero and has the same sign than the covariance.

Moments of a random variable: The moments of a random variable can be seen as an alternative way to describe a RV from the PDF. The n -th statistical moment of the random variable X is defined by:

$$\langle X^n \rangle = \int_{-\infty}^{+\infty} x^n f(x) dx$$

The first moment is the mean value μ_X . With this first moment, we can define the n -th centered moment:

$$\langle \delta X^n \rangle = \int_{-\infty}^{+\infty} (x - \mu_X)^n f(x) dx$$

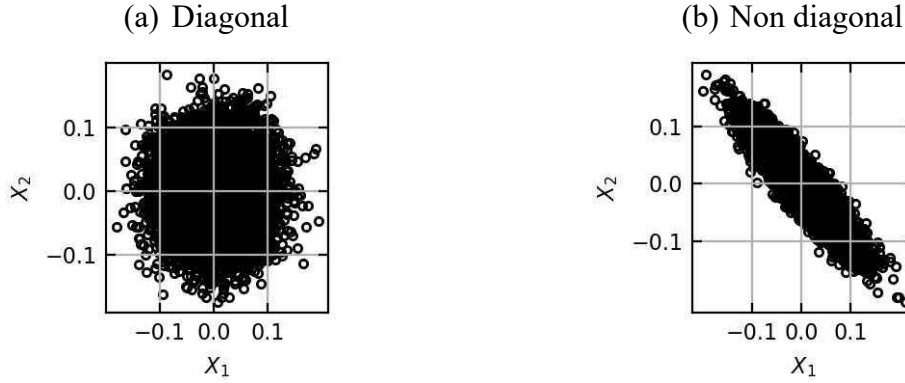


Figure 1.4 - Example of realizations of a 2D joint distribution: With diagonal covariance matrix (left) and non-diagonal covariance matrix (right)

When the random variable is multivariate, this moment is called the **marginal moment**.

Moreover, it is possible to calculate the **mixed moment** of a multidimensional RV $\mathbf{X} = (X_1, \dots, X_p)$ following the PDF $f_{\mathbf{X}}(\mathbf{x})$:

$$\langle \delta X_i \delta X_j \dots \delta X_k \rangle = \int_{-\infty}^{+\infty} (x_i - \mu_{X_i}) (x_j - \mu_{X_j}) \dots (x_k - \mu_{X_k}) f_{\mathbf{X}}(\mathbf{x}) d\mathbf{x}$$

When the probability density function is not known, and when a sample $(X_i)_{i \in \llbracket 1, N \rrbracket}$ with enough elements is available, it is possible to evaluate the mean value $\tilde{\mu}_X$ as stated previously and the n-th central moment of a sample with the following formula:

$$\langle \delta \tilde{X}^n \rangle = \frac{1}{N-1} \sum_{k=1}^N (x_k - \tilde{\mu}_X)^n$$

Equivalently, the mixed moment of a multivariate sample is calculated for a sample $(\mathbf{X}_n)_{n \in \llbracket 1, N \rrbracket} = (X_{1,n}, \dots, X_{p,n})_{n \in \llbracket 1, N \rrbracket}$ of a p dimension multivariate RV with the following formula:

$$\langle \delta X_i \delta X_j \dots \delta X_k \rangle = \frac{1}{N-1} \sum_{n=1}^N (X_{i,n} - \tilde{\mu}_{X_i}) (X_{j,n} - \tilde{\mu}_{X_j}) (X_{k,n} - \tilde{\mu}_{X_k})$$

1.2.3 Surrogate modelling

In this dissertation, the Nusselt number is calculated with CFD for different flow configurations, operating conditions (flowrate, physical properties of the fluid) and models. In this context, the estimation with CFD of Nusselt number Nu for a given set of operating conditions (or inputs) $\mathbf{x}_{inputs} = (x_{input\ 1}, x_{input\ 2}, \dots)$ can be written:

$$h_{conv} = f(\mathbf{x}_{inputs})$$

where, f represents the output of the underlying simulation model and flow configuration.

Similarly, experimental measurements of the heat transfer coefficient can be written as a function of the operating conditions depending on the flow configuration.

In both cases, the estimation of f for a wide range of inputs can be costly and is most of the time not affordable when thousands of inputs must be covered. In these situations, surrogate models can be used. A surrogate model is by definition an approximation of the function f enabling the estimation of the output for given inputs in negligible time. Surrogate models are estimated from available realization of f . For instance, when f evolves as a linear function of the inputs, a linear regression on a limited number of training points $(\mathbf{x}_{inputs,i}, f(\mathbf{x}_{inputs,i}))$ enables the prediction of f for arbitrary inputs in the range covered by the available realizations. In practice, linear regression is not suitable for all functions f and more complex methods are used.

The optimal spatial prediction problem or Kriging from the South African geostatistician D. G. Krige is one of these methods. Ordinary Kriging (OK) is one of the simplest methods used till today for spatial regression problems, its early development and principles are presented by N. Cressie in (Cressie, 1990). Suppose a sample of m noisy observations of a quantity of interest $(f(\mathbf{x}_i))_{i \leq m}$ is available for different inputs $(\mathbf{x}_i)_{i \leq m}$, kriging assumes:

$$f(\mathbf{x}_i) = \mu + \delta(\mathbf{x}_i)$$

where δ is a zero mean stochastic process of known covariance C and μ the mean of the predictor. OK provides a predictor of f denoted f^* based on the observations and the known covariance C which can be used to evaluate f for any other inputs. The estimator of f provided with ordinary Kriging coincides with the Best Linear Unbiased Predictor (BLUP) which minimizes the prediction error (1.13):

$$\langle f(\mathbf{x}) - \sum_{i=1}^m \lambda_i f(\mathbf{x}_i) \rangle^2 \quad (1.13)$$

$$\sum_{i=1}^m \lambda_i = 1 \quad (1.14)$$

This predictor is linear as it is expressed from a linear combination of the observation (1.13), and it is unbiased due to the condition on the weights λ_i in (1.14). The coefficients λ_i corresponding to the BLUP is obtained by combining the covariance matrix and the observations. A recent review of the use of kriging in surrogate modelling can be found in (Kleijnen, 2017; Kleijnen, 2009) in comparison to other surrogate models.

In this dissertation, a different approach using Gaussian processes and Bayesian statistics was applied to estimate a surrogate model.

Gaussian processes (GP) are a simple and general class of models of functions. A short and comprehensive description can be found in (Lloyd, et al., 2014), which introduces Bayesian

statistics and gaussian processes for the linear regression problem. A more detailed description can be found in (Rasmussen & Williams, 2006).

In this dissertation, we are interested in regression problems: predicting continuous quantities from acquired data. When Gaussian processes are used for regression, they are combined with the Bayesian approach that consists of:

- specifying prior beliefs on the parameters of the model that has been chosen using probability distributions
- following rules of probability to update beliefs rationally (maximizing the likelihood) after observing data

For example, let us investigate the use of Bayesian analysis combined to the linear regression model with Gaussian noise on the observed data that can be found in detail in (Lloyd, et al., 2014). A sample of training data $\mathbf{x} = (x_i)_{i \in [1, n]}$, $\mathbf{y} = (y_i)_{i \in [1, n]}$ including error/noise ϵ_i on the measurement of y_i is investigated in order to estimate the underlying function f they represent. The data is written as following for a linear regression model which parameter is the slope m and.

$$y_i = f(x_i) + \epsilon_i, \quad f(x_i) = mx_i \quad (1.15)$$

Priors must be given for this model: the noise and the slope are supposed to follow a zero-mean normal distribution such as $\epsilon_i \sim \mathcal{N}(0, \sigma_\epsilon^2)$ and $m \sim \mathcal{N}(0, 1)$.

Comment: the linear model combined with the prior on ϵ_i and m implicitly defines a joint prior for $\mathbf{y} = \{y_1, \dots, y_n\}$. y_i is written as the sum of two RV following normal distribution implying that

$$y_i \sim \mathcal{N}(0, x_i^2 + \sigma_\epsilon^2), \quad \text{Cov}(y_i, y_j) = x_i x_j$$

which, can be written as a joint Gaussian distribution:

$$\mathbf{y} \sim \mathcal{N}(\mathbf{0}, \mathbf{\Sigma}) \quad (1.16)$$

$$\Sigma_{ij} = x_i x_j + \delta_i^j \sigma_\epsilon^2$$

The presence of noisy inputs implies that the observations are realizations of a random process. Thus, the probability density of the observations given the parameters, called the *likelihood* can be defined.

The different training points (x_i, y_i) are drawn independently which leads to the following expression of the likelihood $p(\mathbf{y} | m, \mathbf{x})$:

$$p(\mathbf{y} | m, \mathbf{x}) = \prod_i \frac{1}{\sqrt{2\pi\sigma_\epsilon^2}} \exp\left(-\frac{(y_i - mx_i)^2}{2\sigma_\epsilon^2}\right)$$

We are now looking for the posterior $p(m | \mathbf{y}, \mathbf{x})$ distribution in order to estimate the slope.

Bayes theorem is written:

$$\text{posterior} = \frac{\text{likelihood} \times \text{prior}}{\text{marginal likelihood}}$$

$$p(m|y, x) = \frac{p(y|m, x)p(m)}{\int p(y|m, x)p(m)dm}$$

By replacing the different elements and keeping the parts which depends on m (only the numerator) it is shown (Lloyd, et al., 2014) that the posterior distribution follows a normal distribution:

$$p(m|y, x) \sim \mathcal{N}\left(\frac{\sum_i x_i y_i}{\sum_i x_i^2 + \sigma_\epsilon^2}, \frac{\sigma_\epsilon^2}{\sum_i x_i^2 + \sigma_\epsilon^2}\right)$$

Its mean value is called the *maximum a priori* (MAP) estimate of m which is the value of m maximizing the likelihood $p(y|m, x)$. An example of estimation of the predictive density of the posterior is given on Figure 1.5. The red shades correspond to the quantiles of the predictive distribution $p(f(x^*)|\mathbf{X}, \mu, \Sigma)$ where $f(x^*)$ is the evaluation of f for an input x^* , $\mathbf{X} = (x, y)$ is the sample of training data, and μ, Σ are the prior beliefs on the model, (slope m following a normal distribution and gaussian noise on the observation of the data). Realizations of the slope are given with solid line, and it is visible that adding training points reduces the sparseness of the predictions. The MAP is not shown but would correspond to the mean slope of the presented lines.

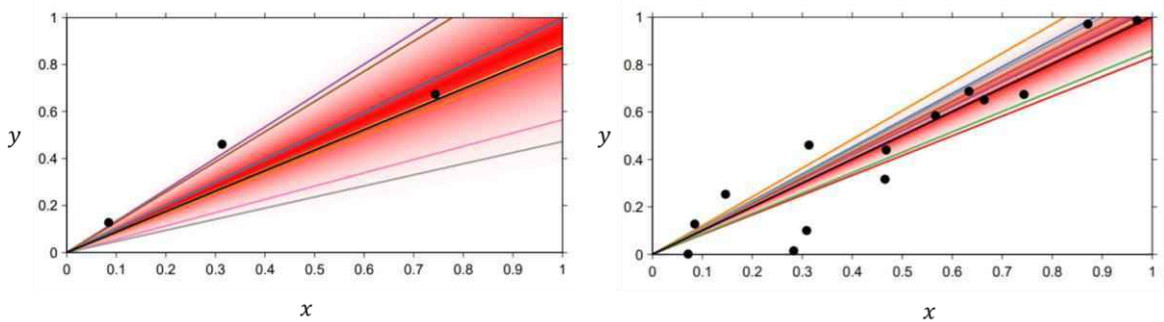


Figure 1.5 – from (Lloyd, et al., 2014): Example of linear regression using a gaussian process of mean μ , kernel Σ and Bayesian statistics. The realization points $\mathbf{X} = (x_i, y_i)_{i \leq N}$ are denoted with black points. The quantiles of the predictive density $p(f(x^*)|\mathbf{X}, \mu, \Sigma)$ at each input locations are given with shades of red. Left: the predictive density is estimated from 3 realizations $(x_i, y_i)_{i \leq N}$, right: estimation from 15 realizations.

It is noticeable in the previous example how the Bayesian linear regression is a Gaussian Process as the model (1.15) combined to the prior on the model parameters is equivalent to define a consistent joint Gaussian distribution of the outputs given in (1.16). In the previous definition, “consistent” means that the observation of the larger set of variables does not impact the distribution of the smaller set. Meaning that if we assume $\mathbf{y} \sim N(\mathbf{0}, \mathbf{\Sigma})$, then $y_i \sim N(0, \Sigma_{i,i})$. Making a prior on model parameters is equivalent to implicitly define a joint prior on the family $(\mathbf{y}_i)_{i \in [1,n]}$ which is a multivariate normal distribution with a covariance matrix (kernel function) depending on the model that is chosen. A Gaussian process is completely specified by its **mean function** $m(x)$ and **covariance function or kernel** $k(x, x')$.

For a gaussian process $f(\mathbf{x})$ we can define these quantities as:

- $m(\mathbf{x}) = \langle f(\mathbf{x}) \rangle$
- $k(\mathbf{x}, \mathbf{x}') = \langle (f(\mathbf{x}) - m(\mathbf{x}))(f(\mathbf{x}') - m(\mathbf{x}')) \rangle$

The GP is denoted:

$$f(\mathbf{x}) \sim GP(m(\mathbf{x}), k(\mathbf{x}, \mathbf{x}'))$$

When data values $(f(\mathbf{x}_i))_{i \in [1,N]}$ evaluated at points $\mathbf{X} = \{\mathbf{x}_1, \dots, \mathbf{x}_N\}$ are available, a gaussian process $f \sim GP(\mu, k)$ can be used to calculate the predictive distribution $p(f(\mathbf{x}^*) | \mathbf{f}(\mathbf{X}), \mathbf{X}, \mu(\cdot), k(\cdot, \cdot))$ (cf. (Duvenaud, 2014)) of the function value $f(\mathbf{x}^*)$ at test point \mathbf{x}^* . The expression takes the form:

$$\begin{aligned} p(f(\mathbf{x}^*) | \mathbf{f}(\mathbf{X}), \mathbf{X}, \mu(\cdot), k(\cdot, \cdot)) \\ = \mathcal{N}(f(\mathbf{x}^*) | \mu(\mathbf{x}^*) + k(\mathbf{x}^*, \mathbf{X})k(\mathbf{X}, \mathbf{X})^{-1}(\mathbf{f}(\mathbf{X}) - \mu(\mathbf{X})), k(\mathbf{x}^*, \mathbf{x}^*) \\ - k(\mathbf{x}^*, \mathbf{X})k(\mathbf{X}, \mathbf{X})^{-1}k(\mathbf{X}, \mathbf{x}^*)) \end{aligned} \quad (1.17)$$

This expression depends importantly on the kernel that is chosen. Different types of kernels have been investigated in reference (Duvenaud, 2014) as well as an automatic way of finding the kernel that is the most adapted to represent data. Examples of kernel that can be chosen with their hyper parameters are visible on Figure 1.6 (plotted in black solid line). In addition, the general shape obtained when plotting the prediction of a function f from which the data is sampled (red or blue curve) are depicted. The choice of the linear kernel (Lin) leads to a linear regression model. In contrast, a squared exponential kernel (SE) leads to smooth prediction of f which slope varies smoothly on the range of the data. Periodic functions can be predicted by using a periodic kernel (Per) which is composed of a periodic function and a gaussian.

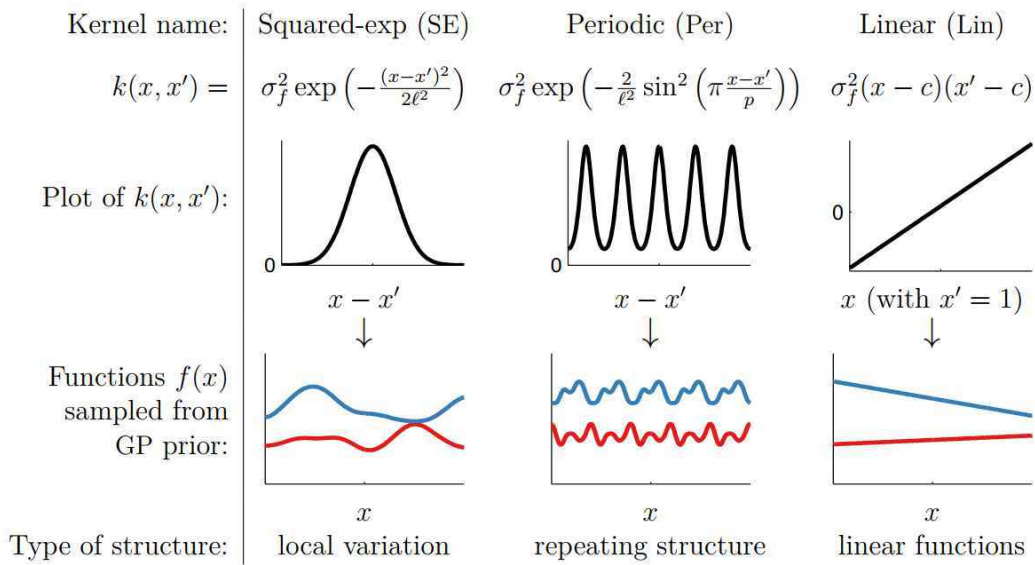


Figure 1.6 – From (Duvenaud, 2014). Examples of kernel for GP (solid black line) and impact on the type of curves (blue and red) that can be found.

Even though the expression (1.17) is complicated, the evaluation of this quantity only need a few matrix operations which takes a fraction of a second with numerical implementations which is quicker by several order of magnitudes than most of CFD runs presented in §1.1. Most of the data generated by CFD codes were further processed by using GP for the design of calibrated *surrogate models* predicting a given output for a cheap computational cost. The methodology used will be presented in the following chapters

An example of the successive steps of generating a GP model in order to reproduce a function with a squared exponential (SE) kernel is shown on Figure 1.7 for the function:

$$f(x) = \frac{5}{x} \cos\left(\frac{x}{2}\right) + 1$$

The estimation of the predictive distribution is done using **scikit-learn** (Pedregosa, 2011) written for the programing language **Python**.

It is visible that for increasing training points ($N = 2, 3$ and 5), the update of the prior beliefs using Bayes theorem leads to predictions getting closer to the true signal. In addition, the estimated standard deviation gets smaller.

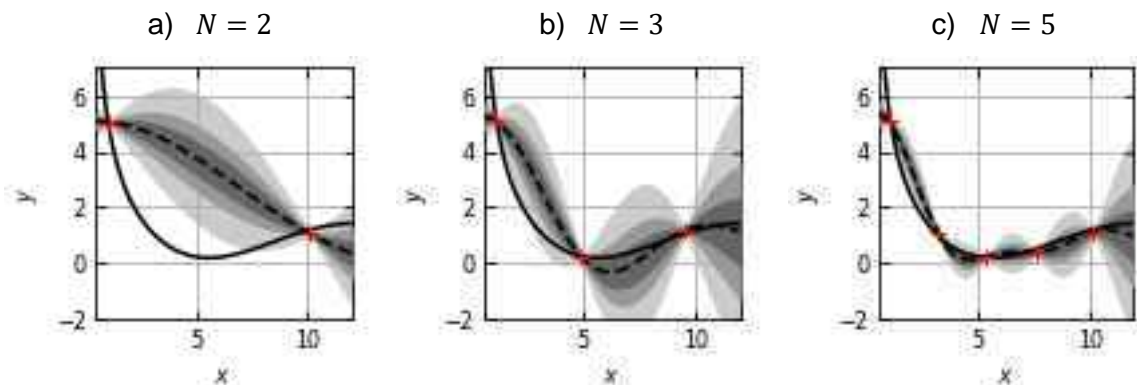


Figure 1.7 - Example of regression of a function f using a GP model with a squared exponential kernel – Red crosses correspond to measured points used in order to fit the true signal in solid black line. The black dashed curve corresponds to the prediction calculated after conditioning the GP with the data points. The shades of grey represent quantiles of the predictive density at each input location.

1.2.4 Numerical methods for UQ

Each source of error/uncertainty identified in §1.2.1 must be investigated and quantified in order to estimate a confidence interval on the computation of the Nusselt number with CFD. This quantification is done using different techniques:

- The uncertainty of the simulation due to uncertain simulation inputs $U_{inputs,exp}$ is estimated by propagating the uncertainty of inputs through the calculation of the Nusselt with CFD. Two methods are tested in this dissertation described in §1.2.4.2.
- The numerical error E_{num} is estimated using Richardson extrapolation combined to a grid convergence method described in §1.2.4.3.

The techniques are presented for the estimation of the uncertainty of scalar outputs, for instance, a local value of the calculated Nusselt number. However, multi-dimensional outputs will also be processed in this dissertation, for instance two dimensional maps of the Nusselt number on a surface. The presented techniques could be extended to these multi-dimensional outputs by simply applying them to each local value. Nevertheless, the computational cost of such an approach is prohibitive for high resolutions maps. Thus, the Proper Orthogonal Decomposition (POD) is used in this work to reduce the dimension of the output data and will be presented in §1.2.4.1.

1.2.4.1 Dimension reduction – Proper Orthogonal Decomposition

POD (Proper Orthogonal Decomposition) is a post-processing technique which generates a modal decomposition of functions based on **observations**. This technique is used in a wide range of domain and is known under different names:

- Karhun-Loève Transform (KLT) in pattern recognition (Sirovich & Kirby, 1987)?
- Principal Components Analysis (PCA) in statistical literature (for example (Diamantaras & Kung, 1996)).
- Proper Orthogonal Decomposition (POD) in mechanical engineering (Lumley, 1967).

The use of POD in fluid mechanics answers to one problematic faced when studying the motion of turbulent flow, which is the reduction of the turbulent motion degrees of liberty to a small number. The first introduction of POD in fluid mechanics has been done by Lumley in 1967 (Lumley, 1967), showing the advantages of this technique to capture the evolution of coherent structures in turbulent flows. The use of POD for this purpose is now widely spread and an early review can be found in (Berkooz, et al., 1993).

The POD is one of the methods used to express for instance a function of time and space $f(\mathbf{x}, t)$ in a function base (cosines, sines, polynomials ...). In most of the cases, the spatial and temporal variations are separated in order to represent the system evolution as the temporal evolution of coherent structures facilitating the comprehension of the evolution. The POD is written:

$$\mathbf{f}(\mathbf{x}, t) \cong \sum_{k=1}^N a_k(t) \phi_k(\mathbf{x}) \quad (1.18)$$

where $(\phi_k)_{k \in [1, N]}$ and $(a_k)_{k \in [1, N]}$ are respectively the modes and components of the decomposition. The mathematical aspect of this decomposition (proof of optimal decomposition, existence...) can be found in an educational way in (Holmes, et al., 1997; Cordier & Bergmann, 2008).

For instance, this method is used in (Podvin, et al., 2020) for the study of the turbulent structures which are generated around an Ahmed body, with \mathbf{f} being the velocity field. This method has been applied for 2D and 3D velocity fields. The spatial distribution of the modes and the temporal fluctuations of the components have been used to describe the behavior of the flow in the wake of the body. POD made simpler the study of this evolution as the number of free parameters in this case has been reduced from the spatial resolution of the initial grid on which the data is retrieved, to a small number of modes. Moreover, POD provided a modal base on which the comparison between experiments and computations was made simpler. Also, the fact that a low number of modes is used to reproduce accurately the behavior of the flow is harnessed for the construction of Reduced Order Models (ROM) (for instance (Holmes, et al.,

1997; Podvin, 2011)). This construction can be done for instance with Galerkin projection of the Navier-Stokes equation combined to the POD decomposition with which the components $a_k(t)$ are then solved. This specific aspect of POD makes its use attractive for optimization problems related to fluid mechanics. In fact, even though the development of CFD and computing performance made easier the study of hydraulic behaviors in industrial system, the large number of free parameters in such problems are not suitable for CFD approach which cost would be prohibitive. An example of the combination of POD to optimization is given in (Bergmann, et al., 2005) where optimization of the aerodynamic behavior of rotary cylinder is done with POD reduced order model.

Different approaches exist for the POD, the one used in this work is based on the snapshot method given in (Sirovich & Kirby, 1987) for human face recognition. In this dissertation, the POD is applied to maps of the Nusselt number or Sherwood number which evolve with the Reynolds number. The Nusselt number defined from the convective wall heat transfer coefficient h_{conv} is taken as example hereinafter.

N_S simulations are used to provide outputs of the Nusselt number field which are called the snapshots. Let us suppose that the dimension of the snapshots is m , corresponding to the discretization of the Nusselt number field on a surface. The j -th snapshot can be written $\mathbf{Nu}^j = (Nu_1^j, Nu_2^j, \dots, Nu_m^j)$. In addition, let us suppose that these snapshots were obtained for different fluid velocity leading to different Reynolds numbers $(Re_j)_{j \in [1, N_S]}$:

$$Nu_i^j = Nu(\mathbf{x}_i, Re_j)$$

Different steps are followed in order to find the modal base. In this dissertation, the whole data is organized in a snapshot matrix A such as:

$$A = \begin{pmatrix} Nu_1^1 & \dots & Nu_1^{N_S} \\ \vdots & \ddots & \vdots \\ Nu_m^1 & \dots & Nu_m^{N_S} \end{pmatrix}$$

In the snapshot methodology, the modal basis is found by computing the 2-point spatial correlation matrix between the different snapshots at the different locations of the field. This matrix is given by $M = \frac{1}{N_S} A^t A$ is computed.

The POD is built in order to satisfy an optimality criterion, the POD provides a reduced dimension subspace of the input vectors on which the error between the projection and the original vector is minimized. It can be proven that finding the POD modes is equivalent to solving an eigenvalue problem on M (Cordier & Bergmann, 2008). The matrix M is positive and symmetric and thus diagonalizable and can thus be written:

$$M = P D^t P$$

where the columns of P are the eigenvectors of M which are the POD modes computed from A .

From the obtained eigenvectors $\phi_1, \dots, \phi_{N_S}$, it is possible to reconstruct the different snapshots with:

$$Nu(x_i, Re_j) = \sum_{k=1}^{N_S} \langle Nu^j, \phi_k \rangle \phi_k(x_i) = \sum_{k=1}^{N_S} a_k(Re_j) \phi_k(x_i)$$

In practice, all the eigenvectors are not kept, and a truncation is done to keep only N_{POD} modes. By construction, the eigenvalues obtained in D are organized from the highest values to the lower values and represent the energy of each mode which in a sense represent their importance. The Relative Information Content (RIC) number is defined as following from the eigenvalues $(\lambda_k)_{k \in [1, N]}$:

$$RIC(i) = \frac{\sum_{k=1}^i \lambda_k}{\sum_{k=1}^{N_S} \lambda_k}$$

Its value gives an indication of the relative importance of each mode which can be used to truncate the POD. In practice, the truncation will be carried out in order to obtain the mean distribution of the Nusselt number over the experiments. The deviation between the truncated POD and the original Nusselt number will be taken into account in the uncertainty of the Nusselt distribution when comparing experiments to CFD in the frame of uncertainty quantification.

The modal base found from the snapshots is then used in order to reconstruct the Nusselt distribution from the truncated POD.

1.2.4.2 Covariance propagation

The operating conditions during heat or mass transfer experiments, which are in this dissertation, the turbulence regime in the test section and the diffusion properties of heat and mass transfer, are obtained through measurements. These measurements usually show aleatory time fluctuations and the models underlying the calculation of the physical properties (diffusion coefficient, thermal conductivity, solubility, density ...) include most of the time an additional uncertainty. In the context of the uncertainty quantification of CFD calculation of the Nusselt number, the experimental configurations, and their operating conditions (flowrate, temperature, physical properties ...) are reproduced. The influence of the uncertainty of the operating conditions on the simulation is quantified through the calculation of the inputs simulation uncertainty $U_{inputs,exp}$ depicted in §1.2.1.

The mean value $\mu_{U_{inputs,exp}}$ and standard deviation $\sigma_{U_{inputs,exp}}$ are calculated with:

$$\begin{aligned}\mu_{U_{inputs,exp}} &= Nu(\boldsymbol{\mu}_{inputs}) - \mu_{Nu(x_{inputs})} \\ \sigma_{U_{inputs,exp}} &= \sigma_{Nu(x_{inputs})}\end{aligned}$$

where, $\boldsymbol{\mu}_{inputs}$ denotes the mean values of the simulation inputs (typically the flowrate, temperature, physical properties). On one hand, $Nu(\boldsymbol{\mu}_{inputs})$ is obtained by considering the simulation for determined inputs (being their mean values $\boldsymbol{\mu}_{inputs}$). On the other hand, $\mu_{Nu(x_{inputs})}$ and $\sigma_{Nu(x_{inputs})}$ are the mean value and standard deviation of the Nusselt number when taking into account the uncertainty of the simulation inputs. They are estimated with propagation techniques. The objective of uncertainty propagation is to estimate the probability density function (PDF) of an output when its calculation relies on uncertain inputs. Two general class of method exist to propagate uncertainty through computations:

- Intrusive methods: the PDF is given, and the propagation is done directly by the solver.
- Non-intrusive methods: The PDF is estimated from realization of the computations.

The commercial CFD software used in this thesis do not include intrusive methods. Thus, only non-intrusive methods of uncertainty propagation will be used and presented.

1.2.4.2.1 Random sampling - Monte Carlo

The first method used in order to propagate uncertainty is **Random Sampling** (RS) coupled with **Monte-Carlo method**. Monte-Carlo methods are statistical approach which aim to build estimators of the output statistical moments based on a large number of realizations and the central limit theorem. The methodology used to propagate the inputs uncertainty on the calculation of the Nusselt number performs the following steps:

- A random sample is generated for the input random variables $(\boldsymbol{x}_i)_{i \leq N_{RS}}$ with a given joint probability density function. Random samples are drawn with a pseudo-random number generator. The theory of these generators will not be covered in this thesis. The random list generator used in this thesis is based on Mersenne twister algorithm. (Matsumoto & Nishimura, 1998).
- An output sample $(Nu(\boldsymbol{x}_i))_{i \leq N_{RS}}$ is evaluated from the sample of inputs by evaluating the response for each element of the sample.
- By considering each draw as the realization of independent and identically distributed random variables and with the **central limit theorem**, the mean and standard deviation of output RV is estimated from asymptotic value of the mean and standard deviation calculated from the sample.

The process for a single input parameter passed as argument in computations is depicted in Figure 1.8.

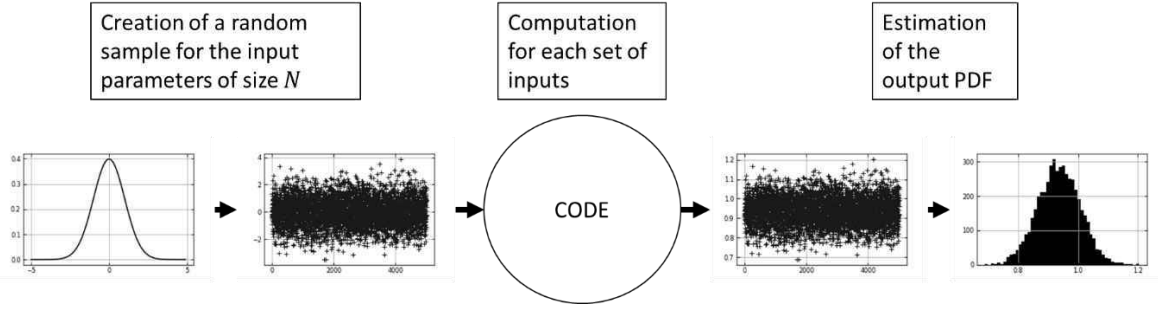


Figure 1.8: Process of propagating a random variable (Gaussian for instance) through a code

The mean and standard deviation of the Nusselt calculation can be written:

$$\mu_{Nu} \approx \frac{1}{N_{RS}} \sum_{i=1}^{N_{RS}} Nu(x_i)$$

$$\sigma_{Nu} \approx \frac{1}{N_{RS} - 1} \sum_{i=1}^{N_{RS}} (Nu(x_i) - \mu_{Nu})^2$$

The disadvantage of this method is the required CPU times for each computation. In fact, these methods require thousands of draws in order to have converged statistics. However, the computation time for each case can take several hour or days with CFD codes. Thus, a **surrogate model** is designed prior to the MC draws with gaussian processes presented in §1.2.3. The evaluation of the CFD output is done with the surrogate model with a negligible computational cost allowing this kind of procedure.

1.2.4.2.2 Deterministic sampling

Another non-intrusive method has been used to propagate the simulation inputs uncertainty. This method is called **Deterministic Sampling (DS)** and is detailed in references (Hedberg & Hessling, 2015; Hessling, 2013). This method originates from the Unscented Kalman Filtering (UKF) which uses **weighted sigma points** in order to propagate the covariance of **gaussian inputs** through nonlinear transformations (Julier, et al., 1995; Julier & Uhlmann, 2004). This method relies on the representation of statistical information of the inputs with a sample, as it is for random sampling exposed in the previous paragraph. The difference between both methods is the number of elements in the sample which is significantly smaller in UKF ($2n$ sigma points for n uncertain parameters for UKF, thousands for RS); and the choice of the elements of the sample, which is not **random** in this case, but done with **deterministic** rules. In both cases, a gaussian distribution is fitted on the realizations of the output, either with the central limit theorem for RS, or by combining the evaluation of weighted sigma points for UKF. UKF presents the advantage of being affordable when the estimation of the output for a given set of inputs is non negligible (as it is for CFD). Nevertheless, it has been shown that the

performance of the UKF is impacted for increasing number of uncertain parameters due to the definition of the weights and sigma points that are chosen to evaluate the output (corresponding to the Standard excitation matrix in Appendix A).

The main idea of evaluating the response of weighted sigma points to deduce the output distribution is kept in the formulation of the DS for uncertainty quantification on CFD simulations given in (Hedberg & Hessling, 2015). The difference resides in the choice of the sigma points and weights. An example of DS ensemble is given on Figure 1.9, where three sigma points $(X_i)_{i \in [1,3]}$ are chosen to represent an input RV X following a univariate gaussian distribution that is given as an input of a function f . In this example, the function f is defined as:

$$f(x) = 3x^{0.8} + 5$$

The response is evaluated for these inputs, allowing at the end of the process to estimate the mean and standard deviation of the random variable $f(X)$ with:

$$\mu_{f(X)} = \langle f(X) \rangle = \sum_{i=1}^3 w_i f(X_i)$$

$$\sigma_{f(X)}^2 = \langle \delta^2 f(X) \rangle = \sum_{i=1}^3 w_i (f(X_i) - \mu_{f(X)})^2$$

where, X_i are the sigma points and w_i are the associated weights. Ensembles with their weights are discussed in (Sahlberg, 2016) for gaussian distributions with some of them reported in Appendix A.

In the general case, the probability density function of the inputs might not be a Gaussian and can even not be available. In these situations, the difficulty of this methodology resides in the choice of the sigma points and the weights. This choice is done by considering the statistical moments of the input random variables. The choice of the sample of n elements $\tilde{\mathbf{X}} = (\tilde{X}_{ij})_{i \in [1,n], j \in [1,p]}$ for an input random variable $\mathbf{X} = (X_j)_{j \in [1,p]}$ composed of p independent variables of mean value $\boldsymbol{\mu}_X$, can be done by respecting successive statistical moments of order m .

In the frame of DS using weighted sigma points, respecting the m -th statistical moment can be written for the parameter X_j as following:

$$\sum_{i=1}^n w_i = 1, \quad \sum_{i=1}^n w_i (\tilde{X}_{ij} - \mu)^m = \langle \delta X_j^m \rangle \quad (1.19)$$

Different strategies exist to choose a sample that respects these moments. In general, to encode m moments, a system of m nonlinear equation needs to be solved which allows to get each sigma point $(\mathbf{X}_i)_{i \in [1,n]}$ of the sample.

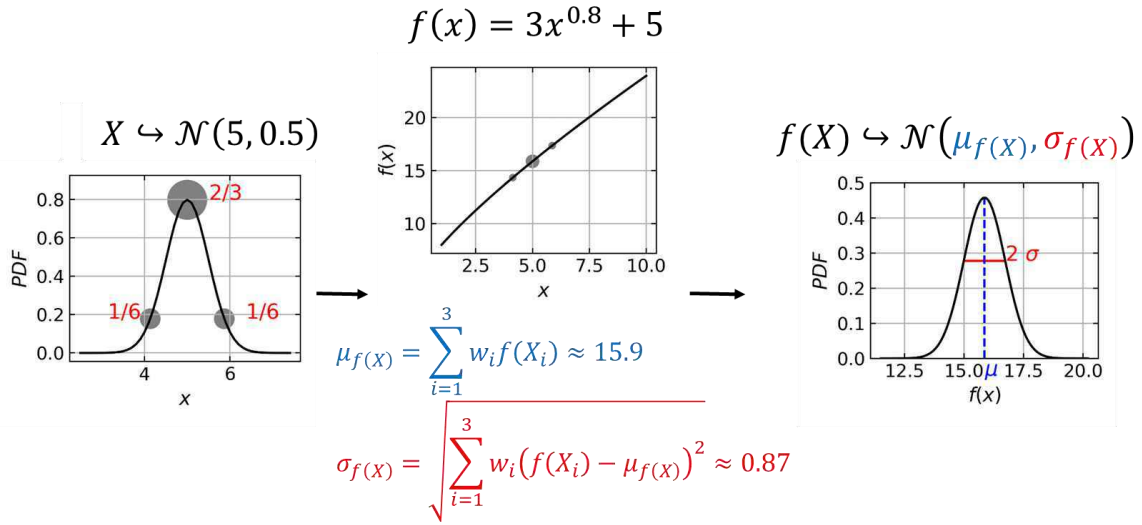


Figure 1.9: Propagation with Deterministic Sampling of the uncertainty of an input following a normal distribution $\mathcal{N}(5, 0.5)$ through the function f . Three sigma points having each a weight representative of the input parameter PDF (left). The evaluation is shown on the middle plot with estimations of the resulting mean value and standard deviation. The output PDF is then shown on the right plot with the calculated mean (in blue) and a 2 sigma interval (red).

Solving nonlinear equations is a hard task, thus another strategy discussed in (Hessling, 2013) consists of choosing sigma points and modifying the weights to reach the aimed statistical moment. In this case, the weights can be chosen by solving linear equations.

The more sigma points are calculated; the more statistical moments can be respected. The work that is presented in the reference (Hedberg & Hessling, 2015) for propagation through CFD simulation shows that respecting four statistical moments are satisfactory for the creation of a sample with five independent uncertain parameters, with negligible change when taking into account higher order statistical moments.

In this dissertation, the method will only be illustrated for the simple case of propagating the variance of a univariate random variable following a normal distribution through the calculation of the Nusselt number with CFD. In this case, the mean value and standard deviation of the output is estimated with:

$$\langle Nu(X) \rangle = \sum_{i=1}^N w_i Nu(X_i)$$

$$\langle \delta^m Nu(X) \rangle = \sum_{i=1}^N w_i (Nu(X_i) - \langle Nu(X) \rangle)^m$$

Where X_i correspond to the sigma points chosen for the uncertain input X , and w_i the associated weights.

1.2.4.3 Grid Convergence Method (GCM)

The equations modelling the dynamics of fluid flow have been set for continuous space and time coordinates. When solving these equations numerically, these coordinates are discretized, inducing an error in the computations. The method used in this thesis to estimate the numerical error is based on ASME work in reference (Coleman & Members, 2009) giving guidelines for its estimation. The approach is known as the Grid Convergence Method (CGM) which is based on the Richardson Extrapolation (RE) (Richardson, 1911). For a computed variable V dependent on the grid of size h , the discretization error called the numerical error is estimated by making a Taylor expansion of V for h :

$$E(V_h) = V_{exact} - V_h = C_1 h + C_2 h^2 + \dots$$

where, C_1, C_2, \dots correspond to the derivative of V when taken as a function of h .

Since its original formulation, this method has been extensively studied in literature leading to a good understanding of the results obtained. Indication of the method is given in (Celik, et al., 2008). The use of this method for non-uniform grids is discussed in (Celik & Karatekin, 1997). The estimation of the numerical error in this dissertation has been done with the following steps:

- Generate m meshes with $(N_i)_{i \in [1, m]}$ cells with a refinement factor desirably such as $r = \frac{h_{coarse}}{h_{fine}} > 1.3$ where h is the cells height
- Evaluate the results of the computation y_{N_i} of the quantity of interest y for each mesh
- Fit a function which is of the type $y_N = \hat{f}(N) = \hat{f}_0 + \frac{a}{N^3}$, with N the number of cells of the model on the data (N_i, y_{N_i}) . \hat{f}_0 denotes the intersection of the regression law for $\frac{1}{N} \rightarrow 0$ and a is another coefficient fitted on the data.
- Determine with the fit the numerical error for a mesh of size N :
 - Bias $\mu_{ENUM}(N) = \hat{f}(N) - \hat{f}_0 = \frac{a}{N^3}$
 - Standard deviation $\sigma_{ENUM} = \sqrt{\frac{1}{m-1} \sum_1^m (\hat{f}(N_i) - y_{N_i})^2}$

1.3 Conclusion

This chapter presented different turbulence models and wall treatment which are available in most of commercial CFD software. The turbulence closure provided by these models and the wall functions which are used have been calibrated in literature on specific test cases.

Therefore, their use in the industry undergoes a validation process which aims to determine their accuracy regarding real life situations in complex geometries. This validation is done in the uncertainty quantification frame which aims to identify and quantify the different sources of uncertainties (epistemic and aleatory) affecting the comparison between CFD and real-life experiments. In the nuclear industry, the validation of these codes is done with the approach given by the ASME guide for the validation of CFD when calculating the heat transfer coefficient. The nomenclature and definitions of the different source of uncertainties have been given in addition to methods to estimate their values.

The validation is done on reduced scale mock-ups of nuclear plant components with reduced Reynolds number due to the difficulty to reach the Reynolds number of an operational reactor in experimental facilities. The transposability of the results between the mock-up and reactor scales is investigated in this dissertation. The extrapolation of the errors and uncertainties from experimental Reynolds numbers to the reactor scale Reynolds numbers could not be done during this thesis. The transposition of the errors to the reactor scale is studied in this dissertation by calculating the evolution of the model error with the Reynolds number.

The first step for the estimation of the model error is the generation of experimental data with which the assessment of the deviation between CFD and experiments will be possible. An important aspect of this work has been the development of a measurement methodology based on the heat and mass transfer analogy. This measurement method has first been tested on a rectangular channel and compared to literature heat transfer coefficient data. The presentation of this step is given in Chapter 2. Then the uncertainty quantification process is applied to CFD computations with two commercial codes used in industry on the rectangular channel case in Chapter 3. Following these preliminary tests, the approach has been reproduced on an industrial geometry. Heat and mass transfer measurements were done in a steam generator water box mock-up for Reynolds number in the range $[10^5, 10^6]$, which will be presented in Chapter 4. These experiments were reproduced with CFD in Chapter 5 with different turbulence models. The comparison between the experimental data and the CFD calculations, and the evolution of the model error will be presented in Chapter 6.

Chapter 2 Mass transfer measurements in a rectangular channel and heat transfer analogy

2.1 Introduction

The work presented in this chapter has been published in the proceedings of the conference ATH'20 (*Advances in Thermal Hydraulics*) (Khayiguian, et al., 2020).

A method based on the heat and mass transfer analogy has been used in order to generate heat transfer data for comparison with heat transfer simulations (CFD). In this study, the mass transfer coefficient has been measured experimentally for an extensive range of Reynolds number in a rectangular channel with the use of gypsum dissolution in water. Heat and mass transfer analogy has been studied in literature, for instance, a review can be found in (Goldstein & Cho, 1995) for measurements with naphthalene sublimation for estimations of thermal transfer in air. For gypsum dissolution in water, partial comparison with heat transfer has been made in (Chang, et al., 2013) for a cylinder in cross flow for Reynolds number around 6700. The measured distribution of the Sherwood number has been found to be in good agreement with heat transfer measurements at equal Reynolds number corroborating the heat and mass transfer analogy assumption. In this dissertation, the Reynolds numbers tested are much higher and the flow configuration is not the same. For these turbulence regimes, the gypsum surface roughness has been found to affect the mass transfer, which deviates from the smooth wall case. In this chapter, the analogy between heat and mass transfer is presented, then the effect of roughness on heat/mass transfer is detailed. Finally, the experimental apparatus and methodology used in order to obtain smooth wall heat transfer data from gypsum measurements will be presented with their results, in comparison of heat transfer data from literature.

2.2 Transposition of the mass transfer coefficient

2.2.1 Heat and mass transfer analogy

Heat and mass transfer are both diffusion process. The analogy between the two phenomena relies on the expression of the heat/mass flux which is either expressed with Fick law for mass diffusion or Fourier law for heat (Bejan, 2013). The similarity of these phenomenological laws leads to transport equations in flows which are the same in both case with different coefficient. For instance, the similarity between the heat and mass transfer can be understood by looking the Reynolds Average Navier Stokes (RANS) equations for mass and energy. The flow is supposed incompressible, and the effect of viscous stress in the energy equation from which the temperature equation is inferred is neglected. No volumetric heat or mass source are present. The equation can be written as following (Bejan, 2013) :

$$\rho C_p u_j \frac{\partial T}{\partial x_j} = \frac{\partial}{\partial x_j} \left[\lambda \frac{\partial T}{\partial x_j} - \rho C_p \overline{u_j' T'} \right]$$

$$u_j \frac{\partial c}{\partial x_j} = \frac{\partial}{\partial x_j} \left[D \frac{\partial c}{\partial x_j} - \overline{u_j' c'} \right]$$

For both quantities $X = T, c$, the term $\overline{u_j' X'}$ represent a fluctuating part due to the turbulence of the flow. The Simple Gradient Diffusion Hypothesis is expressed as following:

$$\overline{u_j' T'} = -\alpha_t \frac{\partial \bar{T}}{\partial x_j}, \quad \overline{u_j' c'} = -D_{m,t} \frac{\partial \bar{c}}{\partial x_j}$$

with, α_t and $D_{m,t}$ respectively the turbulent heat diffusion coefficient and turbulent mass diffusion coefficient, related to the turbulent Prandtl number and Schmidt number: (see §1.1.3.4)

$$Pr_t = \frac{\nu_t}{\alpha_t}, \quad Sc_t = \frac{\nu_t}{D_{m,t}}$$

with, ν_t the eddy viscosity that can be defined for eddy viscosity turbulence model as indicated in §1.1.3.3. The equation above can be non-dimensionalized by introducing the Reynolds, Prandtl number and Schmidt numbers defined in §1.1.2 for a characteristic length D_H and characteristic velocity of the flow U . Moreover, the dimensionless temperature and mass concentration can be defined as following:

$$\theta = \frac{T - T_\infty}{T_w - T_\infty} \quad \phi = \frac{c - c_\infty}{c_w - c_\infty}$$

The subscript w denotes wall quantities and the subscript ∞ reference conditions.

By using D_H as a reference length, and U as reference velocity, the velocity and x - j coordinate derivative are non-dimensionalized as follows:

$$\frac{\partial}{\partial \hat{x}_j} = \frac{D_H \partial}{\partial x_j}, \quad \hat{u}_j = \frac{u_j}{U}$$

The equations can finally be written:

$$\hat{u}_j \frac{\partial \theta}{\partial \hat{x}_j} = \frac{1}{RePr} \frac{\partial}{\partial \hat{x}_j} \left[\left(1 + \frac{\nu_t Pr}{\nu Pr_t} \right) \frac{\partial \theta}{\partial \hat{x}_j} \right]$$

$$\hat{u}_j \frac{\partial \phi}{\partial \hat{x}_j} = \frac{1}{ReSc} \frac{\partial}{\partial \hat{x}_j} \left[\left(1 + \frac{\nu_t Sc}{\nu Sc_t} \right) \frac{\partial \phi}{\partial \hat{x}_j} \right]$$

It can be noticed that for equal Prandtl and Schmidt number, the solutions of these equations are the same for equal boundary conditions, equal diffusion properties and flow configuration. The difference between the two situations could arise from the turbulent Prandtl number and Schmidt number. In fact, as it has been quickly presented in §1.1.3.4, the turbulent Prandtl/Schmidt number evolves when getting close to the surface which could affect the Sherwood and Nusselt number comparison. Several orders of magnitude separate the Prandtl number of water and the Schmidt number of gypsum dissolving in water. Nevertheless, in both cases, the boundary layers are driven by convection.

The heat/mass transfer at the fluid/wall are described with the Nusselt/Sherwood number defined in §1.1.2. The solution of the equations for energy and mass as depicted in the equations above gives the function describing the general behavior of the heat and mass transfer. With the use of Vaschy-Buckingham theorem, it is possible to write this solution as a function of the dimensionless numbers and dimensionless coordinates:

$$Nu = g(Re, Pr, \hat{x})$$

$$Sh = g(Re, Sc, \hat{x})$$

For identical flow configuration, boundary conditions and Prandtl and Schmidt numbers, the heat and mass transfer should be the same. Thus, the methodology used in this chapter in order to obtain the heat transfer coefficient from the gypsum dissolution technique has been to:

- Find the functional relationship g for the Sherwood number in the experimental range of Schmidt and Reynolds number, based on the experiments results and literature.
- Transpose the relation to the aimed Prandtl number in order to evaluate the Nusselt number.

2.2.2 State of the art

A rich literature is available for the heat and mass transfer analogy, the most classical method to obtain the heat transfer coefficient from the knowledge of mass transfer coefficient is the

Chilton--Colburn J-factor analogy (see for instance (Bejan, 2013)). This analogy relies on the Reynolds analogy between heat transfer and wall friction for turbulent flow and can be written in a simplified way as following:

$$Nu = \frac{1}{2} C_f Re Pr^{\frac{1}{3}}, \quad Sh = \frac{1}{2} C_f Re Sc^{\frac{1}{3}}, \quad C_f = \frac{\tau_w}{\frac{1}{2} \rho U_\infty^2} \quad (2.1)$$

where C_f is the friction coefficient, defined from the wall shear-stress τ_w , the density ρ and a reference velocity U_∞ . One can also express the friction factor C_f as a function of the Reynolds number in order to express the Nusselt number (respectively Sherwood) number as a function of only the Reynolds and Prandtl (resp. Schmidt) numbers.

Reynolds's analogy expressed for heat and mass transfer in (2.1) can also be re-written as following:

$$F = \frac{Nu}{Sh} = \left(\frac{Pr}{Sc} \right)^{1/3}$$

The coefficient $\frac{1}{3}$ relating to the dependency of the heat (resp. mass) transfer to the Prandtl (resp. Schmidt) number is not suitable for all the configuration. Thus, the transposition factor F is written as a function of the Prandtl and Schmidt number as following:

$$F = \left(\frac{Pr}{Sc} \right)^n$$

where n is chosen in the range [0.3, 0.4] depending on the configuration.

The use of the analogy between heat and mass transfer for estimation of the Nusselt number from Sherwood measurements has been widely used with the naphthalene sublimation technique for measurements in air. In this case, the Schmidt and Prandtl number are of the same order of magnitude. A written article by *Goldstein and Cho* (Goldstein & Cho, 1995) reviews different measurements that have been carried out with the naphthalene and presents the pros and con of this method. Also, experimental validation of the analogy is presented in (Kulkarni, et al., 2017) and (Mittal, et al., 2017) for laminar and turbulent boundary layer flow and separated flow for a backward facing step. In these two cases of heat and mass transfer measurements, the transposition factor calculated was coherent with the previous formulation and showed spatial distributions of the transfers similar in both cases. For the gypsum dissolution, measurements have been done for a cylinder exchanging with water in crossflow at $Re = 6700$ and $Sc = 1500$ in (Chang, et al., 2013). A scaling of the Sherwood number by $Re^{1/2} Sc^{1/3}$ was proposed in order to compare the results to mass transfer measurements from (Sanitjai & Goldstein, 2001) with naphthalene sublimation at $Re = 29\ 100$, $Sc = 2.28$, and to heat transfer measurements from (Van Meel, 1962; Sanitjai & Goldstein, 2004) respectively at $Re = 5320$, $Pr = 0.71$ and $Re = 6630$, $Pr = 139$. The comparison is depicted on Figure 2.1,

showing that the gypsum dissolution profile is similar to other measure of heat and mass transfer.

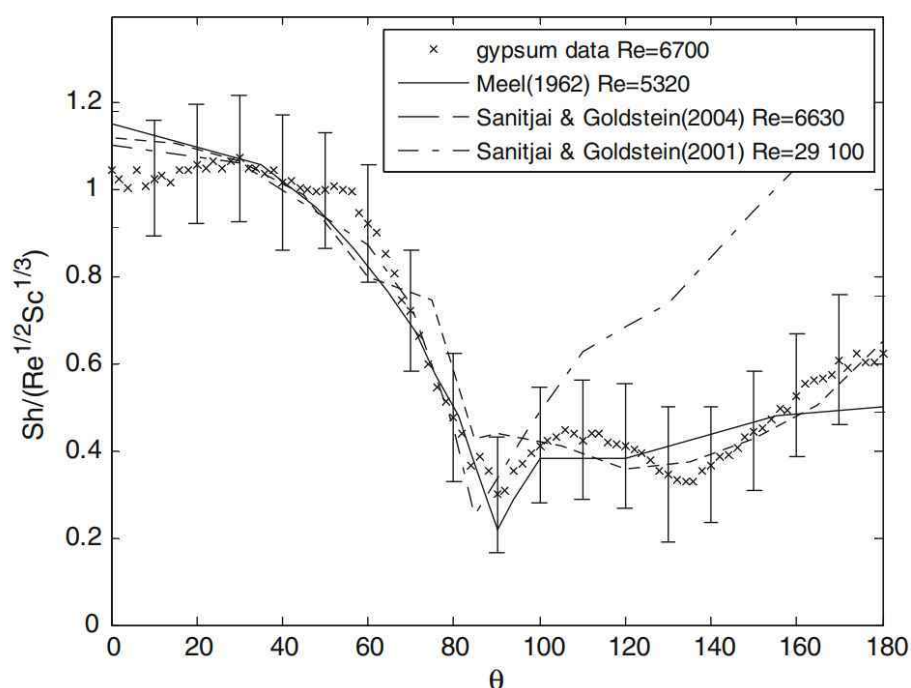


Figure 2.1 comparison of the radial distribution of the Sherwood number and Nusselt number around a cylinder in cross flow obtained with gypsum dissolution, naphthalene sublimation and heat transfer measurements. The Sherwood number is scaled by $Re^{1/2}Sc^{1/3}$ and the Nusselt number by $Re^{1/2}Pr^{1/3}$. From (Chang, et al., 2013).

In both cases of heat and mass transfer, the Sherwood (resp. Nusselt number) is proportional to $Re^{1/2}$ and to $Sc^{1/3}$ (resp. $Pr^{1/3}$). It should be noted that the difference for high angle θ at $Re = 29\ 100$ are well known and are not due to differences in the Schmidt or Prandtl numbers but to the higher Reynolds number. The similarity of heat and mass transfer measurement in this particular configuration shows that the analogy between heat and mass transfer can be of use to assess the spatial distribution of the transfers from one domain to the other.

The use of gypsum dissolution for estimation of the heat transfer coefficient in identical configuration is almost nonexistent in the scientific literature. Most of the work concerns the geological field and the Flow Accelerated Corrosion (FAC) field. Some of these works were of interest, especially the ones concerning the study of the surface aspect of the gypsum after dissolution which was found to be essential for understanding the mass transfer with water. This specific aspect will be presented in the following section.

2.2.3 Roughness effect on the flow

The calculation of the Sherwood number from the gypsum dissolution relies on the measurements of the surface wear as the gypsum sample dissolves in water. It has been shown in (Wang & Ewing, 2016; Wang & Ewing, 2017) that roughness develops as the dissolution occurs. The roughness elements affect the flow in the vicinity of the wall, enhancing in return the mass transfer with the gypsum sample. The roughness effect must thus be considered when transposing the measurements to smooth wall Nusselt number.

The impact of roughness on friction, heat transfer and mass transfer has been studied in the past for many types of roughness elements and for different Prandtl/Schmidt numbers. Nikuradse (Nikuradse, 1950) was one of the pioneer in calculating the effect of roughness on the head loss and velocity profile in a pipe with a methodical approach: he created an artificial roughness by fixing sand grain at the walls and showed that the behavior of the near wall friction depends of the relative roughness e/R where e and R are respectively the roughness elements height and the pipe radius. The evolution of the near wall friction with the Reynolds number and the surface roughness in pipe flow is given on Figure 2.2. For Reynolds numbers such as $\log(Re) < 3.2$, the flow is laminar, and the roughness does not affect the friction factor behavior. Differences start appearing for turbulent flows where both the roughness height and Reynolds number affect the evolution of the friction factor:

- when the roughness elements are small enough to lie inside the viscous sublayer, the pipe can be considered smooth, and the friction only depends on the Reynolds number. The boundary layer thickness decreases for increasing Reynolds number, therefore, the size from which the roughness starts to be “intrusive” decreases for higher turbulence regime.
- when the relative roughness increases, the friction reaches a transition region where it depends simultaneously on the Reynolds number and the roughness height.
- if the roughness continues increasing, the friction factor becomes Reynolds number independent, it is the fully developed turbulent flow.

The effect of roughness on heat, mass and momentum transfer has been studied in literature for different shape, aspect ratio of roughness elements while the most relevant parameters have been investigated in order to quantify precisely the effects.

Differences have been observed for regular roughness (Dawson & Trass, 1972; Berger, et al., 1979; Lolja, 2005) and non-regular roughness (Wang & Ewing, 2017; Postlethwaite & Lotz, 1988; Coney, 1981). For non-regular roughness, typically eroded/corroded surfaces, the difficulty lies in the research of the parameters impacting the measures.

In the case of gypsum surface, the surface aspect goes from a smooth wall at the beginning of the dissolution to a naturally roughened surface after dissolution. Gypsum roughness has been studied in the past in the geological field in order to understand structures that appears due to erosion/dissolution in karst systems (Blumberg, 1970; Allen, 1971; Blumberg & Curl, 1974; Villien, et al., 2005).

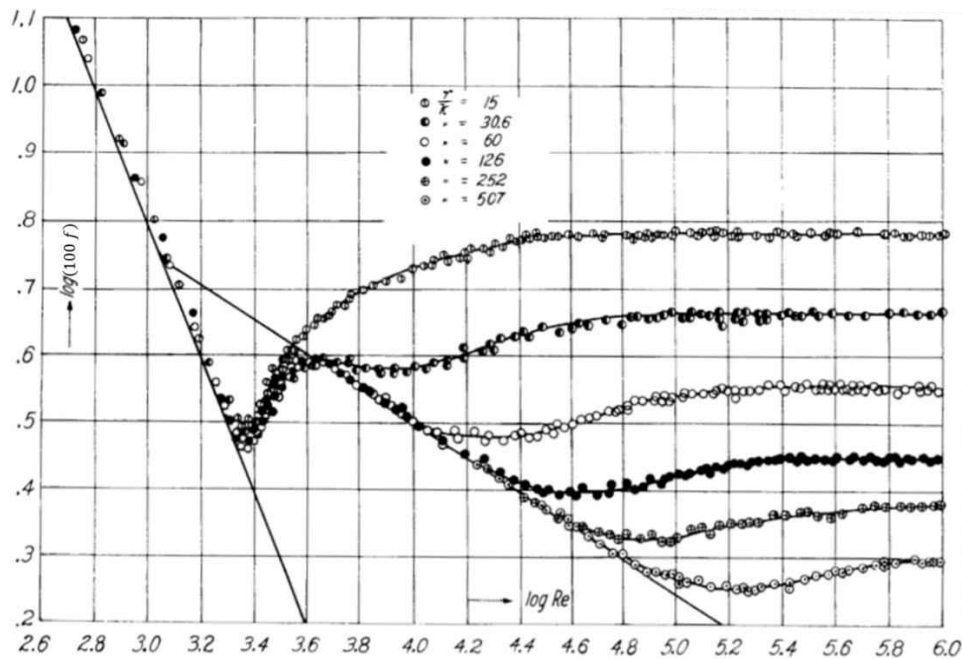


Figure 2.2: relation between the friction factor f used to calculate the pressure drop per unit of length for given relative roughness e/R and Reynolds number Re . From (Nikuradse, 1950).

These studies mainly focused on the evolution of the surface roughness elements shape which evolves during the dissolution and tends to reach a *scallop* aspect resembling corroded/eroded surfaces. In addition, it has been shown that the initiation of these roughness elements is impacted by the initial defects in the gypsum sample due to the formation of macro pores during the casting or due to eroding elements in the flow damaging the gypsum lining during the dissolution. In fact, the presence of these defects was shown to accelerate the appearance and growth of the surface roughness. The enhancement of mass transfer due to its development has been studied and quantified for pipe flow for Reynolds numbers going up to 200 000 (Wang & Ewing, 2016; Wang & Ewing, 2017). The enhancement has been correlated to the peak to valley roughness e_{p-v} and the spacing between the roughness elements l_{str} . The enhancement of the mass transfer due to the surface roughness is given in comparison to the non-dimensional peak to valley on Figure 2.3, for regular roughness (Dawson & Trass, 1972) and gypsum natural roughness (Wang & Ewing, 2017). It is noticeable that the effects of roughness differ importantly whether it develops naturally or remain static and organized.

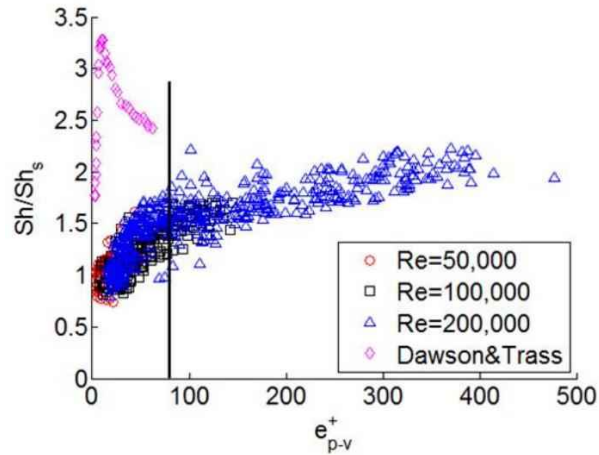


Figure 2.3: evolution of the roughness enhancement of the Sherwood number with the dimensionless roughness height (peak to valley). From (Wang & Ewing, 2017).

2.3 Experimental setup and configuration

The experiments that will be presented in this chapter have been conducted in Framatome's experimental facilities. The objective of these experiments was to test the gypsum methodology on a documented case in order to verify the transposability of the measure to the heat transfer coefficient before experiments on more complex geometries. A schematic view of the experimental setup is depicted on Figure 2.4. The test loop is an closed circuit where water is pumped from a tank which contains 250 m^3 of water at ambient temperature. The water temperature is kept constant through a heater. The flowrate in the test section is adjusted electronically with a valve in order to control the pressure drop of the pump. A secondary circuit by-passing the test section is used in order to reach the targeted working temperature. Two thermocouples provide the inlet and outlet temperature of the test section which is a rectangular channel. The absolute and differential pressure is measured along the test section. The test section can be seen on Figure 2.5.

The gypsum sample is molded in a 3D printed cast which is then inserted in a metallic holder visible on Figure 2.6. The sample is then mounted flushed to the inner section wall to avoid marching step default. At the inlet, a slowly divergent diffuser is present before entering the rectangular channel. The gypsum lining is located at a length $L = 20D_H$ of the inlet with $D_H = 0.05\text{m}$. The aspect ratio of the duct is defined such as $AR = \frac{\text{width}}{\text{height}} \approx 4.2$.

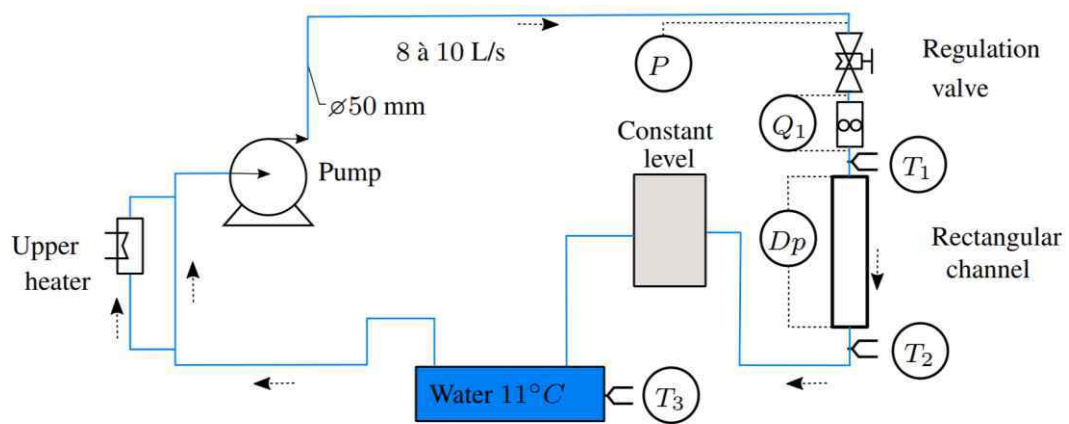


Figure 2.4: schematic view of the experimental loop.



Figure 2.5: view of the rectangular test section. The flow goes from right to left.



Figure 2.6: metallic holder with the gypsum samples molded in 3D printed cast.

2.4 Methodology

Measurements of the mass transfer coefficient have been conducted in the channel where a soluble gypsum part of the wall has been exposed to a stream of water. The gypsum is cast by

mixing water and pure hydrocal ($CaSO_4 \cdot \frac{1}{2}H_2O$) at a ratio balancing density and casting rate. Shortly the gypsum density increases by diminishing the mass ratio $\frac{M_{Water}}{M_{hydrocal}}$ but the time during which the slurry can be cast is shorter in turn. The choice of the water-gypsum ratio has been made after testing several combinations and with the help of indications on the effects of preparation on the cast gypsum found in the literature (Ochoa, et al., 2017; Ochoa, et al., 2018). The ratio has been finally set to $\frac{M_{Water}}{M_{hydrocal}} = 0.8$. Once the mixture is prepared, the slurry is poured within the holder pressed against a Teflon surface. This material choice ensures the smoothest conditions possible. The sample is then placed within a shaker in order to help the entrapped air bubbles to escape the slurry. This process eliminates most defects which potentially modify the dissolution and increase the roughness. Finally, the samples are dried at $50^\circ C$ in an oven for 8 hours, until all the excess water evaporates. Each sample is weighed before and after dissolution to measure their mass loss accurately.

The instantaneous value of the physical properties at the time t are calculated with the mean temperature $T(t) = \frac{1}{2}(T_{in}(t) + T_{out}(t))$ where $T_{in}(t)$ and $T_{out}(t)$ are respectively the inlet and outlet temperature of the test section given by the thermocouples. The temperature discrepancy $T_{out}(t) - T_{in}(t)$ is small within the time period of measurements in front of the respective fluctuations of $T_{in}(t)$ and $T_{out}(t)$. The important mixing in the test section leads to the assumption that the mean temperature $T(t)$ gives a good indication of the temperature in the test section. The acquisition frequency of the thermocouple was set at 2 Hz for experiments lasting between 45 minutes to 4 hours depending on the value of the Reynolds number. These durations denoted t_{exp} were chosen sufficiently high to dissolve enough gypsum for an appropriate measurement of the surface wear with the laser scan, but also sufficiently low to keep a relatively smooth surface topography. We must keep in mind that the gypsum surface naturally develops from a flat surface to a rough one when dissolving in water, thus affecting the mass transfer coefficient, as it has been shown in previous studies (Wang & Ewing, 2016; Wang & Ewing, 2017). Temperature measurements in time made possible the calculation of c_w , the wall concentration of $[Ca^{2+}]$ thanks to data from (Blount & Dickson, 1973) reported in (Klimchouk, 1996) which makes a review of the variables affecting gypsum dissolution. The solubility c_w is tabulated for different temperature, enabling its estimation for arbitrary temperature using linear interpolation. Furthermore, the gypsum diffusion coefficient, D_{gypsum} , can be calculated via the Stokes–Einstein equation by assuming that the diffusion coefficient is proportional to the ratio $\frac{T}{\mu(T)}$ where T is the fluid temperature and $\mu(T)$ the dynamic viscosity at temperature T . The value of D_{gypsum} at $25^\circ C$ was obtained from (Wang, et al., 2015). This assumption was derived from Stokes law which enables the estimation of the viscous forces applied to a sphere in a viscous fluid. Einstein applied this formula in order to estimate the diffusion coefficient for a spherical particle following a Brownian motion in the fluid (see for instance (Miller, 1924)). The article (Simpson & Carr, 1958) compares this model

to experiments for ions H^+ in water on an extended range of temperature and indicates a good agreement with experimental data until approximately $40^\circ C$ from which the bias between measurements and the model start to increase.

The height of the surface wear is obtained with a laser scan of the surface. The surface sample was not originally flat due to the molding which has been done in 3D printed cast. The gypsum lining curvature followed the borders which have been extracted in order to correct the topography obtained from the scan. The impact of this correction is an increased uncertainty at the leading edge of the sample where the curvature was the most important. The corrected surface wear height is denoted $w(x, y)$. The density of the gypsum ρ_{gypsum} is obtained from the weight loss and the volume loss measured for each experiment.

The temporal average of the local Sherwood number $\overline{Sh(x, y)}$ on the gypsum surface and the standard deviation σ_{Sh} are then estimated on the time period t_{exp} as:

$$\overline{Sh(x, y)} = \langle Sh(x, y, t) \rangle_t = \left\langle \frac{\rho_{gypsum}}{c_w(T(t))} \frac{D_H}{D_{gypsum}(T(t))} \frac{w(x, y)}{t_{exp}} \right\rangle_t$$

$$\sigma_{Sh}(x, y) = \sqrt{\langle (Sh(x, y) - \overline{Sh(x, y)})^2 \rangle_t}$$

where, the operator $\langle \cdot \rangle_t$ denotes the time average value during the experiment.

The instantaneous Reynolds and Schmidt numbers are calculated with thermal properties evaluated at the temperature $T(t)$ and the flowrate.

$$Re(t) = \frac{U(t)D_H}{\nu(T(t))}, \quad Sc(t) = \frac{\nu(T(t))}{D_{gypsum}(T(t))}$$

The characteristic velocity $U(t)$ is calculated from the flowrate by assuming a flat profile of the velocity in the channel. Moreover, the evolution of ν with the temperature is retrieved from IAPWS 2008 data base (Huber, et al., 2009).

The time average and the standard deviation of the Reynolds number and Schmidt number introduced earlier are then calculated from the measurements of the flowrate and temperature during the experiments.

$$\overline{Re} = \langle Re(t) \rangle_t, \quad \text{and}, \quad \sigma_{Re} = \sqrt{\langle (Re(t) - \overline{Re})^2 \rangle_t}$$

$$\overline{Sc} = \langle Sc(t) \rangle_t, \quad \text{and}, \quad \sigma_{Sc} = \sqrt{\langle (Sc(t) - \overline{Sc})^2 \rangle_t}$$

The heat and mass transfer analogy tells us that the evolution of the mass transfer coefficient between the soluble wall and the stream of water along the surface is analogous to the development of the heat transfer coefficient that is often referred as Graetz problem, and which is indicated in schematical way on Figure 2.7.

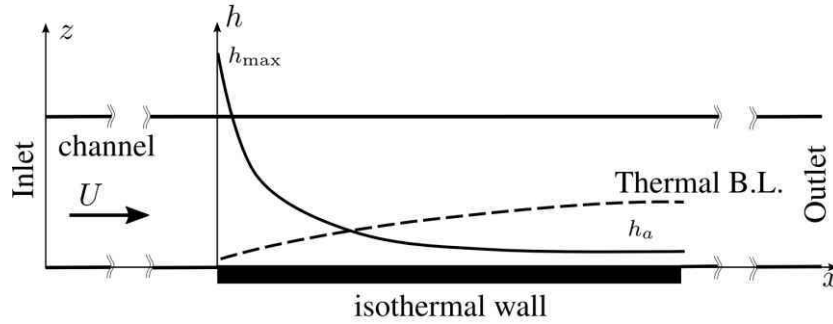


Figure 2.7: evolution of the heat transfer coefficient for a developing boundary layer.

The heat transfer coefficient goes from a maximum value (subscript max) at the leading edge of the fixed temperature wall to an asymptotic value (subscript a) at the end of the thermal boundary layer development. Elements on the dynamic of the thermal gradients are given in literature (Deissler, 1954; Sparrow, et al., 1957; Boelter, et al., 1948; Notter & Sleicher, 1972; Sleicher Jr, 1956).

The experimental Sherwood number Sh is found to evolve from a maximum value to an asymptotic value which is also kept far downstream of the sample location. Furthermore, the dissolution rate is homogeneous in the spanwise direction y . Thus, the mass transfer coefficient in the spanwise direction is averaged (averaging operator $\langle \cdot \rangle_y$) and the standard deviation is calculated. These are referred respectively as $\widehat{Sh}(x)$ and σ_{Sh} . Then an exponential decay law is fitted to the data, providing \widetilde{Sh}_{max} , \widetilde{Sh}_a and l parameters:

$$\begin{aligned}\widehat{Sh}(x) &= \langle \overline{Sh}(x, y) \rangle_y \\ \sigma_{Sh}(x) &= \sqrt{\langle (\overline{Sh}(x, y) - \widehat{Sh}(x))^2 \rangle_y} \\ \widetilde{Sh}(x) &= (\widetilde{Sh}_{max} - \widetilde{Sh}_a) \exp\left(-\frac{x}{l}\right) + \widetilde{Sh}_a\end{aligned}$$

In addition, the parameters \widetilde{Sh}_{max} and \widetilde{Sh}_a are calibrated in order to fit the mean value of the Sherwood number associated with the mass loss. This last process yields the parameters, $Sh_{cal,max}$ and $Sh_{cal,a}$. The successive steps of the process are depicted on Figure 2.8.

The different values of the asymptotic Sherwood number have been obtained at high Schmidt number depending on the temperature of the flow. The Schmidt number ranges from 700 to 1800. A transposition to low Schmidt number ($Sc = 10$) has been carried out to make a comparison with heat transfer coefficient correlations from the literature for fluids having a Prandtl in the range $[1, 10]$.

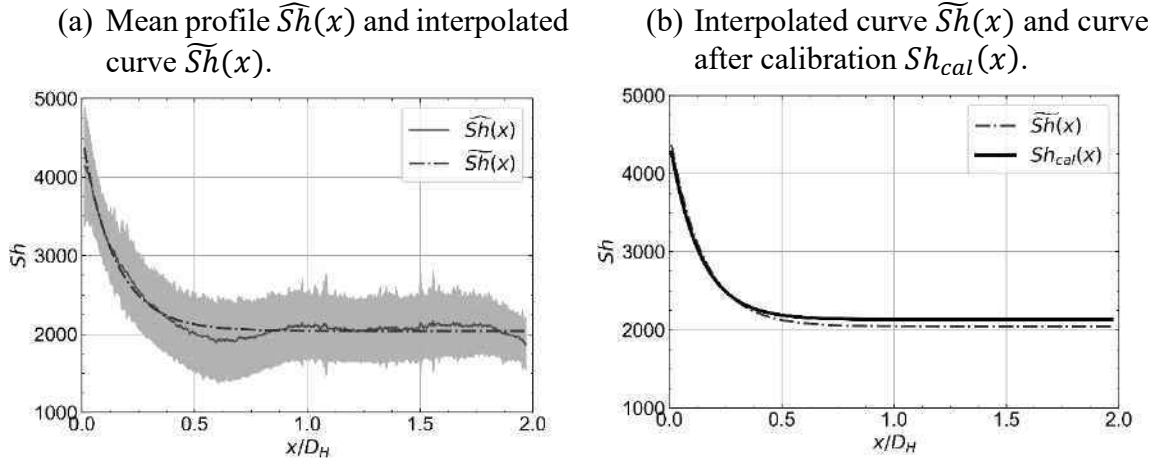


Figure 2.8: evolution of the local Sherwood number profiles at different steps of the normalization process. The gray zone in figure (a) gives the 2σ interval calculated when averaging in the transverse direction. The abscissa $x = 0$ corresponds to the leading edge of the gypsum lining.

In (Wang & Ewing, 2017), the enhancement of the mass transfer is correlated to the ratio between the peak to valley roughness e_{pv} and the roughness element spacing l_{str} . The regression law obtained was:

$$F_W = \left(\frac{Sh_R}{Sh_S}\right)_{Wang} = 1.09 \left(\frac{e_{pv}}{l_{str}}\right)^{0.2} Re^{0.07}$$

This formula has been given for gypsum lining exposed to water for extended dissolution time. In the experiments, in the present experiments, the roughness has been limited and does not present the same aspect as in (Wang & Ewing, 2017). As we want to compare these experiments to heat transfer computations for smooth wall, two transposition factors have been proposed for the scaling of the Sherwood number. A first transposition is done using Gnielinski correlation (Gnielinski, 1967) for heat transfer which originally takes into account the friction, the Reynolds number and the Prandtl number. The correlation written for mass transfer is as following:

$$Sh_G(Re, Pr = Sc, f) = \frac{\frac{f}{8} (Re - 1000) Sc}{1 + 12.7 \left(\frac{f}{8}\right)^{\frac{1}{2}} (Sc^{\frac{2}{3}} - 1)}$$

with, f being the Darcy friction factor calculated as follows:

$$\frac{1}{\sqrt{f}} = -2 \log_{10} \left(\frac{e}{3.71 D_H} + \frac{2.51}{Re \sqrt{f}} \right)$$

where, e and D_H are respectively the equivalent sandgrain roughness and the hydraulic diameter of the duct. Here the sandgrain roughness is defined as three times the root mean square (RMS) roughness height measured on each sample (Wang & Ewing, 2016). The transposition factor calculated between two situations at different Schmidt numbers Sc_1, Sc_2 , and different wall friction coefficient f_1, f_2 is expressed as following:

$$F_1 = \frac{Sh_G(Re, Sc_1, f_1)}{Sh_G(Re, Sc_2, f_2)} = \frac{f_1 Sc_1}{f_2 Sc_2} \times \frac{1 + 12.7 \left(\frac{f_2}{8}\right)^{\frac{1}{2}} (Sc_2^{\frac{2}{3}} - 1)}{1 + 12.7 \left(\frac{f_1}{8}\right)^{\frac{1}{2}} (Sc_1^{\frac{2}{3}} - 1)}$$

This transposition factor has been proposed for the quantification of the roughness effect of the mass transfer, as it takes into account the roughness height of the gypsum sample through the use of the friction factor f .

To characterize the roughness height to the turbulence inner friction length scale l^+ , we also define the non-dimensional roughness height e^+ as:

$$e^+ = \frac{e}{l^+} = \frac{eu^*}{\nu} = \frac{e Re}{D_H} \sqrt{\frac{f}{8}}$$

with u^* the friction velocity.

Another transposition factor F_2 based on Dawson-Trass correlation (Dawson & Trass, 1972) for the Sherwood number is given and compared to F_1 . This transposition factor does not take into account friction unlike F_1 and its use for transposition of Sherwood data obtained with gypsum should deviate from smooth wall data when the roughness height at the sample surface reaches sufficient height to affect the boundary layers.

$$Sh_{DT}(Re, Sc) = 0.0153 Re^{0.88} Sc^{0.32}, \quad F_2 = \frac{Sh_{DT}(Re, Sc_1)}{Sh_{DT}(Re, Sc_2)} = \left(\frac{Sc_1}{Sc_2}\right)^{0.32}$$

A total of 27 measurements have been performed at different temperatures and flowrates. The experimental mass transfer coefficient has been compared to heat transfer coefficient from literature obtained for smooth wall conditions, fixed temperature condition, established thermal and hydraulic boundary layer.

2.5 Results and analysis

2.5.1 Evolution of the operating conditions

The flowrate and temperature at the inlet of the rectangular channel were found to fluctuate in time. The resulting instantaneous Reynolds number and Schmidt number in the channel were thus fluctuating during the experiments. A part of the Reynolds number evolution with time is given on Figure 2.9a for a measure done at $Re \approx 28\,400$.

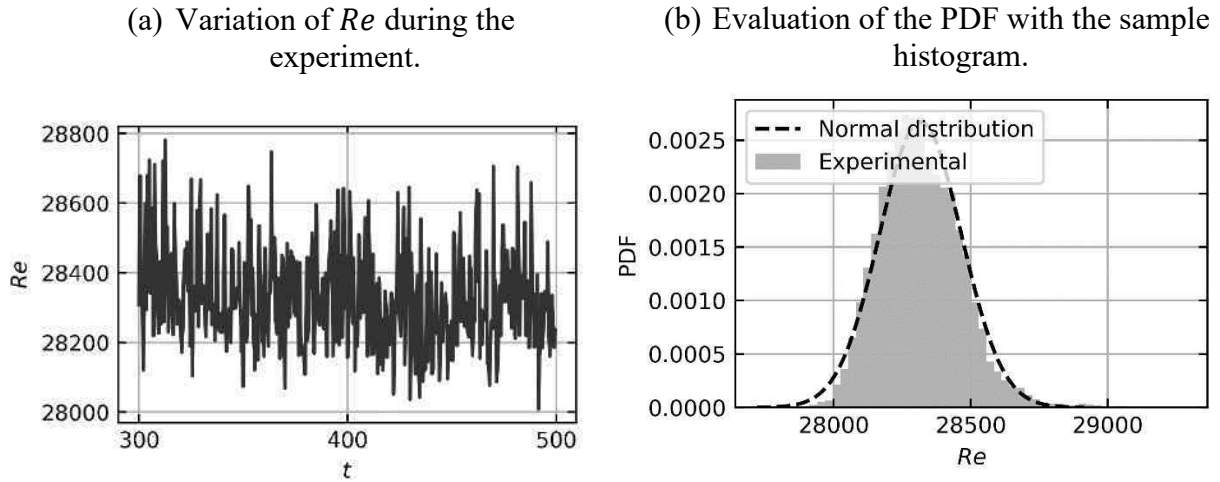


Figure 2.9: evolution of the Reynolds number during the experiment at $Re \approx 28\,400$. (a) random fluctuations of the Reynolds number and (b) comparison of the sample histogram to the normal distribution defined from the mean and standard deviation μ_{Re} and σ_{Re} of the Reynolds number during the experiment.

The total sample of approximately 10^4 realizations is arranged on a normed histogram plot with 50 bins. The normal distribution $\mathcal{N}(\mu_{Re}, \sigma_{Re})$, defined with the calculated temporal mean and standard deviation of the Reynolds number, is superimposed to the histogram on Figure 2.9b. In most of the experiments, the random fluctuations were shown to be well represented by a gaussian random variable. Exceptions were observed when the temperature in the channel was not established and evolved in time. An example is given on Figure 2.10 where the Reynolds increases during the experiments due to the rise of the temperature in the channel. In this case, the resulting PDF is distorted and deviates from the normal distribution. It has been assumed that the additional impact of this trend on the mean Nusselt number is negligible. However, the resulting standard deviation is higher in these cases.

The same behavior is observed for the Schmidt number, thus, for the heat transfer computations, the water Prandtl number is also assumed to be uncertain and to follow a normal distribution. In addition, it has been observed that the Reynolds and Schmidt number fluctuations are correlated. A sample of realizations for an experiment at $Re \approx 19\,200$ and $Sc \approx 1300$ is shown on Figure 2.11a, while the estimated probability density function is given on Figure 2.11b. The non-diagonal elements of the covariance matrix are non-zero in this case.

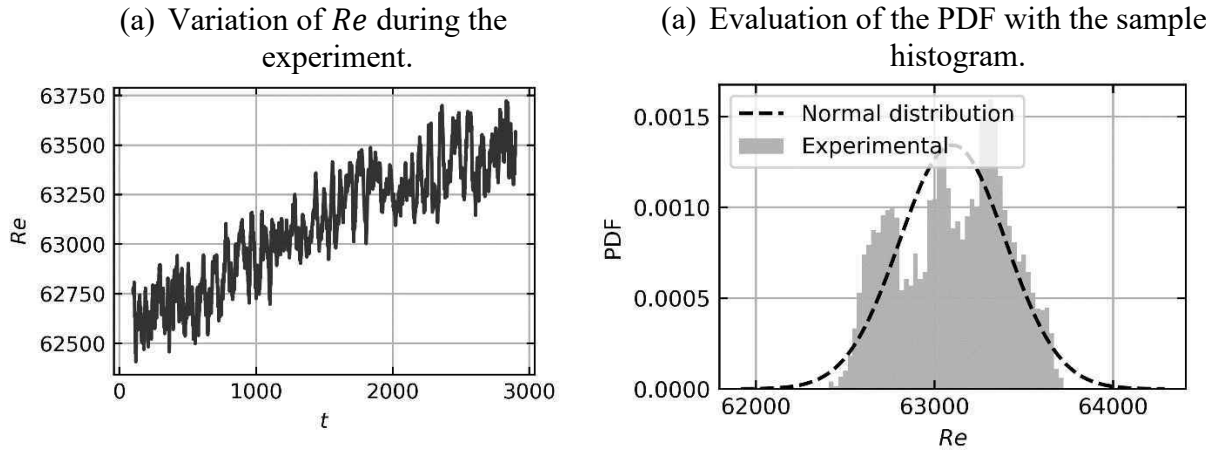


Figure 2.10: evolution of the Reynolds number with respect to time during an experiment where the temperature is not established (a) and approximate probability density function (b).

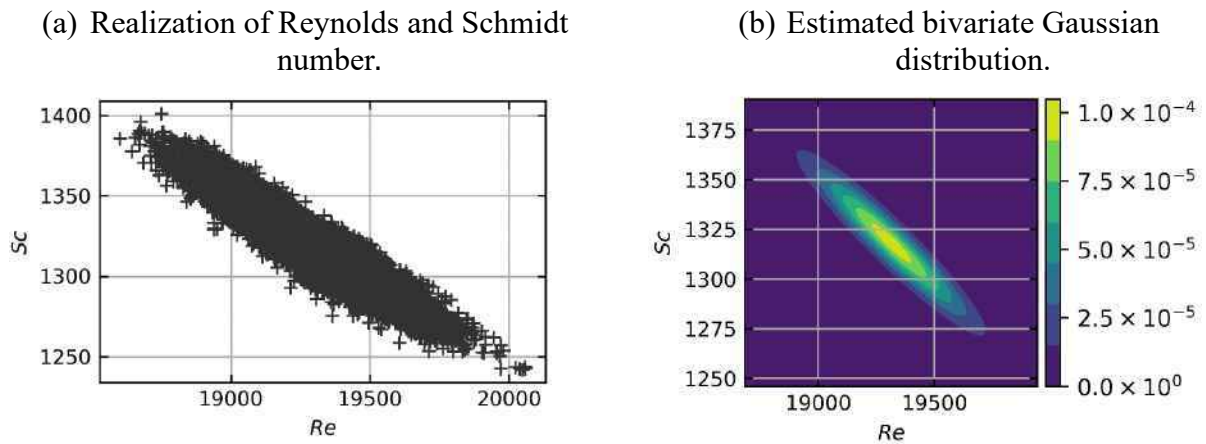


Figure 2.11: estimation of the probability density function for an experiment at $Re \approx 19\,200$. The realizations of the Reynolds and Schmidt numbers during the experiment are shown on (a) and contours of the estimated probability density function is shown on (b).

The Pearson correlation $\rho_{Re,Sc}$ coefficient is calculated in order to estimate the covariance matrix for given Reynolds and Schmidt numbers. This coefficient is defined by:

$$\rho_{Re,Sc} = \frac{Cov(Re, Sc)}{\sigma_{Re}\sigma_{Sc}}$$

The impact of this coefficient in the joint Gaussian probability density function can be seen on Figure 2.12. In the rectangular channel experiments, the Pearson coefficient takes its value in the range $\rho_{Re,Sc} \in [-1, -0.8]$ for the different experiments, which indicates a strong correlation between the Reynolds and Schmidt number fluctuations. Moreover, the standard deviation calculated from the time fluctuation of the Reynolds and Schmidt number during the dissolution has been found to be approximatively around 2% to 5% of the mean value.

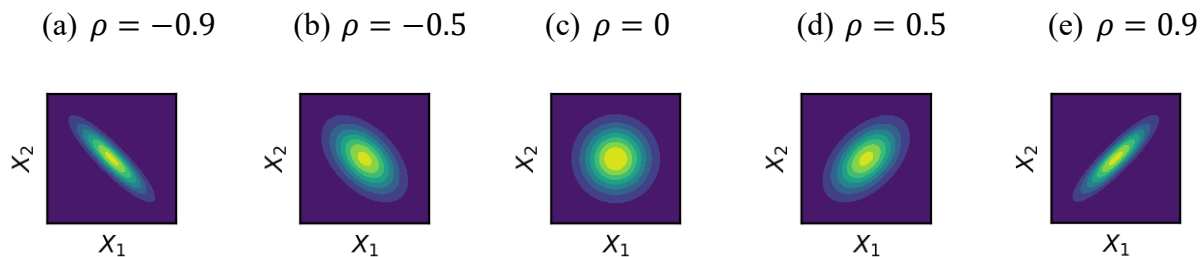


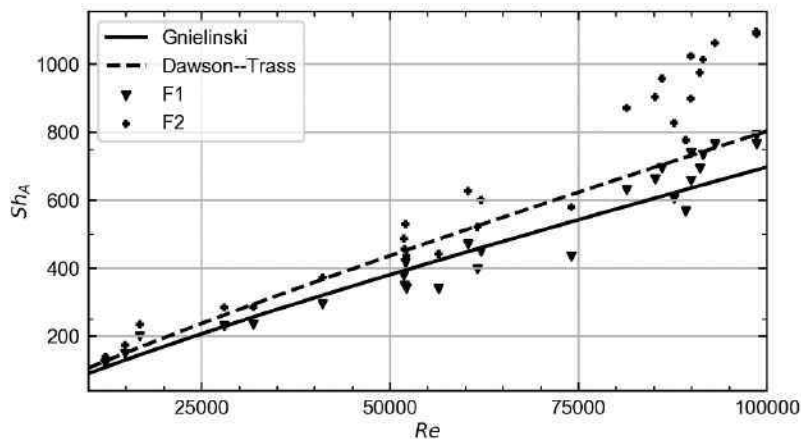
Figure 2.12: Effect of the Pearson coefficient on the shape of the joint probability distribution isocontours. High values of the probability density function are given in yellow and low values in blue.

2.5.2 Evolution of the Sherwood number on the experimental range

For every experiment, the Sherwood number (Sh_{max} and Sh_a) has been transposed from the experimental Schmidt number measured in the range $Sc \in [700, 1800]$ to $Sc = 10$ using the F_1 or F_2 factors. This has been done in order to compare it to the asymptotic Nusselt number for a fluid at a Prandtl number $Pr = 10$. The evolution in respect to the Reynolds number of the values are compared for a Reynolds number in the range $[10^4; 10^5]$. The comparison of the experimental asymptotic Sherwood number, which has been transposed with the two factors F_1 and F_2 , to the Nusselt number calculated with Gnielinski correlation and the Sherwood number calculated with Dawson—Trass correlation can be seen on Figure 2.13. Each set of data is compared to the correlation from which its transposition originates. It is noticeable that the F_1 transposition factor, which includes the friction coefficient provides results that are close to Gnielinski correlation. The Dawson—Trass correlation F_2 factor gives good results until a critical Reynolds from which the experimental data deviates. At this critical Reynolds number, the wall can no longer be considered as hydraulically smooth. This deviation is well correlated to the increase of the non-dimensional roughness height e^+ in the different experiments with the Reynolds number visible on Figure 2.14. This deviation has remained even though the exposition time has been initially adapted to keep approximately the same mass loss during each experiment. It is found on Figure 2.14 that the deviation from the smooth wall law of the averaging non-dimensional roughness e^+ corresponds approximately to the sample verifying $e^+ \geq 20$, indicating the necessity to use friction correction. This critical value is close to $e^+ \approx 25$ given in (Wang & Ewing, 2017) for the same situation of naturally developing roughness with gypsum dissolution.

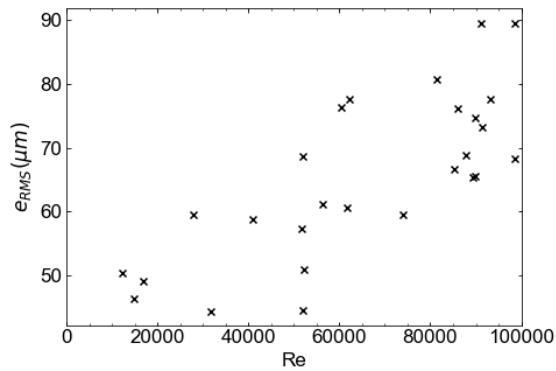
Table 2.1 : correlation from literature.

Gnielinski (Bergman, et al., 2011)	$Nu(Re, Pr, f) = \frac{\frac{f}{8}(Re - 1000)Pr}{1 + 12.7\left(\frac{f}{8}\right)^{\frac{1}{2}}(Pr^{\frac{2}{3}} - 1)}$
Dawson—Trass (Dawson & Trass, 1972)	$Sh(Re, Sc) = 0.0153 Re^{0.88} Sc^{0.32}$
Sieder—Tate (Bergman, et al., 2011)	$Nu(Re, Pr) = 0.031Re^{0.8} Pr^{\frac{1}{3}}$
Dittus—Boelter (Bergman, et al., 2011)	$Nu(Re, Pr) = 0.021Re^{\frac{4}{5}} Pr^{0.4}$

Figure 2.13: comparison of the asymptotic Sherwood number transposed to $Sc = 10$ with the transposition factors F_1 and F_2 .

The transposed points obtained with F_1 are compared to correlation from literature. The heat transfer correlations have been obtained from Sieder–Tate, Dittus–Boelter, Gnielinski, (Bergman, et al., 2011) and are reported in Table 2.1. The transposed measurements points are shown on Figure 2.15 with their measurement uncertainty bar and the grey zone corresponds to the mean deviation of the points from the calculated correlation. The comparison (using the analogy and from the experimental work) of the Nusselt or Sherwood number is shown on Figure 2.16 and the values found from our measurements are in good agreement with the known correlations. The Nusselt number obtained from the transposition of gypsum dissolution data is slightly higher than the data from the heat transfer domain. Besides Dittus–Boelter correlation, all the correlations are within the experimental uncertainty of the gypsum data.

(a) Equivalent sandgrain roughness.



(b) Non dimensional roughness.

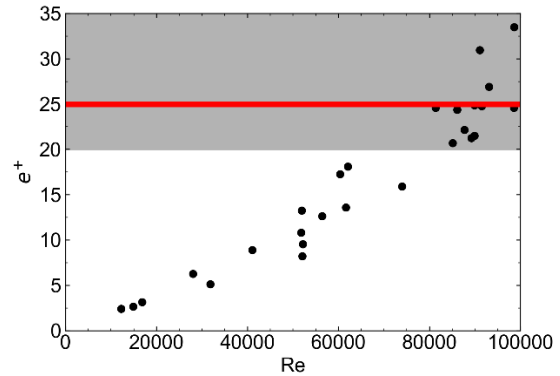


Figure 2.14: roughness measurements: on the right, the red line corresponds to an observed critical value of the roughness height e^+ (Wang & Ewing, 2017) from which the hydraulically smooth wall condition ends. In grey, the region for which the influence of the roughness is non-negligible for the conducted experiments.

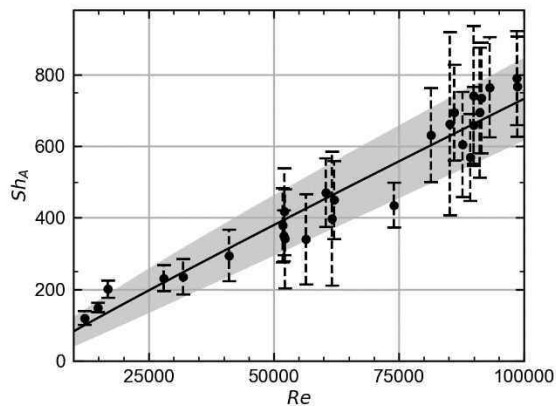


Figure 2.15: correlation on the asymptotic Sherwood number extracted from the data points and uncertainty calculated on the correlation ($\mu_{Sh} \pm 2\sigma_{Sh}$ interval in grey).

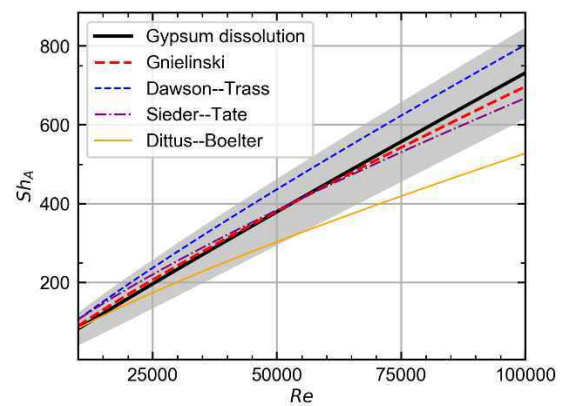


Figure 2.16: comparison of correlation obtained with gypsum to different correlations indicated on Table 2.1. The grey zone corresponds to the $\pm 2\sigma_{Sh}$ interval.

In addition, the ratio between the maximum value and the asymptotic value of the Sherwood number is determined and reported on Figure 2.17. It is found to be in the range [1.5, 2.5]. This value is in good agreement with the available data on the heat transfer coefficient evolution in the thermal entrance region of a pipe for a developed hydraulic boundary layer (Deissler, 1954; Boelter, et al., 1948; Sleicher Jr, 1956). These studies give a ratio between 1.3 and 3.5 for this range of Reynolds number.

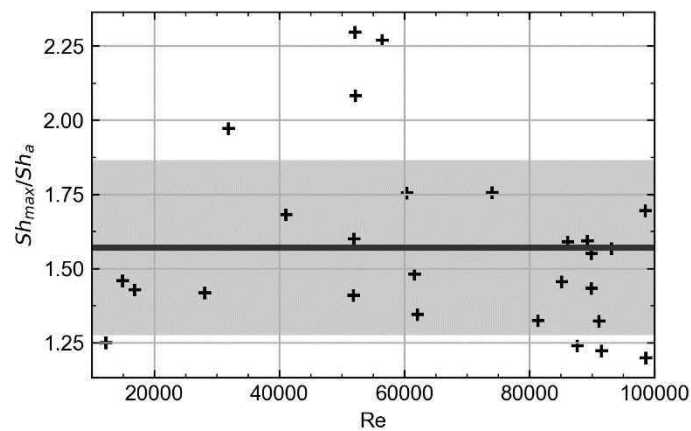


Figure 2.17: ratio between the maximum and asymptotic value of the Sherwood number along the gypsum surface. Mean value over the experiments is indicated with the horizontal line while the grey zone gives the $\mu \pm 2\sigma$ interval zone.

2.6 Conclusion

Mass transfer experiments in a rectangular channel were conducted in Framatome's experimental facilities with gypsum dissolution technique. The objective was to gain experience on this measurement methodology and prepare the future experiments on more complex geometries for **generation of heat transfer coefficient data**. For this purpose, the mass transfer coefficient obtained with the gypsum dissolution has been post-processed using the heat and mass transfer analogy. Two transposition factors have been tested for the comparison with heat and mass transfer correlations from literature. From the experiments, the following conclusions can be proposed:

- the casting of the gypsum has an important role: the water/gypsum mixing ratio has been chosen by making a compromise between the casting rate and final density of the gypsum. The essential parameters that must be controlled are the defects near the gypsum surface and its smoothness when dried.
- the surface topography must be measured with accuracy in order to process the roughness and transpose the measure to smooth walls. The transposition factor which did not consider the surface roughness showed deviation from smooth wall for the higher Reynolds number experiments. This factor is not suited for the scaling of the Sherwood number obtained with gypsum dissolution to smooth wall data.

In this flow configuration, Darcy-Colebrook equation was available in order to estimate the friction factor. In addition, the functional relation between mass transfer, surface roughness and the Schmidt number was given with Gnielinski correlation for turbulent heat transfer.

These two correlations were essential for the transposition of the Sherwood number to smooth wall Nusselt number. The resulting Nusselt number obtained from the transposition of the gypsum measurements showed good agreement with heat transfer data from literature. The obtained data will be processed in the next chapter in order to compare calculations of the heat transfer coefficient with CFD simulations. Nevertheless, these correlations might not be suitable in different flow configurations; thus, one of the two following solutions has to be considered in order to use gypsum dissolution technique for heat transfer data generation:

- to estimate the transposition factor by studying the Sherwood number on a wider range of Schmidt number and roughness aspects.
- To measure the transposition factor by making additional heat transfer measurements.

Chapter 3 Uncertainty quantification on the rectangular channel

In thermal hydraulics studies, *Computational Fluid Dynamics* (CFD) softwares are powerful tools used to resolve the fluid motion in 3D. In this chapter, the experiments conducted on the rectangular channel presented Chapter 2 are reproduced with two commercial softwares with the Realizable $k - \epsilon$ (RKE) turbulence model that has been described in Chapter 1. This turbulence model is tested with or without wall law (with fine or coarse near wall meshing). The model will first be described, then, a comparison will be carried out with the experimental data discussed in Chapter 2. In addition, the simulation's inputs uncertainty will be propagated with the two methods given in §1.2.4.2. Finally, the model error will be calculated for Reynolds numbers in the range $[10^4, 10^5]$.

3.1 Presentation of the CFD model

3.1.1 Geometry

The geometry is the replica of the rectangular duct mock-up presented in Chapter 2. The gypsum lining is replaced in this case by a heated wall at fixed wall temperature condition. A CAD view can be seen on Figure 3.1, with the heated wall given in red. A summary of the channel dimensions is given Table 3.1

Table 3.1: dimensions of the rectangular channel.

Duct length	$34 D_H$
Aspect ratio $AR = \frac{\text{Width}}{\text{height}}$	≈ 4.2
Dimensions of the heated surface	$1.2 D_H \times 2D_H$
Abscissa of the start of the heated surface	$\approx 22D_H$

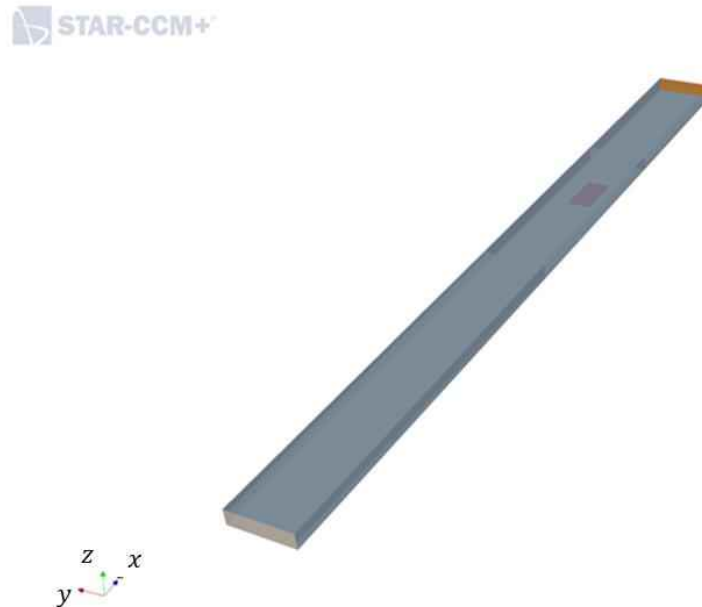


Figure 3.1: view of the geometry for simulations in the rectangular duct. Inlet in beige, adiabatic wall in grey, outlet in orange. The location of the gypsum sample during the experiment is given in red.

3.1.2 Grid

Different meshes have been tested for simulations carried out with the commercial CFD softwares STAR-CCM+ and Fluent. Two different methodologies are used for the two softwares: the range of flowrate imposed at the channel inlet is wide, inducing for a fixed near wall mesh a large difference of the y^+ values (see §1.1.3.5) on the surface of interest in the extreme cases. Thus, the near wall meshing has been adapted in order to reduce the bias due to evolution of y^+ values with the Reynolds number. In this study, all the grids are composed of hexahedral cells.

Two grids were designed for STAR-CCM+ simulations in order to test the differences between simulations with and without wall functions:

- grid 1S: the mesh is designed with near wall cells remaining in the viscous sublayer of the boundary layer. In other words, the grid has been set up in order to respect $y^+ \leq 1$ for all the computations.
- grid 2S: the near wall mesh size is adapted to every case in order to respect $y^+ \in [30, 50]$ on all boundaries. The height of the cell is generated with an empirical correlation. The surface size of the cells is refined near the measurement location of the gypsum sample indicated in red on Figure 3.1. This has been done in order to have a better spatial discretization of the heat transfer coefficient in the streamwise direction.

Sections of the grids 1S and 2S at the fixed temperature wall location are given on Figure 3.2. For 1S, the section meshing is the same at the inlet, with a hyperbolic refinement in the extruding direction in order to reduce the number of cells far from the interest region. For 2S, different refinement levels are shown.

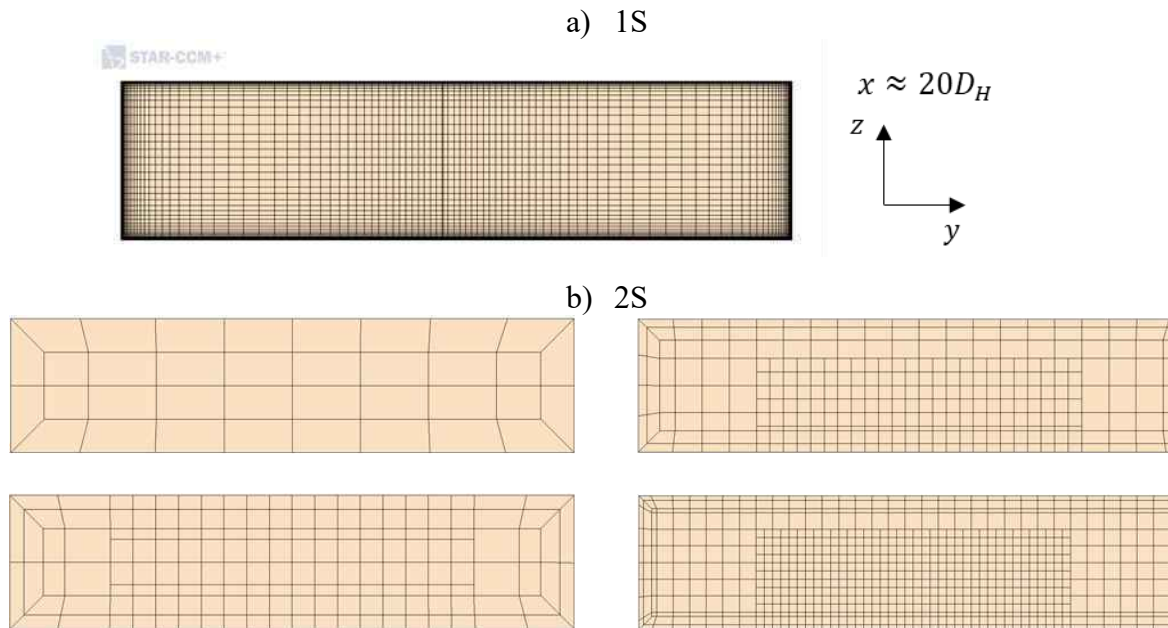


Figure 3.2: view of a section of the channel near the fixed temperature wall for the different meshing strategies: grid 1S (a) and grid 2S(b). For grid 2S, different refinement levels are depicted.

For Fluent simulations, two meshing approaches have been used as well:

- grid 1F: the near wall cell height is set such as the non-dimensional wall distance respects $y^+ < 1$ on all the boundaries.
- grid 2Fa and 2Fb: two grids have been designed in order to respect $30 < y^+ < 100$. Contrarily to grid 2S no adaptive near wall meshing has been set. The simulations were divided in two groups according to the flowrate imposed at the inlet of the channel.

Sections of the different grids 1F, 2Fa and 2Fb are shown on Figure 3.3. A summary of the number of cells for each grid is given in Table 3.2

Table 3.2 : approximate number of cells for the different grids.

Grid	Min number of cells	Max number of cells
1S	≈ 1 750 000	
2S	≈ 10 000	≈ 230 000
1F	≈ 1 920 000	
2F	≈ 110 000	≈ 220 000

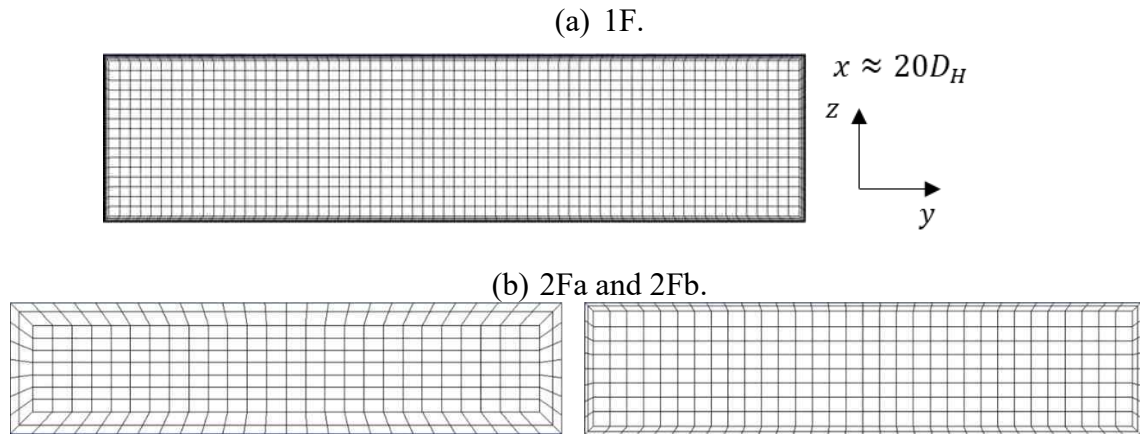


Figure 3.3: mesh1F and 2F: view of a section of the channel at the inlet near the fixed temperature wall for the different meshing strategies. (a) Grid 1F with near wall refinement and (b) 2F without.

The surface mesh refinement zone corresponding to the measurement location on the experiments described in Chapter 2 is shown on Figure 3.4.

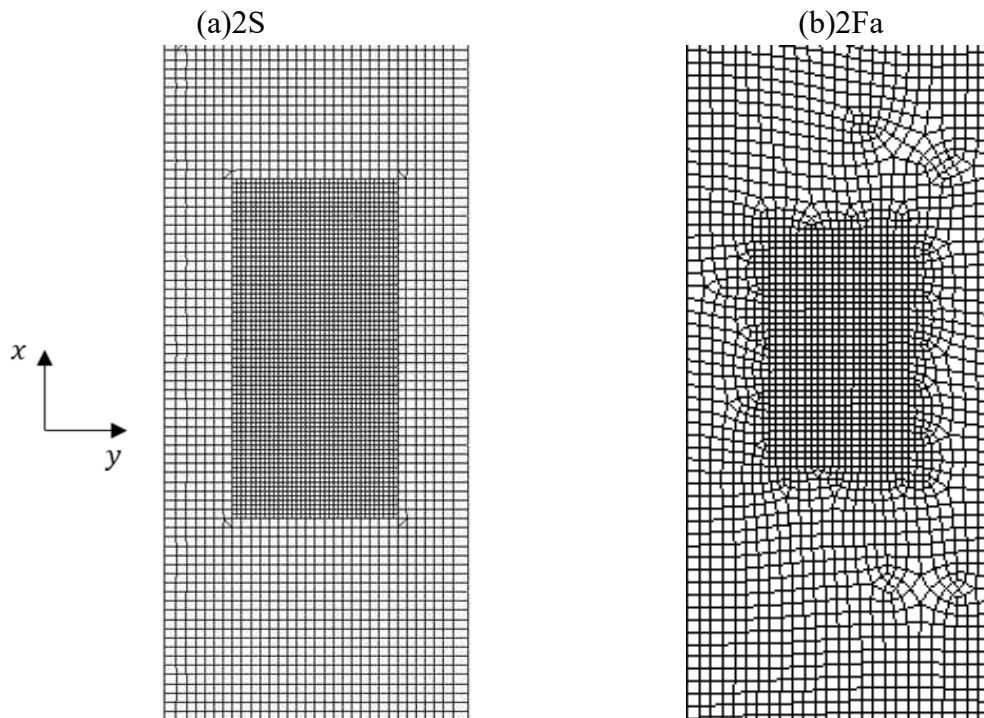


Figure 3.4: view from the top of the mesh in the refinement region near the gypsum measurement location: (a) grid 2S for a high flowrate situation and (b) grid 2Fa.

3.1.3 Boundary conditions and physical properties

Table 3.3 : physical properties of Water.

Parameter	Value
Density	$\rho = 998.8 \text{ kg} \cdot \text{m}^{-3}$
Dynamic viscosity	$\mu = 1.10 \cdot 10^{-3} \text{ Pa} \cdot \text{s}$
Thermal conductivity	$\lambda = 0.587 \text{ W} \cdot \text{m}^{-1} \cdot \text{K}^{-1}$
Specific heat coefficient	$C_p = \frac{\lambda Pr}{\mu}$

The boundary conditions that have been imposed are set as constant as following:

- Fixed temperature surface T_{wall} at the location corresponding to the position of the gypsum samples during the experiments. The position can be seen in red on Figure 3.1. The wall temperature is set to $T_{wall} = 303K$.
- Adiabatic surface on the side boundaries.
- Imposed volumetric flowrate Q with a flat velocity profile at the inlet at temperature $T_{in} = 300K$.

The inlet volumetric flowrate Q is parametrized by the Reynolds number as following:

$$Q = \frac{\mu Re S}{\rho D_H}$$

where, S is the area of the section of the channel. The physical properties of the fluid are indicated on Table 3.3. It can be noticed that the specific heat coefficient C_p of the fluid is set up accordingly to the thermal conductivity λ , dynamic viscosity μ and targeted Prandtl number Pr .

The simulations have been parametrized by the Reynolds and Prandtl number. The flowrate and specific heat coefficient are adjusted accordingly. The range covered by the Reynolds number and Prandtl number are respectively $[10^4, 10^5]$ and $[2, 10]$.

3.1.4 Data processing

The output data extracted from the simulations is the Nusselt number over the heated wall:

$$Nu(x, y) = \frac{h_{conv}(x, y) D_H}{\lambda} = \frac{q_w(x, y) D_H}{\lambda(T_{wall} - T_{in})}$$

where, $q_w(x, y)$ is the wall heat flux surface distribution. The other parameters have been described earlier.

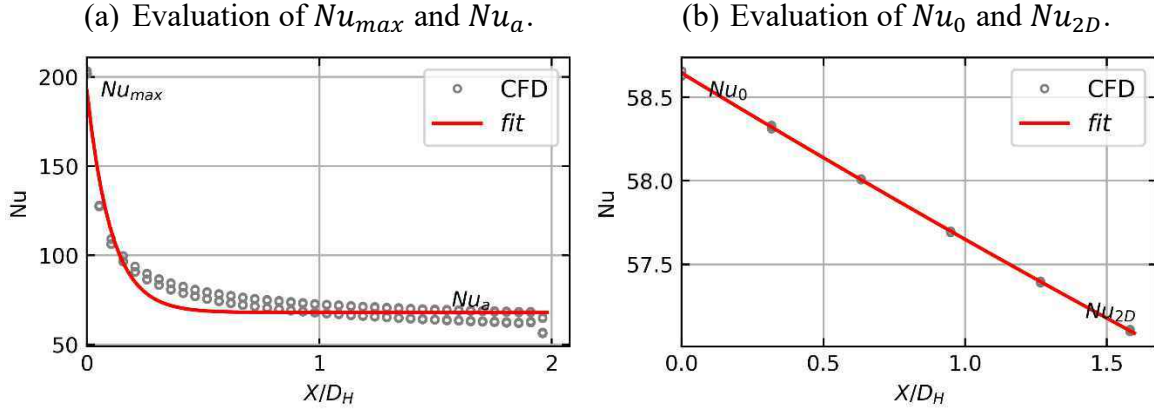


Figure 3.5: evaluation of the parameters describing the Nusselt profile for simulations at $Re = 10^4$ and $Pr = 2$. The exponential fit is given in red and the CFD values of $Nu(x)$ on the grid is black circles. (a) extraction of the fit parameters Nu_{max} and Nu_a for the simulation on Grid 1S and (b) extraction of Nu_0 and Nu_{2D} on Grid 2S.

The variations of the Nusselt number in the transverse direction y has been found negligible in front of the variations in the direction x since the lateral walls were relatively far from the heated wall. Some variations in the y direction were still noticeable in some cases as it can be seen on Figure 3.5a where the data obtained from the heated wall is arranged in a (x, Nu) . The abscissa x on the graph is set to zero at the leading edge of the heated wall. In the experiments, the evolution following the x direction has been found to fit well an exponential decay function in comparison to other decreasing functions. An exponential function is thus fitted on the profile obtained from CFD on the $Nu(x, y)$ data:

$$Nu(x) = (Nu_{max} - Nu_a) \exp\left(-\frac{x}{l}\right) + Nu_a$$

Important differences were noticed on the Nusselt number evolution between the refined wall mesh simulations and the coarse wall mesh simulations. In fact, when coarse wall mesh are used, the establishment of the Nusselt number starting at the leading edge of the heated wall is not reproduced as it is visible on Figure 3.5b. The exponential decay function is not adapted in this situation, thus, two additional quantities are extracted from the CFD simulations Nusselt number in order to retrieve the maximum value of the Nusselt number at the leading edge and the minimum value at the end of the wall:

- the value $Nu_0 = Nu(x = 0)$, corresponding to the Nusselt number at the leading edge of the heated wall.
- the value at the end of the heated wall $Nu_{2D} = Nu(x = 2D_H)$.

The average value of Nu_0 and Nu_{2D} in the y direction is taken. The fit and the evaluation of the different parameters is shown on computations for fine and coarse near wall meshing on

Figure 3.5. The difference at the leading edge of the heated wall is visible between the grids 1S and 2S. The same difference has been observed for grids 1F and 2F.

3.2 Investigation of the Nusselt number along the heated wall

3.2.1 Results of the CFD simulations

3.2.1.1 Differences between the models

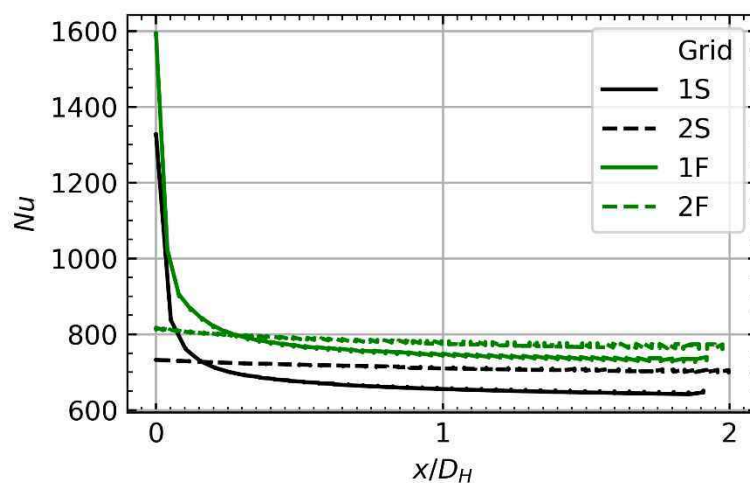


Figure 3.6: comparison of the Nusselt profile along the heated wall for the different CFD models for $Re = 100\,000$ and $Pr = 10$. Computations with Fluent (green) and STAR-CCM+ (black).

Differences are observed on the establishment of the Nusselt number between the models. An example is given on Figure 3.6 for $Re = 10^5$ and $Pr = 10$. Models with fine near wall meshing $y^+ < 1$ (Grid 1S and Grid 1F) do not use wall laws and reproduce the thermal entrance effect which is observed in experiments (cf. Chapter 2). This effect is not captured by the models with unrefined near wall meshing $y^+ \geq 30$ (Grid 2S and Grid 2F) using wall laws. However, as soon as the thermal boundary layer is close to be established, the difference between the Nusselt number obtained with or without law reduces significantly.

In addition, for equivalent model with different codes, a slight bias is observed between 1F and 1S, and 2S and 2F. Fluent computes a higher value of the heat transfer coefficient than STAR-CCM+. The differences might be due to different numerical schemes and grids which were not the same in the two cases. The difference of the wall function implementation between the two softwares should not be the cause as it is visible that the models 1S and 1F which does not use wall functions still show differences. The differences between the codes still has to be investigated.

3.2.1.2 Nusselt number of established thermal boundary layer

The Nusselt number for an established boundary layer is given by Nu_a and Nu_{2D} described in §3.1.4. The results of Nu_a computed without wall law is depicted on Figure 3.7 for the simulation inputs Re, Pr given by the design of experiment $U_{50}(10^1 \times 5^1)$. Only three Prandtl number are showed on the figure for clarity. The dependence of the Nusselt number to the Reynolds number and Prandtl number is calculated by making a regression with a power law.

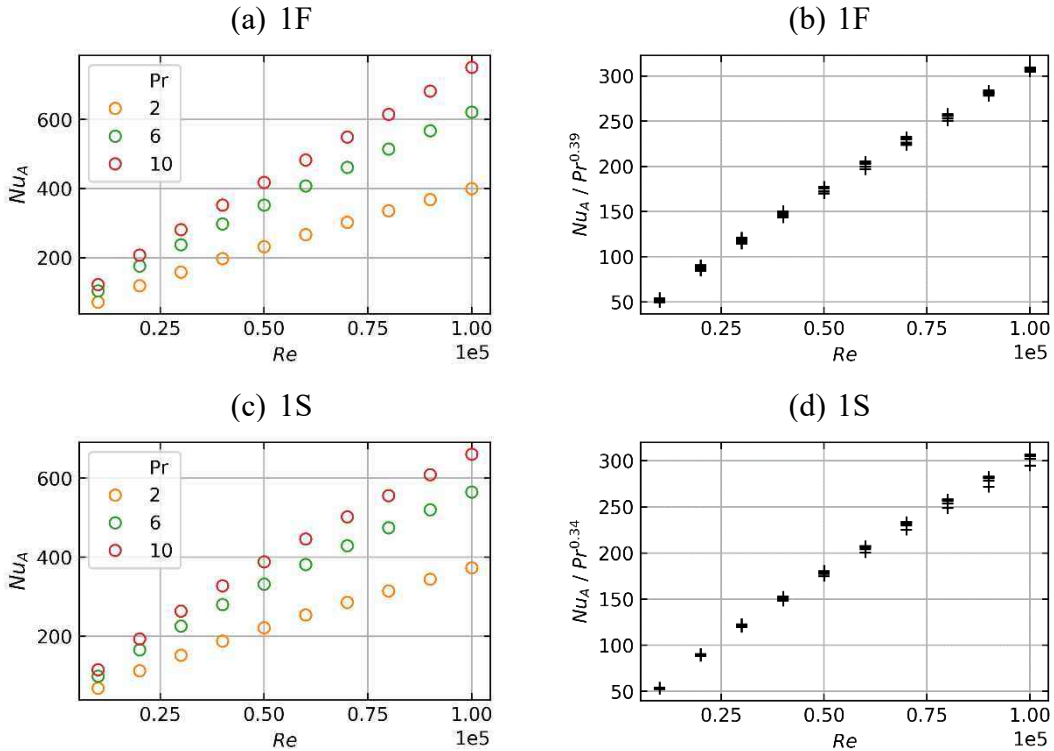


Figure 3.7: asymptotic Nusselt number calculated with Grid 1F ((a) and (b)) and Grid 1S ((c) and (d)). The Nusselt is divided by Pr^c with $c=0.39$ for 1F (b) and $c=0.34$ for 1S (d).

For the models 1S and 2S, the asymptotic Nusselt number is found to depend on $Pr^{0.34}$, while $Pr^{0.39}$ has been found for models 1F and 2F. The results on the asymptotic Nusselt number for wall law computations (2S and 2F) are very similar to $y^+ < 1$ (1S and 1F) computations. A power law is fitted for Nu_{2D} , which can be written:

$$Nu_{2D} = a Re^b Pr^c \quad (3.1)$$

The coefficient a, b and c are given for each model in Table 3.4.

Table 3.4 : coefficient of the fitted power law fit on Nu_{2D} .

Meshing	a	b	c
Grid 1S	0.0449	0.763	0.34
Grid 2S	0.0163	0.857	0.34
Grid 1F	0.0358	0.779	0.39
Grid 2F	0.0334	0.793	0.39

The comparison between the correlations obtained from the different simulations for the quantity Nu_{2D} on Figure 3.8 for $Pr = 10$.

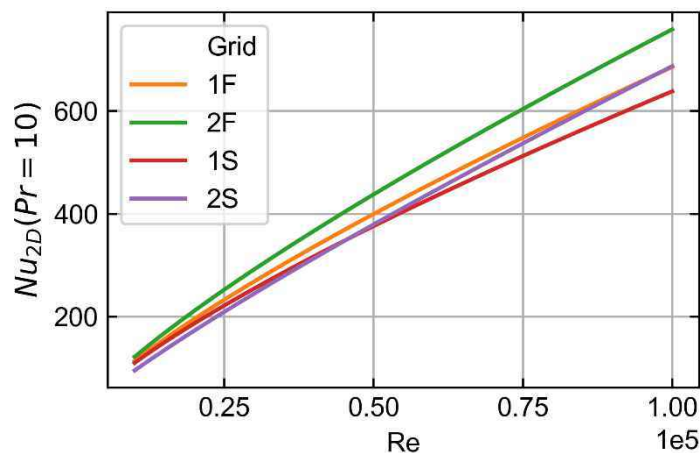


Figure 3.8: comparison of the different correlations given for the asymptotic Nusselt number for the different software and grids.

The results correspond to what is observed on the Nusselt profile at $Re = 10^5$ on Figure 3.6: the value of the Nusselt number calculated with Fluent is larger than with STAR-CCM+. Furthermore, the Nusselt number calculated with wall laws (Grid 2F and 2S) is larger when the calculation is carried out without wall laws (Grid 1F and 1S).

3.2.1.3 Establishment of the Nusselt profile

The entrance effect at the leading edge of the heated wall due to the establishment of the thermal boundary layer is analyzed. It has been noticed on Figure 3.6 that resolution with or without wall law changes significantly the calculated fields on this zone. The maximum value of the Nusselt number Nu_0 is compared for all the different models on Figure 3.9a. The value Nu_{max}/Nu_a is given for the computations with grid 1S and grid 1F as a function of the Reynolds number on Figure 3.9b. For models with wall laws, it is visible that this entrance effect is not taken into account which leads to significantly lower values of the Nusselt number at the leading edge of the heated wall for grid 2S and 2F.

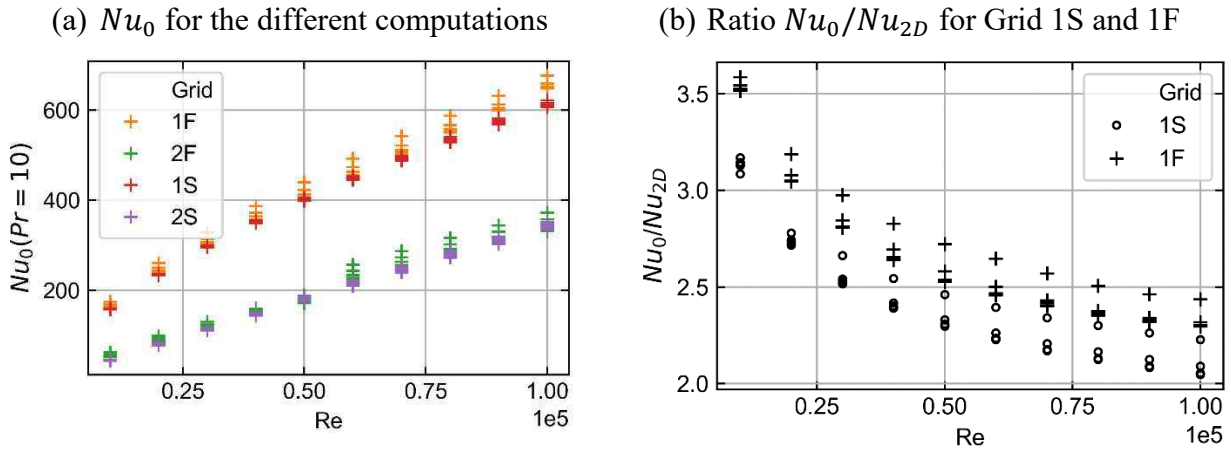


Figure 3.9: comparison of the entrance effect for the different computations. (a) Maximum Nusselt number on the profile as a function of the Reynolds number for all computations. (b) Comparison for Grid 1S and 1F of the ratio Nu_{max}/Nu_a .

Nevertheless, the difference over the heated wall between model with and without wall laws decreases with the Reynolds number and for lower Prandtl numbers. In fact, this observation is based on the decrease of the characteristic length of the exponential fit with the Reynolds number as it is seen on Figure 3.10. On this figure, l is plotted as a function of the Reynolds number for three different Prandtl numbers for Grid 1S and Grid 1F. It is noticeable that this length increases for lower Prandtl number. For the higher Reynolds numbers, the characteristic length is in the range [5%, 10%] of the hydraulic diameter D_H . At this regime, the boundary layer is developed on most of the heated wall.

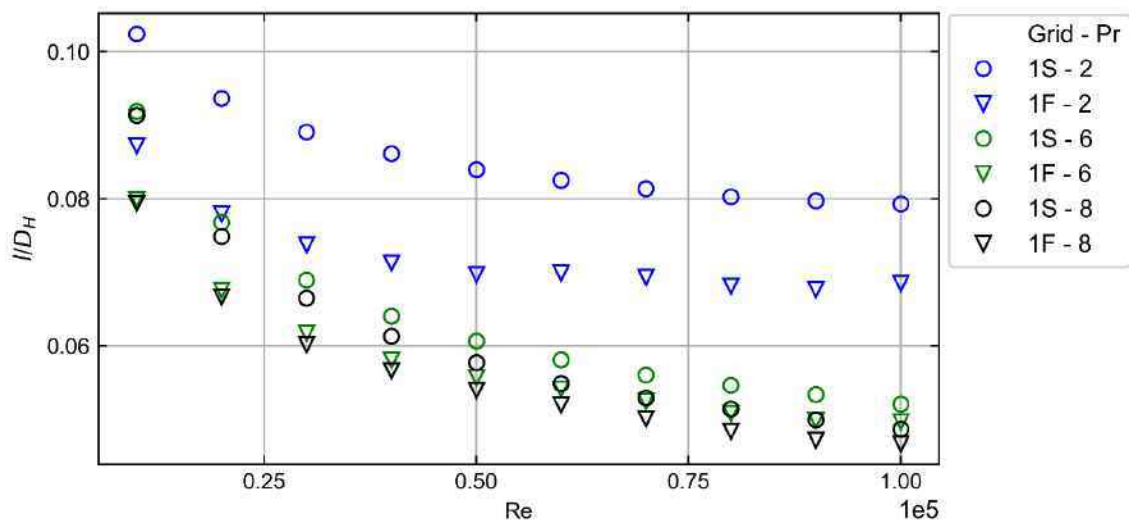


Figure 3.10: evolution of the characteristic length of the exponential fit for Grid 1S and Grid 1F.

3.2.2 Comparison to experiments

The comparison is carried out with the experimental data obtained with gypsum dissolution in Chapter 2, and with data obtained in literature for turbulent heat transfer.

3.2.2.1 Established thermal boundary layer Nusselt number

The asymptotic Nusselt number obtained in Chapter 2 is compared to the correlation obtained with gypsum dissolution $Nu_{a,exp}$ and to Gnielinski correlations for turbulent heat transfer indicated in Table 2.1. The comparison is depicted for the different grids on Figure 3.11 for simulations at $Pr = 10$.

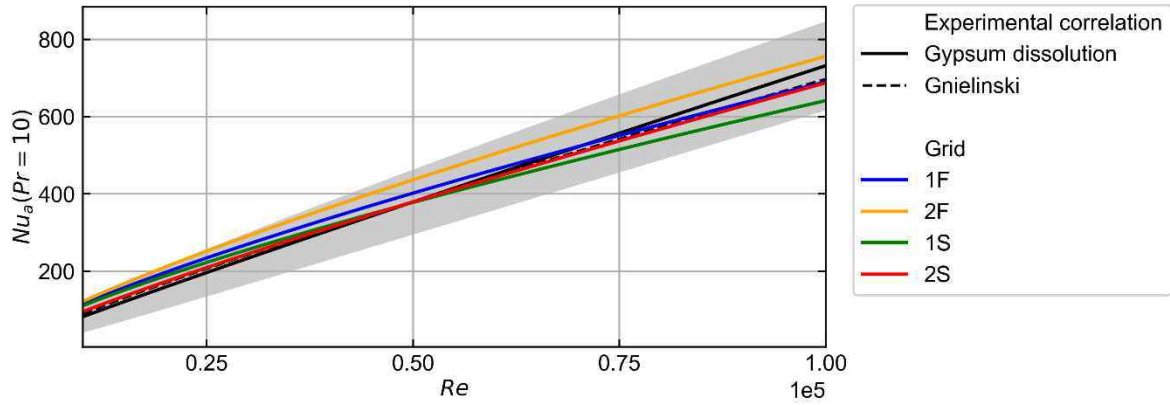


Figure 3.11: comparison of the asymptotic Nusselt number obtained from experimental correlations and numerical correlations for the different grids. The grey zone corresponds to the interval $Nu_{a,exp} \pm 2 \sigma_{exp}$ of the gypsum dissolution experiments correlation.

A first observation for this Prandtl number is that all the numerical simulations are within the $Nu_{a,exp} \pm 2 \sigma_{exp}$ interval indicated in grey on Figure 3.11, with σ_{exp} the estimated standard deviation of the correlation corresponding to the root mean square error between the experimental points and the correlation.

The comparison between numerical and experimental data from the gypsum dissolution measurement is given on a logarithmic scale in Figure 3.12. The same is done with Gnielinski correlation of heat transfer coefficient on Figure 3.13. This bias corresponding to the mean value of the error $E_{CFD/EXP}$ is given relatively to the computed value of the Nusselt number in percent:

$$Bias = 100 \frac{Nu_{CFD} - Nu_{EXP}}{Nu_{CFD}}$$

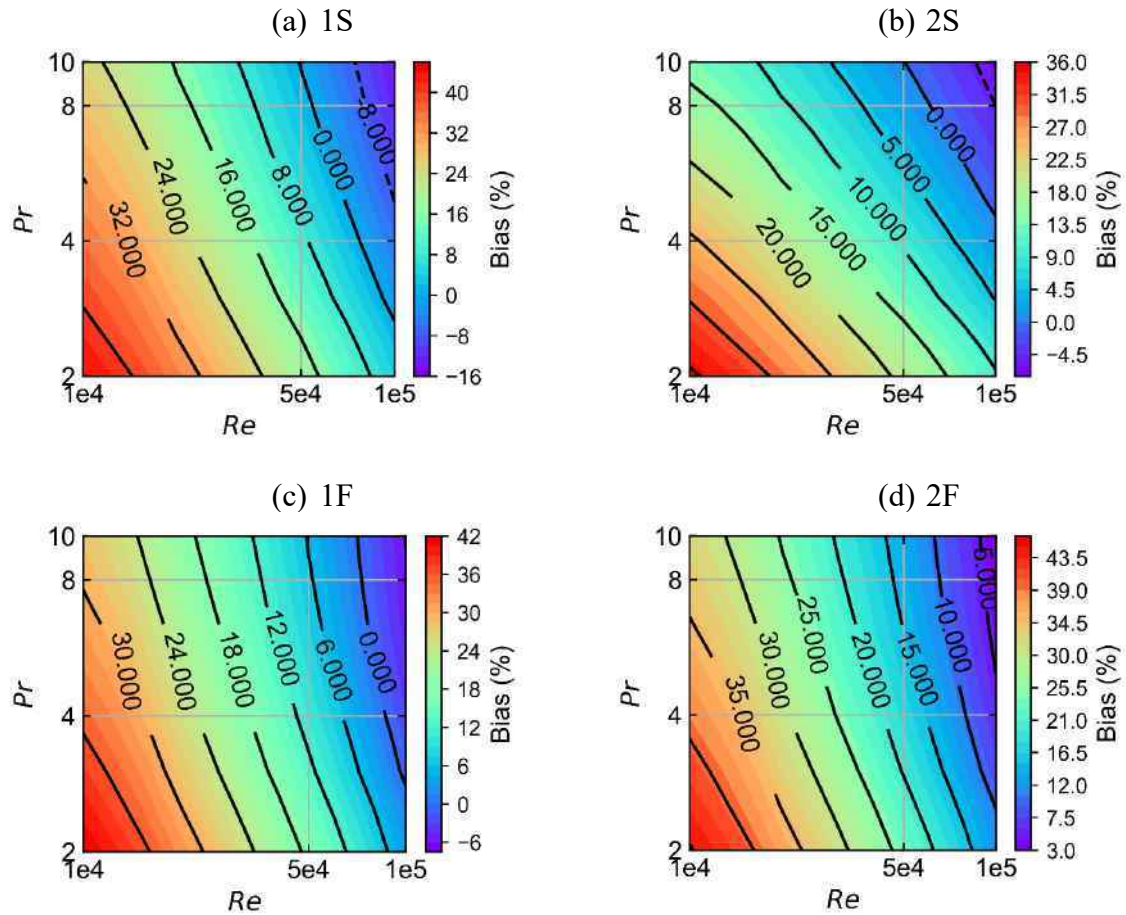


Figure 3.12 : relative bias on the calculation of the asymptotic Nusselt number compared to gypsum dissolution experimental data.

The accuracy of the models indicated by the bias, is globally the same. When comparing the data to the correlation obtained with gypsum dissolution measurement, the bias decreases with increasing Reynolds number. Moreover, the bias is larger for the higher Prandtl numbers. The bias values obtained for the higher Reynolds number are in the range $[-15\%, 10\%]$ of the CFD values. The bias is similar when comparing with Gnielinski correlation. Its values remain in the range $[-10\%, 25\%]$ for all the performed computations which is slightly better than the comparison with gypsum for low Reynolds. The bias decreases for increasing Prandtl number, especially for Grid 2S which seems more sensible to variations of the Prandtl number. Finally, with Gnielinski correlation, the iso-contours curve for increasing Reynolds number and reach horizontal line which indicate that the bias tends to become independent of the Reynolds number. This behavior is visible for low Prandtl number for all grids. For Grid 2S, this tendency is much more visible as it seems that the bias stabilizes to a value in the range $[0\%, 15\%]$ which depends only on the Prandtl number. This behavior is less visible with Gypsum dissolution where the iso-contours are parallel.

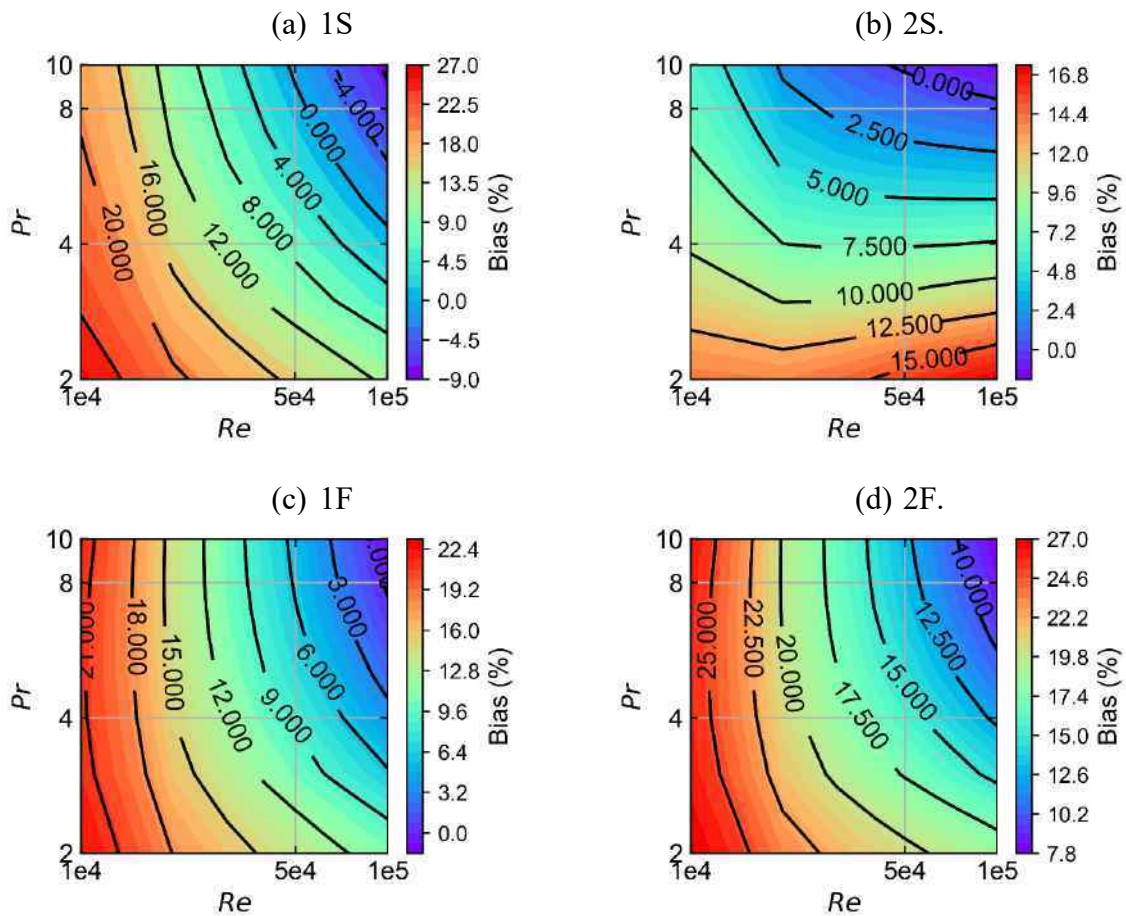


Figure 3.13 : relative bias on the calculation of the asymptotic Nusselt number compared to Gnielinski correlation.

3.2.2.2 Establishment of the Nusselt profile

For all the simulations, the Nusselt number maximum is reached at the leading edge of the heated wall where the temperature gradients are the most important. This result has also been observed on the experimental data obtained from gypsum dissolution as it can be seen on Figure 2.17. The ratio between the leading-edge value and the established boundary layer value of the Nusselt number is found to be in the range [1.5, 2.5]. No clear tendency with the Reynolds number is visible as the experimental data in this zone are too noisy. The characteristic length has not been processed as the uncertainty on the leading edge were too large. In literature, the ratio can be found in (Boelter, et al., 1948) for a wide range of hydraulic conditions. It is shown that the impact of the establishment of the velocity profile at the entrance region has a significant impact, as the shape of the developing thermal boundary layer and the amplitude at the leading-edge changes drastically for varying geometries. For a circular pipe with a long calming section at the entrance, the value is found to range in [1.5, 2.5] and is found to decrease

with the Reynolds number. In comparison, the ratio calculated from the Nusselt profiles obtained on the grid 1S and 1F were in the range [2 , 3] as depicted on Figure 3.9.

3.3 Determination of the uncertainty $U_{inputs,exp}$

3.3.1 Introduction

The uncertainty quantification process applied to the rectangular channel simulation consists of assessing the values of the different sources of errors and uncertainties depicted in §1.2.1. In this paragraph, $U_{inputs,exp}$, the uncertainty resulting from the propagation of the uncertainty of the simulation's input parameters will be quantified. In this numerical case corresponding to the reproduction of the experiments presented in Chapter 2, two input variables of the simulation are uncertain when comparing to experiments :

- the Reynolds number at the inlet of the channel which was found to fluctuate around 2% to 5% of the mean value during the experiments. This fluctuation was the result of the fluctuation of the temperature and flowrate in the channel. The Reynolds number is adjusted in the simulation with the inlet flowrate.
- the Prandtl number of the simulation which value is adjusted by modifying the specific heat of water. During the mass transfer measurements experiments, the Schmidt number was found to fluctuate around 2% to 5% due to the fluctuation of the temperature in the channel.

The flowrate at the inlet of the channel and the specific heat of water were thus set as uncertain in order to reproduce the variability of the Reynolds and Schmidt numbers observed during the experiments (see §2.5.1). In addition, the fluctuation of both non dimensional quantities were correlated. The Pearson correlation coefficient was introduced:

$$\rho_{Re,Sc} = \frac{Cov(Re, Sc)}{\sigma_{Re}\sigma_{Sc}}$$

This coefficient was found to vary in the range $[-1, -0.8]$ for all experiments, with a mean value of the coefficient $\mu_{\rho_{Re,Sc}} = -0.89$. This mean value of the Pearson correlation coefficient calculated from the experiments has been chosen for the generation of the bivariate Gaussian distribution representing the probability density function of the two dimensional input random variable (Re, Pr) that will be propagated through the calculation of the Nusselt number.

Two approaches have been tested in order to propagate the inputs uncertainty through the computation of the heat transfer coefficient:

- Method 1: a surrogate model is designed from the computations of the heat transfer coefficient. This surrogate model is generated using Gaussian processes §1.2.3 with the python library **scikit-learn**. Monte Carlo draws were used on this surrogate model to propagate the inputs uncertainty §1.2.4.2.1.
- Method 2: the propagation is achieved with Deterministic Sampling (DS) presented in §1.2.4.2.2. The output uncertainty is estimated from N computations with N depending on the number of inputs and of the aimed accuracy.

3.3.2 Method 1: Surrogate model and Monte-Carlo method

This first method implemented to propagate the input uncertainty is based on random sampling. This method which is described in §1.2.4.2.1 estimates the mean value and standard deviation of the output from large number of computations of the heat transfer coefficient. The CPU time for one computation with CFD makes this approach unfeasible for most of industrial application. Thus, an intermediate step is added in order to design a surrogate model which can estimate the CFD response as a function of the input parameters with an affordable cost. This surrogate model is generated from the results of CFD computations which are combined with Bayesian statistics and Gaussian process theory described in §1.2.3.

In this work, the surrogate model predicting the Nusselt number is designed using gaussian processes and Bayesian statistics. Its training relies on observations; thus, a design of experiment (DoE) map is designed in order to choose the inputs for computation of the heat transfer coefficient. Different technics are used to generate a DoE, some which are sequential in order to refine iteratively the surrogate model by adding data where the surrogate model accuracy is not fine enough. Other DoE are predefined, such as uniform, maximizing entropy and others. Elements on various DoE can be found in (Kleijnen, 2018). In this work, a uniform design (UD) has been generated in order to cover the range of input conditions.

$$\begin{aligned} Re &\in [10^4, 10^5] \\ Pr &\in [2, 10] \end{aligned}$$

This UD is written $U_{50}(10^1 \times 5^1)$. This notation $U_n(q_1^{s_1}, \dots, q_p^{s_p})$ is given for UD with mixed levels, where U stands for Uniform, n gives the total number of runs, q_j the number of level and s_j the number of factors. This design is depicted on Figure 3.14.

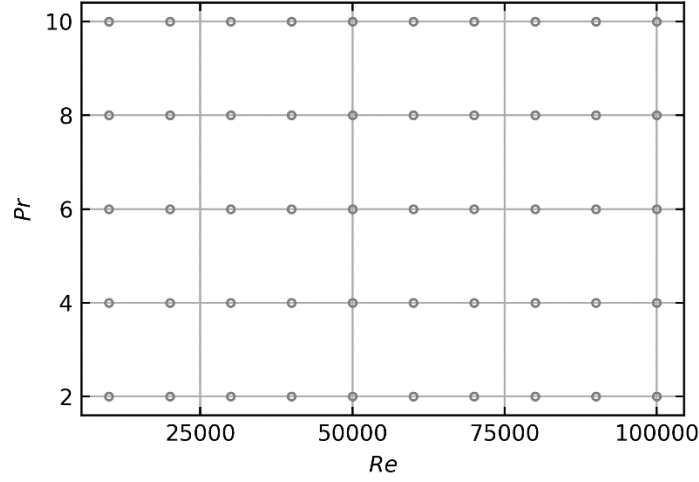


Figure 3.14: levels of the Reynolds and Prandtl number for the uniform design $U_{50}(10^1 \times 5^1)$.

Literature and experiments on the rectangular channel (cf. Chapter 2) indicate a trend of the Nusselt number which is unchanged on the investigated range of simulation inputs. In this case, the design $U_{50}(10^1 \times 5^1)$ is appropriate for the creation of the surrogate model and do not require local refinement at specific region of the DoE. For an input space with a higher dimension and for more complex responses, other DoE should be used in order to have an accurate surrogate model and limit the number of CFD runs required.

The data inputs are written $\mathbf{X} = (\mathbf{x}_1, \mathbf{x}_2, \dots, \mathbf{x}_N)$ and the outputs $\mathbf{y} = (y_1, y_2, \dots, y_N)$. Each output y_i is the asymptotic Nusselt number computed with CFD with simulation inputs $\mathbf{x}_i = (Re_i, Pr_i)$. The outputs are considered as a realization of a random Gaussian process $f \sim GP(\mu, k(\mathbf{x}, \mathbf{x}'))$ with μ the mean of the Gaussian process and k the covariance function.

A joint prior is given for the realizations $\mathbf{y} = (y_1, y_2, \dots, y_N)$ by assuming a Squared-Exponential (SE) kernel. In addition, the output is assumed to include white noise of mean zero and of variance σ_e^2 . In this case, the covariance (or kernel) function k can be written as following:

$$k(\mathbf{x}_i, \mathbf{x}_j) = \sigma_f^2 \exp\left(-\frac{d(\mathbf{x}_i, \mathbf{x}_j)^2}{2l^2}\right) + \sigma_e \delta_{ij}$$

where, $d(\mathbf{x}_i, \mathbf{x}_j)$ is the cartesian distance between \mathbf{x}_i and \mathbf{x}_j , σ_f is the signal variance, l is a characteristic length and δ_{ij} is the Kronecker function. The “training” of the gaussian process consists of finding the best parameters for the regression of the observation points. This set of best parameters $\boldsymbol{\theta} = (l, \sigma_e, \sigma_f)$ is found by maximizing the likelihood $p(\boldsymbol{\theta}|\mathbf{X}, \mathbf{y})$.

The algorithm used in order to compute the predictive distribution $p(f(x^*) | f(\mathbf{X}), \mathbf{X}, \mu(\cdot), k(\cdot, \cdot))$ mean and variance (1.17) are based on the implementation of Algorithm 2.1 from (Rasmussen & Williams, 2006) in the python library scikit-learn (Pedregosa, 2011). The mean value of the process μ is set to the mean value of the outputs \mathbf{y} .

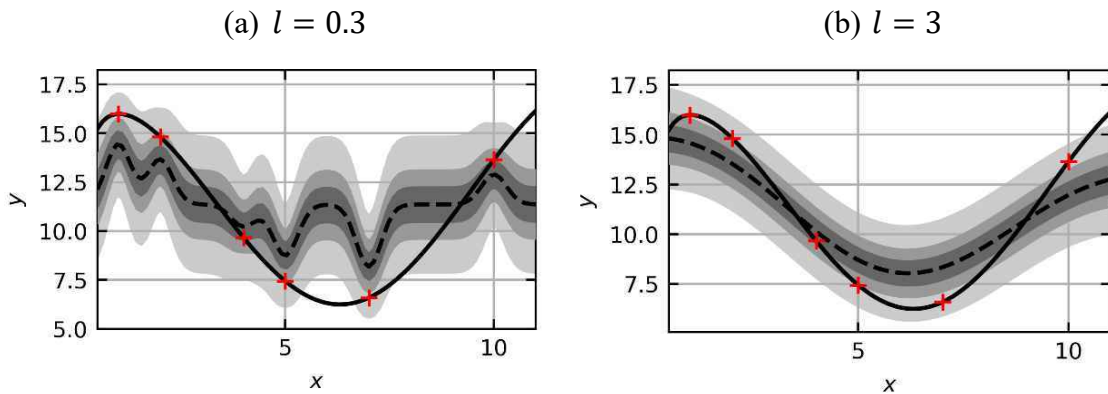


Figure 3.15: data generated from a GP with a SE kernel and test points indicated with red crosses. The predictive mean is indicated with dashed line, the real function with a solid black line. The length scale l of the SE kernel is fixed with (a) $l = 0.3$. and (b) $l = 3$. Shades of grey indicate quantiles of the predictive distribution.

An example of the effect of changing the parameter l can be seen on an arbitrary 1D case depicted on Figure 3.15. This example has been generated with scikit-learn by computing the predictive mean distribution of the GP for the SE kernel summed with white noise with $l = 0.3$ and $l = 3$. The error variance is set to $\sigma_e = 1$ and the signal variance σ_f is adjusted in order to maximize the likelihood. It is visible that the parameters influence on the predictive mean and variance is significant. Large values of l tend to smooth curves while small values of l tend to return the mean value of the gaussian process everywhere except in the immediate vicinity of the test points.

For the rectangular channel case, the SE kernel has been chosen due to the smooth aspect of the response of the gaussian process with this kernel and the limited number of hyper parameters to fit. The input space is two dimensional, thus, two lengths l_1, l_2 are defined respectively for the Prandtl number axis and the Reynolds number axis. Moreover, the data is considered noise free, and a simple Gaussian kernel is used with $\sigma_e = 0$ and $\sigma_f = 1$ in order to fit the exact CFD value on the training points. Once the kernel is chosen and the training data generated, the accuracy of the surrogate model is evaluated by splitting randomly the training data in two groups. One group is used in order to generate the surrogate model and calibrate the values of (l_1, l_2) , the other to estimate the accuracy of the prediction compared to the results of CFD simulations. This step is repeated N_S times, allowing to estimate the mean and variance of the surrogate model which indicates its accuracy. In this study, a split 80%/20% of training/evaluation data is used. Finally, when the surrogate model is trained and the

accuracy is satisfying, random samples of couples Re_i, Pr_i are generated and injected as inputs of the surrogate model to estimate the mean and variance of the output with Monte Carlo method. This method has also been applied for a one-dimensional input space at constant Prandtl number in order to compare its results to Deterministic Sampling described in the following paragraph.

3.3.3 Method 2: Deterministic Sampling

This second approach uses Deterministic Sampling described in §1.2.4.2.2. It provides an estimation of the mean and standard deviation of the CFD output for uncertain simulation inputs from a weighted sample of the Nusselt computations. In this chapter, only the Reynolds number of the simulated test section is set as uncertain following a univariate Gaussian distribution $Re \sim N(\mu_{Re}, \sigma_{Re})$. It has been indicated in §1.2.4.2.2 that the sigma points that are used to create the deterministic sample ensembles are chosen in order to respect the statistical moments of the input random variables. The four centered statistical moments of the normal distributions of variance σ^2 are:

$$\langle \delta X \rangle = 0, \quad \langle \delta X^2 \rangle = \sigma^2, \quad \langle \delta X^3 \rangle = 0, \quad \langle \delta X^4 \rangle = 3\sigma^4$$

Ensembles used in this work can be found in (Sahlberg, 2016) which also gives a methodology to combine these ensembles. One simple ensemble that can be used to propagate the variance of the input is the Standard ensemble used in the Unscented Kalman filtering (UKF) (Julier & Uhlmann, 2004) (see §1.2.4.2.2) The sigma points $\tilde{\mathbf{X}}$ and the weights \mathbf{W} used are defined as following:

$$\mathbf{W} = \begin{pmatrix} \frac{1}{2} \\ \frac{1}{2} \end{pmatrix}, \quad \tilde{\mathbf{X}} = \begin{pmatrix} \mu + \sigma \\ \mu - \sigma \end{pmatrix}$$

It can be easily verified that this ensemble respects the three first moments. Instead of using this ensemble, an extension called the ‘‘Zero Padding’’ ensemble has been chosen. The difference between these two ensembles is the presence of the centered point $Re = \mu_{Re}$ which is combined with a more important weight in order to reproduce the fourth statistical moment.

$$\mathbf{W} = \begin{pmatrix} \frac{1}{6} \\ \frac{1}{6} \\ \frac{2}{3} \end{pmatrix}, \quad \tilde{\mathbf{X}} = \begin{pmatrix} \mu - \sqrt{3}\sigma \\ \mu + \sqrt{3}\sigma \\ \mu \end{pmatrix}$$

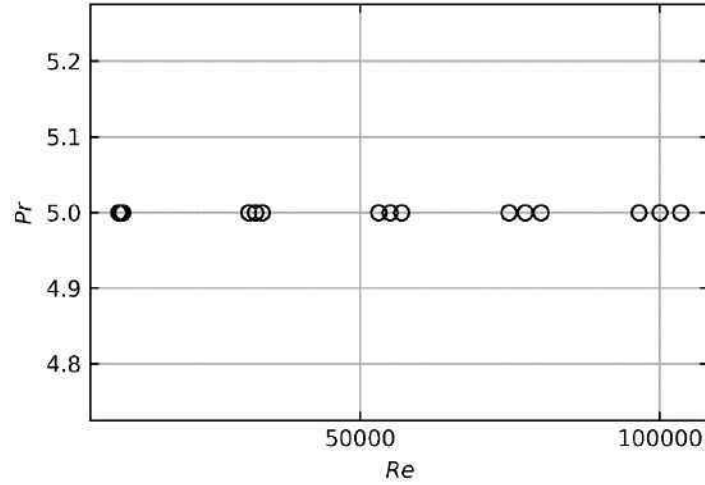


Figure 3.16: design of experiment used for the CFD runs for the propagation of five uncertain Reynolds numbers through the calculation of the Nusselt number with Deterministic Sampling.

We can verify that this ensemble reproduces the four first statistical moment of any Gaussian distribution X . This verification is done by calculating each of the four first centered moments with the weighted approach:

$$\begin{aligned}
 w_1 + w_2 + w_3 &= 1 \\
 \left(\frac{1}{6}(\mu - \sqrt{3}\sigma) + \frac{1}{6}(\mu + \sqrt{3}\sigma) + \frac{2}{3}\mu \right) &= \mu \\
 \left(\frac{1}{6}(\mu - \sqrt{3}\sigma - \mu)^2 + \frac{1}{6}(\mu + \sqrt{3}\sigma - \mu)^2 + \frac{2}{3}(\mu - \mu)^2 \right) &= \frac{1}{6}3\sigma^2 + \frac{1}{6}3\sigma^2 = \sigma^2 \\
 \left(\frac{1}{6}(\mu - \sqrt{3}\sigma - \mu)^3 + \frac{1}{6}(\mu + \sqrt{3}\sigma - \mu)^3 + \frac{2}{3}(\mu - \mu)^3 \right) &= 0 \\
 \left(\frac{1}{6}(\mu - \sqrt{3}\sigma - \mu)^4 + \frac{1}{6}(\mu + \sqrt{3}\sigma - \mu)^4 + \frac{2}{3}(\mu - \mu)^4 \right) &= 3\sigma^4
 \end{aligned}$$

Only the mean μ_{Nu} and standard deviation σ_{Nu} of the Nusselt number are of interest in this present work. They are calculated with:

$$\mu_{Nu} = \sum_{i=1}^3 w_i Nu(Re_i) \quad (3.2)$$

$$\sigma_{Nu} = \sqrt{\sum_{i=1}^3 w_i (Nu(Re_i) - \mu_{Nu})^2} \quad (3.3)$$

The design of experiment map used in order to estimate the mean and standard deviation of the uncertain output Nu is depicted on Figure 3.16. The Prandtl number is fixed and set to $Pr = 5$.

The mean and variance of the output Nusselt number are estimated for five uncertain Reynolds number.

3.3.4 Summary of performed computations

The computations performed for the different grids and software are recapitulated in Table 3.5.

Table 3.5 : approaches used for uncertainty propagation through RANS simulations with the different grids

Meshing	$U_{50}(10^1 \times 5^1)$	DS – Zero Padding
Grid 1S	Yes	Yes
Grid 2S	Yes	No
Grid 1F	Yes	No
Grid 2F	Yes	No

3.3.5 Results of the propagation

3.3.5.1 Method 1: Surrogate model and Monte-Carlo method

This method relies on the creation of a surrogate model \widehat{Nu} estimating the response of CFD codes for arbitrary simulation inputs (Re and Pr). First, the accuracy of the surrogate model is estimated. The methodology to estimate the accuracy of the surrogate model is as follows:

- The data points Re_i, Pr_i, Nu_i retrieved from the CFD simulations on the DoE are split in two groups : 80% of the data $Re_{train,i}, Pr_{train,i}, Nu_{train,i}$ is used to train the surrogate model \widehat{Nu} , while 20% of the data $Re_{eval,i}, Pr_{eval,i}, Nu_{eval,i}$ is used to evaluate the error between the predictions $\widehat{Nu}(e_{eval,i}, Pr_{eval,i}) - Nu_{eval,i}$
- This process is repeated N_S times, the separation of the data in two groups is done randomly considering a equal probability for each point of the DoE. This is done with a method implemented in scikit-learn based on pseudo random numbers generator.
- The mean and standard deviation of the prediction error are retrieved from the N_S samples.

In this work, $N_S = 500$, the mean error is estimated over the 500 prediction of the error which is found to be on inferior to 0.1% of the given value which is assumed to be negligible. One of the random separations of training and evaluation points is given on Figure 3.17a, the Nusselt number is given with a colormap. On Figure 3.17b and Figure 3.17c, the mean and standard deviation of the surrogate model is calculated for Grid 2S. The surrogate model based on the computations with this grid showed the biggest values of standard deviation which is given in percent of the mean predicted value.

On the case depicted Figure 3.17b and Figure 3.17c, the standard deviation is found to be approximately 0.25% of the prediction at the center of the domain. This standard deviation grows larger on the border and reaches 1 to 2%. On the center of the domain, the prediction error is neglected when estimating $U_{inputs,exp}$. Nevertheless, on the border of the $Re - Pr$ space, the diminution of the surrounding data leads to an increased error which can have an impact on the prediction of the Nusselt number. Thus, the surrogate model that is generated for predicting the Nusselt number is bounded to the range of Reynolds number:

$$Re \in [2 \cdot 10^4, 9 \cdot 10^4], \quad Pr \in [3, 9]$$

The simulation inputs Re, Pr probability density function is modelled with a joint gaussian distribution. During the experiments, the Reynolds and Schmidt values have been found to fluctuate in the worst case about 2% around their mean value. Thus, a sample has been generated for a 2D joint Gaussian distribution \mathbf{X} around different mean points $\boldsymbol{\mu}_X = (\mu_{Re}, \mu_{Pr})$ with a covariance matrix defined as following:

$$Cov(Re, Pr) = \begin{pmatrix} \sigma_{Re}^2 & C \\ C & \sigma_{Pr}^2 \end{pmatrix}, \quad C = \rho_{Re,Sc} \sigma_{Re} \sigma_{Pr}$$

where, $\sigma_{Re} = 0.02 \mu_{Re}$ and $\sigma_{Pr} = 0.02 \mu_{Pr}$. C is calculated from the Pearson correlation coefficient $\rho_{Re,Sc} = -0.89$ (see §3.3.1).

The surrogate model designed for prediction of the established thermal boundary layer Nusselt number is denoted with the symbol $\widehat{Nu}(Re, Pr)$. A sample of 10 000 realization of this joint Gaussian distribution has been generated with a pseudo random number generator implemented in the python library numpy. The mean value and standard deviation of the Nusselt number are computed by estimating the mean and standard deviation of the predictions for each realization of the sample $(Re_i, Pr_i)_{i \in [1, 10\,000]}$:

$$\mu_{Nu} = \frac{1}{10\,000} \sum_{i=1}^{10\,000} \widehat{Nu}(Re_i, Pr_i)$$

$$\sigma_{Nu} = \frac{1}{10\,000 - 1} \sum_{i=1}^{10\,000} (\widehat{Nu}(Re_i, Pr_i) - \mu_{Nu})^2$$

The uncertainty due to the uncertain simulation inputs $U_{inputs,exp}$ mean value and standard deviation are then calculated with:

$$\mu_{U_{inputs,exp}} = Nu(\mu_{Re}, \mu_{Sc}) - \mu_{Nu}$$

$$\sigma_{U_{inputs,exp}} = \sigma_{Nu}$$

(a) Example of repartition between training and evaluation data

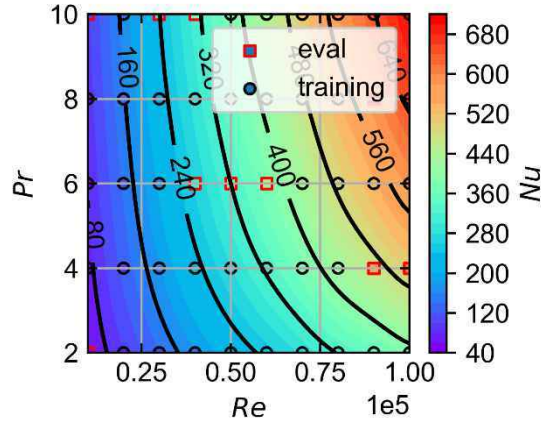
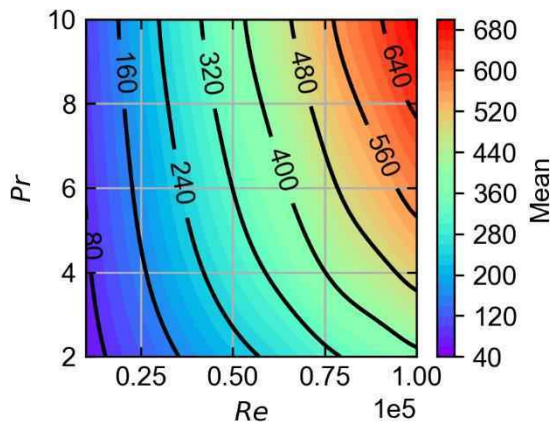
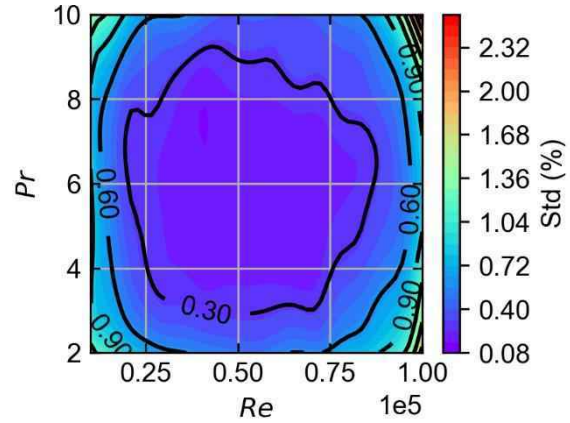
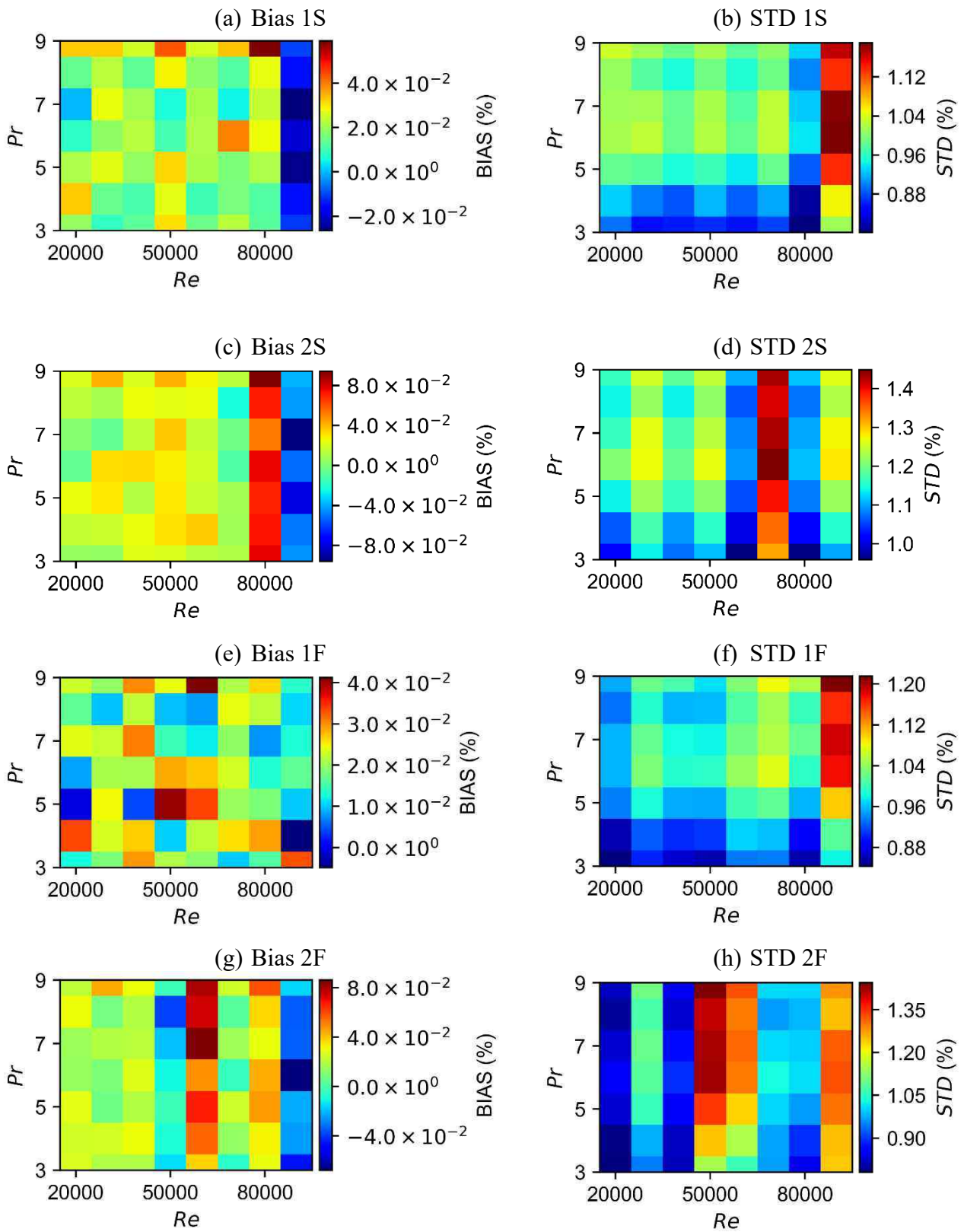
(b) Mean of the N_S surrogate model(c) Standard deviation of the N_S surrogate model

Figure 3.17 :construction of the surrogate model for the established boundary layer Nusselt for Grid 2S. (a) Example of training (○) – evaluation (□) separation of the data for one of the N_S surrogate model created. (b) Resulting surrogate model mean and (c) standard deviation.

The relative bias and standard deviation on the computation of the Nusselt number are defined as following:

$$Bias = 100 \frac{\mu_{U_{inputs,exp}}}{Nu(\mu_{Re}, \mu_{Sc})}$$

$$STD = 100 \frac{\sigma_{Nu}}{Nu(\mu_{Re}, \mu_{Sc})}$$

Figure 3.18 : *BIAS* and *STD* for the different computations

The results for all grids are depicted on Figure 3.18. The relative bias is lower than 0.1% of the value given by CFD $Nu(\mu_{Re}, \mu_{Pr})$ on most of the studied range and is thus assumed negligible. The standard deviation is found to be in the range [1%, 2%] of the CFD estimation $Nu(\mu_{Re}, \mu_{Pr})$. Moreover, it can be noticed that the differences between the grids are small. The propagation of the boundary condition uncertainty on this case yields low standard deviation and bias due to the low uncertainty on the Reynolds number and Schmidt number during the experiment. The impact they have on the computed Nusselt number is limited and can be assumed negligible with respect to the experimental uncertainty.

3.3.5.2 Method 2: Deterministic Sampling

Deterministic sampling (DS) has been used to propagate the uncertainty of one uncertain parameter which is the Reynolds number. This uncertainty has been estimated for the Nusselt number at the exiting edge of the heated wall Nu_{2D} for the five following mean Reynolds number: 10 000, 32 000, 55 000, 77 500 and 100 000 at $Pr = 5$. The Reynolds number is assumed to follow a normal distribution $\mathcal{N}(\mu_{Re}, \sigma_{Re})$ where the standard deviation σ_{Re} is defined as follows:

$$\sigma_{Re} = 0.02 \mu_{Re}$$

The objective of these computations was to compare for a simple case this method with the previous one relying on surrogate modelling and Monte Carlo draws. The method 1 depicted in the previous section is reproduced for the propagation of the uncertain Reynolds number defined previously for Nusselt obtained at $Pr = 5$. The generation of the training data for the training of the surrogate model was done by transposing the data obtained on the DoE depicted Figure 3.14 to $Pr = 5$ by using the Prandtl dependency found in Table 3.4. Only the results are presented, as the process has already been described in the previous section.

The calculation of the mean value of the Nusselt number μ_{Nu} and its standard deviation σ_{Nu} with DS is realized with equations (3.2) and (3.3). An example of propagation with DS is given on Figure 3.19. The $\mu_{Nu} \pm 2\sigma_{Nu}$ interval calculated is given and covers the 3 runs.

The uncertainty $U_{inputs,exp}$ is quantified around the five Reynolds numbers. The standard deviation and bias are given in percent of the CFD simulation on Figure 3.20:

$$\begin{aligned} \mu_{U_{inputs,exp}} &= 100 \frac{Nu(\mu_{Re}, Pr = 5) - \mu_{Nu}}{Nu(\mu_{Re}, Pr = 5)} \\ \sigma_{U_{inputs,exp}} &= 100 \frac{\sigma_{Nu}}{Nu(\mu_{Re}, Pr = 5)} \end{aligned}$$

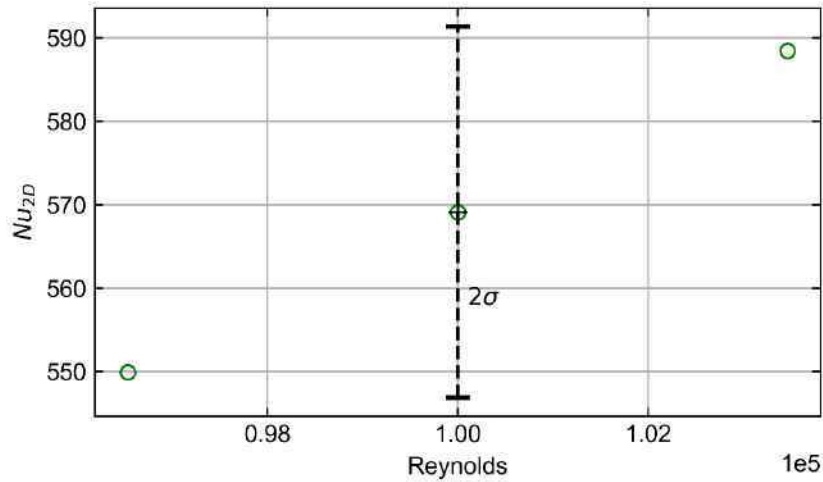


Figure 3.19: example of the resulting standard deviation of the Nu_{2D} for $Re = 100\,000$. The CFD runs values are given with the symbols (\circ). The mean and standard deviation of Nu_{2D} are respectively given by the black cross and error bar. The total error bar length is 4σ

The bias is found to be lower than 1% for all the estimation points. Moreover, no visible tendency is observed. The maximum value is about -0.18% of the CFD run for $Re = 77\,500$. The standard deviation fluctuates in the range $\sigma_{U_{inputs,exp}} \in [1.5\%, 2\%]$, and as for the bias, no visible tendency is observed.

The comparison between the results yielded by the two propagation methods is given on Figure 3.21. It should be reminded that the first approach to propagate the uncertainty of inputs relies on the training of a surrogate model for the prediction of the Nusselt number in the range $Re \in [10^4, 10^5]$. The bias is similar for both methods and lower than 1%. For $Re = 10^5$, the difference is more significant but is most certainly due to the loss of accuracy of the surrogate model around this Reynolds number which is on the border of the Reynolds domain. The standard deviation is also similar for both methods and no evolution is observed with the Reynolds number. In both case, $\sigma_{U_{inputs,exp}}$ remains in the range $\sigma_{U_{inputs,exp}} \in [0.015 Nu_{CFD}(\mu_{Re}), 0.02 Nu_{CFD}(\mu_{Re})]$ where $Nu_{CFD}(\mu_{Re})$ is the Nusselt number estimated at a given mean Reynolds number.

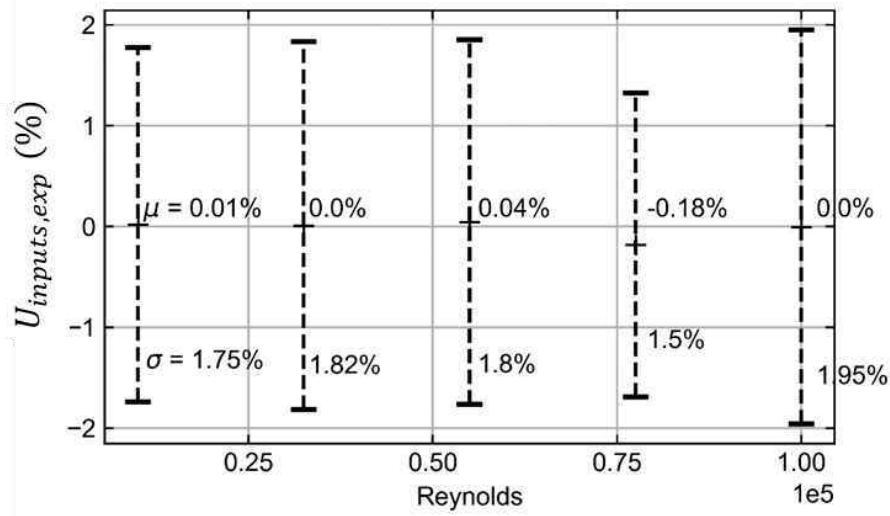


Figure 3.20: results of the uncertainty quantification with Deterministic Sampling for Grid 2S. The bias is close to zero and is indicated with text for each estimation point. The standard deviation is given with error bars.

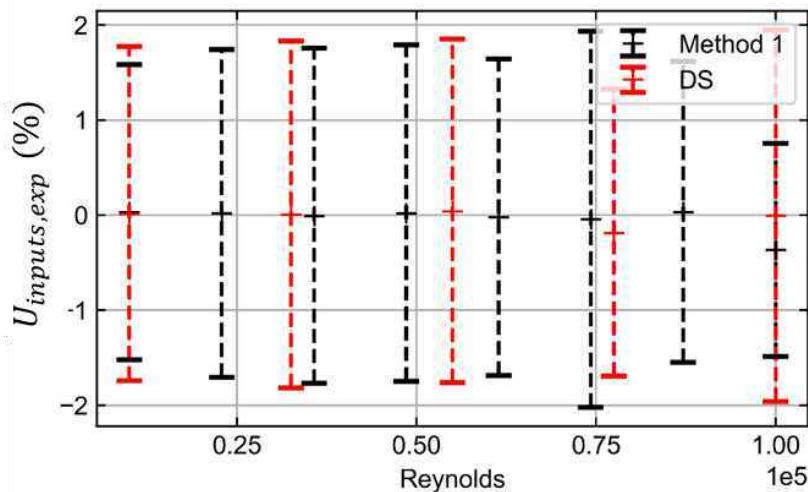


Figure 3.21 : comparison of the bias and standard deviation of $U_{inputs,exp}$ between method 1 and method 2 (in % of the CFD simulation prediction)

3.3.5.3 Conclusion

Two methods have been presented in order to propagate the uncertainty of the simulation inputs through the calculation of the established thermal boundary layer Nusselt number with CFD. For this study, the relative standard deviation of the resulting uncertainty has been found to be of the same order of magnitude as the uncertainty of the inputs which is around 2% for the experiments on the rectangular channel. This low level of uncertainty on the inputs does not

affect the mean value as the bias induced $\mu_{U_{inputs,exp}}$ has been found to be lower than 0.1% of the Nusselt number for most of the CFD runs with the different models. This low bias is mostly due to the smoothness of the CFD response and the quasi-linear behavior in respect to the Reynolds and Prandtl numbers. Differences are observed with the surrogate modelling methodology when propagating one or two uncertain parameters. In the latter case, the correlation between the two parameters has been considered and the resulting uncertainty has been found smaller than for a unique uncertain parameter. Finally, the uncertainty found by both methods are similar, differences are only visible on the border of the design of experiment map where the accuracy of the surrogate model designed in method 1 decreases.

3.4 Estimation of the model error E_{model}

The mean and standard deviation of the model error E_{model} are estimated from the different sources of uncertainty:

$$\begin{aligned}\mu_{E_{model}} &= \mu_{E_{CFD/EXP}} + \mu_{U_{EXP}} - \mu_{U_{inputs,exp}} - \mu_{E_{num}} \\ \sigma_{E_{model}} &= \sqrt{\sigma_{E_{CFD/EXP}}^2 + \sigma_{U_{EXP}}^2 + \sigma_{U_{inputs,exp}}^2 + \sigma_{E_{num}}^2}\end{aligned}$$

The different sources of uncertainty are chosen as follows:

- **Error between the computations and experiments $E_{CFD/EXP}$** : the mean value is calculated as in §3.2.2 by comparing the correlations obtained for the Nusselt number with the different models to the correlation from Gnielinski and the correlation from the gypsum dissolution measurements. The standard deviation is taken as zero as the computations are noise-free. The potential randomness of the realization of the experimental data is taken into account in the experimental uncertainty U_{EXP} .
- **Experimental uncertainty U_{EXP}** : the standard deviation has been estimated during the experiments as a function of the Reynolds number. This standard deviation is calculated by combining the temporal variations of the measurements and the square error between the experimental point and the calculated correlation. Its value is high for low Reynolds number reaching 70% of the predicted value but decreases significantly for the higher Reynolds number to 10%. The bias is assumed to be zero, which has been partially verified on this case by comparing to other heat transfer correlation from literature. For Gnielinski correlation, the mean is assumed to be zero, and the standard deviation on the correlation is defined as 10% of the experimental value.
- **Numerical error E_{NUM}** : this source of error has been assumed negligible with respect to the other sources of error and uncertainty. A rough estimation of this error has been achieved with a grid convergence at a specific Reynolds number (see §1.2.4.3), which yielded a bias and standard deviation around 1% of the calculated Nusselt number. The obtention of this error will be presented with more details in Chapter 6.
- **Uncertainty of the simulation inputs $U_{inputs,exp}$** : the bias is negligible when compared to $E_{CFD/EXP}$. Furthermore, its standard deviation can also be neglected with

respect to the standard deviation of U_{EXP} . Thus, the contribution of this uncertainty to the modelling error on the rectangular channel case was neglected.

Only the bias calculated from the difference between experiments and CFD runs and the standard deviation due to the experimental uncertainty are important in order to quantify E_{model} . This remark underlines the importance of experimental data for the quantification of the model error of CFD.

The bias of the model error is approximated to be the bias of $E_{CFD/EXP}$. The evolution with the Reynolds and Prandtl number is depicted on Figure 3.12 when comparing to the correlation obtained from gypsum dissolution measurements and on Figure 3.13 when comparing the simulation calculation of the established Nusselt number Nu_{2D} to Gnielinski correlation. It is visible that the bias is more important with Gypsum dissolution for low Reynolds reaching 40% for the lowest Prandtl numbers. For the higher Reynolds numbers, this bias is in the range $[-10\%, 10\%]$ of the CFD value. When comparing with Gnielinski correlation, the bias is lower for the smaller Reynolds number reaching in the worst case 30%. For the higher Reynolds number, the bias is in the range $[-10\%, 17\%]$. For both experimental data, the bias is similar for high Reynolds number.

The evolution of the model error is depicted for $Pr = 2$ and $Pr = 10$, for Grid 1S and 2S on Figure 3.22 and for Grid 1F and 2F on Figure 3.23. The bias and the standard deviation are given relatively to the estimation of the Nusselt number with CFD:

$$Bias = \frac{Nu_{CFD} + \mu_{E_{model}}}{Nu_{CFD}}, \quad STD = \frac{\sigma_{E_{model}}}{Nu_{CFD}}$$

The difference in the calculation of the model error with Gnielinski correlation and gypsum dissolution data is significant for the lowest Reynolds numbers. For the largest Reynolds number, the bias between experiments and CFD is similar for both experimental data. In both cases, the bias stabilizes itself for high Reynolds numbers and is lower for the higher Prandtl number. For all grids except (2F), the calculation with CFD underestimates the value of the heat transfer coefficient for high Prandtl number and high Reynolds number. For $Pr = 10$ the bias stabilizes to negative values in the range $[-10\%, 0\%]$. For low Prandtl numbers, CFD overestimates the heat transfer coefficient. The difference between models with or without wall laws is similar for the implementation in commercial codes: the value with wall law yields results approximatively 10% higher than without.

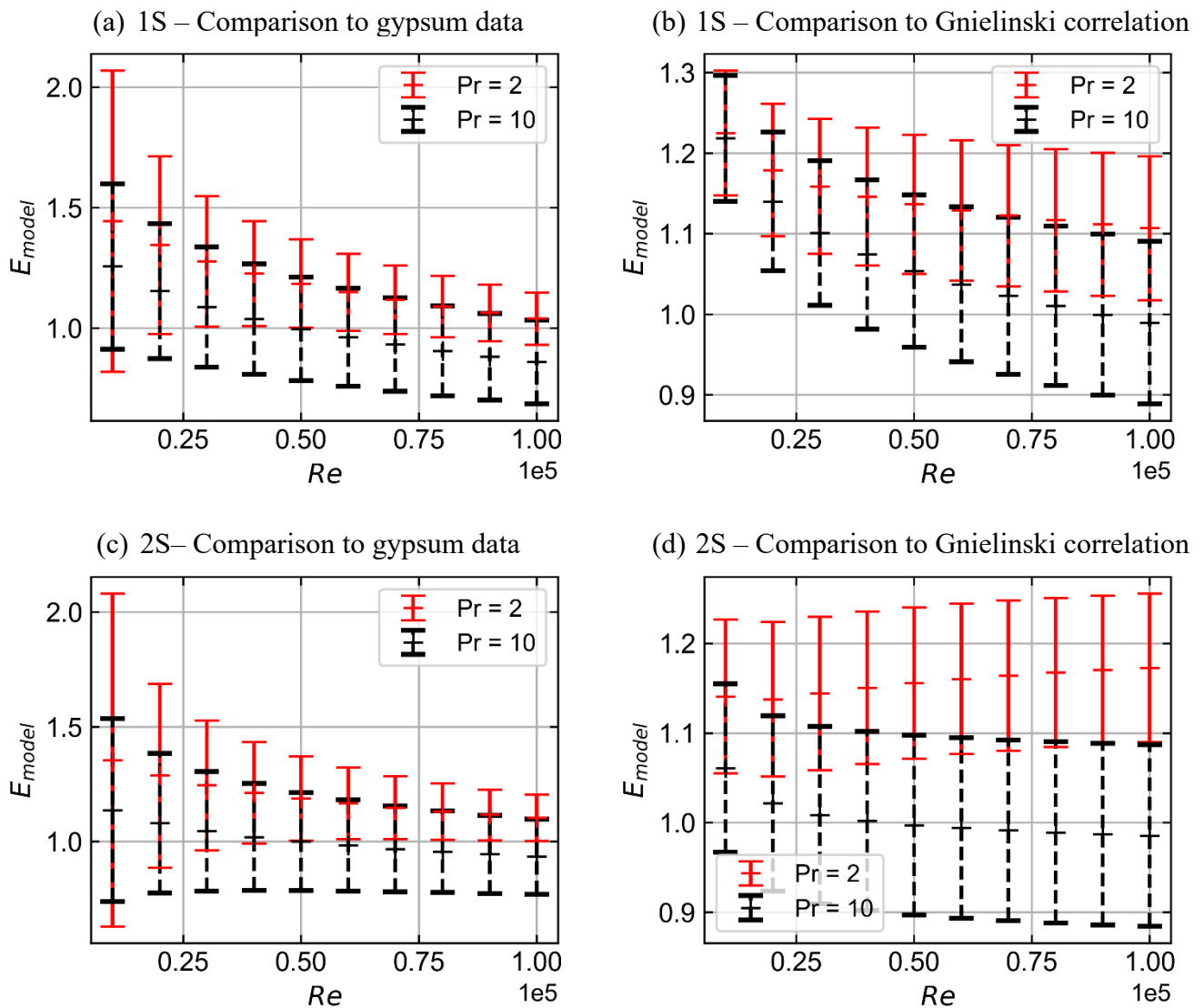


Figure 3.22 : evolution of the model error mean and standard deviation for Prandtl number equal to 2 and 10 for grid 1S and 2S. The model error is estimated with gypsum data on (a) and (c), and with Gnielinski correlation (b) and (d). Cross symbols indicate the bias relatively to Nu_{CFD} and the error bar gives a $\pm \sigma_{E_{model}}$ interval.

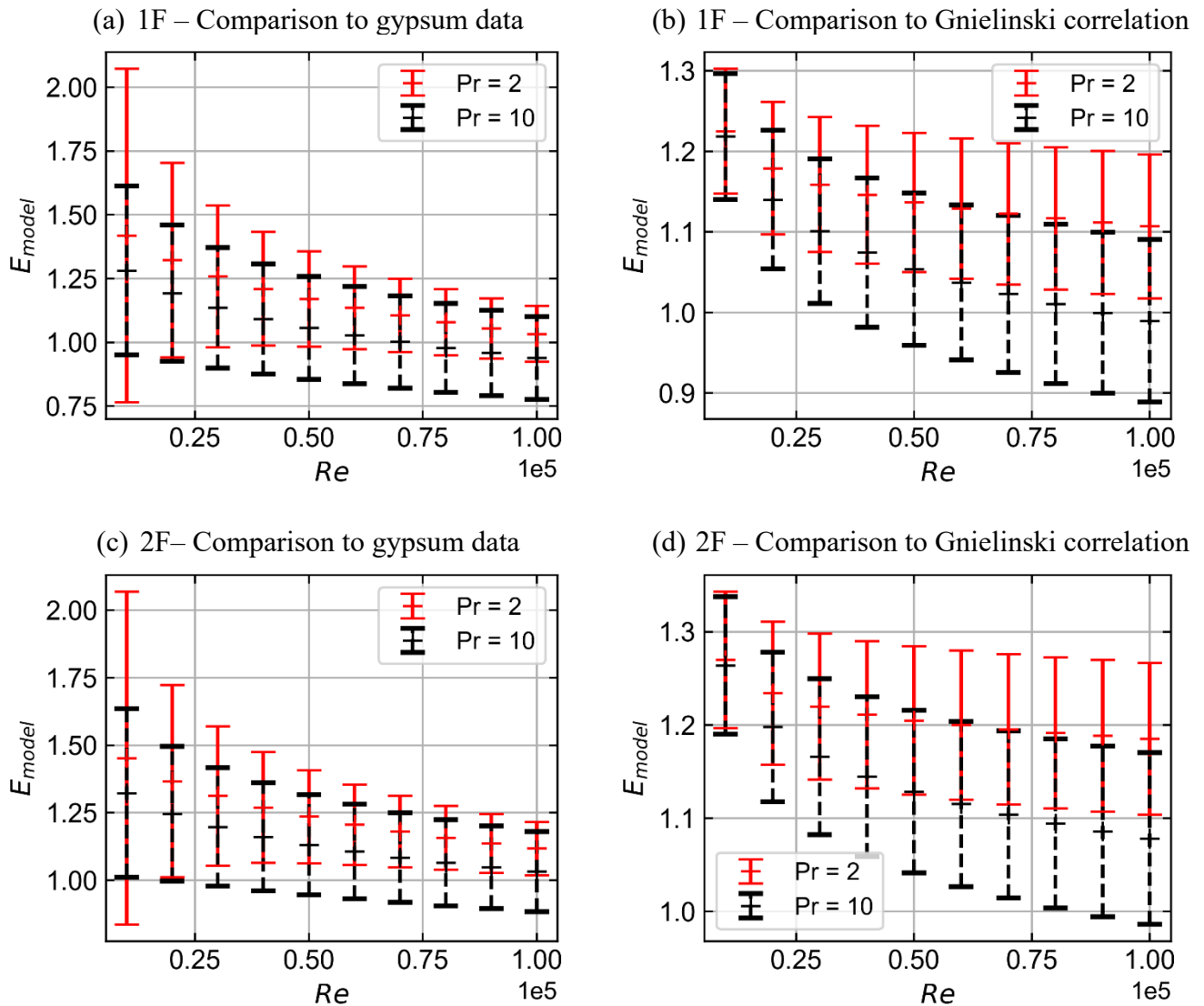


Figure 3.23 : evolution of the model error mean and standard deviation for Prandtl number equal to 2 and 10 for grid 1F and 2F. The model error is estimated with gypsum data on (a) and (c), and with Gnielinski correlation (b) and (d). Cross symbols indicate the bias relatively to Nu_{CFD} and the error bar gives a $\pm \sigma_{E_{model}}$ interval.

3.5 Conclusion

The experiments that were conducted in the rectangular channel have been reproduced numerically with CFD. This has been realized in order to quantify the model error defined in §1.2.1. In this case, the quantification relied on the estimation of:

- the experimental uncertainty on the Nusselt number U_{EXP} .
- the error between CFD and experiments $E_{CFD/EXP}$ which has been calculated for the different models and for experimental data originating from gypsum dissolution measurements and Gnielinski correlation for turbulent heat transfer in a pipe.
- the uncertainty when considering uncertain inputs $U_{inputs,exp}$.

The work that has been achieved enabled to draw the following conclusions:

- the Nusselt number obtained from CFD for an established thermal boundary layer is in a good agreement with the experimental data, whether it is with the gypsum measurements or Gnielinski correlation. The bias has been found to decrease with the Reynolds number and remain within the experimental uncertainty.
- the establishment of the Nusselt number at the leading edge of the heated wall is not well captured by model including wall laws. However, this effect reduces for increasing Reynolds numbers and Prandtl numbers presenting shorter establishment lengths.
- both methodologies tested in order to propagate the inputs uncertainty give similar results. The first methodology which relies on surrogate models presents the advantage of enabling the quantification of this uncertainty on a global scale. The second one based on Deterministic Sampling has the advantage to have a significantly lower cost. These two approaches can be used according to the situation. Nevertheless, it has been shown that this source of uncertainty is negligible.

Finally, the uncertainty quantification on the rectangular channel highlighted the importance of experimental measurements for the estimation of the model error. In fact, in this study, all other source of error/uncertainty have been neglected with respect to the standard deviation of the experimental uncertainty and the mean value of the gap between CFD and experiments. These two quantities were found to be of the same order of magnitude.

The methodology that has been used on the rectangular channel to quantify the model uncertainty will be reproduced on a more complex geometry presented in the following chapters. However, the results on the rectangular channel seem to indicate that the validation process should focus on the comparison between CFD and experiments. In fact, the operating conditions during the mass transfer experiments depicted in Chapter 2 were well controlled. The resulting uncertainty on the input parameters of the simulations were low as well, with an impact on the calculations of the Nusselt number screened by the experimental uncertainties.

Chapter 4 Heat and mass transfer measurements in a steam generator mock-up

4.1 Introduction

The previous mass transfer experiments presented in Chapter 2 showed the possibility to use gypsum dissolution in order to estimate the heat transfer coefficient for an isothermal wall by using heat and mass transfer analogy. Thus, this methodology is adapted in this chapter for measurements in a steam generator water box mock-up, in an impinging jet configuration. During the experiments, roughness develops on the dissolving gypsum surface and affects the flow which in return affects the mass transfer coefficient. This phenomenon leads to an enhancement of the mass transfer which has been observed and quantified for gypsum in the case of pipes in (Wang & Ewing, 2017) and investigated in the rectangular channel. These methodologies could not be used in the experiments that will be presented in this chapter due to the difference of flow configuration which did not allow to use the same correlations. Since correlations were not available, a measurement device has been adapted from (Mourgues, et al., 2013) in order to retrieve surface average values of the heat transfer coefficient on the measurement locations in addition to the mass transfer data obtained with gypsum dissolution. The combination of both heat and mass transfer experimental data could then be used to have a more reliable transposition of the Sherwood maps yielded by the gypsum dissolution technique to Nusselt maps.

4.2 Experimental setup

4.2.1 Presentation of the mock-up

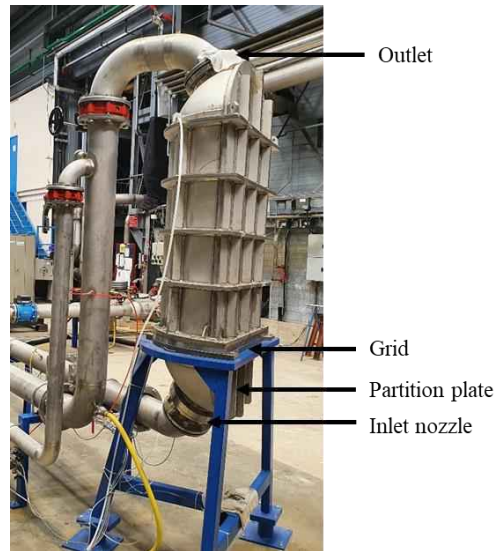


Figure 4.1: Framatome's technical center facility – Steam generator water box mock-up.

A test campaign has been launched in a **1/5 scale** mock-up of a one-half steam generator water box (SGWB). The objective is to study the behavior of **heat and mass transfer coefficient** at different locations of the test section with the evolving flowrate. A view of the mock-up can be seen on Figure 4.1. The test section corresponding to the SGWB is the bottom part of the mockup below the grid. Six measurements location are provided to make measurements of the heat and mass transfer coefficient in the test section:

- four measurements locations are available on the **partition plate**. These locations are given on Figure 4.2a. Both heat and mass transfer measurements were carried out on the four visible slots by inserting measurement devices. Only one location could be measured at a time. The heat and mass transfer between the flow and the measurement locations are driven by the **impingement of a jet** exiting the inlet nozzle visible Figure 4.2b. The approximative impingement region is given in red on Figure 4.2a.
- another measurement location is available in the **inlet nozzle** which connects the hydraulic loop to the SGWB. The part that must contain the gypsum sample can be replaced thanks to flanges depicted on Figure 4.2b at the junction between the inlet pipe and the test section.
- the last location is on the grid **or tubular sheet**. An area zone of the bottom part of the grid between the upper volume of the mock-up and the water box can be replaced by a gypsum sample used for mass transfer measurements. It is necessary to dismantle the upper part of the mock-up with the help of an electric hoist available in the facility to place the sample.

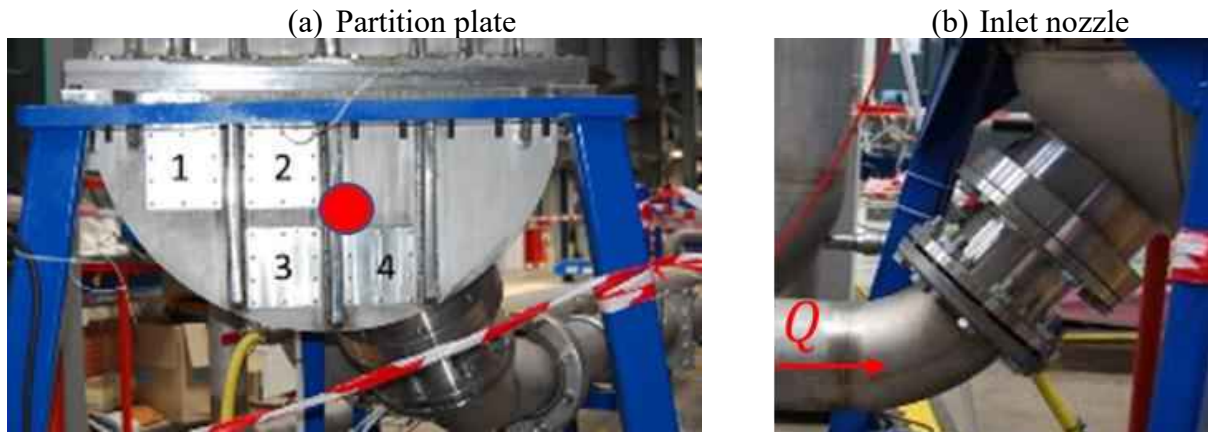


Figure 4.2: Framatome's technical center facility – Steam generator water box mock up. (a) Partition plate with the four measurements location and the approximative location of the stagnation zone in red. (b) Inlet nozzle of the mock-up, the direction of the flow is indicated with the red arrow.

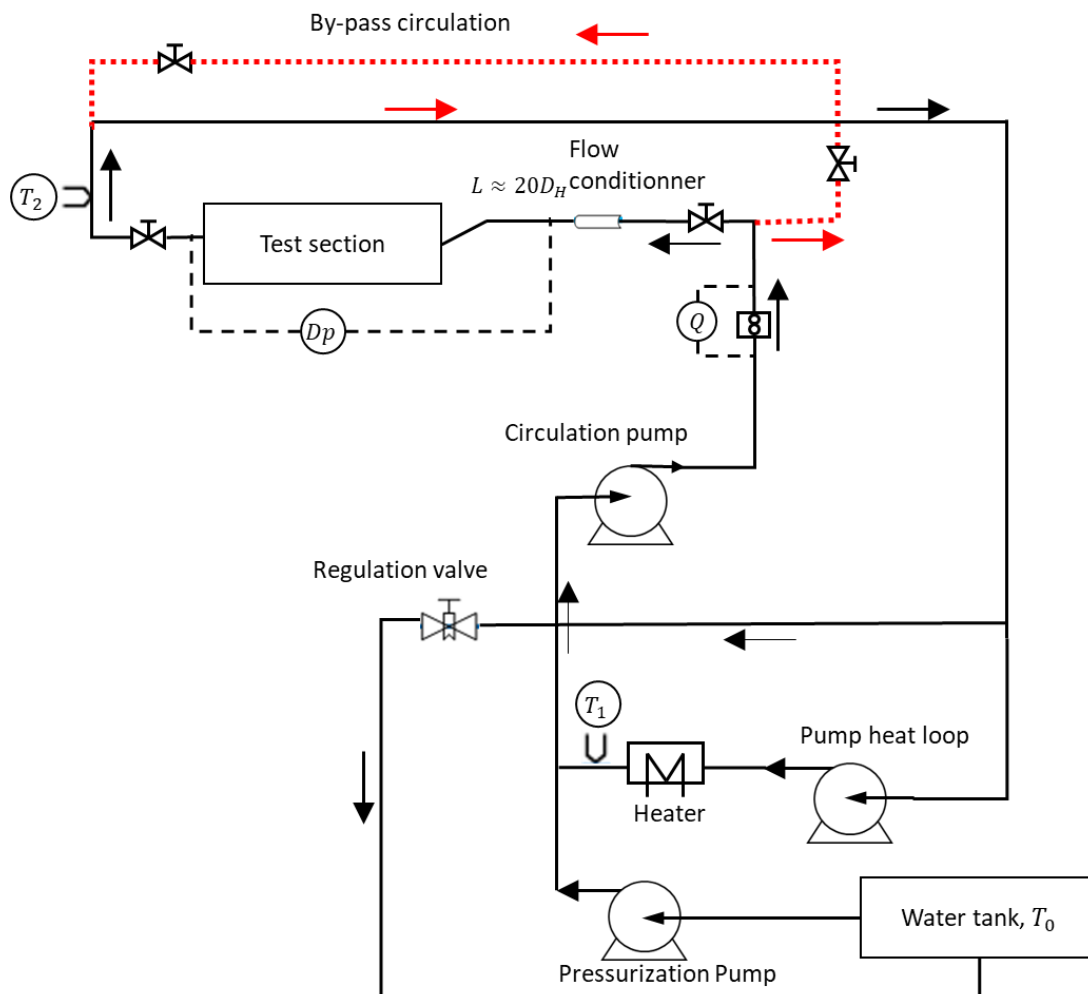


Figure 4.3: schematic view of the experimental setup

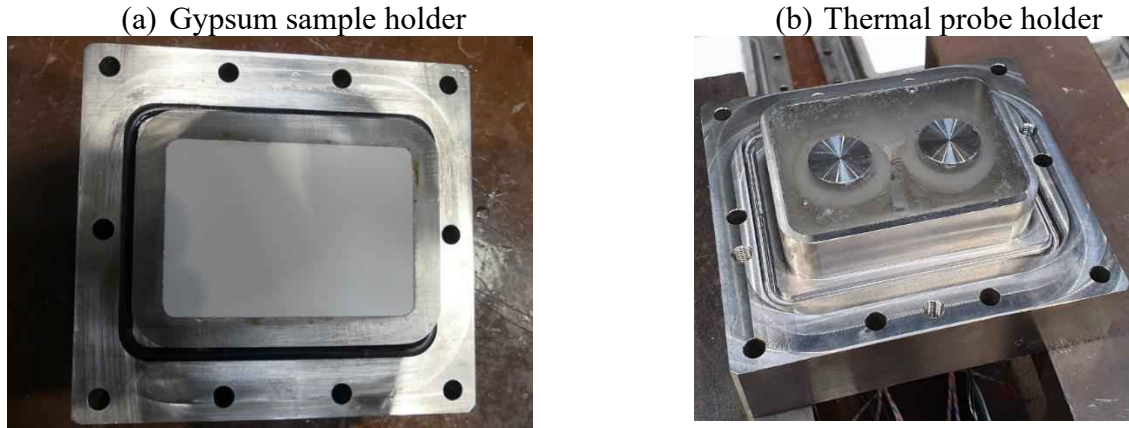


Figure 4.4: view of the measurement device for the partition plate: (a) Mass transfer measurement device (b) Heat transfer measurement device.

A schematic view of the experimental setup is given Figure 4.3, it consists of a closed loop of circulating water in which the flowrate, temperature and pressure are imposed. The water is pumped from a tank which contains 250 m^3 of water at ambient temperature. The pressurization pump is used in order to fill the loop and pressurize the circuit. The water is heated in a secondary loop. The circulation pump punctures water from the heater loop in order to reinject hot water in the test section. The first step when operating the mock-up is to by-pass the test section in order to heat the water in the loop. The water is heated progressively as the temperature of the loop reaches the set point temperature of the heater. The pump is briefly stopped, the measurement device is then placed flushed to the wall before connecting the test section to the loop. Then, the by-pass is switched which enables the filling of the test section and the static pressure is increased to $P = 5\text{ bars}$. The circulation pump is then re-started and is used with the regulation valve in order to impose the flowrate. The water passes through a rectifier which flattens the velocity profile in the inlet pipe. The water then flows through the inlet pipe which is approximately $20 D_H$ long, where D_H is the diameter of the pipe. The water then enters the SGWB section below the grid from the nozzle of the pipe and impinges the partition plate where the gypsum samples or the heat transfer measurement device are located, before going through the grid and exiting the test section in the upper volume. The inlet and outlet temperatures, the flowrate and the static pressure are measured in the loop with an acquisition frequency of 2Hz. When operating the loop with gypsum dissolution measurements, the by-pass must be switched after each experiment in order to drain the water of the test section and replace the dissolved sample. The heat transfer measurement device is connected directly to an acquisition system which retrieves data during the circulation. Thus, the measurements done for different flowrates can be recorded in-line and do not require this whole by-passing process for successive experiments. The devices used for the measurement on the partition plate are depicted on Figure 4.4.

The fabrication process of the gypsum samples is the same than in Chapter 2 at the difference that the slurry is poured directly in the metallic holder in order to have a flatter surface after

the cast when compared to 3D printed molds. Gypsum dissolution measurements yield two dimensional maps obtained by scanning the surface wear at the end of the experiment. The heat transfer measurement device is used to retrieve the surface average heat transfer coefficient on two circular surfaces visible on Figure 4.4b. The methodology used to retrieve the heat and mass transfer coefficients is described in the following section. In this dissertation, only heat and mass transfer coefficients on the partition plate data will be presented.

4.2.2 Heat and mass transfer for an impinging jet

The heat and mass transfer measurements that will be presented in this chapter are performed on a plate which is impinged by a circular jet. Impinging jets have been of particular interest in the thermal hydraulic field because of the high transfer rates involved in this configuration between the flow and walls. The heat and mass transfer between the impinging jet and the plate has been investigated in the literature and the main characteristics affecting the transfer rates are:

- the nozzle/plate non dimensional distance Z/D_H with Z the wall distance and D_H the diameter of the nozzle.
- whether the jet is confined or unconfined,
- whether the jet is submerged or a free surface jet
- the shape of the nozzle
- the angle formed by the jet axis and the plate normal
- the Reynolds and Prandtl numbers of the jet
- the presence of multiple jets in grids.

A wide literature exists on the effect of these parameters on the heat and mass transfer rates. A review for single circular jet can be found in (Jambunathan, et al., 1992), from which Figure 4.5 has been taken. This figure depicts the different zones of the jet:

- Zone 1: developing flow, initial mixing region. The surrounding fluid is entrained into the jet leading to a reduction of the speed. This zones contains a core visible with dotted lines. This core corresponds to the zone where $U_m \approx U_n$, with U_m and U_n being respectively the velocity at the centerline and at the nozzle exit. This region gets smaller as the distance from the nozzle exit increases until $Z \sim 6 D_H$ where it disappears
- Zone 2: established jet. In this region, the axial velocity decreases and it has been shown that the decrease of the velocity is proportional to the distance from the end of the core.
- Zone 3: deflection zone. In this region the decrease of the axial velocity is much higher, leading to the rise of the static pressure. This zone has been found to be approximatively $2D_H$ large
- Zone 4: wall jet. The flow in this region shows an important rise of the transversal velocity followed by a decrease at greater distances. In this region, the heat transfer is higher than for parallel flow because of the higher generation of turbulence by the shear between the wall jet and the flow

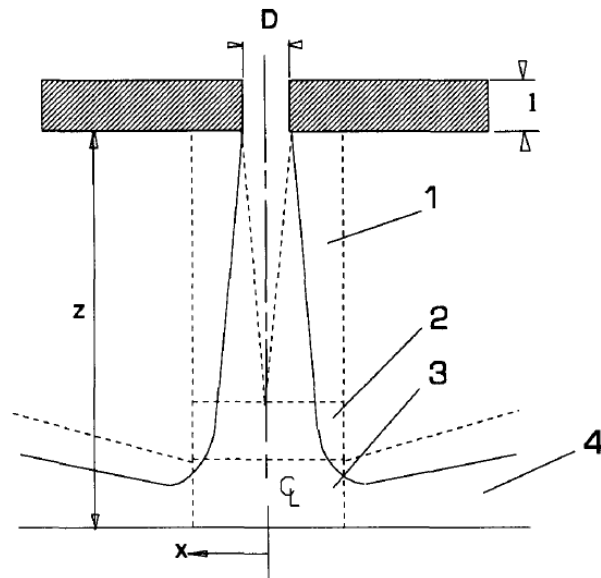


Figure 4.5: flow zones in an impinging jet – zone 1, initial mixing zone ; zone 2, established jet ; zone 3, deflection zone ; zone 4, wall jet. From (Jambunathan, et al., 1992)

The heat and mass transfer in the steam generator mock-up corresponds to an oblique circular jet, confined and submerged with a nozzle-to-plate distance $Z/D_H = 2$. For this nozzle to plate spacing, zone 2 disappears as the impingement occurs before the establishment of the jet. The impact of this parameter is important on the heat and mass transfer coefficient as it can be seen on Figure 4.6 from (Jambunathan, et al., 1992):

- A local minimum is present at the stagnation point. In this region, it has been shown for analytical solution of laminar flow that the Nusselt number is proportional to $U_m^{0.5}$. Moreover, the heat transfer in this zone is maximized for high turbulent intensities.
- Peaks at $X/D_H \approx 0.5$ and $X/D_H \approx 2$. The first peak is due to the increase of the transversal velocity in the deflection zone. The second is due to the presence of vortices that forms in the shear regions.

A more recent review can be found in (Zuckerman & Lior, 2006) which analyzes more precisely the physical mechanism involved in jet impingement to understand the different behavior of the heat transfer in the different region of the plate.

Furthermore, the topology is subject to variations, and important difference are expected for the steam generator mock-up which cumulates distinctive characteristics. First of all, the jet axis is oblique, the inclination of the impinging jet has been found to affect the symmetry of the radial distribution (Ma, et al., 1997) as it can be seen on the radial distribution of the Nusselt number on Figure 4.7. Moreover, the position of the maximum heat transfer has been found to vary with the jet inclination. In addition, the pipe upstream of the nozzle is bent as depicted in Figure 4.2b and a length $l \approx 2D_H$ is left for water before exiting the nozzle and impinging the partition plate. The enhancement of the heat transfer coefficient by modifying the geometry of

the nozzle has been studied in literature in the frame of passive control which aims to modify the jet structure without energy inputs.

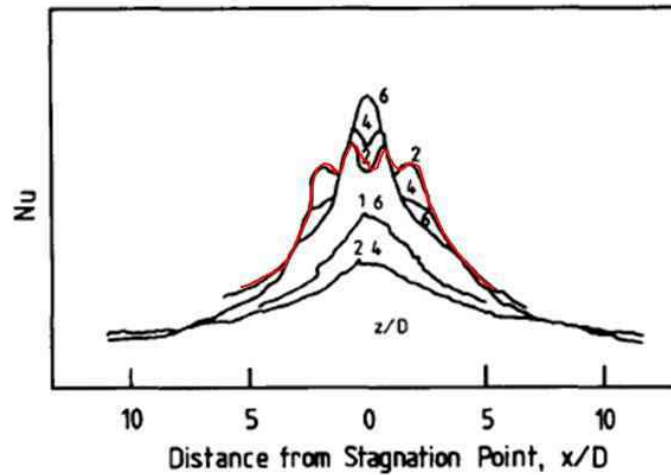


Figure 4.6: effect of the nozzle/plate non dimensional distance on the radial variation of the heat transfer coefficient centered around the stagnation point. In red, the case $Z/D_H = 2$ corresponding to the mock-up situation is highlighted. From (Jambunathan, et al., 1992)

Elements can be found for instance in (Brouillot, 2016) for the study of heat transfer with lobed jet. At the exit of the nozzle of the steam generator water box mock-up, the velocity and turbulent profiles are significantly affected by the bend. The effect of bent pipe on the velocity and turbulent intensity profile can be found in different sources (Sudo, et al., 1998; Sakakibara & Machida, 2012; Kalpakli & Örlü, 2013). The curvature affects the velocity distribution, the flow in the center of the pipe is displaced outwards due to centrifugal forces, while the flow on borders of the pipe travel inward. These displacements induce the appearance of two counter rotating vortices which behavior has been studied and observed to be unsteady for turbulent flows. A view of the velocity field on a section downstream the bend can be seen on Figure 4.8, which is obtained with Particle Image Velocimetry (PIV) in (Kalpakli & Örlü, 2013). In the mock-up, the distance between the bent section and the nozzle exit is not long enough for the velocity profile to regain its symmetry and will thus affect the jet structure and the resulting heat transfer on the partition plate.

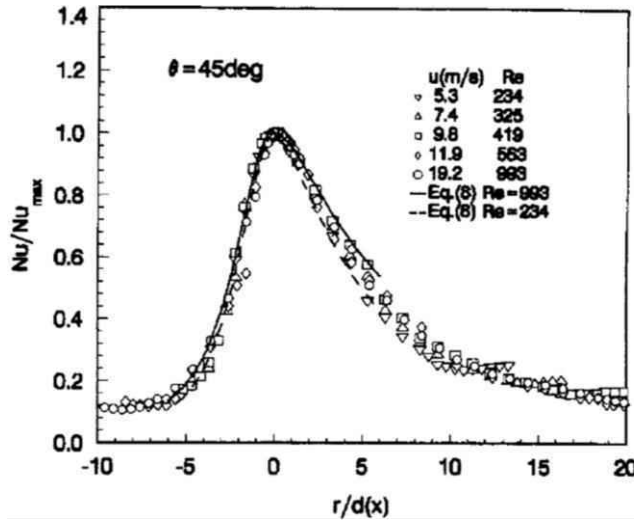


Figure 4.7: radial distribution of the Nusselt number on a plate for an oblique circular jet impinging with an incidence angle $\theta = 45^\circ$. From (Ma, et al., 1997)

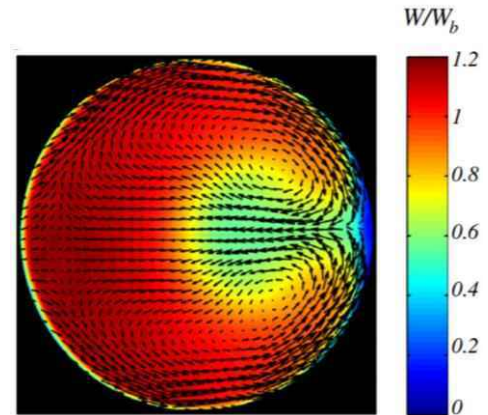


Figure 4.8: transversal velocity vector field downstream a 90° bend pipe and amplitude of the velocity indicated with a heat map. W_b is the bulk speed. From (Kalpakli & Örlü, 2013)

Also, the jet is confined and submerged with important recirculation in the hemispheric volume. Water passes through a grid downstream the bulk which also adds to the complexity of the flow.

Different correlations for heat transfer in the stagnation zone reviewed in (Jambunathan, et al., 1992) are given in Table 4.1. It can be noticed that Hoogendoorn (Hoogendoorn, 1977) introduces the turbulence intensity number Tu in the correlation of the Nusselt number at the stagnation point. Furthermore, correlations are given in (Li & Garimella, 2001) for the effect of the Prandtl number in the range $[0.7, 25.2]$ on the heat transfer for a confined submerged jet. The correlation here introduces the effective heat source to orifice diameter ratio $\frac{D_e}{D}$.

Table 4.1 : correlation from literature.

Source	Correlation
Popiel and Boguslawski (1988) (Jambunathan, et al., 1992)	$1.2 \leq \frac{Z}{D} \leq 5$ and $4\,000 < Re < 63\,000$ $Sh_s = \left(0.508 + 0.051 \frac{Z}{D}\right) Re^{0.5} Sc^{0.4}$
Hoogendoorn (1977) (Jambunathan, et al., 1992)	$1 \leq \frac{Z}{D} \leq 10$ and $Re = 66\,000$ $\frac{Nu_s}{Re^{0.5}} = 0.65 + 2.03 \left(\frac{Tu Re^{0.5}}{100}\right) - 2.46 \left(\frac{Tu Re^{0.5}}{100}\right)^2$
Li and Garimella (Li & Garimella, 2001)	$7.1 < Pr < 25.2$, $1 < \frac{Z}{D} < 5$, $4\,000 < Re < 23\,000$ $Nu_s = 1.409 Re^{0.497} Pr^{0.444} \left(\frac{l}{D}\right)^{-0.058} \left(\frac{D_e}{D}\right)^{-0.272}$

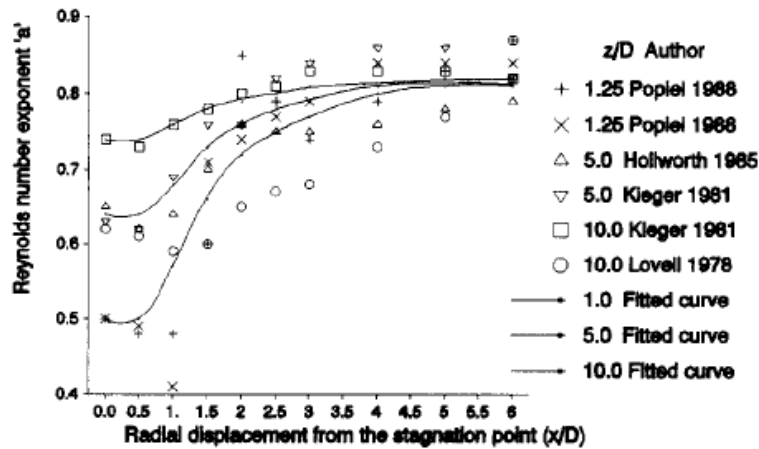


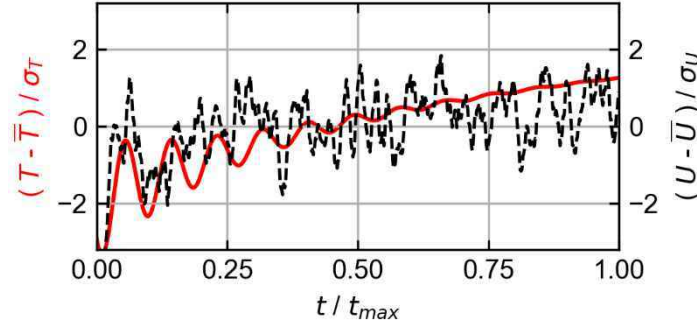
Figure 4.9: evolution of the exponent a with the radial displacement from the stagnation point for the empirical law $Nu \propto Re^a$. From (Jambunathan, et al., 1992).

By combining various experimental data in (Jambunathan, et al., 1992) it is suggested that $Nu \propto Re^a$ with a depending on the distance from the stagnation point as depicted on Figure 4.9. Near the stagnation zone, the exponent is smaller than in the wall jet region as the flow tends to be laminar. This tendency decreases with increasing Z/D . Far from the stagnation region, the differences due to Z/D reduce significantly.

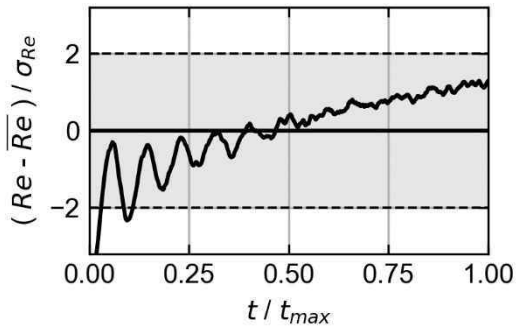
4.2.3 Data reduction

4.2.3.1 Time averaging process

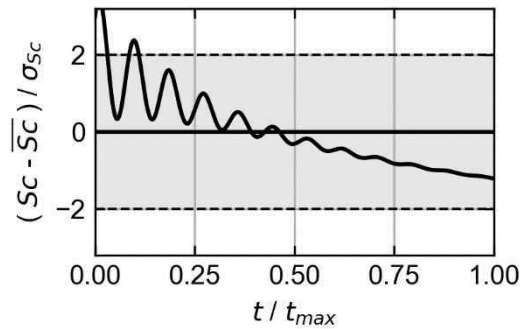
The objective of the measurements on the steam generator mock-up is to study the evolution of the heat and mass transfer rates according to the flowrate. The non-dimensional quantities that are related to heat transfer are the Nusselt number and the Prandtl number. For mass transfer, the equivalent quantities are the Sherwood number and the Schmidt number. The turbulence regime is given by the Reynolds number Re . Their definition is given in §1.1.2. The characteristic length used in the expression of the Nusselt, Sherwood and Reynolds number is the diameter of the inlet nozzle. The characteristic velocity of the Reynolds number is U the mean velocity in the inlet pipe calculated from the flowrate and the section of the pipe, assuming a uniform velocity profile. The temperature $T(t)$ during the experiment is calculated by averaging the inlet and outlet temperatures obtained with thermocouples upstream and downstream the test section. The difference of temperature between these two locations is negligible in front of the temporal variation of the temperature during the experiments. Thus, this temperature has been assumed representative of the test section temperature. The physical properties are calculated over time from the temperature evolution and are averaged over time with operator $\langle \cdot \rangle_t$. in the same way as in Chapter 2.

(a) Evolution of temperature fluctuations $(T - \bar{T}) / \sigma_T$ and velocity fluctuation $(U - \bar{U}) / \sigma_U$ 

(b) Evolution of the Reynolds number fluctuations.



(c) Evolution of the Schmidt number fluctuations.

Figure 4.10: evolution of the boundary conditions during dissolution for an experiment at $\bar{Re} = 7.5 \cdot 10^5$ and $\bar{Sc} = 1.2 \cdot 10^3$

An example of the evolution of the Reynolds number and Schmidt number during the gypsum dissolution is given on Figure 4.10 for an experiment at $\bar{Re} = 7.5 \cdot 10^5$ and $\bar{Sc} = 1.2 \cdot 10^3$. It is visible on Figure 4.10a that after the beginning of the dissolution, the surface average velocity calculated from the flowrate stabilizes quickly and presents random fluctuations. In contrast, during all the experiment, the temperature evolves with a clear predictable behavior. The behavior of the Reynolds and Schmidt numbers during the experiments are the same than for the temperature, as it can be observed on Figure 4.10b and Figure 4.10c. The approximated standard deviations σ_{Re} and σ_{Sc} in this case are found to be around 3% of the given value of \bar{Re} and \bar{Sc} corresponding to the temperature variations. In this work, the behavior of the boundary conditions during the dissolution due to the temperature establishment is assumed to be of small significance on the integral value of the Sherwood number that is measured. The impact is assumed to be within the experimental uncertainty range. The trend is thus not corrected and kept for the calculation of the boundary conditions uncertainty. 2σ confidence intervals are shown for comparison with the sample on Figure 4.10a and Figure 4.10b. The signal is most of the time within this interval except at the beginning of the experiment where the fluctuations are the biggest.

4.2.3.2 Mass transfer measurement

The mass transfer coefficient K_C at the sample location is calculated as following for a gypsum lining dissolving in water:

$$K_C = \frac{\rho_{gypsum}}{c_w - c_0} \frac{dh(x, y)}{dt}$$

where ρ_{gypsum} is the density of gypsum, c_w is the solubility of gypsum in water, c_0 is the concentration of the gypsum in the bulk which can be approximated to be zero during the experiment and dh/dt is the height variation rate while dissolving. This quantity evolves in time as the surface roughness develops and enhances the mass transfer. The mass transfer coefficient obtained with gypsum dissolution is an integral value which includes a period where the wall can be considered smooth and another where the roughness affects the transfer.

The correction due to the variations of dh/dt with the roughness evolution will be estimated from the heat transfer coefficient measurements. The raw wear Δh_r is obtained from a laser scan of the sample topography before and after experiment with a resolution of $50 \mu m \times 50 \mu m$.

$$\Delta h_r = h_{after} - h_{before}$$

Then a Gaussian filter of order 0 with $\sigma_{filter} = 1mm$ is applied in order to separate the small spatial fluctuations from the slope/waviness of the surface. The parameters of the filtering have been set in an empirical way by trials. The filtered wear matrix Δh_f is retrieved from the filtering and the roughness matrix e is yielded from $e = \Delta h_r - \Delta h_f$. This matrix is used to obtain all the data related to roughness. The different matrices are depicted on Figure 4.11 for a sample that was obtained from location 2. The local Sherwood number is then calculated as following:

$$\overline{Sh}(x, y) = \left\langle \frac{K_C D_H}{D_m} \right\rangle_t = \rho_{gypsum} D_H \left\langle \frac{1}{c_w D_m} \right\rangle_t \frac{\Delta h_f(x, y)}{t_{exp}}$$

The density ρ_{gypsum} is measured for the different samples, c_w is evaluated from the measured temperature using data from (Klimchouk, 1996), t_{exp} is the dissolution duration and D_m is evaluated at the measured temperature with Stokes-Einstein equation and the diffusion coefficient value at 25°C (Wang & Ewing, 2016) (Simpson & Carr, 1958) as it has been done in Chapter 2. Furthermore, the roughness matrix surface is resampled with $1 cm \times 1 cm$ windows on which the following quantities are determined:

- the RMS roughness e_{RMS} calculated as the root mean square of the surface's peaks and valleys.
- The peak valley roughness e_{pv} which is defined as the mean of the five maximums peak to valley height.
- the ratio between the peak valley roughness and the spacing between the roughness elements $\frac{e_{pv}}{l_{str}}$

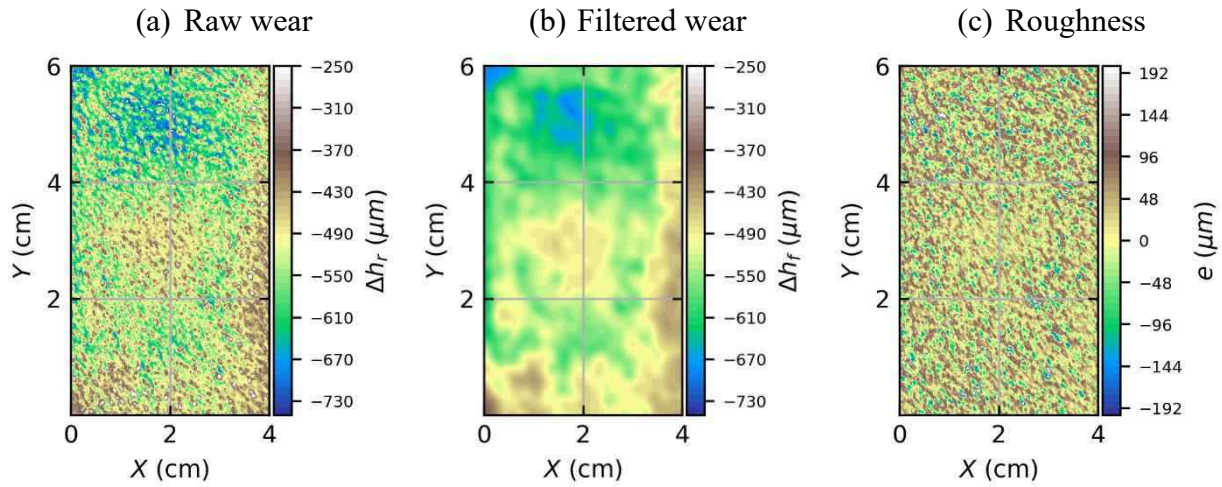
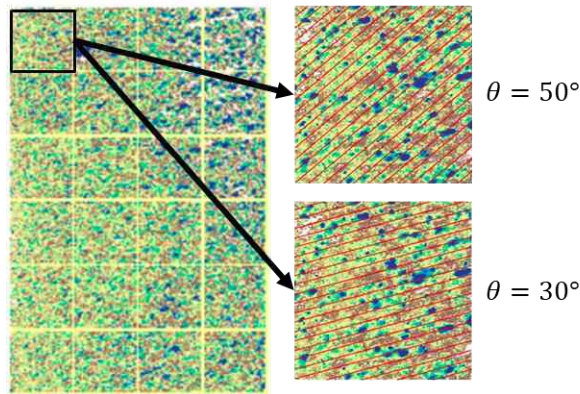
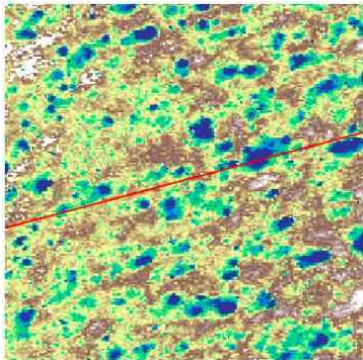


Figure 4.11: example of the treatment of surface data obtained for an experiment on location 2: (a) raw wear Δh_r (b) filtered wear Δh_f and (c) roughness matrix e

(a) Division of the original matrix and extraction of profiles in multiple directions.



(b) Extraction of one line at $\theta = 30^\circ$



(c) Extraction of e_{pv} and l_{str}

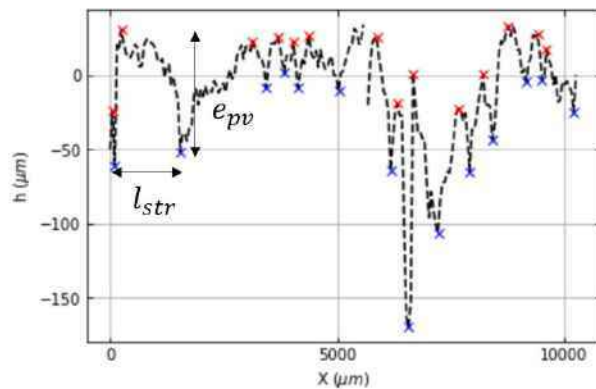


Figure 4.12: steps for the extraction of e_{pv} and l_{str} for $Re \approx 10^6$ and $Sc \approx 6 \cdot 10^2$ (a) division of the original surface in windows of $1 \text{ cm} \times 1 \text{ cm}$ and extraction of profiles for a given range of angles. (b) Example of profile inclined of $\theta \approx 30^\circ$ from the horizontal line and (c) associated height from which e_{pv} and l_{str} are extracted.

The peak to valley roughness e_{pv} and the spacing between roughness elements l_{str} have been calculated by extracting profiles of the roughness matrix in the flow direction. This direction is estimated with the algorithm described in Appendix B. The process applied for the extraction of e_{pv} and l_{str} depicted on Figure 4.12 for an experiment at $Re = 10^6$ and $Sc = 6 \cdot 10^2$ is as following:

- The average and standard deviation of the angle detected is used in order to generate a list of angles to test.
- For each angle, profiles are extracted from the roughness surface.
- All the peaks and valleys are extracted which allow to calculate an average distance between the roughness elements and an average peak to valley height.

The subdivision of the original matrix is given on Figure 4.12a, and the profiles extracted following two different angles are shown in red. The spacing between the profiles has been increased in order to enhance the clarity of the figure but, the successive profiles are stuck together. An example of extraction of peaks and valleys is given Figure 4.12c for a specific profile given on Figure 4.12b. The extracted peak to valley height is averaged over the profiles of the window and averaged for the given angle range.

4.2.3.3 Heat transfer measurement

Two surface average values of the heat transfer coefficient are measured with the device depicted on Figure 4.13. The measurement zones are two discs on top of the device. The heat transfer coefficient on these two surfaces is calculated by estimating the heat flux at the solid/liquid interface and from the estimation of the wall temperature. The heat flux and the wall temperature are estimated with a modified version of the device used in (Mourgues, et al., 2013) for critical heat flux measurements. These two quantities are estimated from measurements with thermocouples depicted with red dot in the steel cylinder body. Two heated cartridges are inserted at the bottom of each probe, leading to the heating of the whole body. The heat is then evacuated from the top of the device where the flow exchanges with the heated surface. An insulating resin is poured between the metallic carrier and the two cylindrical probes in order to limit the lateral heat loss and insure a linear temperature gradient profile in the probe and a heat flux in the probe nearly equal to the heat flux in the vicinity of the wall in the fluid region. The temperature profile in each probe is estimated from 4 temperature measurements.

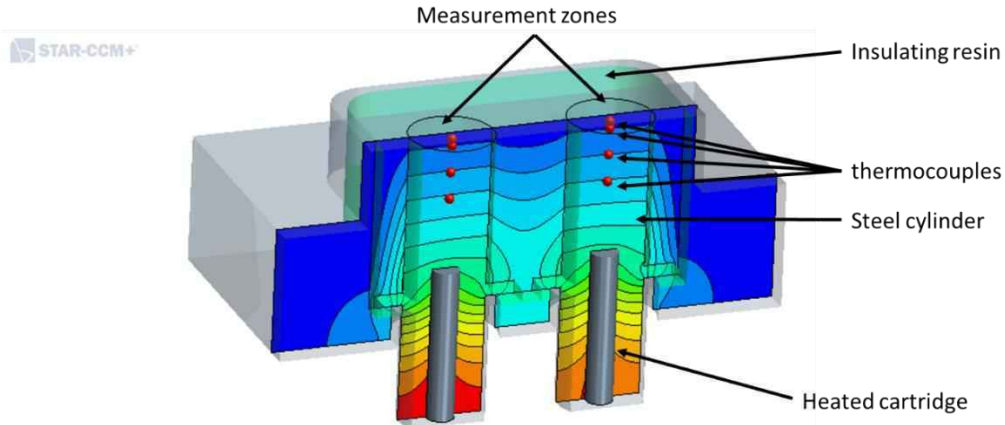


Figure 4.13: view of the measurement device with a computer aided design software. The iso-contours of temperature are given on a section of the model.

The top thermocouple has been placed close to the surface in order to have a better estimation of the wall temperature. The heat flux ϕ and wall temperature T_{wall} are estimated from Fourier law of conduction heat transfer. The heat flux is estimated from the thermal conductivity of the probe and the slope of the temperature profile which is found by minimizing the square error between the data and the regression law of the linear evolution of temperature with the position of the thermocouples:

$$\phi_{probe} = -\lambda \frac{dT}{dx}$$

The wall temperature is then estimated with:

$$T_{wall} = T_4 - \phi_{probe}(X_4 - X_{wall})$$

where, X_4 , T_4 are respectively the position and temperature of the thermocouple near the wall, and X_{wall} the abscissa of the wall boundary.

This leads to the calculation of the heat transfer coefficient with:

$$h_{conv,measured} = \frac{\phi_{probe}}{T_{wall} - T_{ref}}$$

where, the temperature measured at the inlet of the test section was chosen for T_{ref} .

The Nusselt number on the upper and lower side of the measurement device by considering the inlet nozzle diameter as the characteristic length, and the film temperature $0.5 \cdot (T_{ref} + T_{wall})$ for the evaluation of the thermal conductivity of water λ_{water} in.

$$Nu = \frac{h_{conv,measured} D_H}{\lambda_{water}}$$

The dimensions and materials of the measurement device were chosen after numerical simulations. These simulations were done to estimate the lateral heat loss in the cylinder probes and thus estimate the bias on $h_{conv,measured}$ which has been taken into account in the performed measurements. The power of the heated cartridges is controlled electronically in

order to have a fixed wall temperature condition during the experiment. The flowrate and temperature in the test section were stabilized for the measurements.

4.3 Heat and mass transfer measurements on the partition plate

4.3.1 Mass transfer measurements

4.3.1.1 Introduction

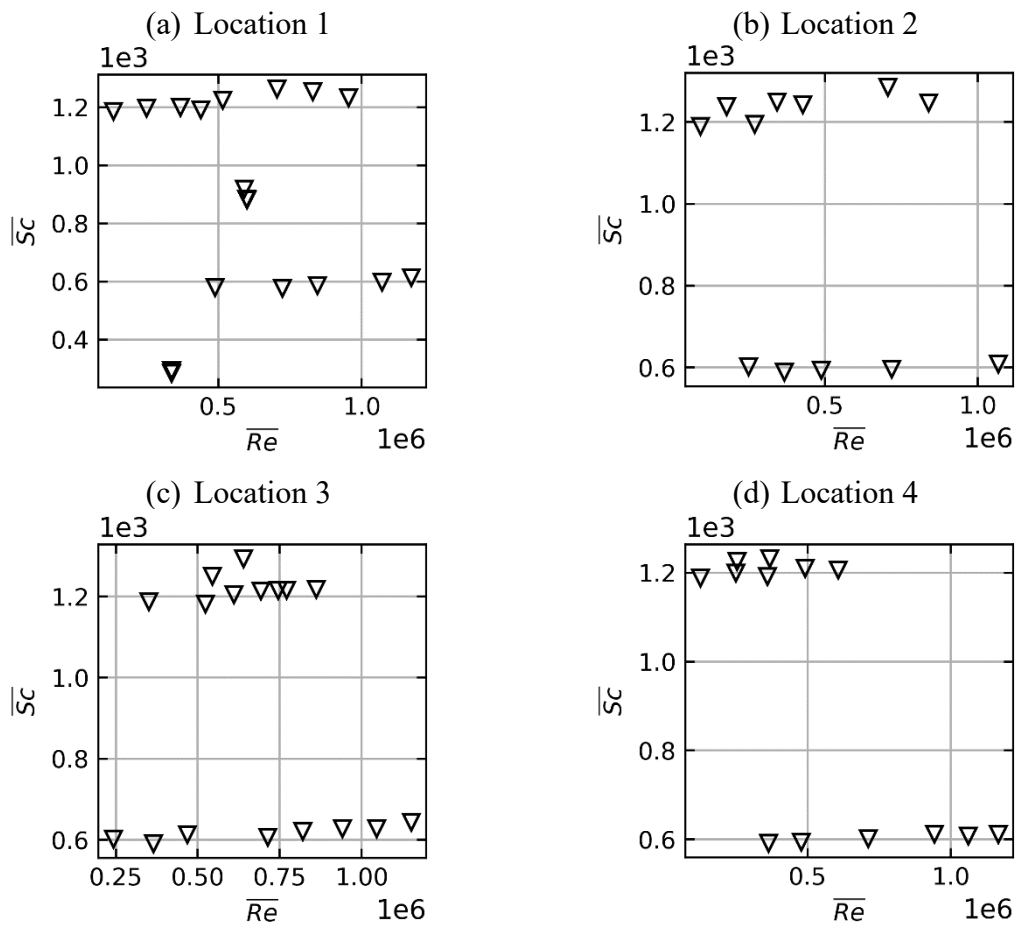


Figure 4.14: Reynolds and Schmidt numbers covered for the experiments on the partition plate on (a) location 1, (b) 2, (c) 3 and (d) 4. The given value corresponds to the average value during the dissolution.

The time average Reynolds number and Schmidt number during the gypsum dissolution is given for all the experiments carried out on the partition plate on Figure 4.14. The experiments that have been performed were done at $Sc \approx 1\,200$ and $Sc \approx 600$.

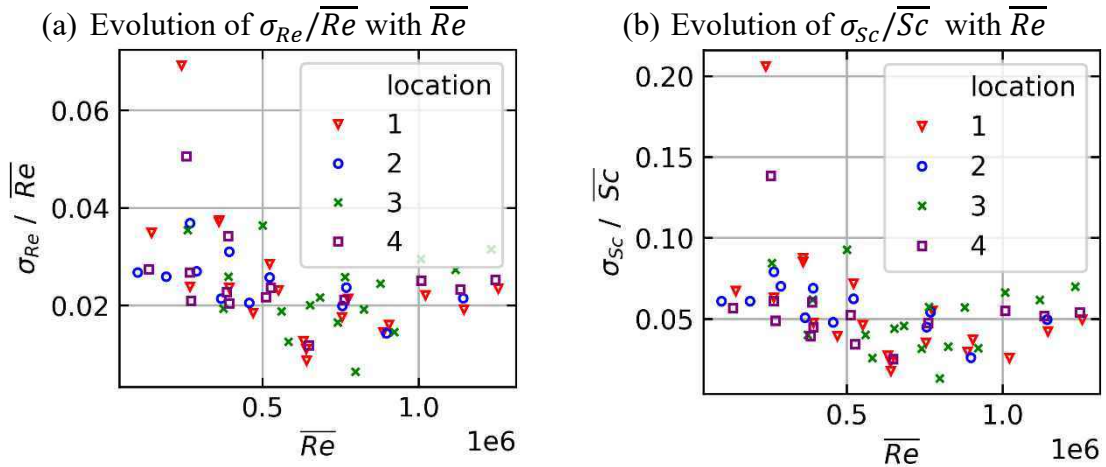


Figure 4.15: evolution of the standard deviations of the operating conditions during the dissolution for all experiments (a) Reynolds number, (b) Schmidt number.

The different measurement locations are indicated on Figure 4.2a. On location 1, additional Schmidt numbers were investigated for $Re \approx 5 \cdot 10^5$.

The operating conditions of the experiment have been averaged over time with the methodology depicted in §4.2.2. The standard deviation of the Schmidt number and Reynolds number σ_{Re} , σ_{Sc} are given for all the experiments on all location on Figure 4.15. The standard deviation of the Reynolds number during dissolution remains low and in most of the case below 3% of \overline{Re} value. For the Schmidt number, the standard deviation is slightly higher and stabilizes around 5-6% of \overline{Sc} .

4.3.1.2 Evolution of the surface average value of the Sherwood number

The evolution of the surface average Sherwood number \overline{Sh}_{mean} is given as a function of the Reynolds number for the different locations on Figure 4.16. The experiments with the highest Schmidt number yielded the higher surface average Sherwood numbers. The Sherwood number has been divided by $\overline{Sc}^{0.44}$ following the correlations obtained in (Li & Garimella, 2001) for impingement at different Prandtl number fluids. This power coefficient might not be adapted as it has been obtained near the stagnation zone of the impinged plate. In comparison, the Sherwood has been measured far from the stagnation zone which might imply a lower coefficient on the power law.

The evolution of this *normalized* Sherwood number for the different locations is given on Figure 4.17. The Sherwood number evolution with the Reynolds number is similar for all locations for low Reynolds. An increased variability appears for higher Reynolds numbers between the locations. Location 1 shows the lowest transfer rates which is coherent with the fact that its radial distance from the stagnation point is estimated to be the largest ($\approx 2.2 D_H$, $1.3 D_H$ for location 2 and 3; or $0.4 D_H$ for location 4).

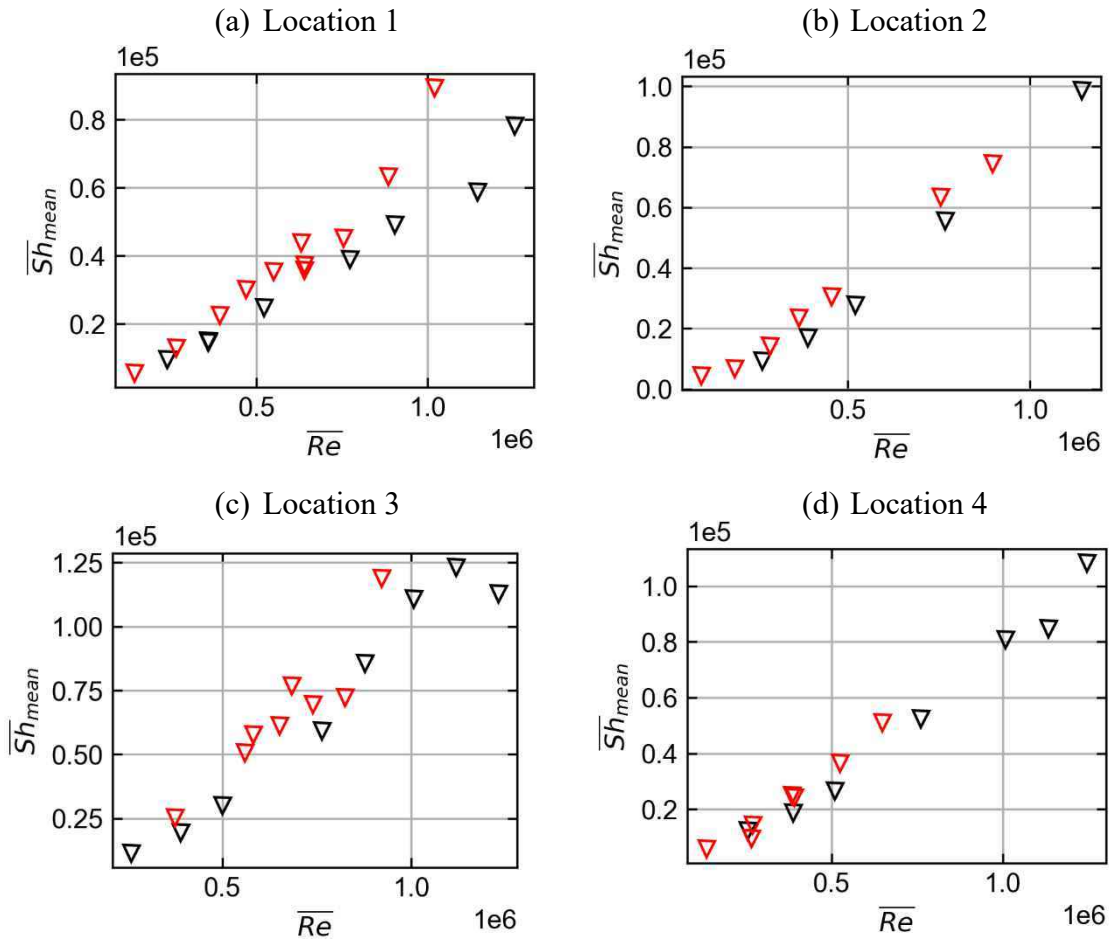


Figure 4.16: evolution of the surface average Sherwood number as a function of the Reynolds number on (a) location 1, (b) 2, (c) 3 and (d) 4. The different colors data obtained at $\overline{Sc} = 6 \cdot 10^2$ (black) and $\overline{Sc} = 1.2 \cdot 10^3$ (red),

The differences between locations 2, 3 and 4 are within the experimental uncertainty which has been found to be in the range 5%, 10% of the given Sherwood number value.

Correlations are given for the surface average Sherwood number at the different locations:

$$\begin{aligned}\overline{Sh}_{mean,1} &= 9.79 \cdot 10^{-5} \overline{Re}^{-1.268} \overline{Sc}^{-0.44} \\ \overline{Sh}_{mean,2} &= 8.33 \cdot 10^{-6} \overline{Re}^{-1.464} \overline{Sc}^{-0.44} \\ \overline{Sh}_{mean,3} &= 1.94 \cdot 10^{-6} \overline{Re}^{-1.587} \overline{Sc}^{-0.44} \\ \overline{Sh}_{mean,4} &= 6.31 \cdot 10^{-6} \overline{Re}^{-1.486} \overline{Sc}^{-0.44}\end{aligned}$$

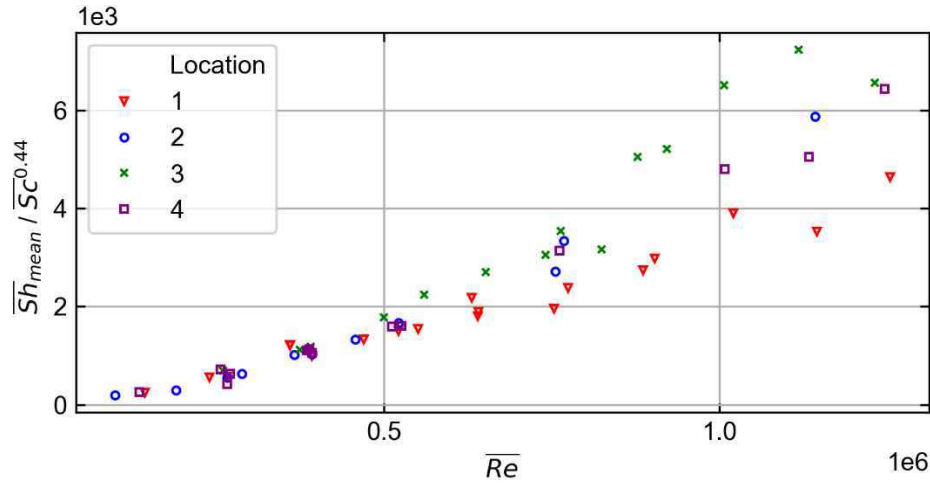


Figure 4.17: evolution of $\overline{Sh}_{mean} / \overline{Sc}^{0.44}$ as a function of the Reynolds number at the different locations

4.3.1.3 Local evolution of the Sherwood number

The surface distribution of the Sherwood number has been found to fluctuate from an experiment to another. However, these fluctuations are small and a general idea of the Sherwood distribution over the gypsum surface at each location is given on Figure 4.18. The view is given from the backside of the partition plate for experiments at $Re \approx 4 \cdot 10^5$. The stagnation point is not measured; it is estimated to be slightly above location 4 which is the nearest sample. This sample presented the most variability from an experiment to another and the largest surface gradients. It is noticeable on location 1, 2 and 3 that a high value of the Sherwood number occurs from the leading edge. This leading edge is hypothetic as the flow is not observed directly during the experiments. Nevertheless, the flow direction is estimated for the different locations from their location relatively to the estimated impingement location, and from the velocity direction measured with the algorithm depicted in Appendix B. The estimated direction of the flow is indicated on Figure 4.18e. The gradients follow the flow direction for these locations and the decrease of Sherwood number is certainly due to the deceleration of the fluid flow. For location 4, a different behavior is observed, as the Sherwood number is lower on the upper side of the sample which is closer to the stagnation region. This behavior is most certainly due to the presence of a local minimum of the Sherwood number near the stagnation region due to lower velocities as it is expected for this configuration (see Figure 4.6).

The proper orthogonal decomposition has been applied to the Sherwood number obtained at the four measured locations in order to study the spatial fluctuations of the Sherwood distribution with the Reynolds and Schmidt number evolution. The module **modred** (Belson, et al., 2014) is used to perform the POD of the full set of the experiments conducted at each specific location with the **Snapshot methodology** described in §1.2.4.1.

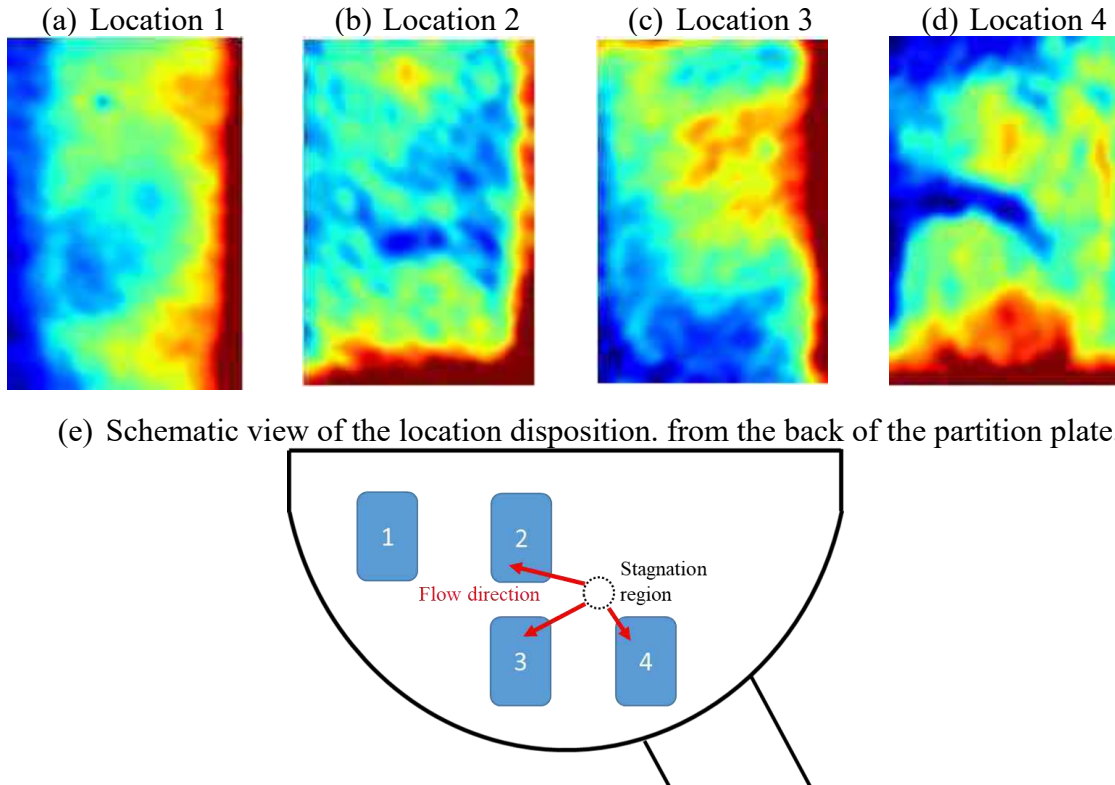


Figure 4.18: evolution of the local Sherwood number over the gypsum sample for all locations at $Re \approx 4 \cdot 10^5$, $Sc \approx 1200$. The local value of the Sherwood number is indicated with a heat map (low Sherwood in blue and large values in red). The view is from the back of the partition plate which is given in a schematic way in (e). The estimated flow direction and stagnation region are indicated respectively with red arrows and dotted line circle.

POD is used to express the Sherwood number $\overline{Sh}(\overline{Re}, \overline{Sc}, x, y)$ as following:

$$\overline{Sh}(\overline{Re}, \overline{Sc}, x, y) = \sum_{k=1}^{N_{SNAP}} a_k(\overline{Re}, \overline{Sc}) \phi_k(x, y)$$

where, ϕ_k are the modes of the POD calculated from the snapshots of the Sherwood distribution obtained with the gypsum dissolution for each couple Re, Sc of the experiments. a_k are the components of the POD which are assumed to depend on the Reynolds number and the Schmidt number. This approach is used in general for snapshots of time evolving velocity field, which results in time evolving components $a_k(t)$. In this present application, the Sherwood number is discretized spatially.

A snapshot matrix $\overline{Sh}(\overline{Re}, \overline{Sc}, x, y)$ obtained from an experiment at operating conditions Re_j, Pr_j is “flattened” into a vector $\overline{Sh}_j = (Sh_j^1, \dots, Sh_j^N)$ where N is the number of local points x_i, y_i . The inverse operation can also be done in order to reshape the vector into a matrix. N_{SNAP} snapshots of the Sherwood number fields are used for the calculation of the modes and components of the POD.

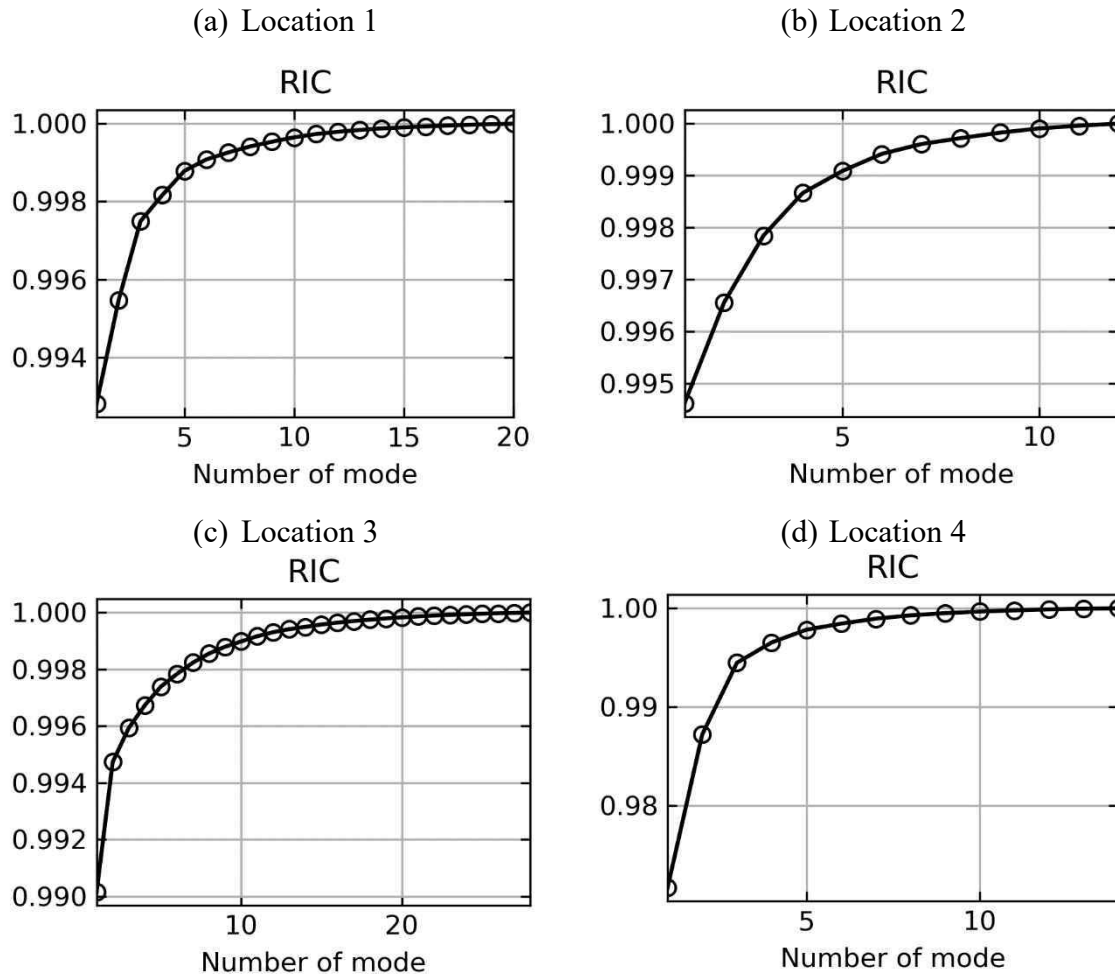


Figure 4.19: relative information content (RIC) of the modes calculated from the POD for all the locations.

In this case, the Sherwood number has been divided by its surface average value in order to construct the snapshot matrix A indicated in §1.2.4.1. This division has been done to “normalize” the importance of all the snapshots which was initially inhomogeneous on the Reynolds range due to higher amplitudes of the transfer at high Reynolds.

The modes ϕ_k and components a_k of the snapshots are calculated with modred. As indicated in §1.2.4.1, the POD base is obtained by solving an eigenvalue problem. The relative importance of each mode can be estimated from the eigenvalues associated to each mode.

The relative information content (RIC) of each mode has been calculated and is shown on Figure 4.19. The first mode corresponding in this case approximatively to the mean value over the experiment has been found to contain most of the information ($RIC(1) > 0.99$ for location 1, 2 and 3, while 2 modes are required on location 4 in order to get the same amount of information. For all the locations, no influence of the Schmidt number has been observed on the components other than the scaling of the amplitude of the Sherwood due to the difference of diffusion properties.

Thus, it is assumed that the POD can be written:

$$\overline{Sh}(\overline{Re}, \overline{Sc}, x, y) = \overline{Sc}^{0.44} \left(\sum_{k=1}^{N_{SNAP}} a_k(\overline{Re}) \phi_k(x, y) \right)$$

The scaling by $Sc^{0.44}$ has been chosen in order to be consistent with the choice done earlier in the correlation given in §4.3.1.2, in comparison to literature's data near the stagnation zone of an impinging jet.

The truncation of the POD of the Sherwood number distribution to the N_{POD} is written:

$$\overline{Sh}(\overline{Re}, \overline{Sc}, x, y) = \overline{Sc}^{0.44} \left(\sum_{k=1}^{N_{POD}} a_k(\overline{Re}) \phi_k(x, y) \right) + \epsilon_{N_{POD}} = \overline{Sh}_{N_{POD}}(\overline{Re}, \overline{Sc}, x, y) + \epsilon_{N_{POD}}$$

where, N_{POD} is the truncation order, $\overline{Sh}_{N_{POD}}$ is the truncated POD of the Sherwood number and $\epsilon_{N_{POD}}$ is the truncation error between the original snapshot and the reconstruction from N_{POD} modes.

The results on location 1 are depicted Figure 4.20. The surface distribution of the first mode ϕ_1 gives the general shape of the local Sherwood and is coherent with the observed data. The increase of the coefficients a_1 associated to this mode is correlated to the Reynolds number increase between the different experiments. The second mode appearance results in an increase of the surface gradients of the Sherwood distribution. The expression of this mode increases the value of the mass transfer coefficient at the leading edge of the gypsum wall on the right of the sample. Its appearance seems to be more significant for large Reynolds numbers. However, this mode seems to be of importance only for few experiments where no distinctive characteristics were observed (no correlation to roughness, wear, or Schmidt number during experiment). It has been assumed that the appearance of this mode is related to border effects which appear under conditions that were not identified. The third mode ϕ_3 impacts the value of the Sherwood number on the upper part of the sample where the amplitude is reduced. Variation of a_3 are observed for experiment at Reynolds number above $5 \cdot 10^5$. The lower Reynolds numbers show approximatively constant values of a_3 .

The root-mean-square-error (RMSE) and the mean absolute error (MAE) have been calculated between the original snapshots $\overline{Sh}_j = (\overline{Sh}_j^1, \dots, \overline{Sh}_j^N)$ and their truncated POD $\overline{Sh}_{N_{POD},j} = (\overline{Sh}_{N_{POD},j}^1, \dots, \overline{Sh}_{N_{POD},j}^N)$ with N_{POD} modes as following:

$$RMSE(Re_j, Sc_j) = \sqrt{\frac{1}{N-1} \sum_{n=1}^N \left(\frac{\overline{Sh}_{N_{POD},j}^n - \overline{Sh}_j^n}{\overline{Sh}_{N_{POD},j}^n} \right)^2}$$

$$MAE(Re_j, Sc_j) = \frac{1}{N-1} \sum_{n=1}^N \frac{|\overline{Sh}_{N_{POD},j}^n - \overline{Sh}_j^n|}{\overline{Sh}_{N_{POD},j}^n}$$

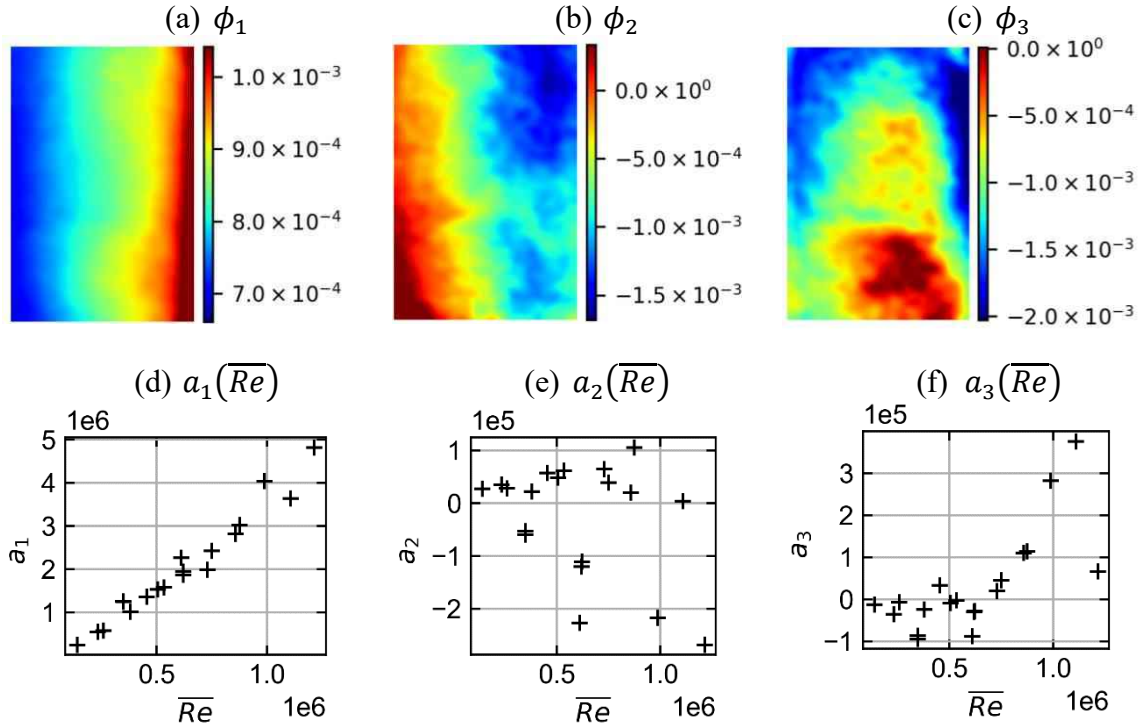


Figure 4.20: first three modes ϕ_1, ϕ_2, ϕ_3 of the POD on location 1 and associated components a_1, a_2, a_3 plotted as function of the Reynolds number during the dissolution.

These two errors yield an approximation of the local difference between the reconstruction and the original map in percent relatively to the reconstruction. Their value is given for location 1 on Figure 4.21. In this case, the difference between the reconstructed and original maps is around 10%. The *MAE* gives lower values than the *RMSE* which is due to the square exponent on the difference which tends to increase the weight of high local differences. Finally, a power law is fitted for a_1 at location 1 and has the following expression:

$$a_1(\overline{Re}) = 0.0933 \overline{Re}^{1.271} \quad (4.1)$$

The fit is given on Figure 4.22. The experimental points are on average around 10% of the predicted value with the fit. In the worst case, the deviation is around 15%.

The first three modes calculated from the POD on location 2 and the components calculated for the different snapshots are given on Figure 4.23. The first mode ϕ_1 contains most of the information on the surface distribution of the Sherwood number. The maximum Sherwood number is at the bottom right side of the sample. It then evolves slightly on the surface and presents small gradients when compared to location 1. The evolution of the first component a_1 is correlated to the Reynolds number's evolution as for location 1.

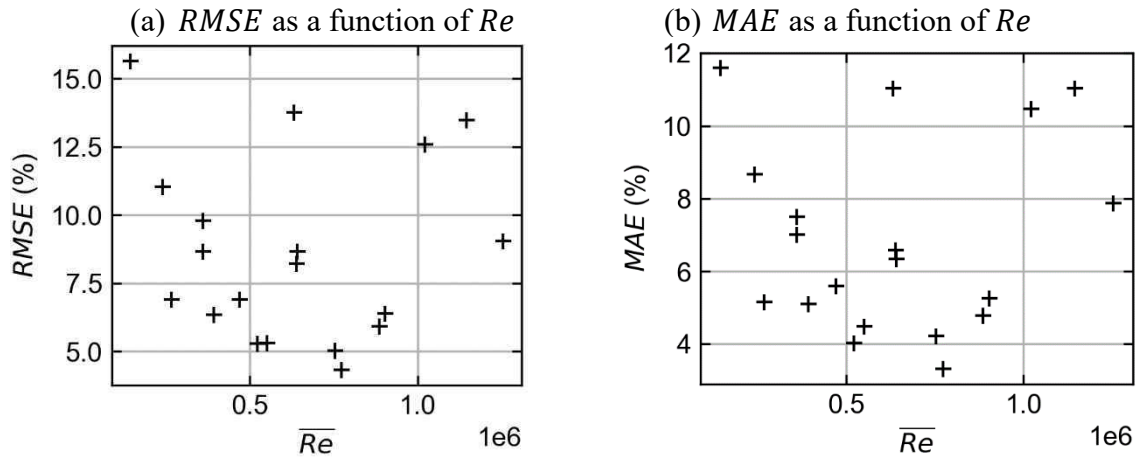


Figure 4.21: Surface average truncation error with $N_{POD} = 1$ for the different experiments on location 1 (a) RMSE and (b) MAE.

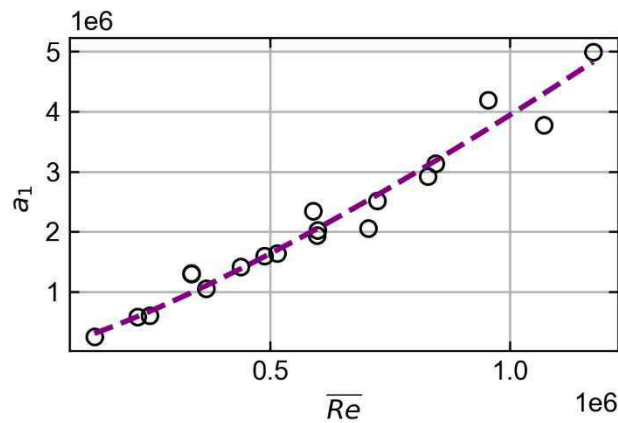


Figure 4.22: correlation for a_1 as a function of the Reynolds number for location 1. The experimental points are depicted with circles, the fit is given with the purple dotted line.

The second mode ϕ_2 behavior is different, most of the components show similar values, only two snapshots present significant differences of amplitude as it can be seen on Figure 4.23e. The parameters which govern its appearance are not identified. Finally, the values of the component a_3 stays approximatively constant until $Re > 5 \cdot 10^5$ where its amplitude increases significantly. Its effect is an enhancement of the local Sherwood number at the leading edge of the sample and on the left-hand side of the sample. This mode has increasing importance as the Reynolds increases as it can be seen on Figure 4.23f.

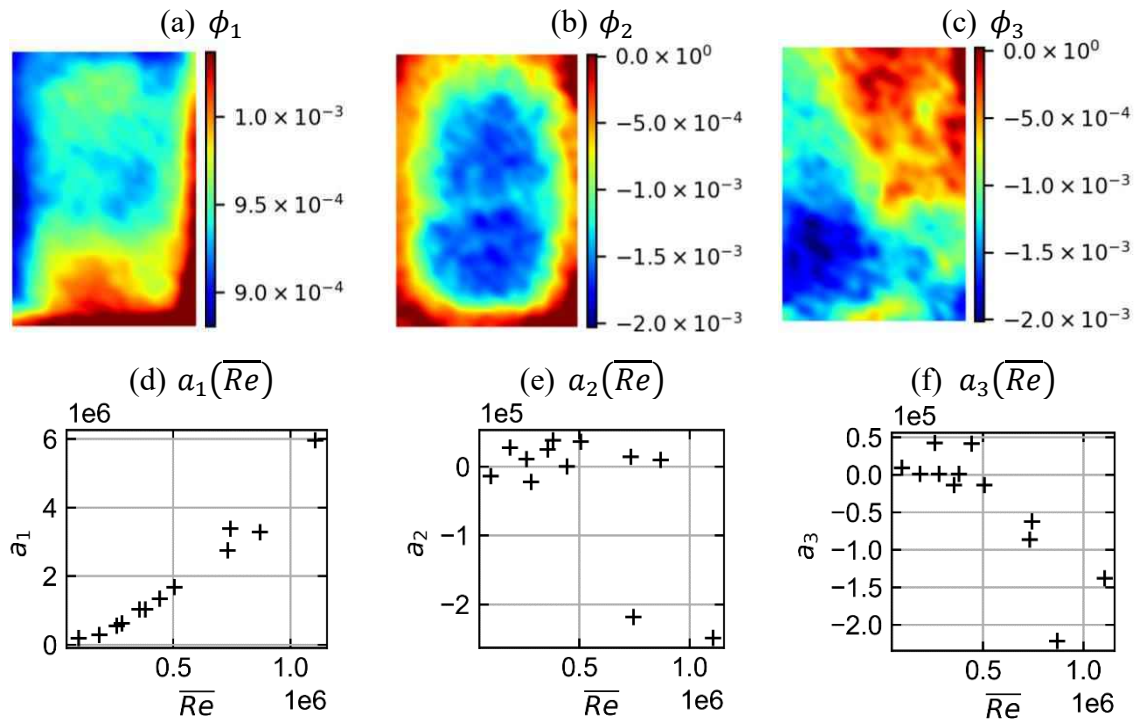


Figure 4.23: first three modes of the POD on location 2 and associated components plotted as function of the Reynolds number during the dissolution.

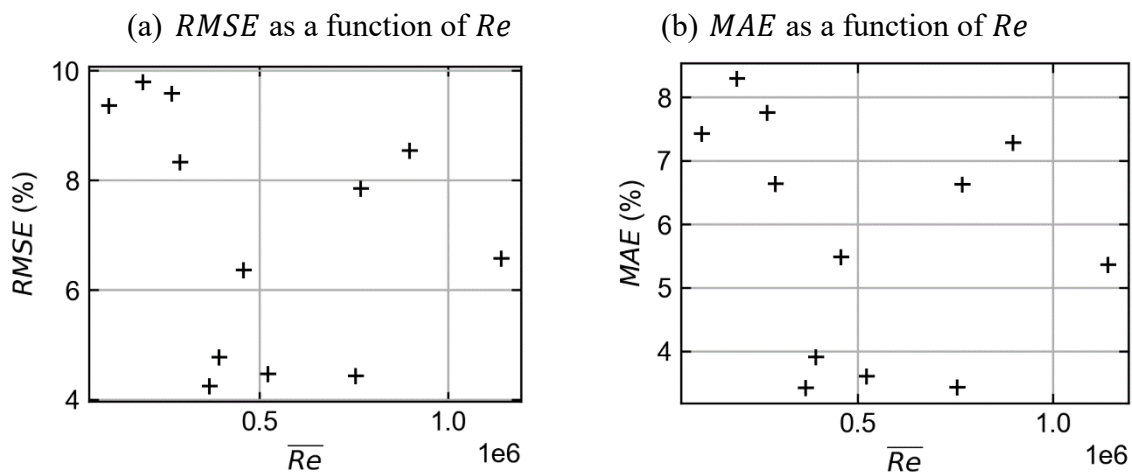


Figure 4.24: calculated bias between the reconstructed map and the original map when using one mode. (a) RMSE and (b) MAE for the different experiment on location 2

For this location, the POD has been truncated to the first mode only which leads to the RMSE around 10% and MAE around 8% in the worst case. The results for all the snapshots are given on Figure 4.24. A power law is fitted on the component a_1 evolution with the Reynolds number, the fit is compared to the experimental points on Figure 4.25. The average deviation between

the correlation and the points is 11% with maximum deviation for the lowest Reynolds numbers (30%). The calculated correlation for a_1 is:

$$a_1 = 0.0101 Re^{1.447} \quad (4.2)$$

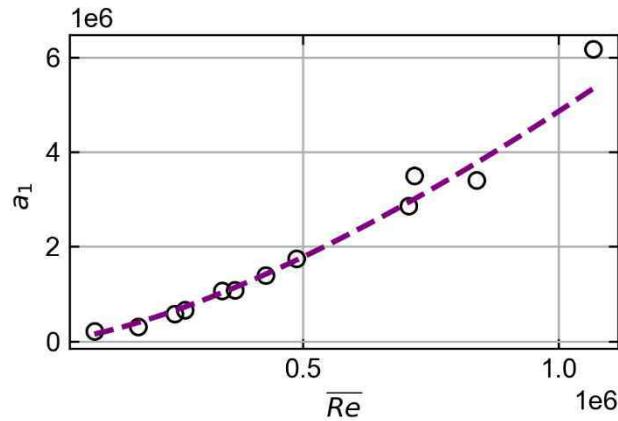


Figure 4.25: correlation for a_1 as a function of the Reynolds number for location 2. The experimental points are depicted with circles, the fit is given with the purple dotted line.

The same process is applied on location 3, the three modes calculated from the POD on location 3 and the components calculated for the different snapshots are given on Figure 4.26. As for the previous locations, the first mode ϕ_1 contains most of the information on the surface distribution of the Sherwood number. The Sherwood number presents its maximum value at the leading edge on the upper right side of the sample. The gradients follow the flow direction and goes from maximum to minimum at the bottom left side of the sample. The component a_1 increases with the Reynolds number similarly to the other locations. For this location, the coefficients related to the second mode ϕ_2 and the third mode ϕ_3 shows significant variation only for some experiments at high Reynolds. The impact of ϕ_2 is a reduction of the mass transfer at the bottom left side of the sample. For ϕ_3 , the component alternates between negative and positive values.

The distribution of ϕ_3 seems to be related to the holes from which the gypsum slurry is poured when casting the gypsum sample. The coordinates of one of the holes coincides with the red spot that can be seen on Figure 4.26c. This result indicates a potential additional effect of the casting on the dissolution other than the defects due to air trapped bubbles initiating roughness. This phenomenon had been captured on other locations, but the experiments were filtered as the quality of the data was too low. The POD has finally been truncated to one mode. The RMSE and MAE calculated for the different snapshots is given Figure 4.27. The error committed when reconstructing with one mode is around 10% of the reconstructed value. In the worst case (one isolated experiment at $Re \approx 1.5 \cdot 10^5$, this RMSE is around 25%.

Moreover, the power law fitted on the component is compared to the experimental points on Figure 4.28.

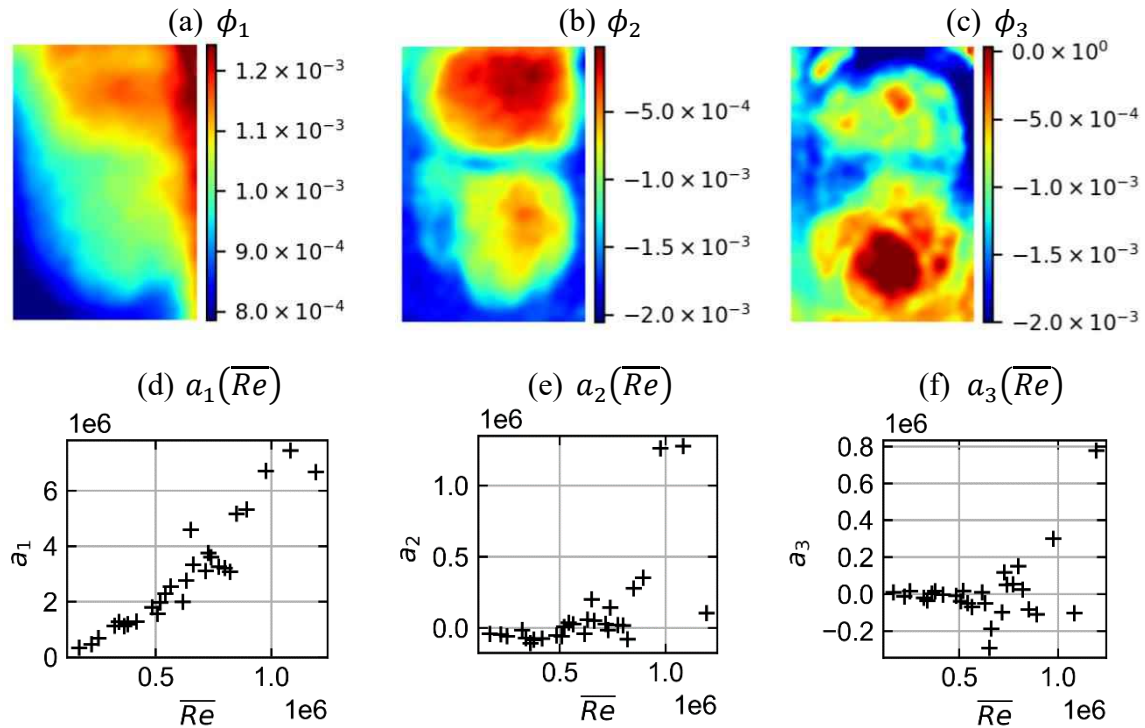


Figure 4.26: first three modes of the POD on location 3 and associated components plotted as function of the Reynolds number during the dissolution.

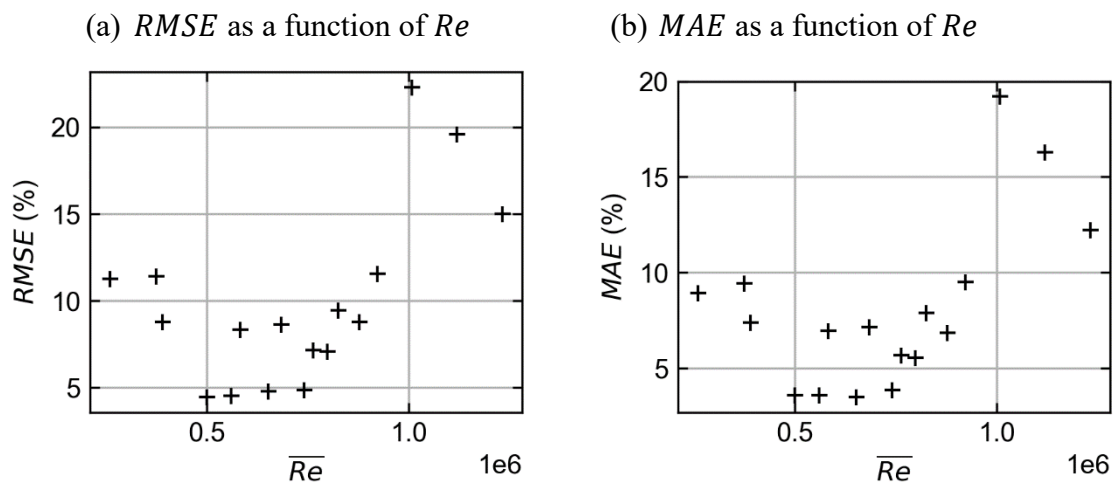


Figure 4.27: calculated bias between the reconstructed map and the original map when using one mode. (a) RMSE and (b) MAE for the different experiment on location 3

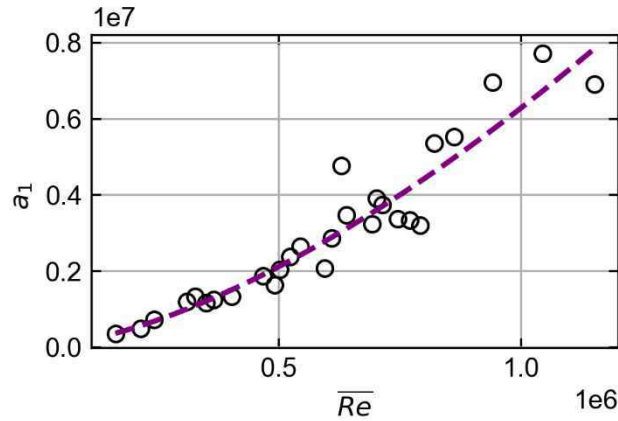


Figure 4.28: correlation for a_1 as a function of the Reynolds number for location 3. The experimental points are depicted with circles, the fit is given with the purple dotted line.

The average deviation between the correlation and the points is 13%. The RMSE has been calculated to be around 60% in the worst case for an experiment. The next biggest deviation is around 25%. The calculated correlation for a_1 is:

$$a_1 = 0.0023 Re^{1.571} \quad (4.3)$$

Finally, the location 4 is investigated and the first three modes are given Figure 4.29. For this location, two modes are required in order to have $RIC > 0.99$. The first mode ϕ_1 shows a maximum value at the bottom of the sample. In this case, the estimated leading edge of the sample on the top left of the sample has a minimal Sherwood. Then the local Sherwood number increases in the vertical direction and reaches its maximum before decreasing and exiting the sample. This samples seems to cross two regions: the stagnation region on the upper side of the sample where a local minimum seems to be reached, and a second region near the deflection zone where the flow accelerates which leads to higher mass transfer and a local maximum.

The second mode ϕ_2 carries more importance for location 4 than for other locations. In this case, the upper side of the sample is not modified, but the local maximum's amplitude is enhanced resulting in a change of the surface distribution. Moreover, the components a_2 show a clear trend for Reynolds above $Re > 5 \cdot 10^5$. The importance of this mode grows with the Reynolds number. The third mode ϕ_3 is also related to the Sherwood number at the center of the sample, however, the component for the different experiments do not have a visible behavior correlated to the experiment Reynolds number.

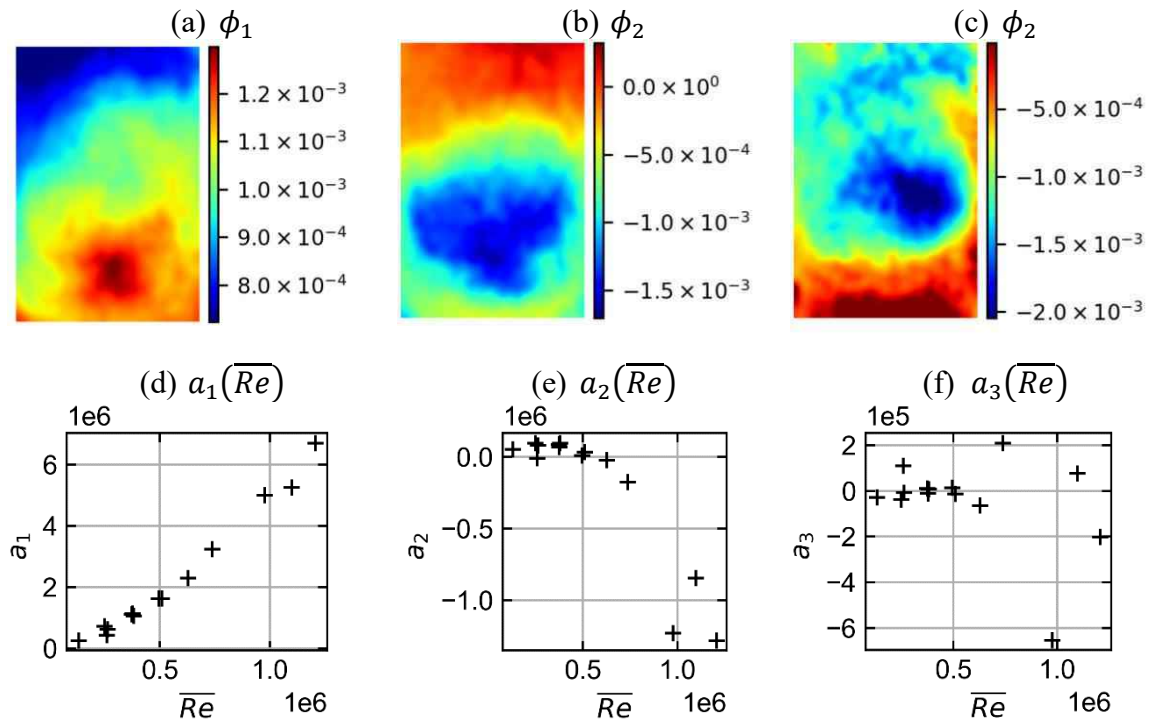


Figure 4.29: first three modes of the POD on location 4 and associated components plotted as function of the Reynolds number during the dissolution.

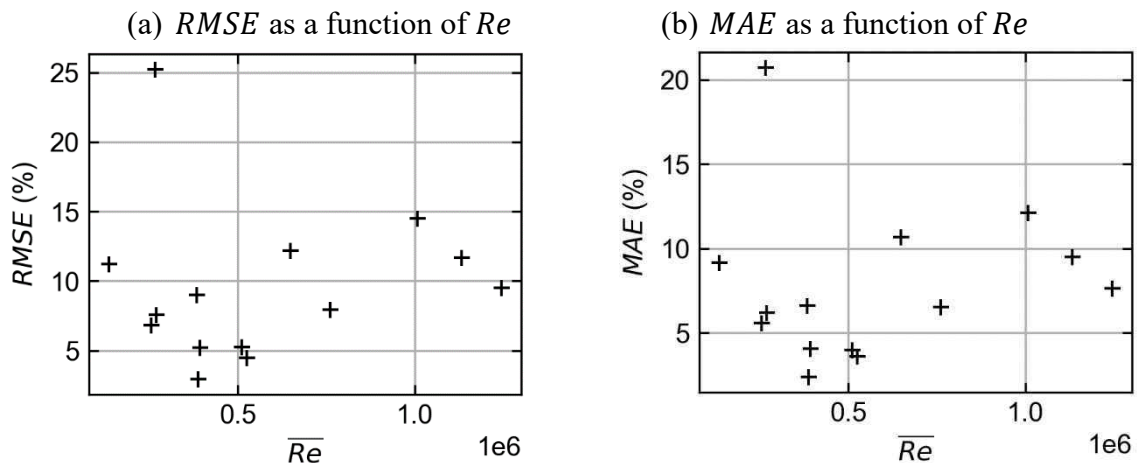


Figure 4.30: calculated bias between the reconstructed map and the original map when using one mode. (a) RMSE and (b) MAE for the different experiment on location 4

For this location, a reconstruction with one mode leads to RMSE and MAE over 20%. Thus, two modes have been used for the reconstruction of the snapshots. The associated RMSE and MAE are given on Figure 4.30 where the relative error of the reconstruction is around 10% of the reconstructed Sherwood. Finally, a correlation is given for the components a_1 in the form of a power law. The power law is compared to the experimental points on Figure 4.31. The

deviation of the experimental points is around 8% of the predicted value. The maximum deviation occurs at low Reynolds number and its value is around 30%. The correlation has been calculated to be:

$$a_1 = 0.0049 Re^{1.505} \quad (4.4)$$

A power law is not adapted for the second mode components. Thus, another method must be used to generate a_2 for a given Reynolds number.

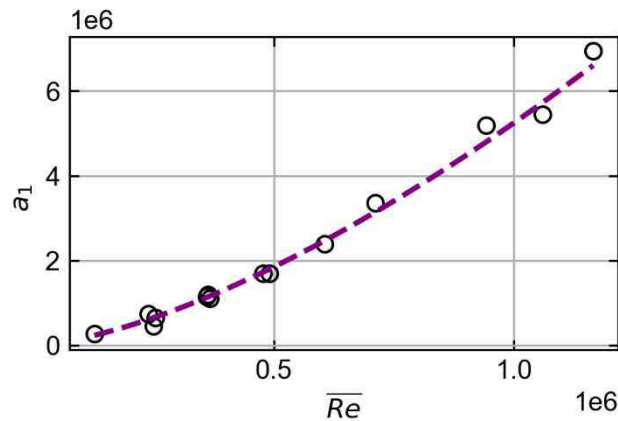


Figure 4.31: correlation for a_1 as a function of the Reynolds number for location 4. The experimental points are depicted with circles, the fit is given with the purple dotted line.

4.3.1.4 Conclusion of the mass transfer coefficient measurements

The results presented in this paragraph have been obtained by measuring the local Sherwood number from the gypsum dissolution technique. Correlations have been given for the surface average Sherwood number at different locations of the partition plate. The scaling of the surface average Sherwood number with the Schmidt number could not be accurately predicted given the measurements, thus a scaling by $Sc^{0.44}$ has been chosen in regard to the available literature on the Prandtl effect on the Nusselt number at the stagnation region for an impinging jet (Li & Garimella, 2001). The measurements were performed further from the stagnation region which could lead to lower exponent on the scaling law. The exponents on the Reynolds number for the correlation of the component related to the first POD mode a_1 were all found to be larger than 1, which means the curve has a positive curvature. This exponent is most certainly due to the effect of roughness that has still to be quantified with smooth wall measurements. Furthermore, the acquisition of Sherwood maps with gypsum dissolution also enabled the investigation of the evolution of the surface distribution with the Reynolds number with the help of POD. No effect of the Schmidt number has been observed on the Sherwood number

distribution over the experimental range, apart from the scaling of the amplitude due to different diffusion properties. For most of the locations (1, 2 and 3), only one mode is important and allows to reproduce the experimental values of the Sherwood maps with an accuracy around 10%. No experimental variables have been found to explain the evolution of the components related to the other modes. The fluctuations of the higher order modes coefficients seem to be related to an impact of non-controlled variables at the casting step. For low Reynolds number, the impact of these variable is not observed. The increase of the Reynolds number gives more importance to these differences, which induce additional variability of the surface distribution. For location 4 which is the nearest to the stagnation region, a local minimum has been observed on the upper half of the sample. The increase of the local Sherwood in the flow direction when reaching the lower part of the sample seem to indicate that location 4 crosses the stagnation zone and the deflection zone where the fluid accelerates. At this location, the surface distribution of the local Sherwood number presents larger variations which might be due to the Reynolds evolution from an experiment to the other. Thus, two modes had to be considered for the reconstruction of the Sherwood maps with POD in order to have the same accuracy than other locations. Finally, correlations have been given for the evolution with the Reynolds number of the components a_1 associated to the first POD mode ϕ_1 for all locations.

4.3.2 Heat transfer measurements

The heat transfer coefficient on the four locations of the partition plate depicted Figure 4.18 has been investigated for $Pr \approx 6$ and $Re \in [10^5, 10^6]$. The experimental conditions (Re, Pr) for each experiment are given on Figure 4.32.

In addition, measurements were carried out for $Pr \approx 4$ and $Pr \approx 8$ on location 1 in order to investigate the influence of the Prandtl number on the measured Nusselt.

The time average of the surface average Nusselt number on the upper and lower half of the measurement device (resp. \overline{Nu}_U and \overline{Nu}_D) are depicted for all locations on Figure 4.33. The error bars give a $\pm 2 \sigma_{Nu}$ interval which is calculated from:

- the propagation of the uncertainty on the position of the thermocouples and of the measured temperature through the calculation of the Nusselt.
- the temporal fluctuations of the instantaneous Nusselt number calculated during the experiment.

The relative error on the calculated Nusselt number is around 10% and remains stable on the whole range of the data. The correlations for the different locations are obtained with power laws that can be written:

$$Nu(Re, Pr) = a Re^b Pr^c$$

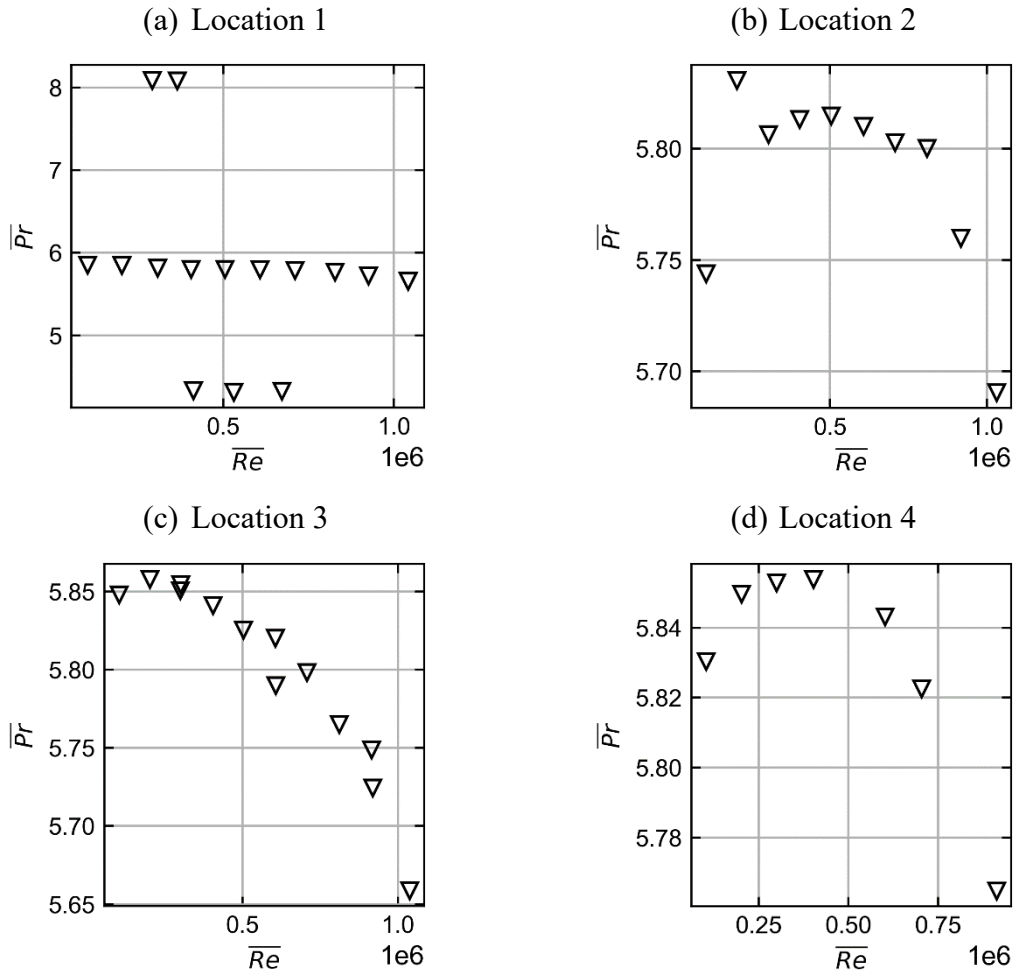


Figure 4.32: boundary conditions Re, Pr swept for the different locations.

In these experiments, c has been set to 0.44 as it has been done for mass transfer measurements (see §4.3.1.2), the coefficient a and b are given for the different locations on Table 4.2. The coefficient b for location 1, 2 and 3 are between 0.7 and 0.9. These coefficients are comparable to the coefficients depicted on Figure 4.9 obtained for different radial displacement. Moreover, location 4 is the nearest of the stagnation zone. In this zone, the exponent b of the power law fit is expected to be lower and is found to be in the range $[0.5, 0.6]$ on Figure 4.9 for comparable nozzle to plate spacing. This is observed for Nu_D where the $b = 0.57$.

The average value $Nu_m = \frac{1}{2}(\overline{Nu}_U + \overline{Nu}_D)$ is compared for the different locations on Figure 4.34. On location 4, the values on the upper and lower half of the device are given in dotted line. The Nusselt number on the upper side of the device \overline{Nu}_U has approximately the same amplitude as Nu_m on locations 1, 2 and 3. In comparison, the values of \overline{Nu}_D are much lower than at other locations. Location 1 which is the further from the stagnation region is the second lowest value of the Nusselt number.

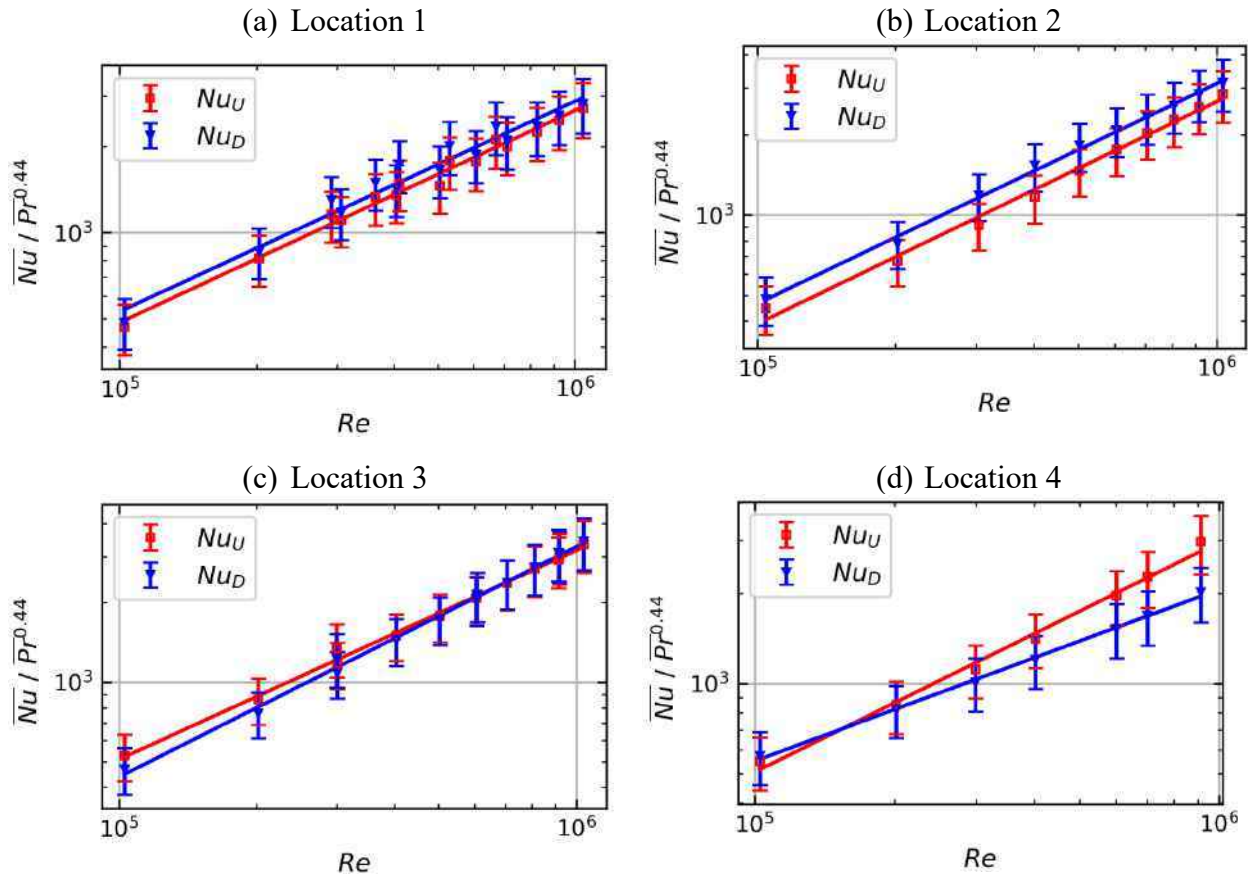


Figure 4.33: evolution of the Nusselt number as a function of the Reynolds number at location 1. (a) evolution of Nu_U and Nu_D with the Reynolds number (fit plotted with solid line)

Table 4.2 : coefficient a , b of the power law fitted on the experimental data

Location		a	b
1	$Nu_{U,1}$	0.109	0.740
	$Nu_{D,1}$	0.128	0.734
2	$Nu_{U,2}$	0.0297	0.834
	$Nu_{D,2}$	0.0389	0.826
3	$Nu_{U,3}$	0.0626	0.792
	$Nu_{D,3}$	0.0215	0.872
4	$Nu_{U,4}$	0.0843	0.766
	$Nu_{D,4}$	0.851	0.571

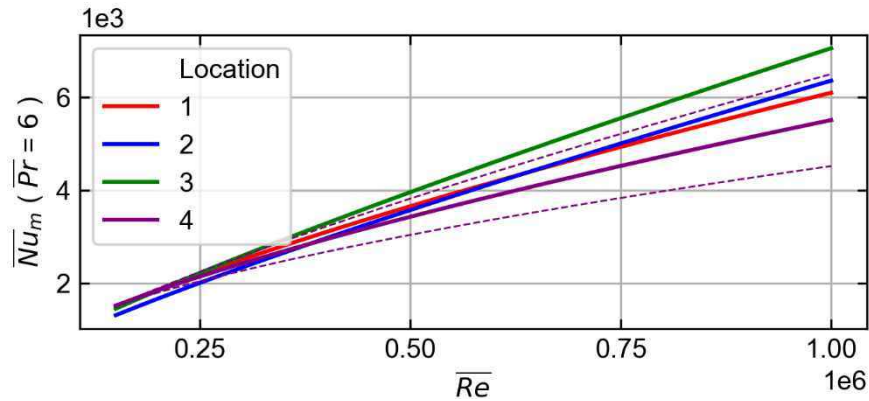


Figure 4.34: comparison of the mean Nusselt number over the surface Nu_m at the different locations on the experimental range. Nu_D and Nu_U are given in purple dotted line for location 4.

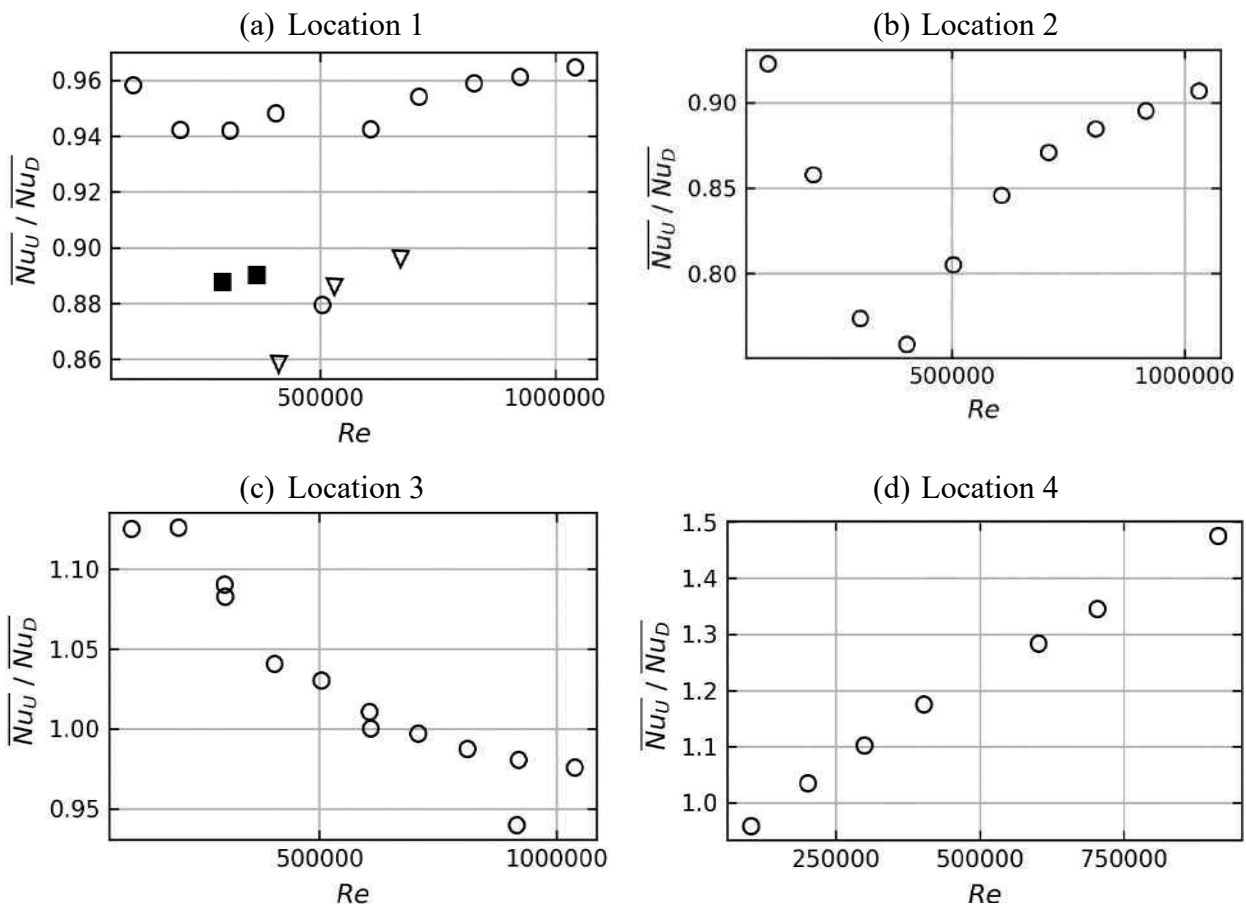


Figure 4.35: ratio Nu_U / Nu_D as a function of the Reynolds number for the different location on the partition plate. ($Pr = 4 : \nabla$, $Pr = 6 : \circ$, $Pr = 8 : \blacksquare$).

Finally, the ratio $\overline{Nu}_U/\overline{Nu}_D$ is given on Figure 4.35 for the different locations. No clear behavior of $\overline{Nu}_U/\overline{Nu}_D$ is visible with the Prandtl number on location 1, the evolution of the ratio with respect to the Reynolds number seems to increase in both case with similar trend, the value is quite stable and shows small differences on the upper and lower half values. For location 2, the ratio first decreases from 0.9 to 0.75, then bounces back and reaches values around 0.9 at high Reynolds number. For location 3, the Nusselt number on the upper side \overline{Nu}_U is initially 10% bigger than \overline{Nu}_D for low Reynolds number. The ratio then decreases for increasing Reynolds numbers and reach values around unity. For location 4, the Nusselt is uniform at low Reynolds. For increasing Reynolds number, the ratio $\overline{Nu}_U/\overline{Nu}_D$ increases significantly and reaches 1.5 for the highest Reynolds number covered. It seems that the value would still get larger by extending the range of the data. The detailed comparison of the heat and mass transfer coefficient will be done in the next section.

4.4 Transposition of mass transfer data with the heat and mass transfer analogy

4.4.1 Data processing

Heat and mass transfer coefficient values were obtained through measurements on the four locations of the partition plate depicted on Figure 4.2a

- The local Sherwood number is obtained at the four locations. The Reynolds number covered for the different experiments is in the range $[10^5, 10^6]$. The Schmidt number is in the range $[600, 1200]$.
- The surface average Nusselt number is calculated from the measurements on the upper and lower parts of each location. The experiments cover the range of Reynolds number $[10^5, 10^6]$ for Prandtl number in the range $[4, 8]$.

These measurements were used in order to calculate the transposition factor from gypsum dissolution data to heat transfer data in the case of a fixed temperature wall exchanging with water. This transposition factor considers the difference between the diffusion properties of heat and ions which dissolve from the gypsum. Moreover, this transposition also takes into account the difference of the surface aspect which is rough for mass transfer and smooth for heat transfer. The zones on the upper side and lower side (resp. U and D) extracted from the gypsum surface to make the comparison with heat transfer data are depicted on Figure 4.36. These zones correspond to the measurements zones for heat transfer data depicted on Figure 4.13. The surface average Sherwood and Nusselt numbers obtained from these zones are depicted respectively by symbols $\overline{Sh}_U, \overline{Sh}_D$ and $\overline{Nu}_U, \overline{Nu}_D$.

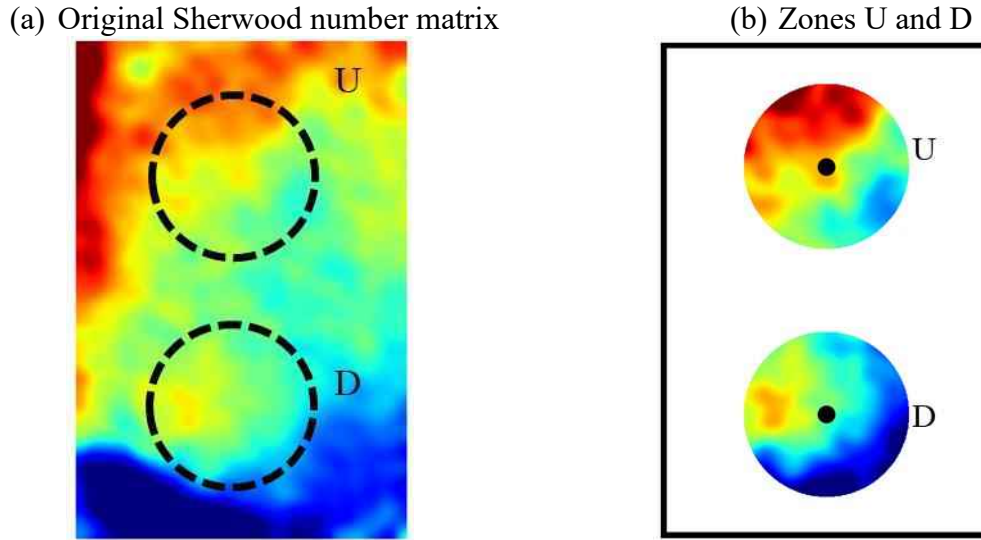


Figure 4.36: extraction of mass transfer data for transposition factor calculations (a) original Sherwood number distribution with extractions zones indicated inside the dotted lined circles. (b) Extracted zones U and D on which the surface average Sherwood numbers \overline{Sh}_U and \overline{Sh}_D are calculated.

Three transposition factors F_1, F_2, F_3 are calculated for the different experiments at the different Reynolds number \overline{Re} :

$$F_1 = \frac{\overline{Sh}(\overline{Re}, \overline{Sc})}{\overline{Nu}(\overline{Re}, Pr = 6)}, \quad F_2 = F_1 \left(\frac{6}{\overline{Sc}} \right)^{0.44}, \quad F_3 = F_1 \left(\frac{6}{\overline{Sc}} \right)^{0.33}$$

F_1 denotes the transposition factor which consider the differences between the diffusion properties and the surface aspect of the measurement \overline{Sh} . \overline{Nu} is estimated for Reynolds number \overline{Re} at $Pr = 6$ with the correlations given in Table 4.2. The effect of roughness is assumed to be independent of the Schmidt number. The effect of the roughness on the heat and mass transfer is thus separated from the effect of the diffusion properties leading to the definition of F_2 and F_3 which are estimation of the roughness enhancement, considering the Schmidt and the Prandtl numbers impact on the transfer can be modelled by a power law.:

$$\frac{\overline{Sh}}{\overline{Nu}} \propto \left(\frac{\overline{Sc}}{Pr} \right)^c \times F(Re, e^+)$$

with $c = 0.44$ for F_2 and $c = 0.33$ for F_3 . e^+ is the non-dimensional roughness height defined from the turbulence inner friction length scale l_+ based on estimation of the friction velocity u^* from Darcy friction factor as in §2.4.

$$e^+ = \frac{e}{l_+} = \frac{e Re}{D_H} \sqrt{\frac{f}{8}}$$

$$\frac{1}{\sqrt{f}} = -2 \log_{10} \left(\frac{3 \times e_{RMS}}{3.71 D_H} + \frac{2.51}{Re \sqrt{f}} \right)$$

where, e a characteristic height of the roughness (RMS roughness, peak-valley roughness or other).

The function $F(Re, e^+)$ denotes the similarity function quantifying the enhancement of the heat and mass transfer with the Reynolds number and the non-dimensional roughness e^+ . The independency of F to the Schmidt number is found to be false for mass transfer with regular V-shaped grooves roughness in (Dawson & Trass, 1972). However, the fluctuations of the data obtained with gypsum dissolution has been found to be important due to the high discrepancy of the surface aspect between experiments. These important variations screened the variations due to the Schmidt number.

The experimental transposition will then be compared to the transposition given in (Wang & Ewing, 2017):

$$F_W = \left(\frac{Sh_R}{Sh_S} \right)_{Wang} = 1.09 \left(\frac{e_{pv}}{l_{str}} \right)^{0.2} Re^{0.07}$$

where, e_{pv} is the peak to valley and l_{str} is the spacing between roughness elements which extraction from the gypsum samples surface is described on Figure 4.12.

The non dimensional peak to valley roughness e_{pv}^+ will also be used to investigate the effect of the roughness on the heat and mass transfer.

4.4.2 Surface distribution

The ratio $\overline{Nu}_U / \overline{Nu}_D$ and $\overline{Sh}_U / \overline{Sh}_D$ of the heat and mass transfer on the upper and lower part of the measurement devices (position U and D) are compared on Figure 4.37.

The ratio is compared for the original maps and the reconstructed maps from the truncated POD of the Sherwood number Sh_1, Sh_2, Sh_3 with respectively 1, 2 and 3 modes. The heat and mass transfer measured with the heat transfer coefficient measurement device and the gypsum dissolution technique on location 1 and 2 show similar distributions: the ratio remains stable with the Reynolds number showing small variations. The deviation between the heat and mass transfer points shows small changes on the experimental range. The results on location 3 shows a decrease of the ratio with the Reynolds number for both heat and mass transfer measurements. Moreover, the deviation between these two sets of data gets more significant as the Reynolds increases. These differences might be due to larger heat transfer rates at the leading edge compared to mass transfer due to the establishment of the thermal boundary layer. The large difference between the diffusive properties of heat and mas transfer in the presented measurement might explain partially this behavior. This entrance effect has been discussed in §2.4, and the impact should decrease with the Reynolds number.

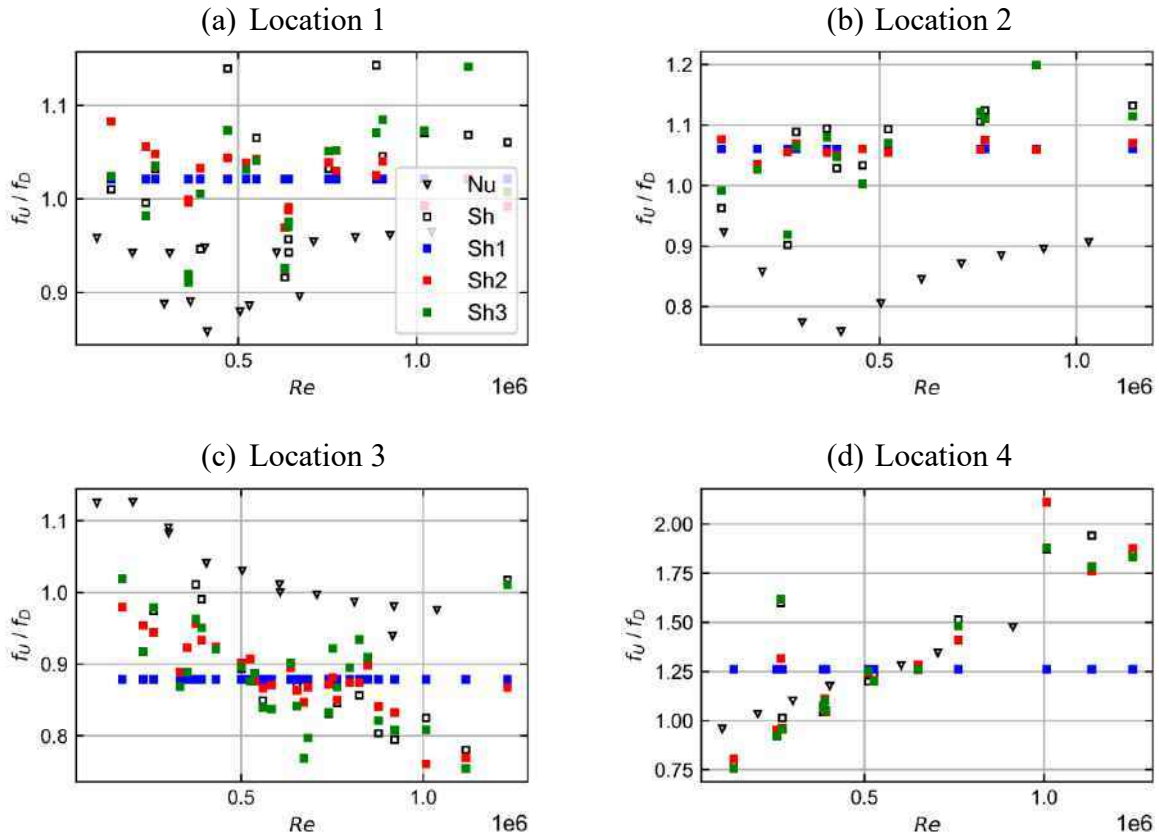


Figure 4.37: ratio $\overline{Nu}_U / \overline{Nu}_D$ as a function of the Reynolds number for the different location on the partition plate compared to $\overline{Sh}_U / \overline{Sh}_D$. The ratio is calculated from the original maps and the truncated POD of the Sherwood number Sh_1, Sh_2, Sh_3 calculated respectively with 1, 2 and 3 modes (blue, red and green).

Another reason could explain the increasing difference for larger Reynolds numbers. During gypsum dissolution, the flow is affected by the roughness as it progresses across the gypsum surface. Furthermore, when the gypsum dissolves, the surface flatness is affected and could impact the flow in the vicinity of the surface resulting in slightly distorted surface distribution. These effects should be more significant for increasing Reynolds number as the boundary layers get thinner. The enhancement of the Sherwood number along the gypsum surface has been also investigated in §4.3.1.3. It has been shown that the surface distribution changes for increasing Reynolds number because of the appearance of secondary modes. The influence of each POD mode on the surface distribution of the Sherwood number compared to the heat transfer measurements is given on Figure 4.37. The ratio obtained with one mode corresponds approximatively to the mean value of the ratio over the Reynolds range for all the locations. The additional effect of mode 2 and 3 on locations 1 and 2 is low and do not ameliorate the comparison between heat and mass transfer. The results on location 3 are slightly different, the inclusion of mode 2 for $Re < 5 \cdot 10^5$ yields a lower difference between heat and mass transfer but deteriorate the comparison for higher Reynolds number.

Furthermore, an increase of the discrepancy of the surface distribution between the different experiments is observed when considering mode 3. The evolution of the ratio is much more significant for heat and mass transfer on location 4. The heat transfer coefficient ratio evolves with the Reynolds from 1 to 1.5 and from 0.75 to 1.75 for mass transfer coefficient. In both cases, the results show an increase of the ratio with the Reynolds number. This evolution is present for mass transfer measurements when taking into account mode 2 which impacts the distribution by translating the maximum heat transfer present in mode 1 on the bottom of the sample up. As for the other locations, the ratio calculated from heat transfer yields larger values at low Reynolds number. The deviation between $\overline{Nu}_U/\overline{Nu}_D$ and $\overline{Sh}_U/\overline{Sh}_D$ is similar than for other locations.

In conclusion, the surface distribution of the heat and mass transfer fluxes remains approximatively constant for evolving Reynolds number on these three locations. The differences between heat and mass transfer distribution are around 20% and are the results of:

- Differences in the diffusion properties which impact the establishment of the thermal and concentration boundary layers. The size of these boundary layers are different when measuring heat and mass transfer. Compared to mass transfer measurements with gypsum dissolution, the heat transfer measurement device could be more affected by the entrance effect due to larger thermal boundary layer. This effect should decrease for higher Reynolds number and could explain the stabilization of the ratio measured on heat transfer data.
- Differences in the surface aspect. Gypsum dissolution technique leads to the appearance of a step at the leading edge of the surface and roughness which enhances the mass transfer coefficient. In contrast, heat transfer measurements are done with a smooth surface. The differences between heat and mass transfer gets more significant for increasing Reynolds number as the boundary layer gets thinner and more affected by the surface changes.

4.4.3 Transposition factor

The three transposition factors F_1 , F_2 and F_3 are calculated and given as function of the average Reynolds number \overline{Re} on Figure 4.38a, Figure 4.38b and Figure 4.38c. The value covered by F_1 are in the range [5, 20]. The difference of the transposition factor for the different Schmidt number is clearly visible on Figure 4.38a, with F_1 returning larger values for the set of experiment presenting Schmidt numbers at $\overline{Sc} = 1200$ (indicated with squares) compared to $\overline{Sc} = 600$ (circles). The differences seem to disappear for F_2 and F_3 when transposing the data to $\overline{Sc} = 6$ with a visible collapse of the data obtained at both Schmidt numbers. The transposition F_2 is lower than 1 for $\overline{Re} < 5 \cdot 10^5$ from which it increases to maximum values around 2 for the higher Reynolds numbers. F_3 follows the same behavior but is translated to higher values.

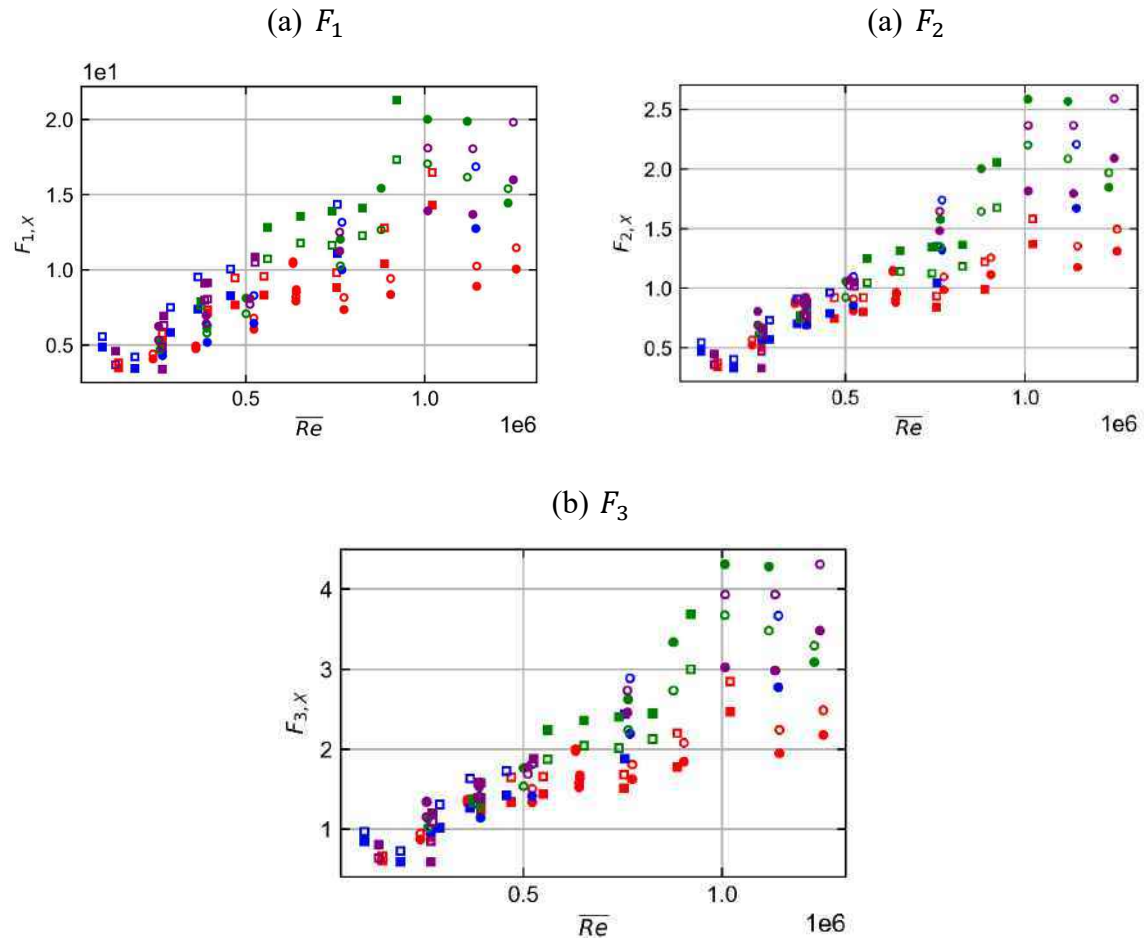


Figure 4.38: evaluation of the transposition factor (a) F_1 , (b) F_2 and (c) F_3 for locations 1 (red), 2 (blue), 3 (green) and 4 (purple). Experimental points obtained at $\overline{Sc} \approx 600$ (\circ) and $\overline{Sc} \approx 1200$ (\square). Data obtained on zones U and D is given respectively with unfilled and filled symbol.

The transposition factor is around unity and increases steadily with the Reynolds number increase. The scaling of the diffusion effect with $c = 0.33$ seems to be more likely than $c = 0.44$. In fact, for equivalent Schmidt number and Prandtl number, the transposition number should be around unity or at least give higher rates for rough surfaces. The coefficient $c = 0.44$ was found in (Ma, et al., 1997) for measurements in the stagnation zone for $Re < 26\,000$. This coefficient might not be adapted for higher Reynolds numbers. In addition, the flow is more turbulent in the wall jet region F_1 where the measurements were carried out. Also, the Prandtl and Schmidt effect on heat and mass transfer might not be constant. In either case, the transposition factor F is multiplied by 4 in between $\overline{Re} = 10^5$ and 10^6 . The effect of diffusion is corrected thereafter by dividing the Sherwood number by $\overline{Sc}^{0.33}$ in order to have a transposition factor around unity for the experiments with the lowest Reynolds number. The evolution of F_3 is studied as a function of the non-dimensional surface roughness e_{pv}^+ .

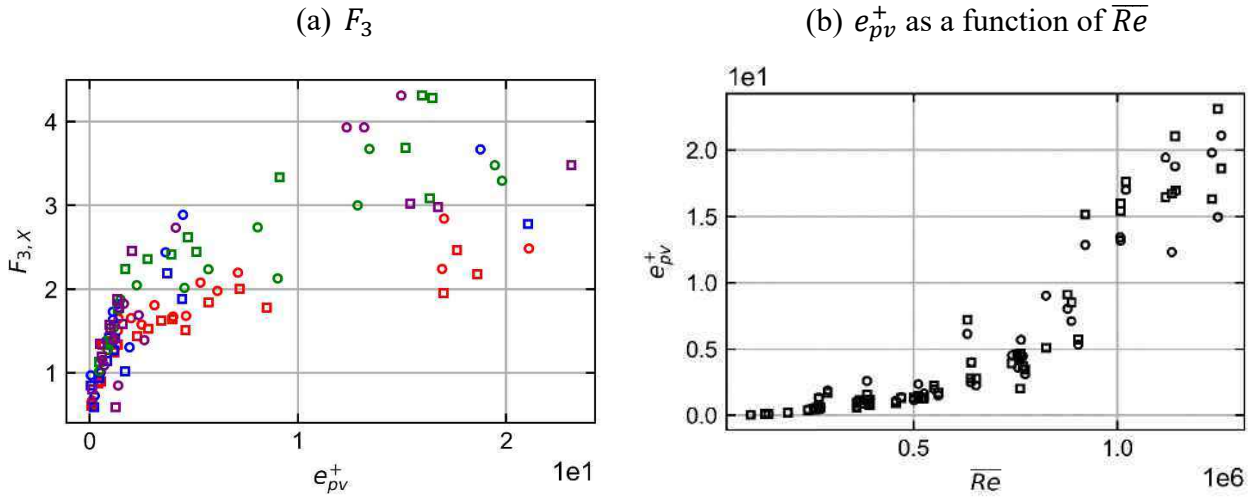


Figure 4.39: effect of the roughness on the transposition factor. (a) Evolution of the transposition factor at $\overline{Sc} = \overline{Pr} = 1$ as a function of e_{pv}^+ on location 1 (red), 2 (blue), 3 (green) and 4 (purple) on U (\circ) and D (\square). (b) Evolution of the calculated e_{pv}^+ on U (\circ) and D (\square) as a function of the Reynolds number.

The evolution of F_3 for equal diffusion properties and changing surface aspect with e_{pv}^+ is given on Figure 4.39a. Two zones are visible on this figure: for $e_{pv}^+ < 5$, the transposition factor is below 1 and increases rapidly from 1 to 2. Then, the slope of the transposition factor gets lower, and the discrepancy between the different locations increases. This difference could be due to the scaling of F with the Reynolds number as it has been found in (Wang & Ewing, 2017). All the locations are not exposed to the same local Reynolds number, implying a different effect of the roughness on the mass transfer at each location. The roughness e_{pv}^+ is also shown as a function of the experiment Reynolds number \overline{Re} on Figure 4.39b. The non-dimensional roughness is found to increase significantly for experiments such as $\overline{Re} > 5 \cdot 10^5$.

Finally, the Sherwood number for rough surface $\overline{Sh}/\overline{Sc}^{0.33}$, the Sherwood number transposed with Wang correlation and the Sherwood number transposed with F_3 are compared on Figure 4.40 for the different locations. The difference between the rough values and the transposed values is obvious. F_W and F_3 give the same order of magnitude, however, Wang transposition used as such without correcting the Reynolds number seems to be inaccurate. In fact, the transposition seems to overestimate the effect of roughness when compared to the experiment on location 1 where the velocity is the lowest, on location 2 and 3 the results are similar and of the same order of magnitude while the results on location 4 are similar for F_W and F_3 on the lower half D but significantly different on the upper half U .

These differences may also be due to the difference in the extraction of the roughness characteristics.

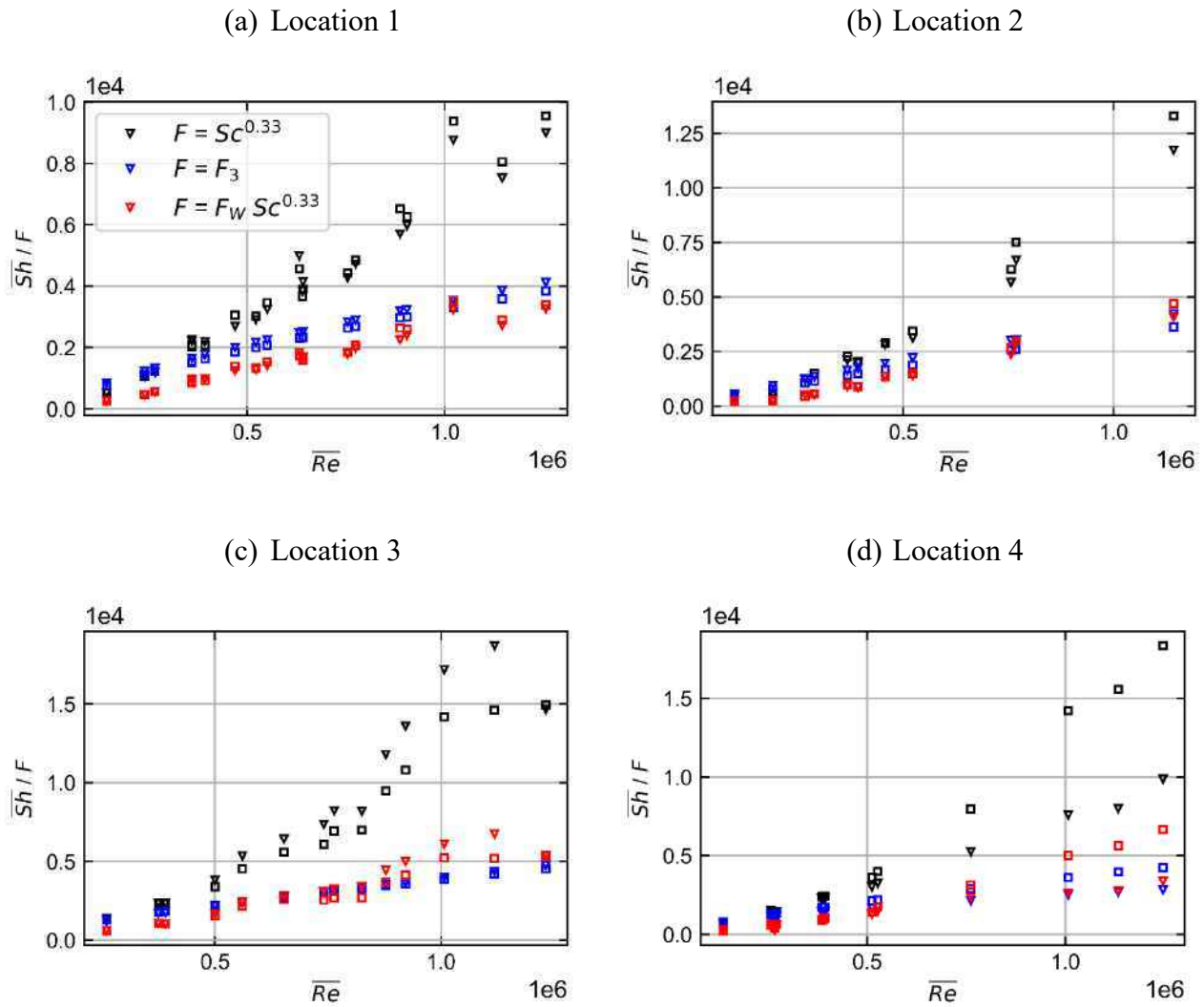


Figure 4.40: comparison of the rough Sherwood number $\overline{Sh}/\overline{Sc}^{0.33}$ (black) to transposed Sherwood numbers \overline{Sh}/F with $F = F_3$ (blue) and $F = F_W$ (red) (Wang & Ewing, 2017). The values estimated on position U are denoted with squares and D with triangles.

4.4.4 Discussion

The heat and mass transfer measurements enabled the calculation of the transposition factor in this configuration of an impinging jet. First, the scaling due to the difference in the diffusion properties seems more coherent with $\overline{Sc}^{0.33}$ than $\overline{Sc}^{0.44}$ which had been chosen in regard to the available data in literature for heat and mass transfer near stagnation region of an impinging jet. In addition, the transposition factor between the Sherwood obtained with gypsum mass

transfer measurement and the Nusselt number obtained with smooth wall heat transfer measurements is well correlated to the roughness which develops during gypsum experiments. However, differences have been observed on the transposition factor between the different measurement locations for equal surface roughness. This could indicate that the transposition depends also on the local Reynolds number at the different measurement locations. This seems coherent with the transposition factor F_W obtained in a S-shaped pipe configuration (Wang & Ewing, 2017) which depends on the Reynolds number. Thus, it seems difficult to determine the heat transfer coefficient amplitude from gypsum measurement alone. Additional tests must be done to determine if a general law can be given on the transposition factor for any configuration by introducing a local Reynolds number or another local information that can be extracted from the gypsum surface after dissolution.

Finally, the surface distribution of the heat and mass transfer coefficients could be partially compared by investigating the ratio between the exchange on the upper and lower half of the measurement's locations. This partial comparison made with the assistance of POD yielded a good agreement between both measurements, yielding stable surface distribution in both cases on locations 1, 2 and 3, and an evolving surface distribution on location 4. This indicates that gypsum measurement can be used to estimate heat transfer coefficient distributions.

4.5 Conclusion

In conclusion, the heat and mass transfer coefficient were measured on the partition plate of the steam generator water box mock-up (SGWB). The mass transfer measurements yielded Sherwood maps on extended zones while heat transfer coefficient measurements allowed to retrieve two surface average values of the Nusselt number over the upper and lower half of the measurement device. Correlations have been given on the surface average values in order to estimate the heat and mass transfer for various operating conditions (Reynolds, Prandtl, Schmidt numbers). Furthermore, the proper orthogonal decomposition (POD) has been applied on the Sherwood maps data at different location of the partition plate. This decomposition gave a general idea of the evolution of the surface distribution of the Sherwood number along the gypsum surface. This distribution has then been compared to the one obtained for the heat transfer coefficient and has been found to be in good agreement. The differences have been discussed in regards of the results:

- The establishment of the thermal and concentration boundary layers are different due to the large difference of heat and mass diffusion properties during the heat and mass transfer experiments. The effect of the developing thermal boundary layer on the surface distribution of the Nusselt number should decrease with the Reynolds number.
- At high Reynolds, the roughness that develops on the gypsum surface affects the amplitude of the transfer and induces distortion of the surface distribution.

Also, the transposition factor between the Sherwood number and the Nusselt number has been investigated. Difficulty remains when separating the effect of the diffusion properties and roughness properties on the similarity function bounding the Sherwood number and the Nusselt number. Nevertheless, it has been observed that the enhancement of the mass transfer due to the development of the surface roughness as gypsum dissolves is divided in two zones, the Sherwood number enhancement first increases significantly until $e_{pv}^+ \approx 5$ from which the slope becomes more moderate. In addition, for $e_{pv}^+ > 5$, the transposition factor is higher for locations with more important mass transfer rates: in decreasing order, the transposition factor is more important for locations 3, 4, 2 and 1. This local behavior of the effect of roughness implies that the current gypsum dissolution methodology might not be sufficient to estimate the amplitude of heat transfer for any flow configuration. However, the surface distribution can be estimated with good confidence.

In this particular configuration of an impinging jet, the combination of heat and mass transfer data obtained in the SGWB mock-up allows to generate Nusselt maps that will be used in Chapter 6 for the uncertainty quantification of CFD codes. This generation will be achieved by scaling the amplitude of the heat transfer thanks to the heat transfer experiments, while the surface distribution will be given by using the truncated POD discussed earlier.

Some uncertainties remain on the similarity of the development of the temperature and concentration boundary layers. In the future, heat transfer measurement could be carried out in the rectangular channel presented Chapter 2 in order to quantify accurately the effect of the thermal boundary layer establishment on the measured surface average value of the Nusselt number. Moreover, the transposition from high Schmidt data $Sc \approx 10^2 \sim 10^3$ to $Sc \approx 1 - 10$ should be investigated by testing intermediary Schmidt numbers when measuring mass transfer coefficient. A more accurate transposition factor due to diffusion effect will naturally lead to quantify more precisely the effect of the gypsum roughness on the mass transfer. Finally, the scaling of the roughness effect by the local Reynolds number should be investigated to verify if a transposition factor can be given for any flow configuration.

Chapter 5 CFD simulations on the steam generator mock-up

5.1 Introduction

Experiments were conducted in a mock-up of a steam generator water box. The retrieved heat and mass transfer coefficient data presented in Chapter 4 make possible the evaluation of CFD codes for heat transfer simulations. The flow configuration of the experiments has been reproduced with commercial CFD softwares and computations of the convective heat transfer coefficient have been performed for Reynolds number in the range $Re \in [10^5, 10^6]$ and Prandtl number in the range $Pr \in [1, 9]$. This chapter presents the different numerical models that have been designed, the data reduction and the results of heat transfer computations on the partition plate of the model. Furthermore, the proper orthogonal decomposition (POD) and Gaussian processes have been used in order to design surrogate models to predict the Nusselt number surface distribution for given Reynolds and Prandtl numbers. Their design and accuracy will be discussed.

5.2 CFD model

5.2.1 Geometry

The geometry of the CFD model is depicted in Figure 5.1. The water first flows through a straight pipe on a distance $L \approx 20D_H$ with D_H the diameter of the pipe. Then it passes through a bended pipe before entering the steam generator water box (SGWB). The flow impinges a plate, which corresponds to the partition plate of a steam generator. The mixing in the water box is important and leads to high transfer rates on the partition plate. Water then flows through a grid, the tubular sheet, before entering a water volume and exiting the test section from the upper part of the geometry.

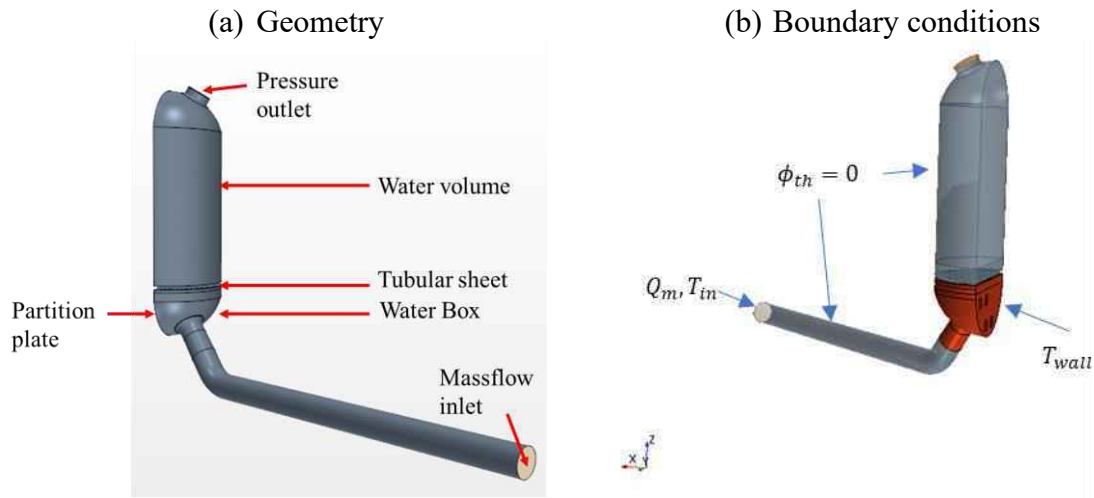


Figure 5.1: CAD model of the SGWB mock-up.

5.2.2 Grid

The simulations done with CFD aim to reproduce the operating conditions covered by the experiments in the steam generator water box mock-up presented in Chapter 4. In these experiments, the flowrates have been set in order to cover the range of Reynolds number $[10^5, 10^6]$. All the CFD models designed for simulations in the SGWB use wall functions (see §1.1.3.5) for the calculation of heat transfer coefficient. The height of the cells adjacent to the flow has been set in order to keep the values of y^+ (see §1.1.3.5) in the range $(30 < y^+ < 300)$ for the Reynolds numbers that were explored. Thus, two grids have been used to constraint the minimum y^+ value:

- LRE (“Low” Reynolds) grid: for the range $Re \in [10^5, 5 \cdot 10^5]$
- HRE (“High” Reynolds) grid: for the range $Re \in [5 \cdot 10^5, 10^6]$

The grids designed for computations with STAR-CCM+ use polyhedral cells, while the one used for Fluent simulations use tetrahedral cells. These meshes will be respectively denoted with the subscript POLY and TET. A grid convergence has been realized in order to estimate the numerical error due to the numerical schemes involved in the resolution of the equations by the solver. The estimation is presented in Chapter 6. This grid convergence has only been carried out for one of the turbulence models tested (Realizable $k - \epsilon$ model). The number of cells in each of the designed grids is indicated in Table 5.1.

Table 5.1 : number of cells in the different grids

GRID	Number of cells
LRE _{POLY}	12 685 520
HRE _{POLY}	8 769 695
LRE _{TET}	11 991 153
HRE _{TET}	11 421 615

5.2.2.1 LRE_{POLY} and HRE_{POLY}

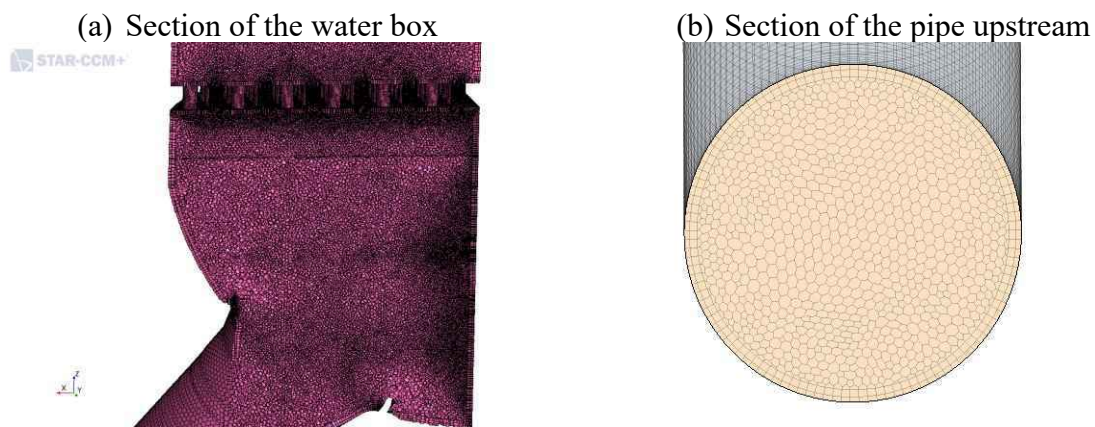


Figure 5.2: view of the grid LRE_{POLY} near the zone of interest: (a) in the water box (b) in the pipe upstream the water box.

The flow domain has been meshed with polyhedral cells in the water box entry box, the tubular plate and the upper part. The grid in the upstream pipe has been done by extruding the mesh at the interface between the pipe and the inlet nozzle of the SGWB downstream the bend in order to have conformal interfaces. The difference between the LRE and HRE meshes is the height of the first prism layer and the total number of prism layer visible on Figure 5.2 in the fluid domain near the walls.

A view of the mesh in the water box and upstream pipe is given on Figure 5.2. The prism layer in the two grids have been set as following:

- In the grid: the minimum non-dimensional wall distance y^+ on the walls is set such as $y_{min}^+ < 1$
- Everywhere else: $y_{min}^+ > 30$

5.2.2.2 LRE_{TET} and HRE_{TET}:

Two grids have been designed for simulations with Fluent. The grids have been realized with tetrahedral cells and prism layers near boundaries. The mesh on the interface between the

upstream pipe and the SGWB has been extruded in the pipe. The same has been executed downstream the tubular plate in order to mesh the upper water volume. The prism layer in the two grids have been designed as following:

- In the grid: $y_{min}^+ < 1$
- Everywhere else: $y_{min}^+ > 30$

A view of the mesh is given on Figure 5.3.

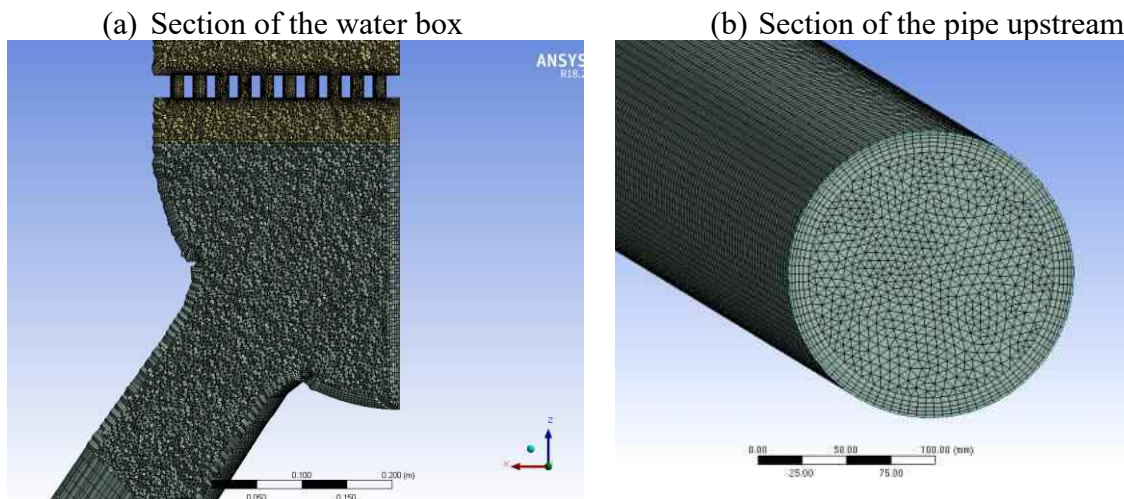


Figure 5.3: view of the grid LRE_{TET} near the zone of interest: (a) in the water box (b) in the pipe upstream the water box.

5.2.3 Physical model

The models that have been adopted for the following simulations are summarized in Table 5.2. The flow is assumed incompressible, with a constant density. Different turbulence models will be compared in this chapter: the Realizable $k - \epsilon$ (RKE), $k - \omega$ SST (KOSST) depicted in §1.1.3.3 will be used for computations on the grids LRE_{POLY} and HRE_{POLY} . Moreover, the simulations were carried out with the Elliptic Blending Reynolds Stress Model (EB-RSM) from (Manceau & Hanjalic, 2002) on this grid. This model is a Reynolds stress transport (RST) model different from eddy viscosity models. RST approaches to model turbulence are more costly as a transport equation is given for each component of the Reynolds stress tensor. Details on this modelling approach can be found in Chapter 11 of (Pope, 2000). The RKE and Scale Adaptive Simulation (SAS) model §1.1.3.3.5 will be used on the grids LRE_{TET} and HRE_{TET} . The near wall meshing has been set in order to guarantee that the non-dimensional wall distance y^+ value (see §1.1.3.5.1) remains such as $y^+ > 30$ everywhere, except on the grid's wall where the mesh has been refined in order to have $y^+ < 1$. Thus, a blended wall law was required and has been used in order to support both cases as depicted in §1.1.3.5.2.

Table 5.2: summary of the physical model for the CFD simulations

Equation	Models
Mass conservation	Incompressible flow
Turbulence	RKE, KOSST, EB-RST, SAS
Equation of state	Constant density
Time evolution	Steady simulation

5.2.4 Boundary conditions and physical properties

The physical properties are given in Table 5.3. The properties are set as constant function of temperature, the specific heat coefficient is parametrized and takes multiple values in order to test different Prandtl numbers.

Table 5.3: physical properties of the fluid

Property	Value
Density	$\rho = 997.561 \text{ kg} \cdot \text{m}^{-3}$
Thermal conductivity	$\lambda = 0.620271 \text{ W} \cdot \text{m}^{-1} \cdot \text{K}^{-1}$
Dynamic viscosity	$\mu = 8.8871 \cdot 10^{-4} \text{ Pa} \cdot \text{s}$
Specific heat	$c_p = \frac{Pr\lambda}{\mu}$

The boundary conditions of the CFD model are depicted on Figure 5.1b. A uniform mass flowrate Q_m is imposed at the inlet of the model, the inlet temperature $T_{in} = 300\text{K}$ is set as constant. The turbulent intensity and turbulent length scale imposed at the inlet are respectively $I_{turb} = 0.1$ and $L_{turb} = 0.1D$ where D is the diameter of the inlet pipe. The boundary conditions in the simulations were set as following:

- A pressure outlet is imposed at the exit of the model
- The walls of the steam generator water box (given in red in Figure 5.1b) are set to be constant at $T_{wall} = 303\text{K}$
- The other walls are set as adiabatic.
- No-slip wall condition is imposed on all walls.

The simulations were also parametrized by the Reynolds number as it has been done in §3.1.3. Once the Reynolds and Prandtl number are chosen, the mass flow inlet is set to $Q_m = \rho \cdot \frac{\pi D^2}{4} \cdot \left(\frac{Re\mu}{\rho D}\right)$ and the specific heat is set to $c_p = \frac{Pr\lambda}{\mu}$.

The CFD runs cover the range $Re \in [10^5, 10^6]$ and $Pr \in [1, 9]$, the design of experiment (DoE) used is given Figure 5.4. The DoE has been adapted differently for computations using STAR-CCM+ and Fluent. The respective simulation inputs of the DoE for both simulations are given

in Appendix C. It has been designed using an in-house tool based on Shannon's information theory and Bayesian statistics in order to maximize the information of the sample. The points $(\mathbf{x}_j)_{j \in [1, M]}$ are taken as realization of a Gaussian process Z with a covariance matrix $C(Z(\mathbf{x}_j), Z(\mathbf{x}_j))$ that has been chosen to be a squared exponential. If we assume that the field that is investigated follows the prior, the design of experiment maximizing Shannon's entropy is the one maximizing the determinant of the covariance matrix. Thus, an optimization procedure is applied on the points $(\mathbf{x}_j)_{j \in [1, M]}$ in order to maximize the determinant of the covariance matrix. This optimization is achieved by switching candidate points of the DoE with other points. The candidates are chosen by evaluating the information content of the points based on their distance from each other. The details on the theory and algorithm will not be covered in this manuscript. A review of the use of Bayesian statistics and information theory for DoE generation can be found in (Chaloner & Verdinelli, 1995).

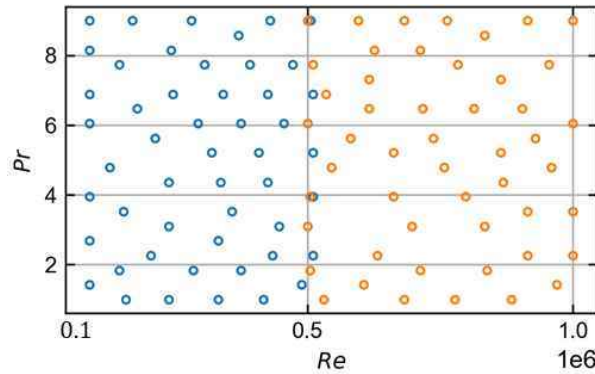


Figure 5.4: design of experiment of the computations for grids LRE (blue) and HRE (red).

5.3 Data reduction

This manuscript focuses on the evolution of the heat transfer coefficient on the partition plate for different flowrates in the mock-up and different diffusive properties. The problem is formulated with dimensionless numbers:

- The diffusive properties of the fluid are given by the Prandtl number
- The turbulent regime for water is given by the Reynolds number.
- The convective heat transfer coefficient is given by the local Nusselt number.

The convective heat transfer coefficient h_{conv} is calculated by the CFD software from the wall heat flux and the wall temperature as following:

$$h_{conv} = \frac{q_w(x, y)}{T_{wall} - T_{ref}}$$

where $q_w(x, y)$ is the wall heat flux obtained from the CFD simulations and T_{ref} is a reference temperature which is chosen to be the inlet temperature in this work. An example of the heat transfer coefficient surface distribution obtained with CFD is given on Figure 5.5. The four visible rectangles give the location of the measurements during the experiments of Chapter 4. The data is extracted on the surface mesh and is then linearly interpolated on a regular grid in order to simplify the comparison with the experiments and the comparison between different grids. Furthermore, the velocity and turbulence of the flow have been extracted on a plane section depicted on Figure 5.6.

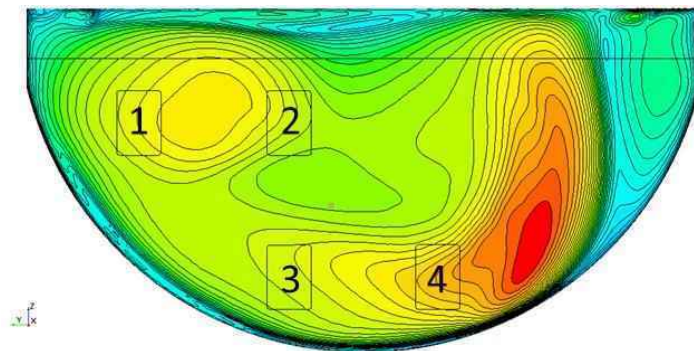


Figure 5.5: heat transfer coefficient surface distribution calculated with CFD at $Re = 10^6$ and $Pr = 6$. Rear view of the partition plate.

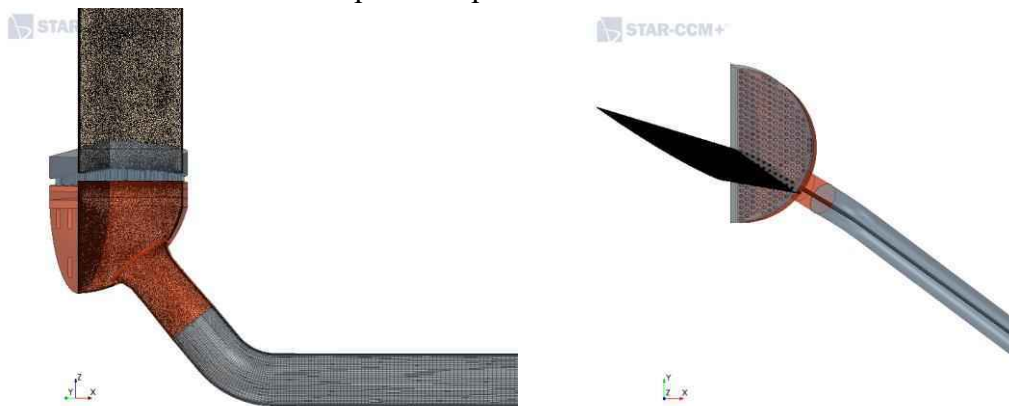


Figure 5.6: view of the vertical plane section including the jet axis on which the velocity field and turbulence is investigated.

5.4 Surrogate models

A surrogate model has been designed for the reconstruction of the Nusselt number on the partition plate for a given turbulence model and grid. This has been carried out for each of the tested turbulence model and for grids LRE and HRE.

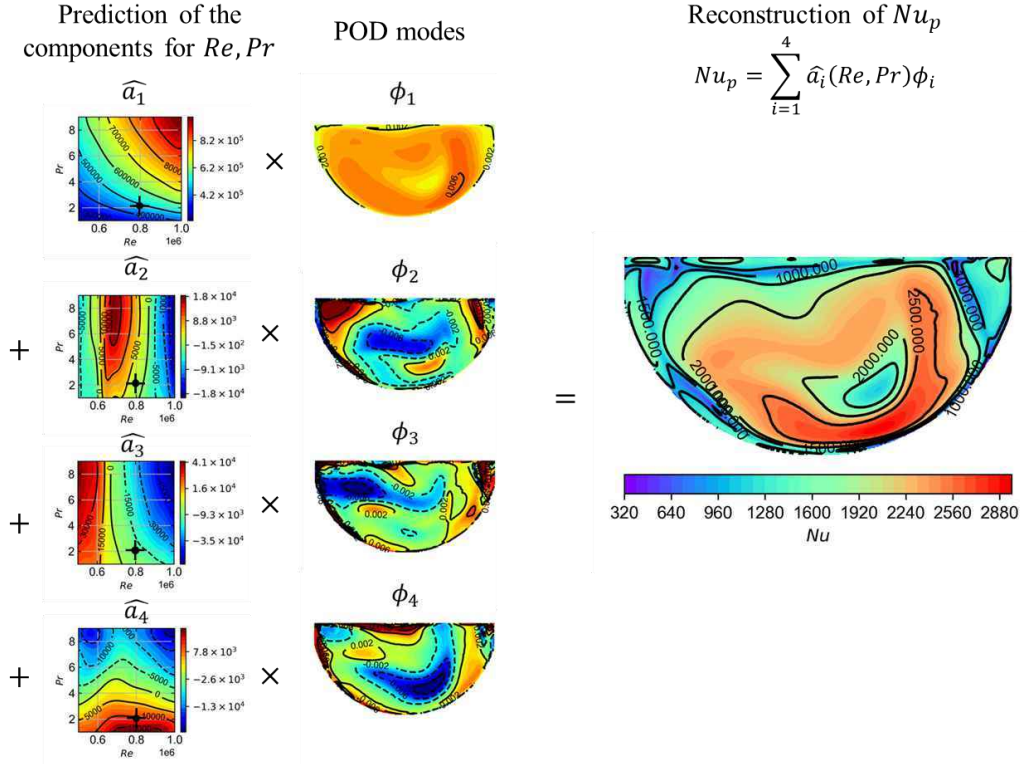


Figure 5.7: Example of prediction of the Nusselt number on the partition plate from the surrogate models \widehat{a}_1 , \widehat{a}_2 , \widehat{a}_3 and \widehat{a}_4 and the modes ϕ_1 , ϕ_2 , ϕ_3 and ϕ_4 for $Re = 8 \cdot 10^5$ and $Pr = 2$. The values of the surrogate models with respect to the Reynolds and Prandtl numbers and the surface distribution of the modes are indicated on a heat map with low values in blue and high values in red. The predicted Nusselt number is indicated on the right side of the figure.

First, the POD has been applied to snapshots of the Nusselt number $(Nu_j)_{1 \leq j \leq N_{SNAP}}$ obtained from the simulation on the DoE given Figure 5.4 with a given model and grid. The POD applied to a snapshot Nu_j for simulation inputs Re_j, Pr_j can be written:

$$Nu_j(Re_j, Pr_j, x, y) = \sum_{n=1}^{N_{SNAP}} a_n(Re_j, Pr_j) \phi_n(x, y)$$

where, a_n are the coefficient of the POD related to the POD modes ϕ_n . A truncation to the r first modes can be done to express the Nusselt number from fewer coefficient and modes at the cost of a truncation error ϵ_r committed when reconstructing the snapshots.

$$Nu_j(Re_j, Pr_j, x, y) = \sum_{n=1}^r a_n(Re_j, Pr_j) \phi_n(x, y) + \epsilon_r(Re_j, Pr_j, x, y)$$

In this work, $r = 4$ has been considered in order to limit the truncation error $\frac{\epsilon_r}{Nu} < 0.05$.

The Nusselt field obtained for arbitrary inputs Re, Pr can also be expressed in the POD base:

$$Nu(Re, Pr, x, y) \approx \sum_{n=1}^r a_n(Re, Pr) \phi_n(x, y) + \epsilon_r(Re, Pr, x, y)$$

Finding the coefficients a_n for these inputs is equivalent to solving an interpolation problem from the realization obtained $(a_n(Re_j, Pr_j))_{1 \leq j \leq N_{SNAP}}$ on the DoE. In this work, gaussian processes (see §1.2.3) were used to predict the four first components of the POD of the Nusselt number. The predictors or surrogate models are denoted $\widehat{a}_1, \widehat{a}_2, \widehat{a}_3$ and \widehat{a}_4 .

The Nusselt number is then reconstructed for arbitrary Reynolds and Prandtl numbers with:

$$\widehat{Nu}(Re, Pr, x, y) = \sum_{n=1}^r \widehat{a}_n(Re, Pr) \phi_n(x, y)$$

The gaussian processes used to predict the components were defined with a squared exponential kernel. A schematic view of the reconstruction from the surrogate models $\widehat{a}_1, \widehat{a}_2, \widehat{a}_3$ and \widehat{a}_4 and the different modes can be seen on Figure 5.7. It is noticeable that the POD enables the reconstruction of the Nusselt number for arbitrary boundary conditions Re, Pr from 4 scalar values $\widehat{a}_1(Re, Pr), \widehat{a}_2(Re, Pr), \widehat{a}_3(Re, Pr)$ and $\widehat{a}_4(Re, Pr)$.

5.5 Results

5.5.1 Introduction

A view of the velocity field for $Re = 10^6$ and $Pr = 6$ is given on Figure 5.8. The velocity V_n is defined from the local velocity \mathbf{u} and the reference velocity U as following:

$$V_n = \frac{\mathbf{u}}{U}, \quad U = \frac{Re \mu}{\rho D}$$

The velocity profile in the upstream pipe is initially flat, then an acceleration of the flow is visible at the bend location in the upper wall, while the flow separates and decelerates at the lower wall. Downstream the bend, the flow is separated in two zones. The flow separation visible on the upper wall leads to the presence of a zone with lower velocity on the upper part of the pipe. On the opposite side, the flow accelerates and is pushed downward.

At the junction of these zone, shear stress is important and leads to higher turbulence. When entering the steam generator water box, the high velocity flow reaches the partition plate and exchanges heat with the fixed temperature wall. The flow then passes through the tubular sheet before entering the upper volume. A reduction of the velocity is visible near the impingement point.

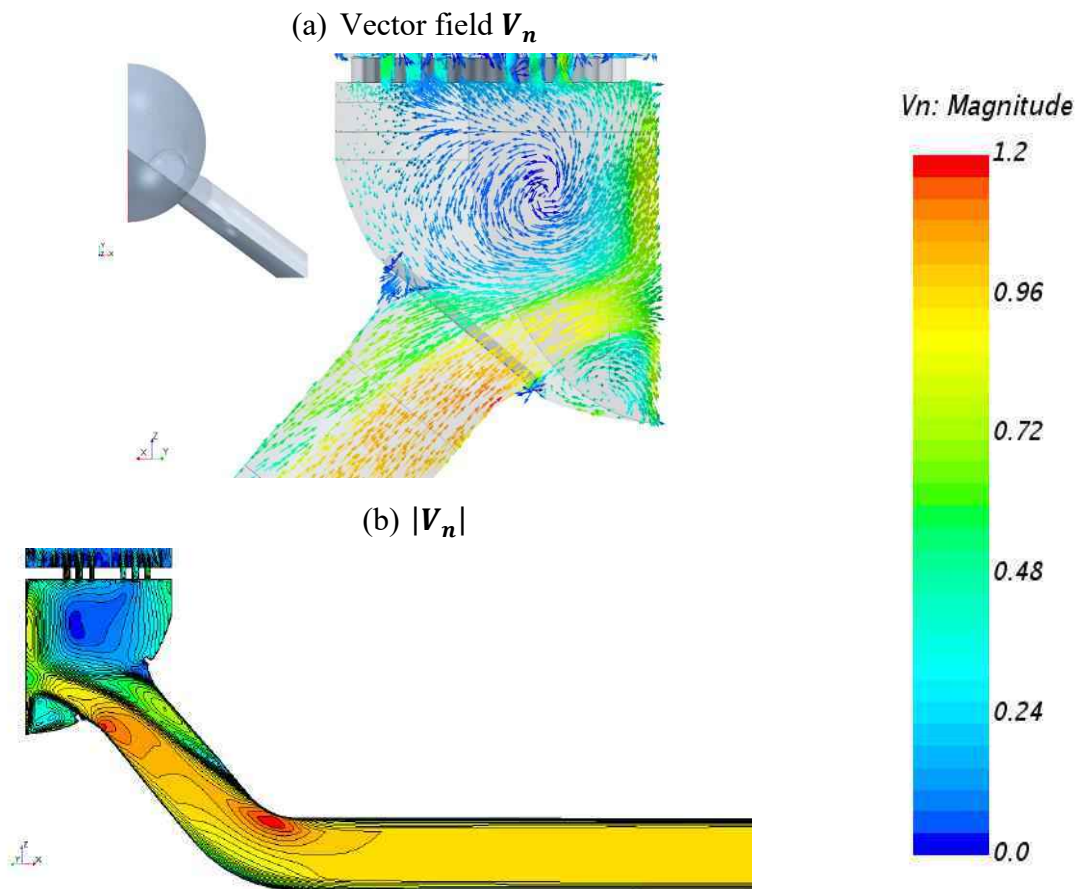


Figure 5.8: view of the velocity on a plane section of the geometry. The magnitude $|V_n|$ is given with a heat map.

The results covered in this chapter focus on the heat transfer coefficient on the partition plate and on the parameters affecting its calculation. The performed simulations made possible the comparison of the heat transfer coefficient in different situations:

- The influence of the type of cell in the grid has been investigated at $Re = 10^6$ and $Pr = 6$ with polyhedral and tetrahedral cells. The computations were carried out with the Realizable $k - \epsilon$ (RKE) turbulence model and with wall functions to allow $y^+ > 30$ meshing. The implementation of this model with two commercial software will be compared.
- The influence of the mesh refinement in the near wall region of the fluid will be examined with two grids at $Re = 5 \cdot 10^5$ and $Pr = 4$.
- The evolution of the Nusselt number surface distribution as a function of the Reynolds and Prandtl numbers will be investigated on the design of experiment (DoE) given Figure 5.4. The different turbulence model tested are the RKE model, the $k - \omega$ SST (KOSST) model, the Elliptic Blending Reynolds stress transport model (EB-RSM) and the Scale Adaptive Simulation (SAS) model.

5.5.2 Influence of the grid

Comparisons between the Nusselt number yielded by Fluent and STAR-CCM+ with HRE_{TET} are given on Figure 5.9a and Figure 5.9b. The Nusselt number obtained through computations with STAR-CCM+ on HRE_{POLY} is given Figure 5.9c. Both simulations were achieved using the Realizable $k - \epsilon$ (RKE) turbulence model with similar wall treatment. The computations were done at $Re = 10^6$ and $Pr = 6$. The stagnation point has been retrieved by looking for the minimum of the velocity near the wall. Its location has been found to fluctuate negligibly around a mean value indicated in blue on Figure 5.9.

Similarities can be noticed on the given Nusselt fields:

- The three fields present banana shaped iso-contours where the Nusselt number takes its maximum values near the stagnation point. This banana shape is included in a central zone delimited by the iso-contour $Nu \approx 4000$.
- A second zone is present on the upper right corner of the partition plate. The velocity in this location is lower resulting in lower Nusselt number.

The size of these zones and the amplitude of the Nusselt number differs in the three cases. The local relative difference between $Nu_{HRE_{TET}}$ obtained with STAR-CCM+ and $Nu_{HRE_{TET}}$ obtained from Fluent on HRE_{TET} at the coordinates (x, y) is calculated as following:

$$\Delta Nu_{SOFTWARE}(x, y) = Nu_{HRE_{TET},S}(x, y) - Nu_{HRE_{TET},F}(x, y)$$

The difference between the two mesh is given by ΔNu_{GRID} making the difference between $Nu_{HRE_{POLY}}$ and $Nu_{HRE_{TET}}$ calculated with STAR-CCM+ on the grid HRE_{POLY} and HRE_{TET} :

$$\Delta Nu_{GRID}(x, y) = Nu_{HRE_{POLY},S}(x, y) - Nu_{HRE_{TET},S}(x, y)$$

The evolution of $\Delta Nu_{SOFTWARE}$ and ΔNu_{GRID} on the partition plate is given on Figure 5.10. The computation with Fluent $Nu_{HRE_{TET},F}$ yields value around 5% to 10% larger than $Nu_{HRE_{TET},S}$ obtained with the same grid with STAR-CCM+.

Furthermore, it can be seen on Figure 5.10a that the difference $\Delta Nu_{SOFTWARE}$ is more important far from the stagnation zone on the far left side of the plate. The demarcation between the main central zone and the secondary zone on the right of the stagnation region presents high gradients of the Nusselt number. Small spatial variations of the distribution of the Nusselt number lead to high differences in this zone. The discrepancies are smaller near the stagnation point. The maximum heat transfer calculated with Fluent is approximatively 6% larger than with STAR-CCM+. Also, differences are noticed on the Nusselt number computed with STAR-CCM+ with mesh HRE_{POLY} and HRE_{TET} Figure 5.10b. Computations with HRE_{TET} yield on average Nusselt number 10% higher than HRE_{POLY} . The Nusselt number differs at the center of the partition plate near the stagnation point. Computations with HRE_{POLY} present a local minimum while none are visible with the tetrahedral mesh.

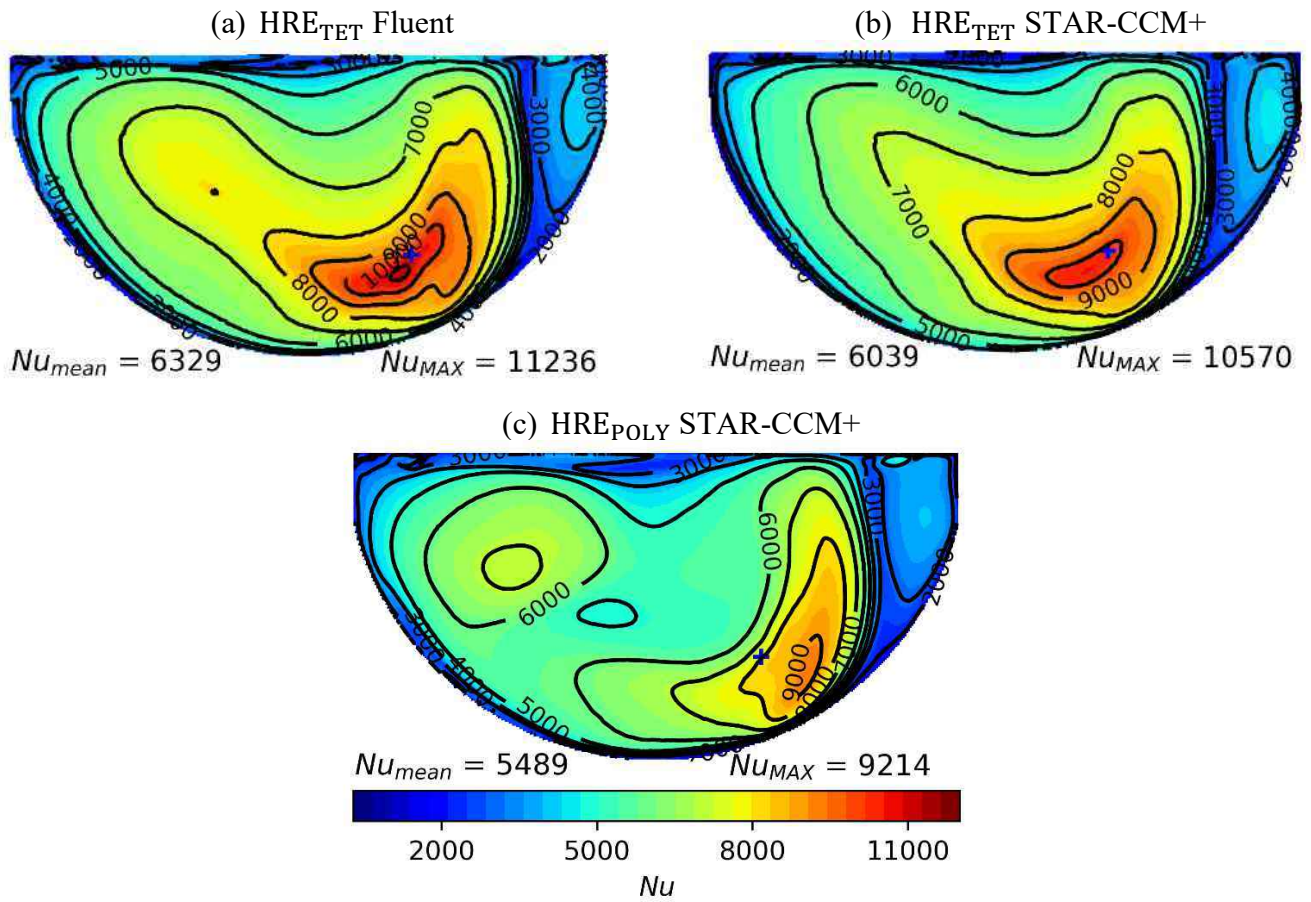


Figure 5.9: comparison of Nusselt number calculated with STAR-CCM+ and Fluent on grid HRE_{TET} and HRE_{POLY} . The comparison is done with the RKE model at $Re = 10^6$ and $Pr = 6$. The blue cross corresponds to the stagnation point.

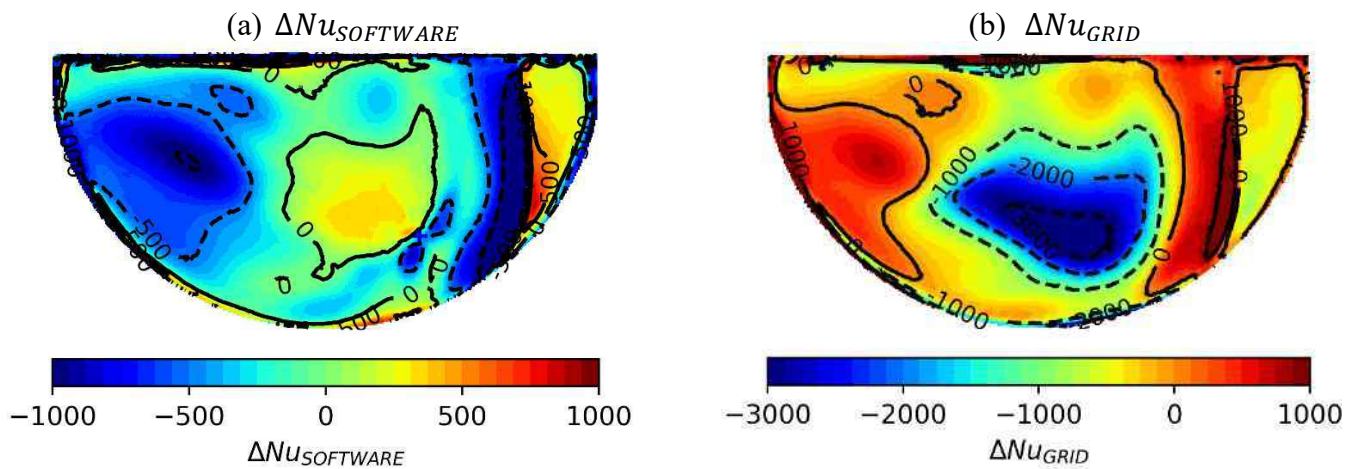


Figure 5.10: surface distribution of ΔNu_{GRID} and $\Delta Nu_{SOFTWARE}$ on the partition plate.

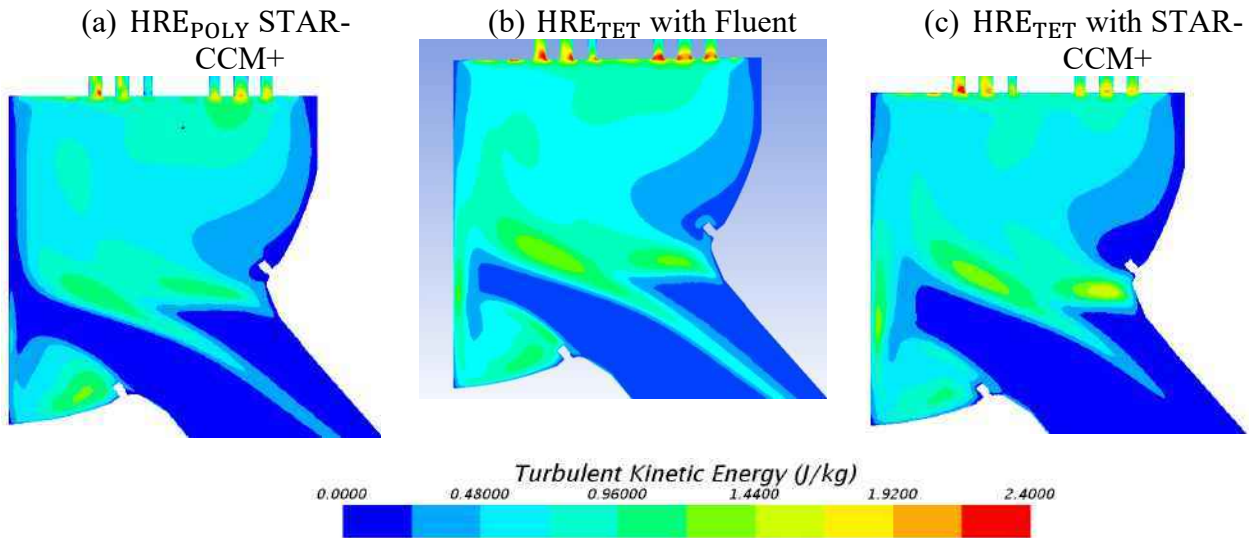


Figure 5.11: comparison of the turbulent kinetic energy computed with (a) STAR-CCM+ on HRE_{POLY}, (b) Fluent and (c) STAR-CCM+ on HRE_{TET} at $Re = 10^6$

These variations might be due to differences in the calculation of the turbulent kinetic energy between the different models. The turbulent kinetic energy k is shown on a plane section containing the jet on Figure 5.11. The velocity difference between the upper and lower regions of the jet depicted on Figure 5.8 leads to shear stress at the junction of these two zones which results in high turbulence kinetic energy. Larger values of k are computed with tetrahedral cells in the shear region around the jet and near the partition plate with tetrahedral meshes. Moreover, the computation with Fluent solver yields higher values of k which could explain the 10% difference on average of the Nusselt number on the partition plate. In the following, simulations with STAR-CCM+ will be carried out on the grids with polyhedral cells and simulations with Fluent with the tetrahedral cells.

At Reynolds numbers around $5 \cdot 10^5$ and $Pr \approx 4$, the computations were performed with both grids LRE, HRE. The variation of the vector field \mathbf{V}_n on the partition plate's vicinity with the different turbulence models has been investigated. The results were obtained with the RKE model, $k - \omega$ SST model (KOSST) and the Elliptic Blending Reynolds stress transport model (EB-RSM) on grids LRE_{POLY} and HRE_{POLY}. A comparison of the velocity fields obtained with the different models is given on Figure 5.12 from the rear of the plate. The vector field \mathbf{V}_n is superposed to contours of the magnitude $|\mathbf{V}_n|$:

- Around the stagnation point for $|\mathbf{V}_n| < 0.6$, the different models and grids give similar surface distribution. On the immediate right side of the stagnation region, differences occur between the different models with LRE_{POLY} grid. In fact, the velocity of the flow going to the bottom right is smaller for the RKE and EB-RSM.
- Differences can be noticed in the zone $|\mathbf{V}_n| > 0.6$. The velocity magnitude varies with the different grids. At the bottom left of the stagnation region; the values of the velocity calculated with the RKE and KOSST models are larger with the HRE grid which yields

lower y^+ values on the cells adjacent to the partition plate. Moreover, the iso contours $|V_n| \approx 0.4$ and 0.6 on the upper left of the plate are further away with HRE_{POLY} leading to lower gradients in this zone.

The local difference $\Delta V_{GRID}(x, y)$ between the grids LRE_{POLY} and HRE_{POLY} is defined as following:

$$\Delta V_{GRID}(x, y) = 2 \frac{|V_n|_{LRE}(x, y) - |V_n|_{HRE}(x, y)}{|V_n|_{LRE}(x, y) + |V_n|_{HRE}(x, y)}$$

This difference corresponds to a relative difference between the calculations of the velocity with the two grids in comparison to the mean velocity $\frac{|V_n|_{LRE}(x, y) + |V_n|_{HRE}(x, y)}{2}$.

The value of $\Delta V_{GRID}(x, y)$ on the partition plate is given on Figure 5.13 for the different turbulent models.

The iso contours computed from the different models show similarities:

- To the right of the stagnation zone, the velocity magnitude obtained with grid HRE is larger than with LRE. A zone is delimited by a banana shaped isocontour $\Delta V_{GRID} \in [10\%, 20\%]$ going from the bottom center of the plate to the upper right.
- A pattern delimited by the iso contours $\Delta V_{GRID} \in [-20\%, 20\%]$ can be seen near the stagnation point. This pattern is present due to the high velocity gradients calculated in this zone where the flow accelerates importantly. Slightly different distributions induce high local differences in these zones.
- For increasing radial distance from the stagnation point, the velocity obtained with the grid LRE becomes larger. The relative difference grows larger due to the scale of the velocity getting lower.

The surface average value on the partition plate of $|V_n|$ denoted $|V_n|_m$ calculated for the two grids LRE and HRE, is given in Table 5.4. The average value $\mu_{|V_n|}$ obtained from the two grids and the surface average value of ΔV_{GRID} denoted $\Delta V_{GRID,m}$ is also given. It can be noticed that the RKE model and EB-RSM model are less affected than the KOSST model showing more important variations. The KOSST gets closer to RKE and EB-RSM models with the HRE grid which has y^+ values closer to 30 on the cells adjacent to the plate. The larger value of $\sigma_{|V|}$ for the KOSST might be due to the non-convergence of the grid for calculations with this model. In fact, the HRE_{POLY} grid contains less cells than the LRE_{POLY} grid. This has been found to affect only slightly the field with the RKE model when the grid convergence was done, however, the simulation with the KOSST might require more refined meshes.

The near wall mesh refinement of the fluid domain has been shown to be of importance in the computations of the near wall velocity. The high gradients zone located near the stagnation zone where the flow accelerates is the most sensitive to the y^+ values on the plate. However, as it has been shown for the RKE and EB-RSM turbulence model, the mean velocity over the partition plate is only slightly affected. High relative differences are also present in low velocity regions far from the stagnation region.

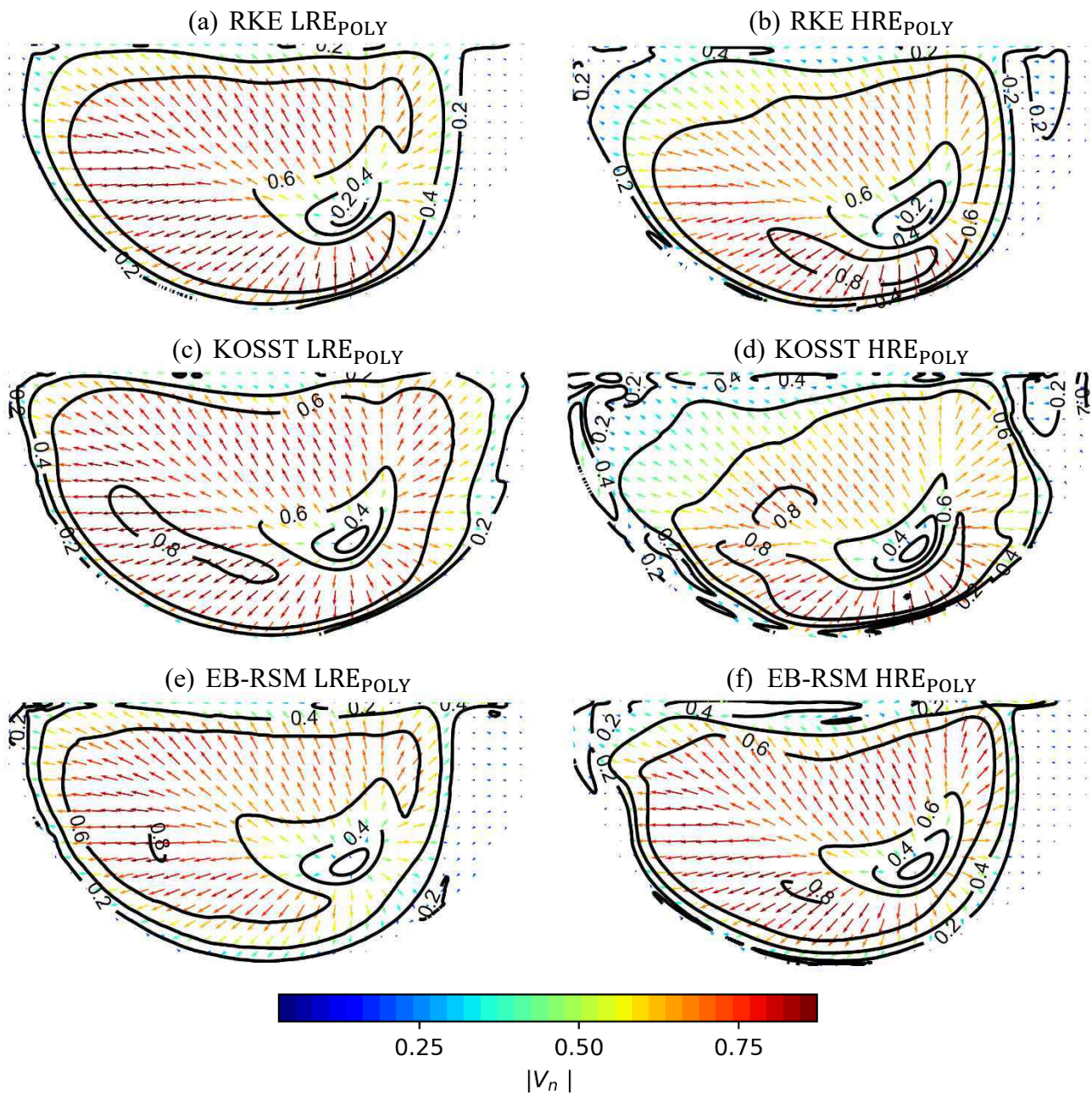


Figure 5.12: velocity on the first cell next to the partition plate. Computations with the polyhedral mesh for $Re \approx 5 \cdot 10^5$ and $Pr \approx 4$

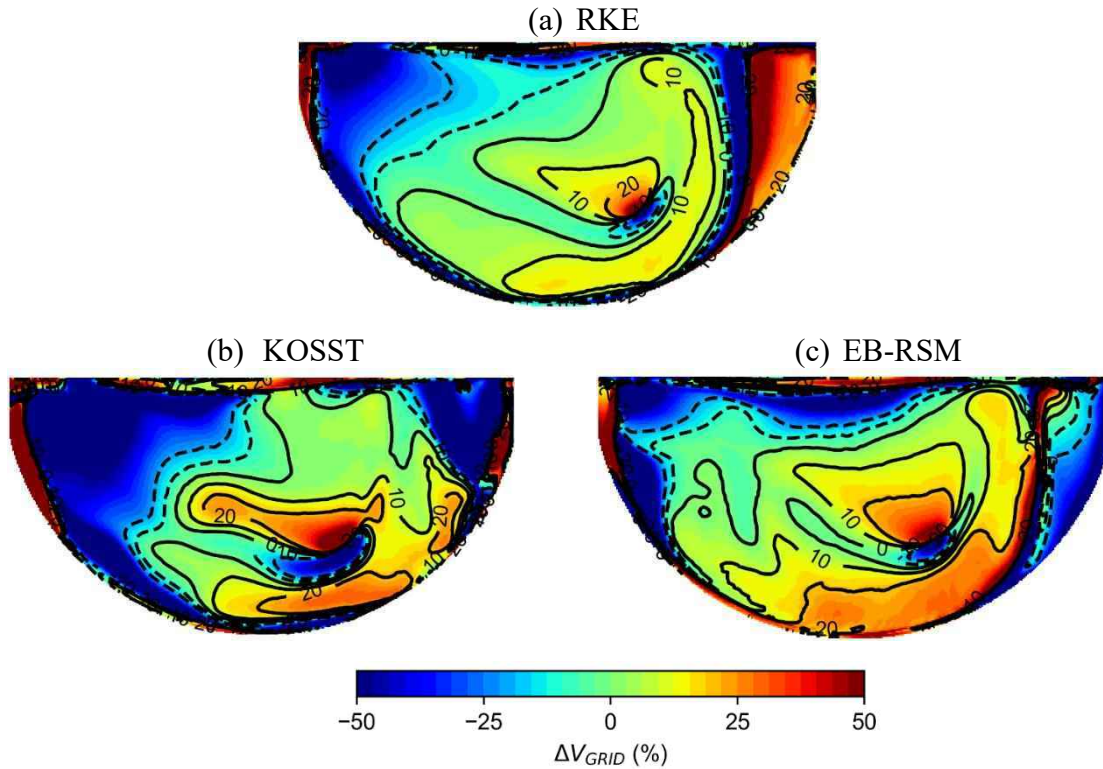


Figure 5.13: ΔV_{GRID} for the different computations at $Re = 5 \cdot 10^5$ and $Pr = 4$ obtained on the polyhedral mesh

Table 5.4: statistics on the field $|\mathbf{V}_n|$ for the different computations.

	$ \mathbf{V}_n _{LRE,m}$	$ \mathbf{V}_n _{HRE,m}$	$\mu_{ \mathbf{V}_n }$	$\Delta V_{GRID,m}$
RKE	0.5088	0.4969	0.5028	2%
KOSST	0.5881	0.5371	0.5626	9%
EB-RSM	0.4782	0.4886	0.4834	-2%

5.5.3 Surface distribution of the Nusselt number

5.5.3.1 Overview

The surface distribution of the Nusselt number on the grids LRE_{TET} and HRE_{TET} are given on Figure 5.14. The computations are carried out with the RKE model and Scale Adaptive Simulation (SAS) model with Fluent at $Re = 5.5 \cdot 10^5$ and $Pr \approx 4$. The Nusselt number obtained with STAR-CCM+ on LRE_{POLY} and HRE_{POLY} with the RKE model, $k - \omega$ SST model (KOSST) and the Elliptic Blending Reynolds stress transport model (EB-RSM) are given on Figure 5.15. Moreover, the maximum Nusselt number Nu_{MAX} and, the mean value and standard deviation of the minimum y^+ on the plate $\mu_{y^+} \pm 2\sigma_{y^+}$ are given for each case.

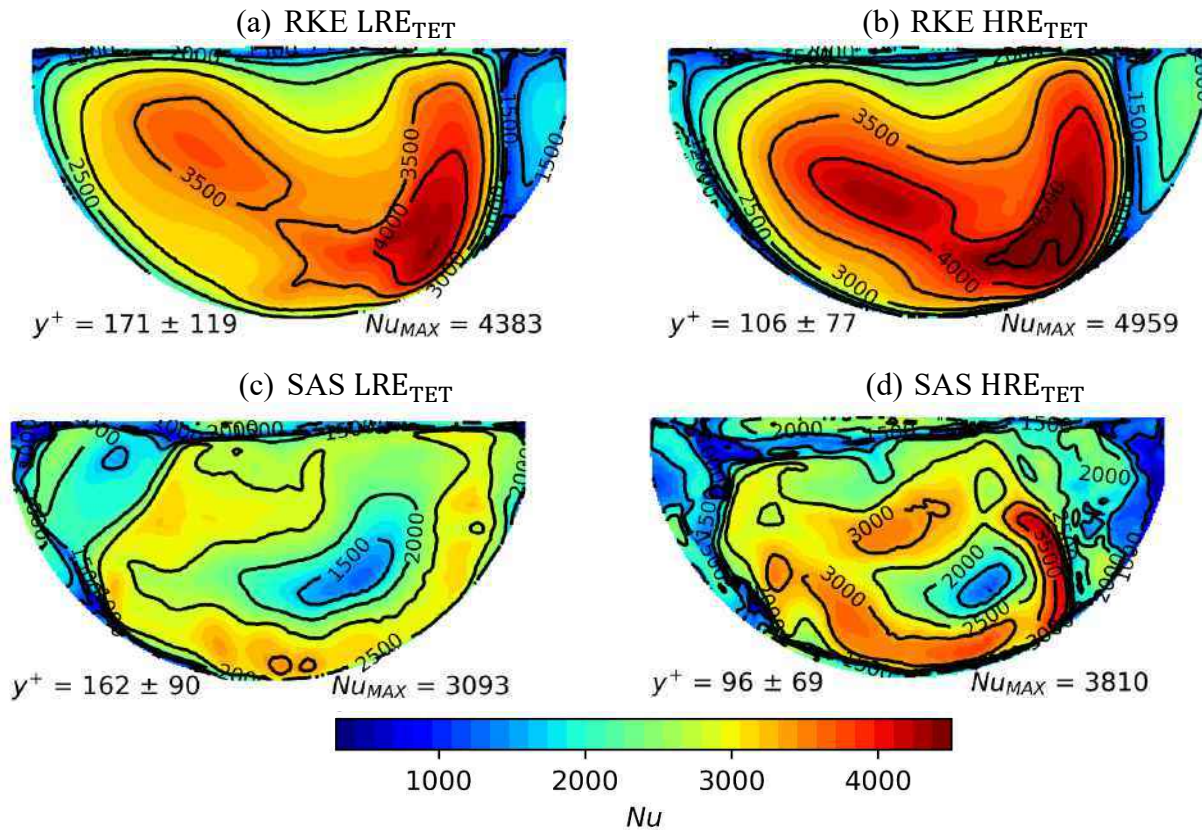


Figure 5.14: surface distribution of the Nusselt number on the partition plate at $Re \approx 5.5 \cdot 10^5$ $Pr \approx 4$ for the different turbulence models on grids LRE_{TET} and HRE_{TET}.

Differences are noticed between the SAS model and the RKE model on LRE_{TET}, HRE_{TET}:

- The Nusselt number computed with the RKE model is significantly higher than the SAS.
- The RKE model do not include a local minimum at the center of the plate contrarily to the SAS model as it has already been found in Figure 5.9.
- For the SAS model, the surface distribution of the Nusselt number has been calculated through the time averaging of a transient simulation with fixed boundary conditions. The resulting field is noisier than with the RKE model. The residuals have been monitored to insure the convergence of the computations. This aspect might disappear by averaging the fields over longer time.
- The results obtained with HRE_{TET} with lower y^+ values yield higher gradients of the Nusselt number around the stagnation zone. The main aspect of both surface distribution are unchanged.

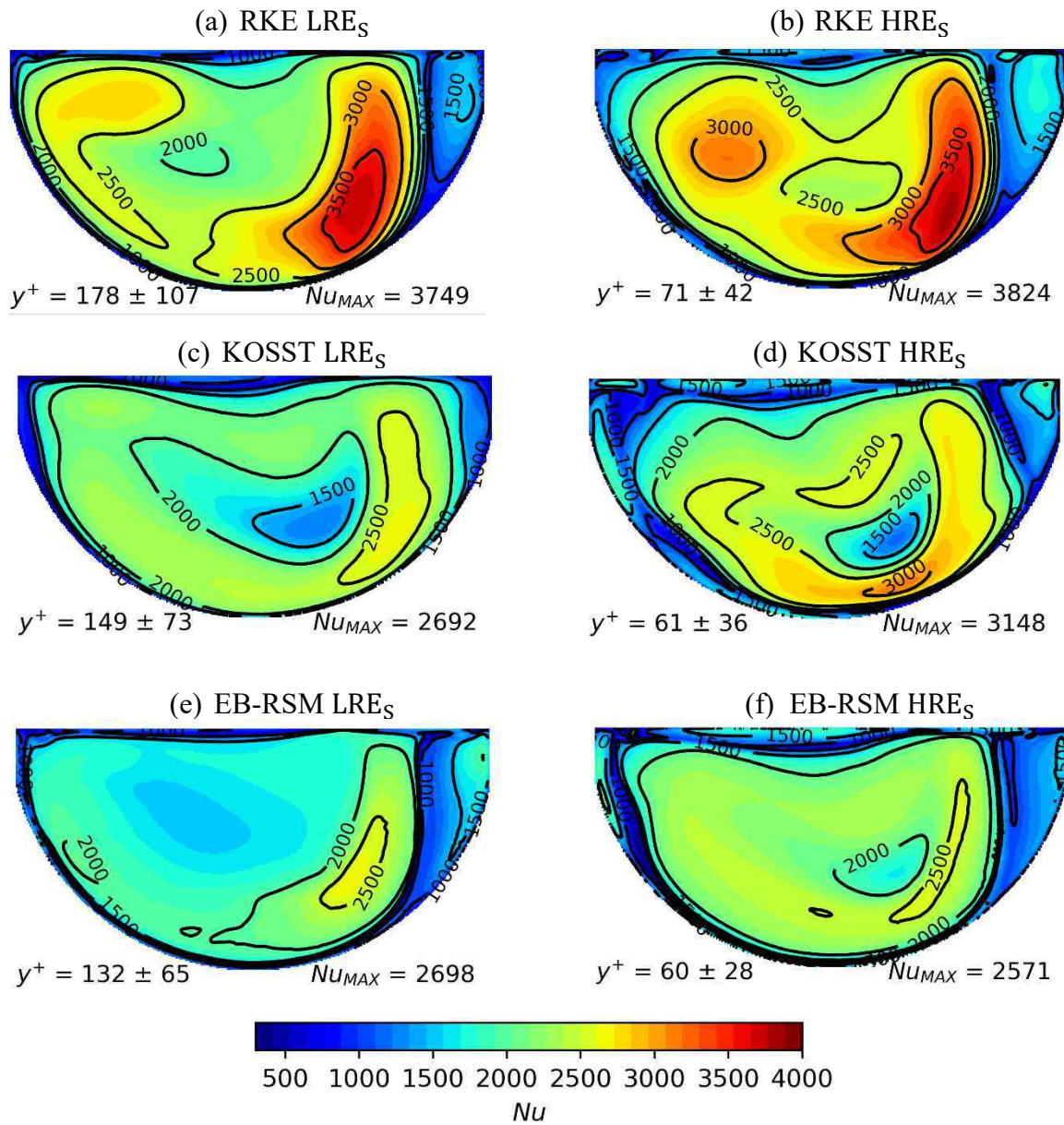


Figure 5.15: surface distribution of the Nusselt number on the partition plate at $Re \approx 4.8 \cdot 10^5$ $Pr \approx 4$ for the different turbulence models on grids LRE_S and HRE_S.

The surface distribution of the Nusselt number obtained from the polyhedral grids LRE_{POLY}, HRE_{POLY} with all the turbulence models presents some similarities. A local minimum is found around the stagnation region. On the right side of this minimum transfer region, a banana shaped zone where the Nusselt number takes its maximum values is visible. On the right of this banana shaped zone, a low Nusselt number region is present for all the cases.

The amplitude, location and shape of these zones differ according to the turbulence model and y^+ values:

- The amplitude of the Nusselt number differs significantly between the turbulence models. The RKE presents the highest values of the Nusselt number.
- The shape and location of the iso contours near the local minimum are sensitive to the y^+ values. High y^+ values on the partition plate result in the translation of the local minimum on the upper left of its location for lower y^+ values. The translation for the RKE and EB-RSM are significant when compared to the translation of the iso contours of the velocity profile presented in §5.5.2.
- The amplitude of the Nusselt number differs with the y^+ values. The RKE model is the less sensitive to these variations while the results obtained from the KOSST and EB-RSM show significant variations.

In conclusion of this first study, the structure of the iso contours of the Nusselt number on the partition plate is similar for all the turbulence models except for the RKE model runs on the tetrahedral grid. However, significant differences are observed regarding the amplitude and location of the isocontours on the partition plate. The model yielding the lowest values of the Nusselt number is the EB-RSM, while the RKE yields the highest values. The KOSST yields approximately 22% lower values of the maximum Nusselt number than the RKE on equivalent grids, which is comparable to the 28% calculated between the SAS and the RKE on the same grids. Finally, the near wall y^+ value has been found to affect the computation of the Nusselt number with the different turbulent models. The RKE using the polyhedral grid is the less sensitive model. The KOSST, EB-RSM and SAS show important variations of the Nusselt surface distribution, mean value and maximum value. This might be due to the fact that the grid convergence which led to the choice of LRE_{POLY} and HRE_{POLY} was realized with RKE simulations. The quality might not be sufficient and is likely to impair the accuracy of the results for too high y^+ values near $Re = 5 \cdot 10^5$ with grids LRE and near $Re = 10^6$ with grids HRE.

The differences between these different models when modelling the heat transfer on the plate are discussed in (Zuckerman & Lior, 2006) which makes a review of the results of numerical studies concerning the heat transfer prediction on plates impinged by turbulent jets. Hybrid methods (such as SAS) and SST methods (as KOSST) are found to have similar performance regarding the prediction of the locations of the maximum values while the performance of RKE are found to be slightly lower on this aspect. In addition, important errors can be anticipated regarding the magnitude of the Nusselt number which are between 15% to 40% depending on the model. In comparison, Reynolds stress models have been found to predict the amplitude of the Nusselt number with a more important error. Considering all these aspects and the cost associated to computations with these models, KOSST, SAS and RKE models should be favored for the predictions of heat transfer coefficient for impinging jet configurations.

5.5.3.2 Nusselt number on the measurement locations

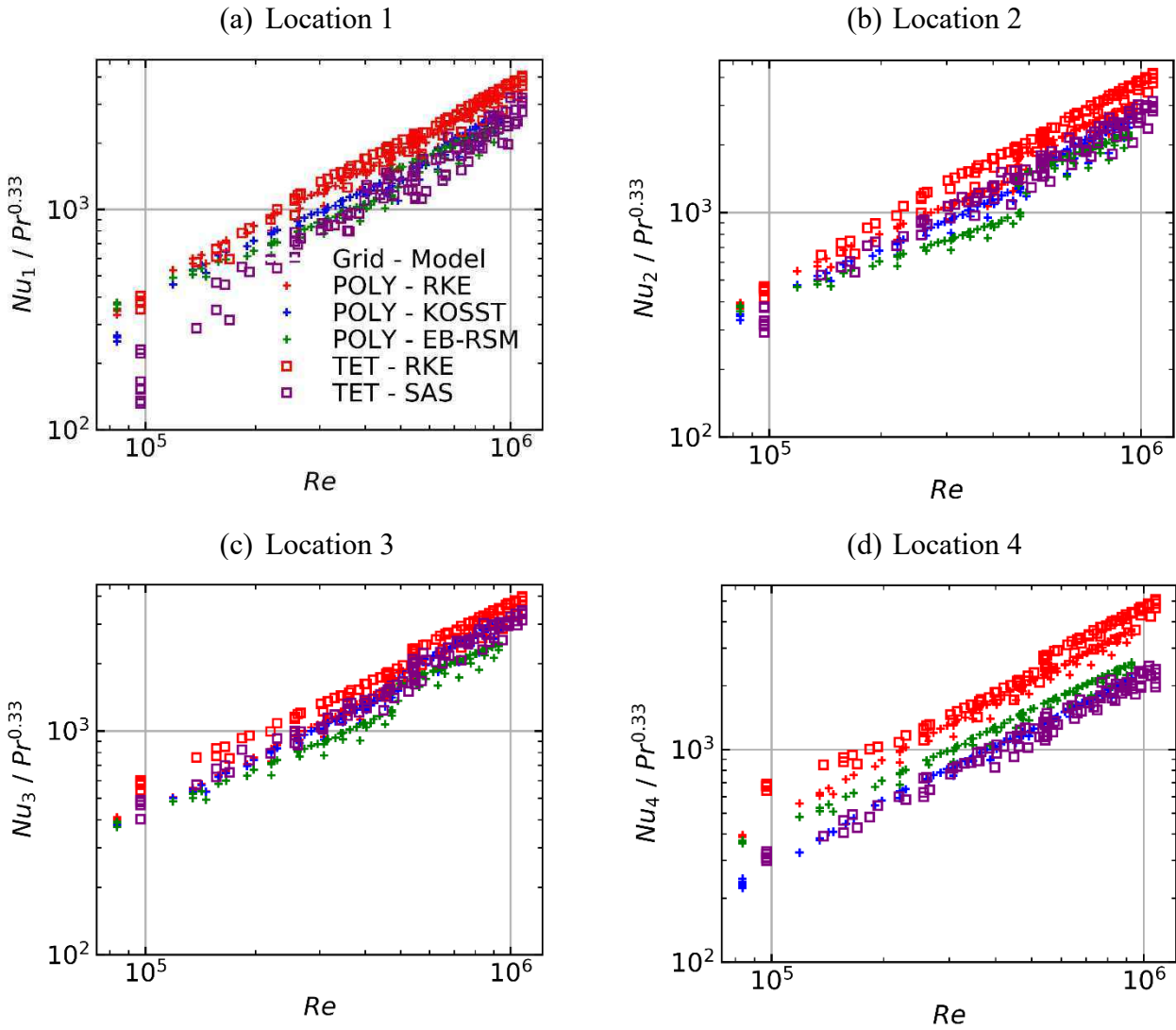


Figure 5.16: evolution of the surface average Nusselt number calculated on the different measurements locations of the partition plate for the different turbulence models. a) Nu_1 , b) Nu_2 , c) Nu_3 and d) Nu_4 .

The surface average Nusselt number obtained on the measurement locations depicted in Figure 5.5 are retrieved and studied as a function of the Reynolds number on the design of experiment presented Figure 5.4. The surface average value of the Nusselt number on the locations 1, 2, 3 and 4 are denoted respectively Nu_1 , Nu_2 , Nu_3 and Nu_4 . The values obtained from different Prandtl numbers simulations are scaled with $Pr^{0.33}$ to be comparable. It is noticeable that the RKE model simulations on the tetrahedral and polyhedral grids yield the larger values of the Nusselt number on all locations.

Some differences are observed between the results obtained with the RKE model on polyhedral and tetrahedral grids. These differences were observed in §5.5.2 and seem to be due mainly to the difference of the grids.

The values of the Nusselt number obtained from the SAS and KOSST simulations are close to each other. In addition, the amplitude of the Nusselt number is approximately 25% lower with these models than the RKE model on locations 2 and 3 where the velocity is the highest on the plate. The largest differences between the models are observed on location 4 which is the closest from the stagnation region. On these locations, the RKE model yields larger values of the Nusselt number.

The simulations with the SAS model at low Reynolds were not sufficiently converged which is visible on location 1 where high variability of the Nusselt distribution was observed. On location 2 and 3, the discrepancy between the values obtained with the EB-RSM and the other models increases near $Re \approx 5 \cdot 10^5$ separating the two grids LRE and HRE. This indicates an increased sensibility of the EB-RSM to high values of the y^+ value on the cells adjacent to the partition plate.

5.5.3.3 Variations with the Reynolds and the Prandtl number

The surface distribution of the Nusselt number evolves with respect to the Reynolds and Prandtl numbers. An example is given on Figure 5.17 for the computations made for $Re = 5 \cdot 10^5$ and $Re = 10^6$ at $Pr = 6$. It can be noticed that increasing the Reynolds number has the effect of elongating the iso-contours of the Nusselt number delimiting the stagnation region for all the turbulence models.

The proper orthogonal decomposition (POD) is applied to the snapshots of the Nusselt number distribution on the partition plate in order to study its evolution with the Reynolds and Prandtl number as depicted in §5.4. The POD is truncated to $r = 4$ modes and components from the original 50 modes that were calculated from the 50 snapshots, in order to limit the mean truncation error over the partition to 5%. The mean absolute error (MAE) between a snapshot of the Nusselt number on the partition plate Nu_j and the truncated POD of this snapshot at order r , $Nu_{j,r}$ is calculated with:

$$MAE(Re, Pr) = \left\langle \frac{|Nu_j(x, y, Re, Pr) - Nu_{j,r}(x, y, Re, Pr)|}{Nu_j(x, y, Re, Pr)} \right\rangle_S$$

where, $\langle \cdot \rangle_S$ is the surface average value over the plate's surface. The evolution of the MAE on the design of experiment and other details on the POD can be found in Appendix D.

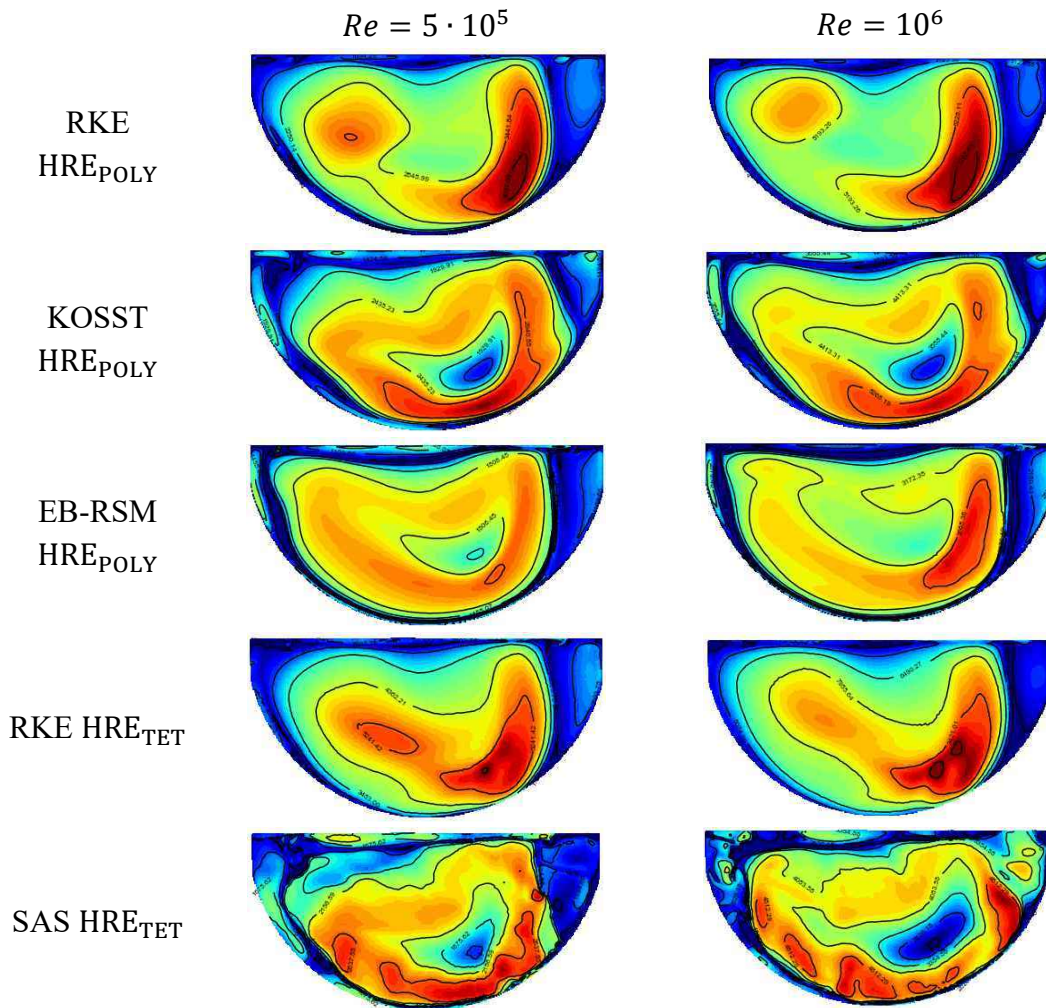


Figure 5.17: evolution of the surface distribution between $Re = 5 \cdot 10^5$ and $Re = 10^6$ at $Pr = 6$. The scale has been adapted by dividing the Nusselt by its maximum value.

Differences around 5% were observed locally on the partition plate in high gradients zones due to the displacement of some contours with evolving Reynolds and Prandtl numbers. The evolution of the MAE for the different models have been found to decrease with respect to the Reynolds number.

- For simulations performed with the RKE turbulence model on LRE_{POLY} , the MAE has been found to be go from 5% for the lower Reynolds numbers, to values lower than 2% for $Re > 2 \cdot 10^5$. On HRE_{POLY} , the error remains under 0.5%.
- The MAE calculated for the reconstruction of the Nusselt number with the RKE turbulence model on LRE_{TET} and HRE_{TET} yields slightly higher errors than for the polyhedral grid. The error remains lower than 4% for $Re > 2 \cdot 10^5$ and reaches 2% at $Re > 3 \cdot 10^5$. On the HRE_{TET} grid, the accuracy is higher and remains globally under 1%.

- For the KOSST model simulations conducted on LRE_{POLY} and HRE_{POLY} , the MAE is around 5% for the lowest Reynolds numbers then decreases and remains around 1-2% for the cases $Re > 2 \cdot 10^5$ except for some isolated snapshots where the MAE is around 2.5-3%
- Similar truncation errors are observed for the reconstruction of the Nusselt number surface distribution calculated with the EB-RSM model, the MAE calculated vary from around 6% to 2-3% on the LRE_{POLY} grid. Then MAE remains around 1-1.5% on HRE_{POLY} .
- The surface distribution of the Nusselt number on the partition plate computed with the SAS model fluctuates more than with the other models. The MAE is found to vary from 30% at $Re = 10^5$ to values in the range 15%-25% for $Re > 2 \cdot 10^5$.

The four modes ϕ_1, ϕ_2, ϕ_3 and ϕ_4 obtained from the POD of the Nusselt number distribution calculated from the RKE simulations on the grid LRE_{POLY} and HRE_{POLY} are given respectively on Figure 5.18 and Figure 5.19. The related POD components a_1, a_2, a_3 and a_4 are calculated for the snapshots of the design of experiment given Figure 5.4. Interpolation are then done in order to predict the values of the components for arbitrary Reynolds and Prandtl numbers in the Reynolds-Prandtl domain as indicate in §5.4. The surrogate models for the predictions of the components are denoted $\widehat{a}_1, \widehat{a}_2, \widehat{a}_3$ and \widehat{a}_4 . Iso contours of the predictions are given Figure 5.20.

The comparison of both grids is analyzed:

- The first mode ϕ_1 is approximatively the same for the two meshes. It gives the general shape of the surface distribution of the Nusselt number. The banana shape is visible and the local minimum as well. The evolution of the component \widehat{a}_1 on the Reynolds Prandtl domain for both grids do not presents any peaks or valleys. The component increase is correlated to both the increase of the Reynolds and Prandtl number.
- The second mode ϕ_2 of the two grids show similar aspects with opposite signs. The same can be said for the isocontours of the components \widehat{a}_2 calculated with the two grids showing. This mode affects the spreading of the stagnation zone and pushes the zone with high values of the Nusselt number away. The evolution of the components is affected by both the Reynolds and the Prandtl number. For high Reynolds numbers, the Prandtl numbers effect is negligible, the isocontours tend to be vertical lines. The spacing between these lines starts to increase significantly for $Pr < 3$.
- The modes ϕ_3 obtained on LRE_{POLY} and ϕ_4 on HRE_{POLY} simulations are similar to mode ϕ_2 . The components are mainly affected by the Reynolds number, moreover, its presence is related to the evolution of the local minimum on the upper left of the partition plate. As a result, the pattern visible on modes ϕ_1 including a local maximum on the upper left region is pushed outwards for large Reynolds values.
- Finally, the last mode ϕ_4 with LRE_{POLY} and ϕ_3 with HRE_{POLY} affects the Nusselt number at the center of the partition plate which decreases for higher Prandtl numbers.

The components are mainly affected by the Prandtl number. The differences between the two grids is higher close to the tubular plate and on the bottom left near the border.

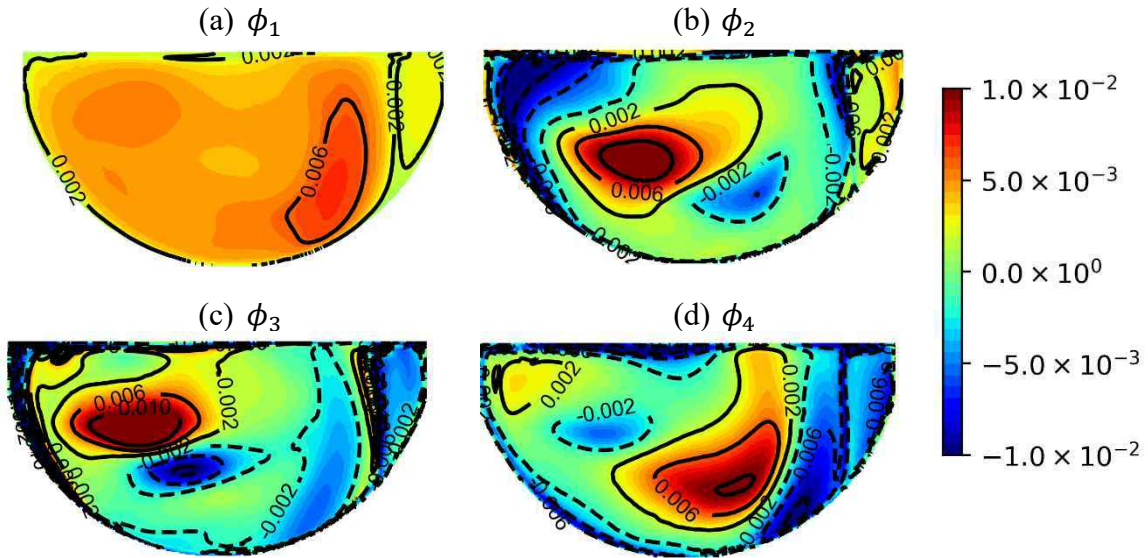


Figure 5.18: modes calculated with the snapshots of the Nusselt number with the RKE model on grid LRE_{POLY}

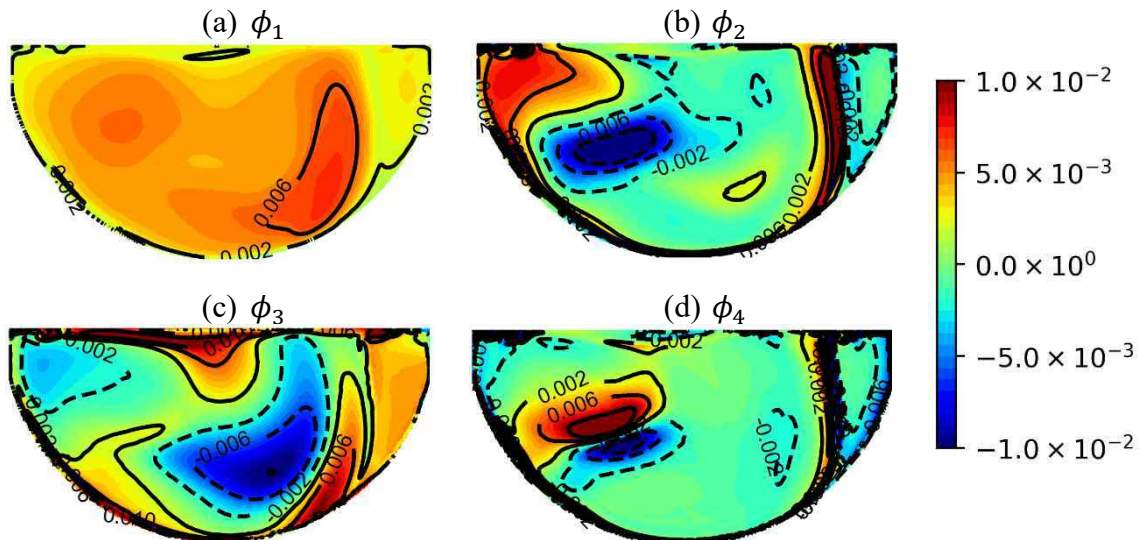


Figure 5.19: modes calculated with the snapshots of the Nusselt number obtained with the RKE model on grid HRE_{POLY}

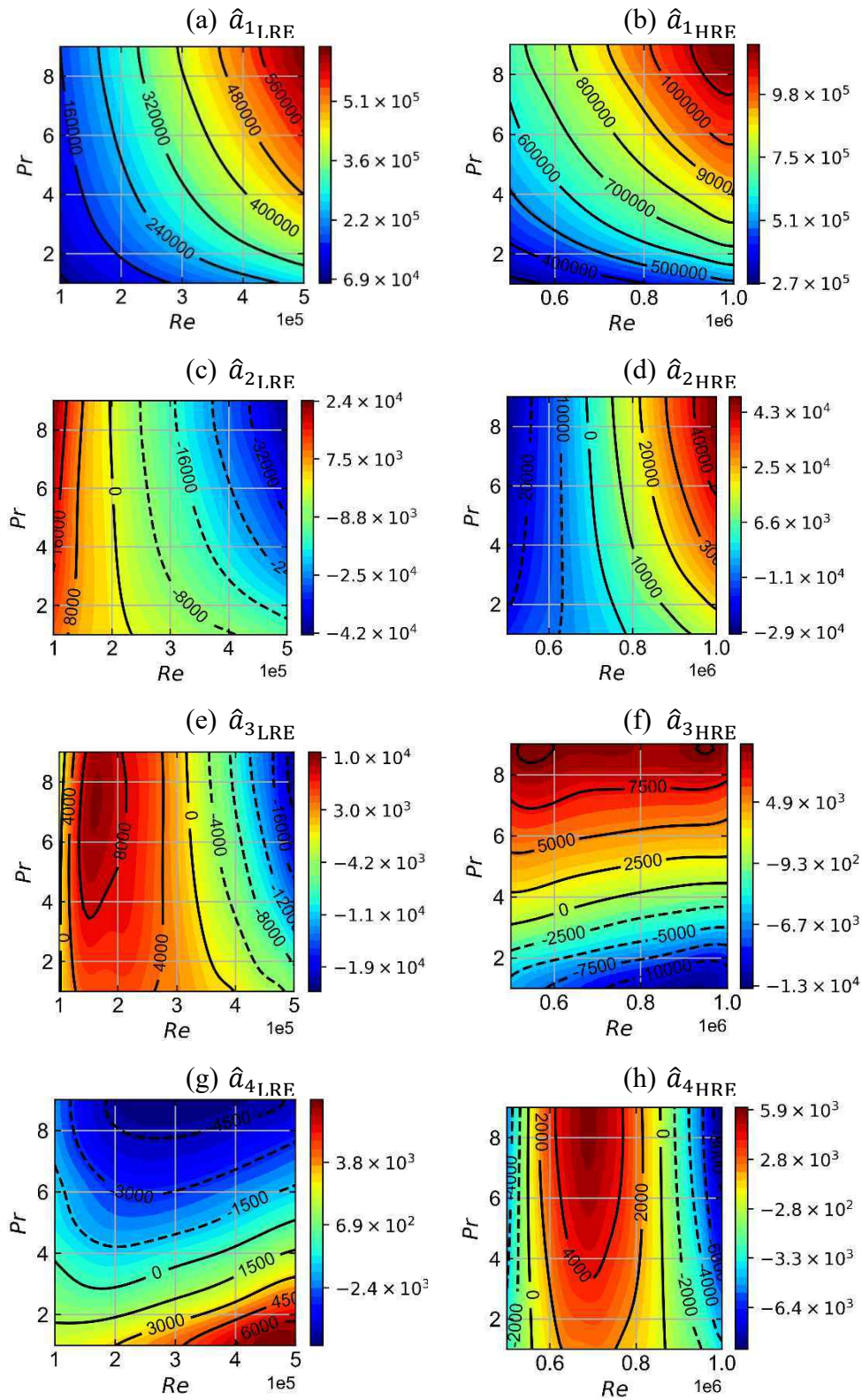


Figure 5.20: predictions of the components associated to the modes obtained with the RKE model on grids LRE_{POLY} and HRE_{POLY} . The predicted values are given with a heat map.

The process has been repeated for the other turbulence models. The details of the POD modes and of the components' evolution are given in Appendix D. The results were similar to the ones obtained for the RKE turbulence model simulations: the first mode gives the mean surface distribution of the Nusselt number, and its component increases monotonously as a function of the Reynolds and Prandtl numbers. Two modes ϕ_2 and ϕ_3 (or ϕ_4) depend mainly on the Reynolds number and affect the spread of the local minimum of the Nusselt number. Finally, the fourth mode ϕ_4 (or ϕ_3 in some cases) affects the Nusselt on the center of the partition plate and depends only on the Prandtl number. Some differences were noticed such as:

- The waviness of the iso-contours of the components a_3 and a_4 on the Design of Experiment (DoE) range (except for the RKE model on the tetrahedral grid): in general, the data included more noise than the RKE model which can explain this tendency.
- The SAS model third and fourth modes are too noisy, the components could not be predicted accurately. Thus, these modes have not been kept for the reconstruction of the Nusselt number.

The accuracy of the prediction on the Nusselt number distribution \widehat{Nu} with the process depicted §5.4 is estimated with the absolute error between \widehat{Nu} on the DoE points Re_j, Pr_j and the snapshots Nu_j obtained for identic inputs (Re_j, Pr_j) on the partition plate with:

$$\Delta Nu_{surrogate,j} = 2 \frac{|\widehat{Nu}(Re_j, Pr_j) - Nu_j|}{\widehat{Nu}(Re_j, Pr_j) + Nu_j}$$

where, $\frac{\widehat{Nu}(Re_j, Pr_j) + Nu_j}{2}$ is the mean value between both values of the Nusselt number.

The mean value and standard deviation of $\Delta Nu_{surrogate,j}$ over all the snapshots $(Nu_j)_{1 \leq j \leq N_{SNAP}}$ has been calculated in order to estimate the local values of the error when predicting the Nusselt number distribution with the surrogate model. The surface distribution of the mean local error $\mu_{\Delta Nu_{surrogate}}$ is given on Figure 5.21 for the different grids and turbulence model. It can be noticed that $\mu_{\Delta Nu_{surrogate}}$ is of the same order of magnitude than the error between the original snapshots of the Nusselt number and their truncated POD. The additional error due to surrogate modelling is negligible when compared to the truncation error.

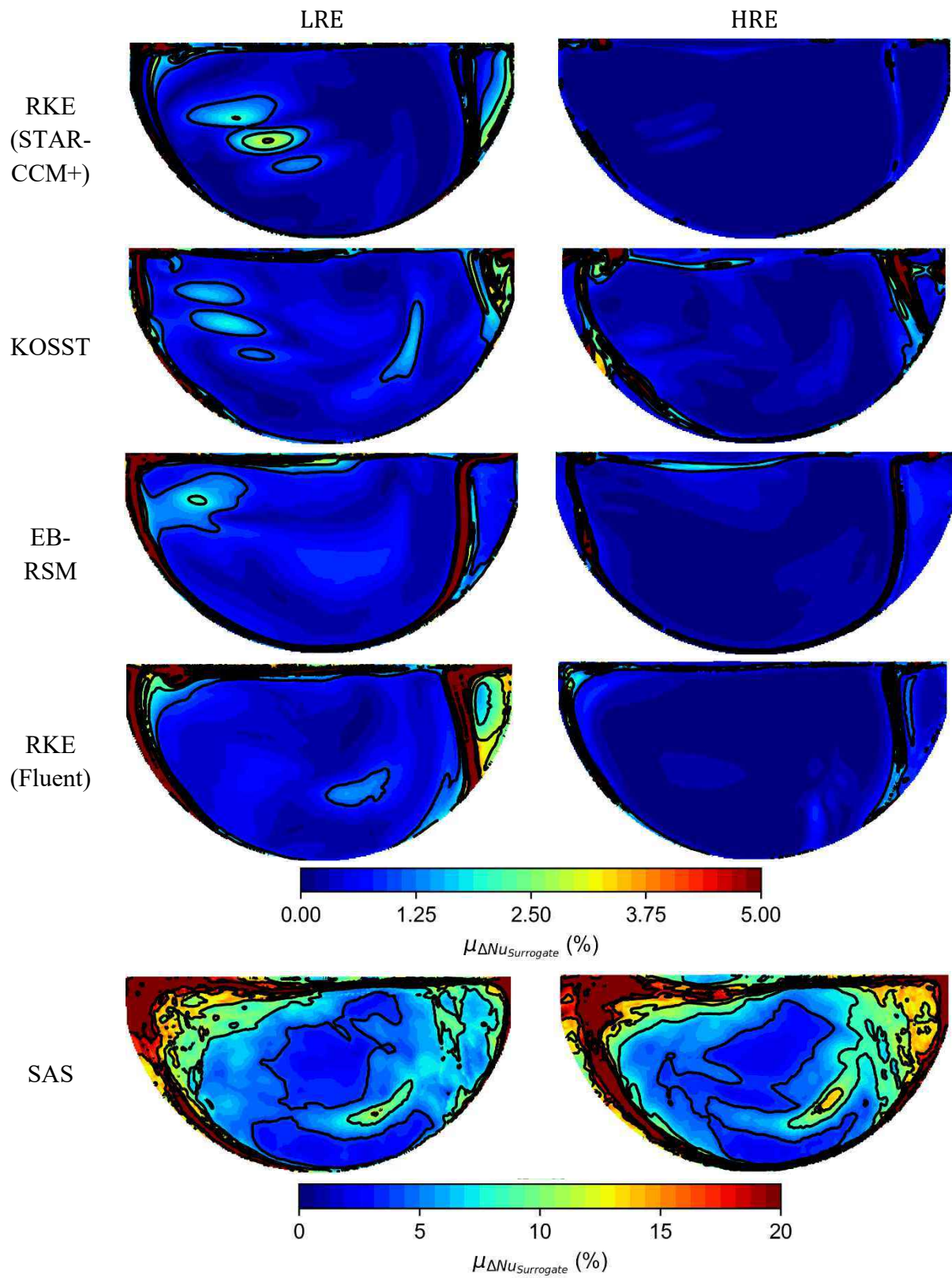


Figure 5.21: evolution of $\mu_{\Delta Nu_{Surrogate}}$ on the partition plate for the different models.

5.6 Conclusion

The experiments on the steam generator presented in Chapter 4 were reproduced with CFD simulations. Different turbulence models and grids have been tested, yielding different Nusselt number on the partition plate where the measurements have been done.

The importance of the grid has been investigated and it has been found that for equal model (RKE), tetrahedral grids and polyhedral grids yield different results regarding the Nusselt number distribution on the partition plate. This difference seems related to differences in the calculation of the turbulent quantities near the plate, where higher turbulence rates were calculated with the tetrahedral grid leading to higher transfer rates. The differences that have been observed on the results of the RKE simulations with STAR-CCM+ and Fluent were significantly decreased when solving on the same grids.

The wall meshing has also been found to have an important impact on the Nusselt distribution, high y^+ values on the cell adjacent to the plate led to lower Nusselt number, and lower gradients. These results might be related to the observation made in Chapter 3, where the maximum Nusselt number at the leading edge of a heated wall is underestimated with wall laws and high minimum y^+ values. Furthermore, it has been observed on Figure 5.17 that the central region of the plate including a local minimum of the Nusselt number spread out as the Reynolds number increases. This effect seems more likely to be due to the minimum y^+ values being too high. In fact, the comparison of the surface distribution of the Nusselt number at $Re = 5 \cdot 10^5$ on Figure 5.15 for different y^+ values corroborate this assumption.

Finally, the turbulence models that have been tested on identical grids led to different surface distribution of the Nusselt number on the partition plate and different amplitudes. These differences will likely affect the comparison with the experimental data, especially near the stagnation region where the gradients are important and the difference between the models is more significant.

Finally, a surrogate model has been designed for each numerical case in order to simplify the comparison to experimental data in the following chapter. These surrogate models have been designed by combining the proper orthogonal decomposition technique to Gaussian processes. This enabled the prediction of Nusselt number 2D maps on the partition plate for arbitrary input conditions with an error being of the same order of magnitude of the POD truncation error which has been limited to 5% for all the cases, except for the surrogate model trained with the SAS data showing increased truncation on the upper left of the plate, far from the impingement region.

Chapter 6 Uncertainty quantification on the steam generator

6.1 Introduction

In this chapter, the model error related to the error induced by the physical model underlying the calculation of the heat transfer coefficient with CFD simulations given in §1.2.1 is investigated on the steam generator water box mock-up case. The model error is calculated from the experimental and numerical data which have been generated respectively with heat and mass transfer measurements presented in Chapter 4 and CFD simulations in Chapter 5. This model error E_{model} can be expressed as the combination of other sources of error and uncertainty as given in (1.11) and (1.12):

$$\begin{aligned}\mu_{E_{model}} &= \mu_{E_{CFD/Exp}} + \mu_{U_{exp}} - \mu_{U_{inputs,exp}} - \mu_{E_{num}} \\ \sigma_{E_{model}} &= \sqrt{\sigma_{E_{CFD/Exp}}^2 + \sigma_{U_{exp}}^2 + \sigma_{U_{inputs,exp}}^2 + \sigma_{E_{num}}^2}\end{aligned}$$

The following sections will each focus on the determination of each term in the previous equations of $\mu_{E_{model}}$ and $\sigma_{E_{model}}$. The process will be done for the different CFD models that have been used for the simulations including:

- different turbulence models (Realizable $k - \epsilon$, $k - \omega$ SST and SAS turbulence models)
- different meshing methodologies (polyhedral and tetrahedral cells)

The evolution of the model error according to the Reynolds number will be investigated on the range $Re \in [10^5, 10^6]$.

6.2 Experimental uncertainty

The experimental uncertainty U_{EXP} plays a key role in the estimation of the model error and more generally of the validation process. This section aims to assess this uncertainty for the heat and mass transfer measurements presented in Chapter 4. The definition of the dimensionless quantities can be found in §1.1.2. The Reynolds, Prandtl, Schmidt, Nusselt and Sherwood numbers are respectively denoted by Re , Pr , Sc , Nu and Sh .

The uncertainty on Re , Pr and Sc were estimated from the evolution in time of the flowrate and temperature during the experiments. The variations of these quantities included random fluctuation and a common time varying fluctuation due to the establishment of the temperature in the mock-up at the start of the experiment. This can be seen on Figure 4.10 showing the evolution of the Reynolds and Schmidt numbers during the gypsum dissolution experiments. The uncertainty of the Reynolds and Schmidt numbers during the mass transfer experiments can be modelled with a joint gaussian distribution with a non-zero covariance between Re and Sc . Its value is estimated by measuring the Pearson correlation coefficient ρ_{EXP} . This coefficient is calculated for the different experiments with:

$$\rho_{EXP} = \frac{Cov(Re_{EXP}, Sc_{EXP})}{\sigma_{Re_{EXP}} \sigma_{Sc_{EXP}}}$$

For the gypsum dissolution experiments on the steam generator water box mockup, the Pearson coefficient has been found to be around -0.9 indicating a high correlation between the Reynolds and Schmidt numbers. This is normal as both quantities are calculated from the temperature which was found to fluctuate significantly in time. The fluctuations of the flowrate could be neglected in comparison, which explains the strong correlation between the Reynolds and Schmidt fluctuations. Finally, the negative covariance is due to the fact that the Reynolds and Schmidt numbers are respectively an increasing function and a decreasing function of the temperature.

The temperature fluctuations during the heat transfer coefficient measurements were smaller. In this case, the experiments have been realized on longer time resulting on the establishment of the temperature which was found to fluctuate around 1% of the mean value. In these experiments, the average of the Pearson coefficient over the experiments was found around $\rho_{EXP} = -0.6$.

Furthermore, ρ_{EXP} has been found to fluctuate from an experiment to the other in the range $[-1,0]$ with 75% of the experiments in the range $[-1,-0.5]$. The fluctuations of these quantities during the experiments induce an uncertainty on the Reynolds and Prandtl numbers of the simulations which will be taken into account for the estimation of $U_{inputs,exp}$ in §6.4.

The evolution of the Nusselt and Sherwood number Nu and Sh on the partition plate of the steam generator mock-up has been studied. The measurements' locations, the measurement device and the respective quantities that have been recovered from the experiments are given on Figure 6.1. The Nusselt number maps $Nu_{exp}(Re, Pr, x, y)$ used for the comparison between experiments and CFD combine the information retrieved from the heat and mass transfer measurements:

- The surface distribution is obtained through the Sherwood number measurements on a surface with a $50\mu m \times 50\mu m$ resolution as shown on Figure 6.1c.
- The amplitude of the Nusselt number is obtained with heat transfer measurements with the device depicted Figure 6.1b.

The predicted Nusselt number field on a given location is given by:

$$Nu_{exp}(Re, Pr, x, y) = \frac{\phi(Re, x, y)}{F(Re, Pr)} \quad (6.1)$$

$$F = \frac{\frac{\phi_U(Re)}{Nu_U(Re, Pr)} + \frac{\phi_D(Re)}{Nu_D(Re, Pr)}}{2}$$

where, ϕ refers to the surface distribution of the Nusselt number which is defined such as the surface average value is equal to one (i.e. $\langle \phi(x, y) \rangle_S = 1$). ϕ_U and ϕ_D refer respectively to the surface average value of the surface distribution ϕ on positions U and D . The surface distribution ϕ does not have any dimension, and corresponds to a function of the Reynolds number only for location 4 where it has been found to fluctuate in the experiments (see §4.3.1.3).

The surface distribution ϕ is predicted from the modal base obtained with proper orthogonal decomposition (POD) applied to the snapshots of the Sherwood number on the different locations (details on the results can be found in §4.3.1.3). On location 1, 2 and 3, one mode is sufficient to estimate the surface distribution on all the experimental range with a satisfactory accuracy. The surface distribution used is thus the first mode ϕ_1 of the POD. The surface distribution of the Sherwood number on location 4 has been found to vary more importantly on the experimental range, two modes were thus required in order to ensure a similar accuracy as the other locations. In this case, the surface distribution is reconstructed by predicting the components a_1 and a_2 for a given Reynolds. The surface distribution is then divided by the

mean value. Power laws reproducing the evolution of the components a_1 with respect to the Reynolds number have been given in §4.3.1.3 on the different locations. The component a_2 is predicted for a given Reynolds number by using Gaussian process. A squared exponential kernel has been chosen for the Gaussian process, moreover, the measured data used to train the model were assumed to present Gaussian noise.

The scaling of the Nusselt number amplitude is calculated from the correlations obtained from the heat transfer measurements on the upper and lower half of the measurement device given in Table 4.2 (for Nu_U and Nu_D). A scaling by $F_U = \phi_U/Nu_U$ would lead to surface average values of the Nusselt number equal to Nu_U on location U . The scaling with $F_D = \phi_D/Nu_D$ would lead to surface average values of the Nusselt number equal to Nu_D on location D . Here, the scaling is done by considering the mean value $F = 0.5 \cdot (F_U + F_D)$ due to slight difference observed between F_U and F_D . The uncertainty on this transposition factor has not been taken into account in the experimental uncertainty.

Nu_{exp} can be seen as a mean value of the realization of the real Nusselt field $Nu_{reality}$ during the experiments. The deviation between these two values is assumed to be a realization of the experimental uncertainty U_{EXP} :

$$\delta_{U_{EXP}} = Nu_{exp} - Nu_{reality}$$

The bias $\mu_{U_{EXP}}$ of the experimental uncertainty is assumed equal to zero. The correction done on the heat transfer coefficient measured by the device presented in §4.2.3.3 ensure that the amplitude obtained from the heat transfer measurements is unbiased. The potential differences between the surface distribution obtained at high Schmidt numbers in the range [600, 1200] and the surface distribution for Prandtl numbers in the range $Pr \in [1, 10]$ are supposed to be negligible. Moreover, the local bias induced by the surface roughness of the gypsum samples will be assumed to be corrected by the truncation of the POD to the first modes. Nevertheless, variability has been observed on:

1. the estimation of the distribution $\phi(x, y)$ denoted $\sigma_\phi^2(x, y)$.
2. the experimental Nusselt number $\sigma_{Nu_U}^2$ and $\sigma_{Nu_D}^2$ obtained on the discs U and D .

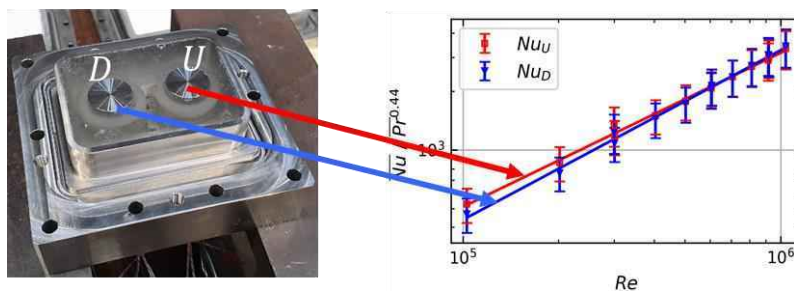
In this work, the standard deviation of Nu_{exp} has been estimated by propagating the uncertainty of ϕ , Nu_U and Nu_D with Monte Carlo methods. A joint normal distribution is given for Nu_U , Nu_D and ϕ . Nu_U , Nu_D and the local values of the spatial distribution ϕ are assumed to be independent. Their standard deviation is given by $\sigma_{Nu_U}, \sigma_{Nu_D}, \sigma_\phi$.

(a) Measurement locations



(b) Heat transfer measurements

$$Nu_U(Re, Pr), Nu_D(Re, Pr)$$



(c) Mass transfer measurements

$$Sh(Re, Sc, x, y)$$

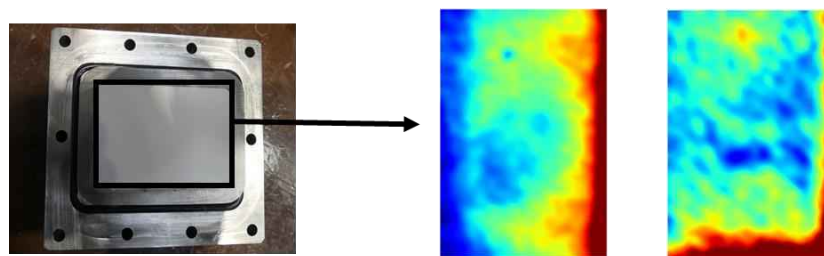


Figure 6.1: Overview of the measurements on the steam generator mock-up. (a) measurement locations on the partition plate. (b) View of the measurement device and evolution of the Nusselt number with the Reynolds number on position U and D . (c) View of the gypsum sample and examples of measured surface distribution on location 1 and 2.

The relative standard deviation σ_ϕ/ϕ of the surface distribution has been estimated by using the local root mean square error $\text{RMSE}(x, y)$ and the local mean absolute error $\text{MAE}(x, y)$, calculated from the predicted surface distribution $\phi(x, y)$ and the distribution of the N_{SNAP} snapshots of the Sherwood number $(Sh_j(x, y))_{j \leq N_{SNAP}}$ obtained from the experiments divided by their surface average value $\langle Sh_j \rangle_S$.

$$\text{MAE}(x, y) = \sum_{j=1}^{N_{SNAP}} \frac{|\phi(Re_j, x, y) - Sh_j(x, y)/\langle Sh_j \rangle_S|}{\phi(x, y)} \quad (6.2)$$

$$\text{RMSE}(x, y) = \sqrt{\frac{1}{N_{SNAP} - 1} \sum_{j=1}^{N_{SNAP}} \left(\frac{\phi(Re_j, x, y) - Sh_j(x, y)/\langle Sh_j \rangle_S}{\phi(Re_j, x, y)} \right)^2} \quad (6.3)$$

The results for the four locations are given on Figure 6.2. The RMSE yields larger values due to the square exponent on the difference term. The deviation of the surface distribution around the 1st mode ϕ_1 is found to be small on locations 1, 2 and 3. The deviation increases near borders. The surface average value of σ_ϕ/ϕ and its maximum value is given on Table 6.1. It is noticeable that the uncertainty on location 4 including more spatial variations is higher. The values of the MAE and RMSE over the positions U and D are indicated in Table 6.2.

Table 6.1: σ_ϕ/ϕ mean and maximum values, estimated with the MAE and RMSE

Location	MAE		RMSE	
	Mean	Maximum	Mean	Maximum
1	5.6%	19%	6.9%	24%
2	5.3%	14%	6.5%	19%
3	5.7%	17%	7.1%	19%
4	8.6%	15%	12%	22%

Table 6.2: σ_ϕ/ϕ on U and D

Location	MAE		RMSE	
	U	D	U	D
1	4.2%	5.3%	5.2%	6.5%
2	4.6%	5.4%	5.6%	6.7%
3	5.4%	4.9%	6.6%	6.0%
4	7.9%	7.6%	11%	11%

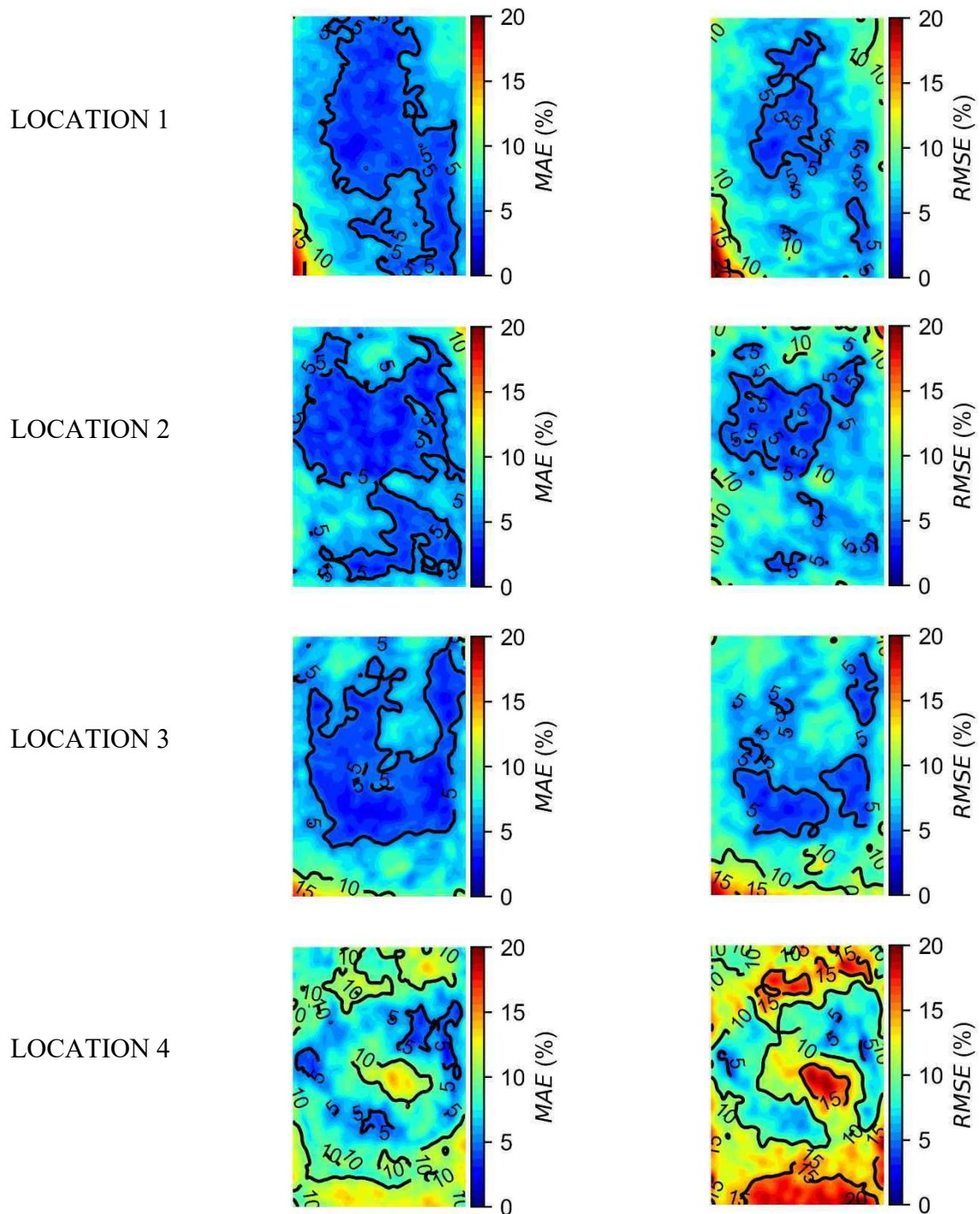


Figure 6.2: Surface distribution of $MAE(x, y)$ and $RMSE(x, y)$ for the different location. The contour corresponds to the iso-values [3.75%, 7.5%, 11.25%, 15%].

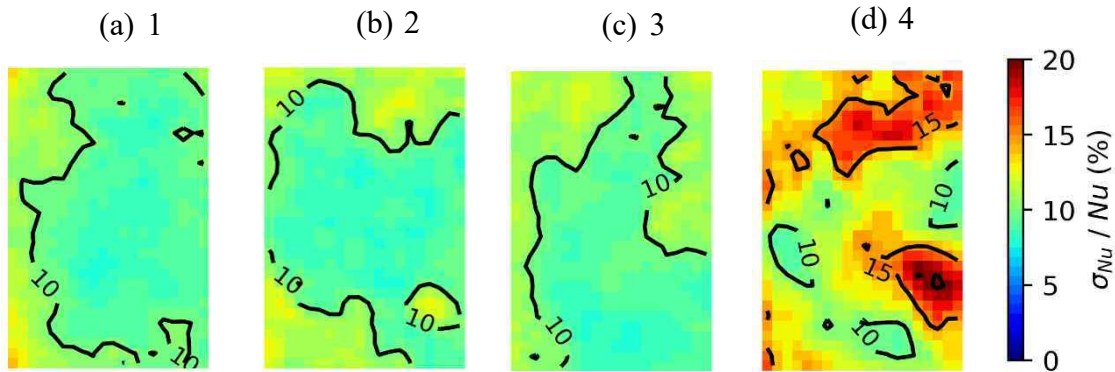


Figure 6.3: Standard deviation of the experimental uncertainty on the Nusselt number for the different locations.

The uncertainty on the Nusselt number Nu_U and Nu_D is due to the fluctuation of the velocity and temperature during the experiments. Their standard deviations σ_{Nu_U} and σ_{Nu_D} were estimated to be 10% of the predicted values Nu_U and Nu_D . The local values of σ_ϕ are taken from the RMSE matrices given Figure 6.2. The resolution of the distribution has been downgraded in order to generate larger samples with Monte Carlo methods for the estimation of the standard deviation $\sigma_{Nu_{exp}}$. A sample of 10^5 elements is generated. The standard deviation of the local Nusselt number is given on Figure 6.3.

In conclusion, the predicted Nusselt number Nu_{exp} combines the surface distribution measured with the gypsum dissolution technique, and the Nusselt calculated from the heat transfer measurement device. The combination of both uncertainties has been propagated with Monte Carlo method which allowed to estimate the standard deviation of the experimental uncertainty $\sigma_{Nu_{EXP}}$. The standard deviation has been found to be in the range [5%, 13%] on locations 1, 2 and 3. On location 4, the standard deviation is higher but remains below 20% on the surface.

The evolution of the experimental uncertainty has been assumed to be constant on the experimental range. Additional work can be done in the future in order to estimate the uncertainty with more accuracy for evolving Reynolds number due to:

- the evolution of the error between the truncated POD of the Sherwood number and the original snapshots with the Reynolds number evolution
- the evolution of the deviation between the experimental points and correlation of the Nusselt number on positions U and D

6.3 Numerical error

The numerical error E_{NUM} relates to the error which arises when solving the equations on discretized grid and space. This error can be reduced by refining the spatial grid. The computations were done for steady state convection; the numerical error will thus be calculated from the estimation of the error due to the mesh refinement. The details on the numerical model (geometry, grid, physical model ...) can be found in §5.2. The runs with the Scale Adaptive Simulations model (see §1.1.3.3.5) were carried out for an unsteady flow, however the influence of the time step on the numerical error will not be covered in this dissertation.

Four grids were designed for the computations of heat transfer with CFD in the steam generator:

- The grids LRE_{TET} , HRE_{TET} with tetrahedral cells. The two grids were used respectively for the computations on the range $Re < 5 \cdot 10^5$ and $Re > 5 \cdot 10^5$.
- The grids LRE_{POLY} , HRE_{POLY} with polyhedral cells.

The numerical error $E_{NUM}(s)$ for a specific grid with cells of size s has been assessed with Richardson extrapolation (see §1.2.4.2).

$$E_{NUM}(s) = Nu_{exact} - Nu_s = C_1s + C_2s^2 + \dots$$

where C_1, C_2, \dots are coefficient that have to be found. In this dissertation, the numerical error is written as following by keeping only the first order term:

$$E_{NUM}(s) = Nu_{exact} - Nu_s = C_1s$$

Instead of defining a grid size s , the evolution of the numerical error is estimated from the number of cells by replacing s by $1/N^3$, where, N is the number of cells in the domain. A linear regression is performed to estimate C_1 and Nu_{exact} which is the Nusselt number calculated when free of error. These parameters are estimated with a least square approach by fitting a linear curve on the evolution of Nu with five grids. Nu_{exact} is estimated by calculating the intersection of the linear regression with the y -axis. The number of cells of each grid is given in Table 6.3. It has been noticed that the grid 1 was too coarse, thus, only the results obtained with grids 2, 3, 4 and 5 will be used to estimate E_{NUM} . An example of the process of calculating the numerical error is given on Figure 6.4. The numerical error on the surface average Nusselt number over the partition plate Nu_{MEAN} at $Re = 5.5 \cdot 10^5$ and $Re = 4.6 \cdot 10^5$ is estimated. The numerical error mean value and standard deviation are found to be below 1% of the predicted value with the reference mesh except for HRE_{POLY} which is around 1.6%. It is noticeable that the regression quality differs from a case to the other. For instance, the evolution of Nu_{MEAN} with the grid size on HRE_{TET} visible on Figure 6.4b seems to be converged. In fact, the fluctuations are within 1% of the prediction of Nu_{MEAN} for the different grid size.

Table 6.3: Number of cells of the different grids. The reference grids are given with bold characters.

Grid	LRE_{POLY}	HRE_{POLY}	LRE_{TET}	HRE_{TET}
1	$2.4 \cdot 10^6$	$3 \cdot 10^6$	$5 \cdot 10^6$	$5 \cdot 10^6$
2	$5.1 \cdot 10^6$	$6.9 \cdot 10^6$	$7.5 \cdot 10^6$	$7 \cdot 10^6$
3	$7.9 \cdot 10^6$	$8.7 \cdot 10^6$	$1.2 \cdot 10^7$	$1.1 \cdot 10^7$
4	$1.2 \cdot 10^7$	$1.3 \cdot 10^7$	$2.2 \cdot 10^7$	$2.1 \cdot 10^7$
5	$2.0 \cdot 10^7$	$3.7 \cdot 10^7$	$3.8 \cdot 10^7$	$6.6 \cdot 10^7$

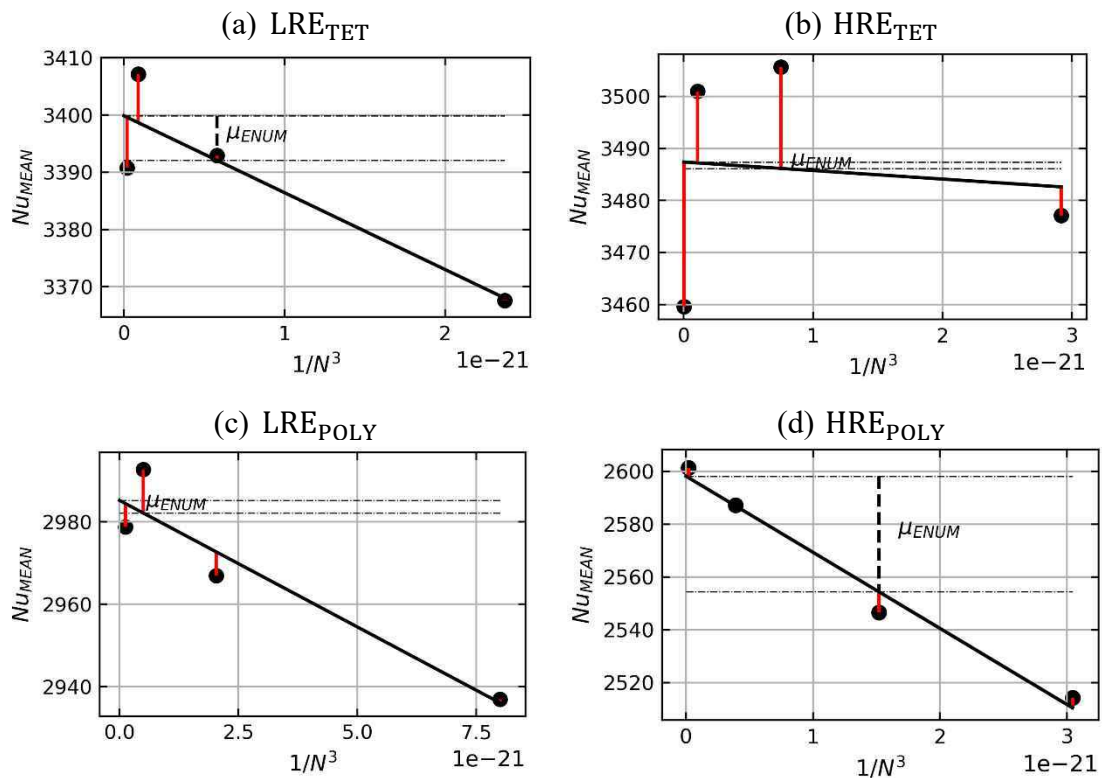


Figure 6.4: Examples of evolution of the mean Nusselt number over the partition plate with $1/N^3$ at $Re = 5.5 \cdot 10^5$ (LRE_{TET} and HRE_{TET}) and $Re = 4.6 \cdot 10^5$ (LRE_{POLY} and HRE_{POLY}). $\mu_{ENUM}(s)$ is calculated from the difference between Nu_{exact} and $Nu(1/N^3)$ given in dashed lines.

The evaluation of this uncertainty has been done for the Realizable $k - \epsilon$ turbulence model (RKE) (see §1.1.3.3.2 for details). The Nusselt number obtained from the different grids were interpolated on the same grid to estimate the local values of E_{NUM} on the partition plate. The results for $Re = 5 \cdot 10^6$ are shown on Figure 6.5. The results at $Re = 10^5$ and $Re = 10^6$ were similar. The bias $\mu_{E_{MEAN}}$ is found to be below 1% for all the grids except for HRE_{POLY} due to a larger cell size. The standard deviation $\sigma_{E_{NUM}}$ is negligible on most of the partition plate except at the junction of low Nusselt and high Nusselt zones where high gradients are present.

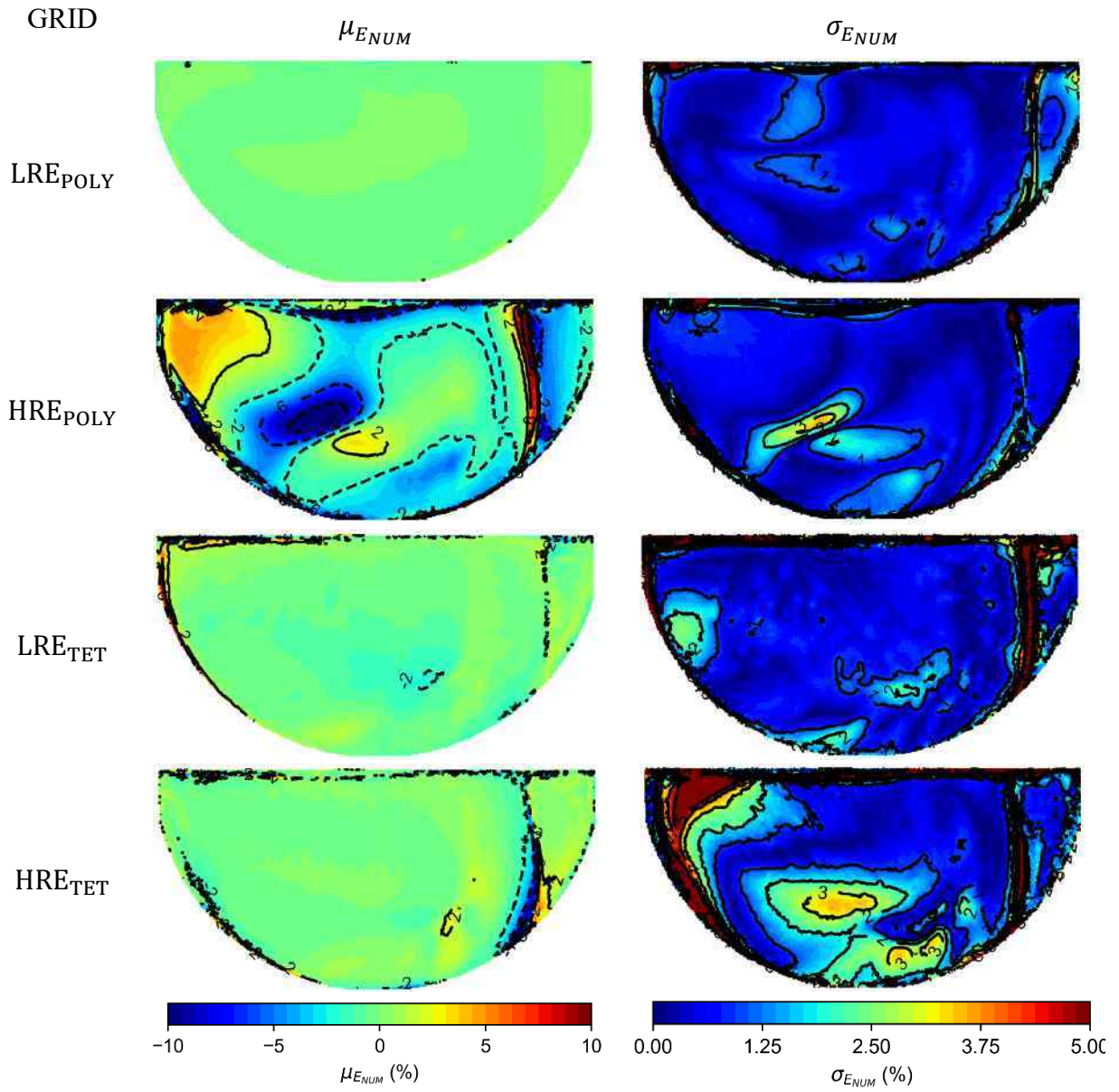


Figure 6.5: Local values of μ_{ENUM} and σ_{ENUM} on the partition plate at $Re = 5 \cdot 10^5$

Table 6.4: μ_{ENUM} and σ_{ENUM} averaged over the partition plate

Grid	$Re = 10^5$		$Re = 5 \cdot 10^5$		$Re = 10^6$	
	μ_{ENUM}	σ_{ENUM}	μ_{ENUM}	σ_{ENUM}	μ_{ENUM}	σ_{ENUM}
LRE _{POLY}	-0.15%	1.7%	-0.09%	0.85%		
HRE _{POLY}			-1.8%	0.97%	-2.1%	1.0%
LRE _{TET}	0.18%	2.5%	-0.21%	1.15%		
HRE _{TET}			-0.13%	1.8%	-0.35%	1.5%

For grids HRE_{POLY} and HRE_{TET}, the standard deviation increases at the center of the plate. The surface average of $\mu_{E_{NUM}}$ and $\sigma_{E_{NUM}}$ are calculated for different Reynolds numbers $Re = 10^5$, $Re = 5 \cdot 10^5$ and $Re = 10^6$ and are given on Table 6.4. On average, E_{NUM} remains approximatively constant for different Reynolds number.

6.4 Propagation of the uncertainty of the simulation inputs

The Reynolds and Schmidt numbers during the gypsum dissolution experiments have been found to fluctuate around 5% of the mean value, while the standard deviation of the Reynolds and Prandtl number during the heat transfer experiments are found to be between 0.5% and 1% of their mean value. The impact of the simulation's Reynolds and Prandtl number uncertainty on the computations of the Nusselt number with CFD is calculated by propagating their covariance through the calculation. The propagation is done with Monte Carlo method depicted in §1.2.4.2.1:

- The Reynolds and Prandtl number are assumed to follow a joint normal distribution. The mean values of the Reynolds number around which the propagation will be performed were chosen in the range $Re \in [10^5, 10^6]$. The mean Prandtl number has been fixed at $\mu_{Pr} = 6$. The covariance matrix is assumed to be diagonal as the Prandtl and Reynolds fluctuations are assumed to be independent.
- A random sample of N_{SAMPLE} element $(Re_i, Pr_i)_{i \leq N_{SAMPLE}}$ following the joint distribution is generated using a random number generator.
- The Nusselt number on the partition plate Nu_i is predicted for each point of the sample using the surrogate models depicted in §5.4. The prediction of the surrogate model is denoted \widehat{Nu}_i .
- The uncertainty on the Nusselt number due to the inclusion of the simulation inputs uncertainty $U_{inputs,exp}$ is then calculated with:

$$\begin{aligned} \mu_{\widehat{Nu}_i} &= \frac{1}{N_{SAMPLE}} \sum_{i=1}^{N_{SAMPLE}} \widehat{Nu}_{CFD,i} \\ \mu_{U_{inputs,exp}} &= \mu_{\widehat{Nu}_i} - \widehat{Nu}(\mu_{Re}, \mu_{Pr}) \\ \sigma_{U_{inputs,exp}} &= \frac{1}{N_{SAMPLE} - 1} \sum_{i=1}^{N_{SAMPLE}} (\widehat{Nu}_{CFD,i} - \mu_{\widehat{Nu}_i})^2 \end{aligned}$$

The additional error due to the surrogate model accuracy can be found on Figure 5.21. It is neglected for all models except for the Scale Adaptive Simulations (SAS) for which the bias and variance of the prediction were more significant (5%-15%).

The standard deviation of the Prandtl number and Reynolds have been set to 5% of the mean value. The covariance matrix C of the joint distribution can be written as following:

$$C = \begin{pmatrix} (0.05\mu_{Re})^2 & 0 \\ 0 & (0.05\mu_{Pr})^2 \end{pmatrix}$$

The bias $\mu_{U_{inputs,exp}}$ has been found to be below 1% of the predicted values $\mu_{\widehat{Nu}}$ for all the computations with a maximum for the SAS model around 0.5%. The standard deviation has been found to be around 4-5% of the predicted mean value $\mu_{\widehat{Nu}_i}$. An example of the surface distribution of the standard deviation $\sigma_{\sigma_{U_{inputs,exp}}}$ is given on Figure 6.6 for simulations with two turbulence models with grid LRE_{POLY}. It is noticeable that for this level of uncertainties, $\sigma_{U_{inputs,exp}}$ can be estimated to have a negligible bias, with a resulting standard deviation on the Nusselt number of the same order of magnitude as the uncertainty on the Reynolds and the Prandtl number uncertainties. No particular behaviour of this error with the Reynolds number has been noticed. Furthermore, the gradients on the plate are negligible and indicate that the variation of the boundary conditions do not affect significantly the surface distribution. An additional test has been performed by modifying the non-diagonal elements in the covariance matrix. The non-diagonal elements have been set in order to have completely correlated variables:

$$C = \begin{pmatrix} \sigma_{Re}^2 & \sigma_{Re}\sigma_{Pr} \\ \sigma_{Re}\sigma_{Pr} & \sigma_{Pr}^2 \end{pmatrix}$$

The resulting standard deviation $\sigma_{U_{inputs,exp}}$ has been found to be reduced to 2.5%-3%.

In conclusion, the impact of the uncertainty of the boundary conditions during the experiments has been propagated though the computations of the Nusselt number with CFD. The bias $\mu_{U_{inputs,exp}}$ induced by the fluctuations is negligible in front of other sources of uncertainty. The variance $\sigma_{U_{inputs,exp}}$ is directly related to the standard deviation of the Reynolds and Prandtl number during the experiments. The experimental Nusselt number's amplitude is calculated with the heat transfer measurements for which the boundary conditions have been found to fluctuate around 1% of the mean value. Moreover, these two fluctuations were correlated in time. The standard deviation $\sigma_{U_{inputs,exp}}/\widehat{Nu}(\mu_{Re}, \mu_{Pr})$ in this case is found to be around 1% which is negligible in the quantification of the model error in front of the experimental uncertainty. This level of uncertainty is significantly lower than the experimental uncertainty on the Nusselt number which standard deviation is around 20% of the provided value.

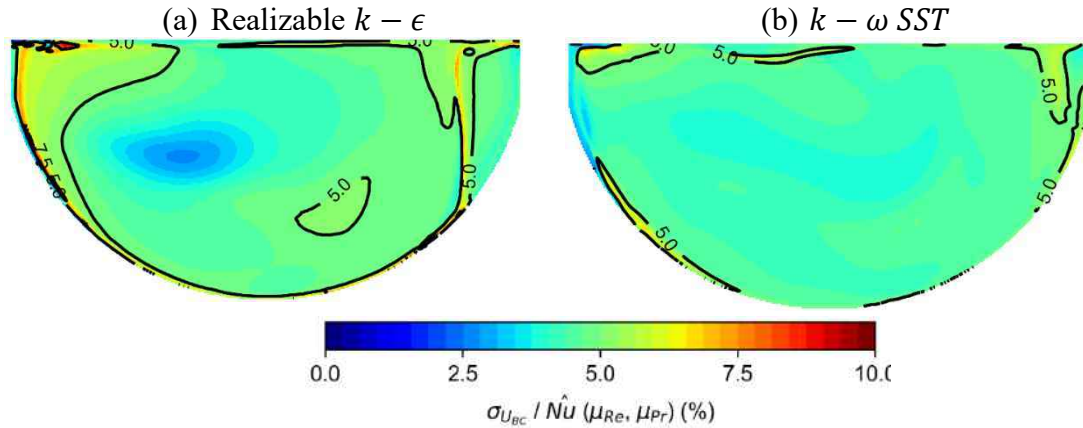


Figure 6.6: Example of surface distribution $\sigma_{U_{inputs,exp}}$ on the partition plate at $Re = 2.5 \cdot 10^5$ and $Pr = 6$

6.5 Gap between the computations and the experiments

The gap $E_{CFD/EXP}$ corresponds to the deviation between the experiments and the calculations with Computational Fluid Dynamics codes (CFD). It has been noticed in Chapter 5 that the computations of the Nusselt number's surface distribution differs between the different turbulence models and grids (type of cell; wall meshing). The four measurement locations on which the comparison between CFD results and experiments were performed are reminded on Figure 6.7a. Examples of the Nusselt number surface distribution calculated with different turbulence models are given on Figure 6.7b.

The importance of the variation of the Nusselt number distribution for the different CFD runs can be seen on Figure 6.7b. Moreover, its shape is affected by the increase of the y^+ values on the cells adjacent to the partition plate for increasing Reynolds number as it can be seen on Figure 5.17. These variations of the surface distribution affect the calculation at the measurement locations:

- the measurement locations 1 and 2 are affected by the displacement of a local minimum heat transfer region from the center of the plate to the upper.
- locations 3 and 4 are affected by this central zone in addition to the position of the “banana” shaped maximum region. Its shape, length and amplitude depend on the turbulence model and wall meshing.

In comparison, the results analyzed in §4.3.1.3 showed less significant variations of the Sherwood number surface distribution with the Reynolds number. Some discrepancies have been observed between the lower Reynolds number experiments and the larger Reynolds number ones, however, they were most certainly due to the increase of the roughness effects at high turbulence regimes.

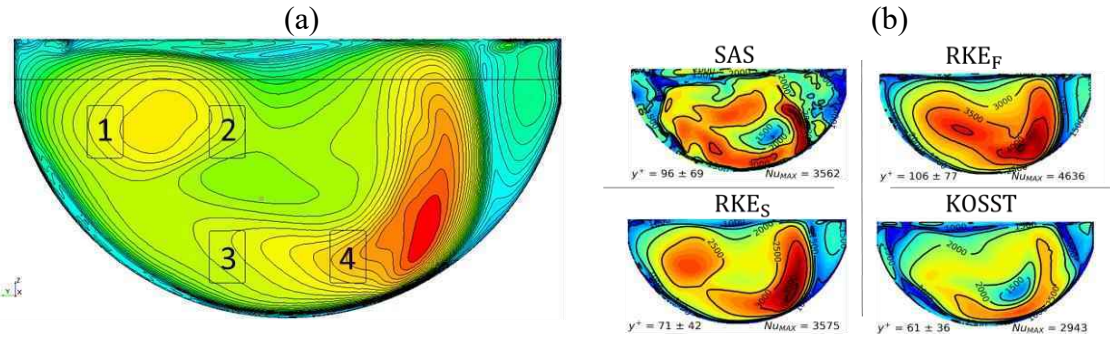


Figure 6.7: (a) Measurement locations and (b) example of surface distribution of the Nusselt number obtained with the different models

In addition, the amplitude of those fluctuations is much lower than the ones observed in the CFD simulations. These fluctuations have been considered in the experimental uncertainty. On location 4, an evolution has been detected by both heat and mass transfer measurements. The ratio between the heat and mass transfer on the upper side and lower side of the measurement device has been found to increase in the measured range which seem to indicate a variation of the local minimum position near the stagnation region on the plate. The mean $\mu_{E_{CFD/EXP}}$ and standard deviation $\sigma_{E_{CFD/EXP}}$ of $E_{CFD/EXP}$ are first calculated as following:

- The mean is calculated by comparing the Nusselt maps generated from the experiments Nu_{EXP} to the calculation of CFD Nu_{CFD} on the measurement locations.
- The standard deviation should be zero as the simulations are deterministic. The randomness of Nu_{EXP} and Nu_{CFD} are taken into account respectively in U_{EXP} and $U_{inputs,exp}$.

The relative root-mean-square-error (RMSE) and the relative mean-absolute-error (MAE) are defined between Nu_{CFD} and Nu_{EXP} as follows:

$$MAE(Nu_{CFD}, Nu_{EXP}) = \frac{\langle Nu_{CFD}(x, y) - Nu_{EXP}(x, y) \rangle_S}{Nu_{ref}} \quad (6.4)$$

$$RMSE(Nu_{CFD}, Nu_{EXP}) = \frac{\sqrt{\langle (Nu_{CFD}(x, y) - Nu_{EXP}(x, y))^2 \rangle_S}}{Nu_{ref}} \quad (6.5)$$

where, $\langle \ \rangle_S$ is the surface average value of the function on the comparison window, and Nu_{ref} is a reference Nusselt number which is chosen to be the maximum of the Nusselt number which is the quantity of interest when calculating. The surface average value of Nu_{CFD} over the partition plate is chosen for Nu_{ref} . This value is representative of the Nusselt number over the partition plate and can be chosen to compare the performance on the different locations. Moreover, it allows to scale easily the relative error that are given in the following presentation of the results.

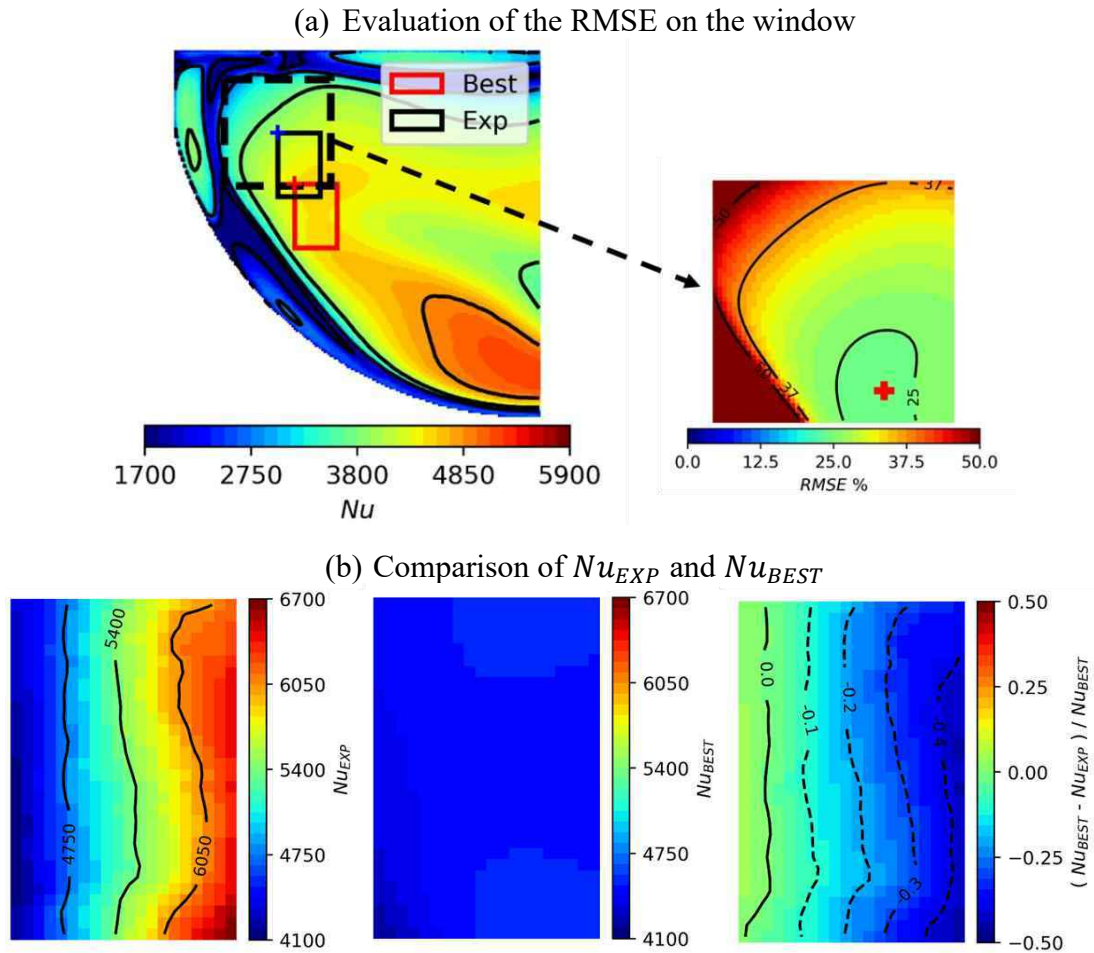


Figure 6.8: Example of the extraction of the RMSE between the experimental Nusselt number Nu_{EXP} and the CFD Nusselt number extracted on a window around the experimental location. The Nusselt number distribution Nu_{BEST} is extracted from the partition plate by translating the location as indicated on (a) The RMSE is calculated from comparison windows translated in the square dashed window. The original comparison window is given in black solid lines. The minimum RMSE location on which Nu_{BEST} is extracted is given in red. The comparison is shown on (b).

It has been observed that the variations of the non-dimensional wall mesh height y^+ on the first cell layer over the partition plate results in the fluctuations of the surface distribution affecting importantly the comparison between Nu_{EXP} and Nu_{CFD} . An example is given on Figure 6.8, for computations done with the elliptic blending Reynolds stress model (EB-RSM). On Figure 6.8a, the Nusselt distribution over the partition plate Nu_{CFD} is shown, with the position of the measurement device. It is visible by looking to the experimental Nusselt number Nu_{EXP} on Figure 6.8b that the shape of the surface distribution Nu_{CFD} differs from the experiment at the measurement position. However, the straight lines isocontours of the Nusselt number visible on Nu_{EXP} can be found by translating the comparison window to the bottom right of the

original location. The best fit is tracked with the minimum of the RMSE error defined in (6.5) and is visible in red on Figure 6.8a.

Table 6.5: Surrogate models used for the determination of the error $E_{CFD/EXP}$.

Turbulence model	Surrogate model	Software
Realizable $k - \epsilon$ (Polyhedral grid)	\widehat{Nu}_{RKE_S}	STAR-CCM+
Realizable $k - \epsilon$ (Tetrahedral grid)	\widehat{Nu}_{RKE_F}	Fluent
$k - \omega$ SST	\widehat{Nu}_{KOSST}	STAR-CCM+
Scale Adaptive Simulation	\widehat{Nu}_{SAS}	Fluent

The evaluation of $E_{CFD/EXP}$ is realized with predictions of Nu_{CFD} with the surrogate model trained from the computations results on the range depicted Figure 5.4. The notation for each turbulence model is given in Table 6.5.

6.5.1 Realizable $k - \epsilon$

The RKE model has been tested with STAR-CCM+ (RKE_S) and Fluent (RKE_F) on different grids (respectively on polyhedral and tetrahedral grids). The grid influence on the computations has been investigated in §5.5.2. The comparison of the Nusselt number obtained with the two grids has been performed with STAR-CCM+: simulations performed with the tetrahedral grid yielded higher values of the Nusselt number. The use of the same grid for computations with both softwares reduces the difference between their results.

The local difference between CFD and experiments is evaluated over the range $Re \in [10^5, 10^6]$. The local relative error $\Delta Nu(x, y)$ is defined as follows:

$$\Delta Nu(x, y) = \frac{Nu_{CFD}(x, y) - Nu_{EXP}(x, y)}{Nu_{ref}} \quad (6.6)$$

The surface average value of Nu_{CFD} over the partition plate is chosen for Nu_{ref} . The average of $\Delta Nu(x, y)$ calculated over the simulations Reynolds number range $Re \in [10^5, 10^6]$ and for $Pr = 6$ is given for $Nu_{CFD} = \widehat{Nu}_{RKE_S}$ and \widehat{Nu}_{RKE_F} on Figure 6.9. Moreover, the evolutions of the MAE and RMSE defined in (6.4) and (6.5) are given as a function of the Reynolds number for all location on Figure 6.10. On most of the Reynolds range, the simulations with both models underestimate the Nusselt number's amplitude on locations 1, 2 and 3. This underestimation stabilizes at high Reynolds number. In addition, it can be noticed that switching to a finer mesh near $Re = 5 \cdot 10^5$ reduces importantly the deviation between the experiments and the simulations on location 2 for RKE_S and location 3 for RKE_F. This might be due to the fact that locations 2 and 3 are both closer to the stagnation point, respectively on the upper side and lower side of the plate.

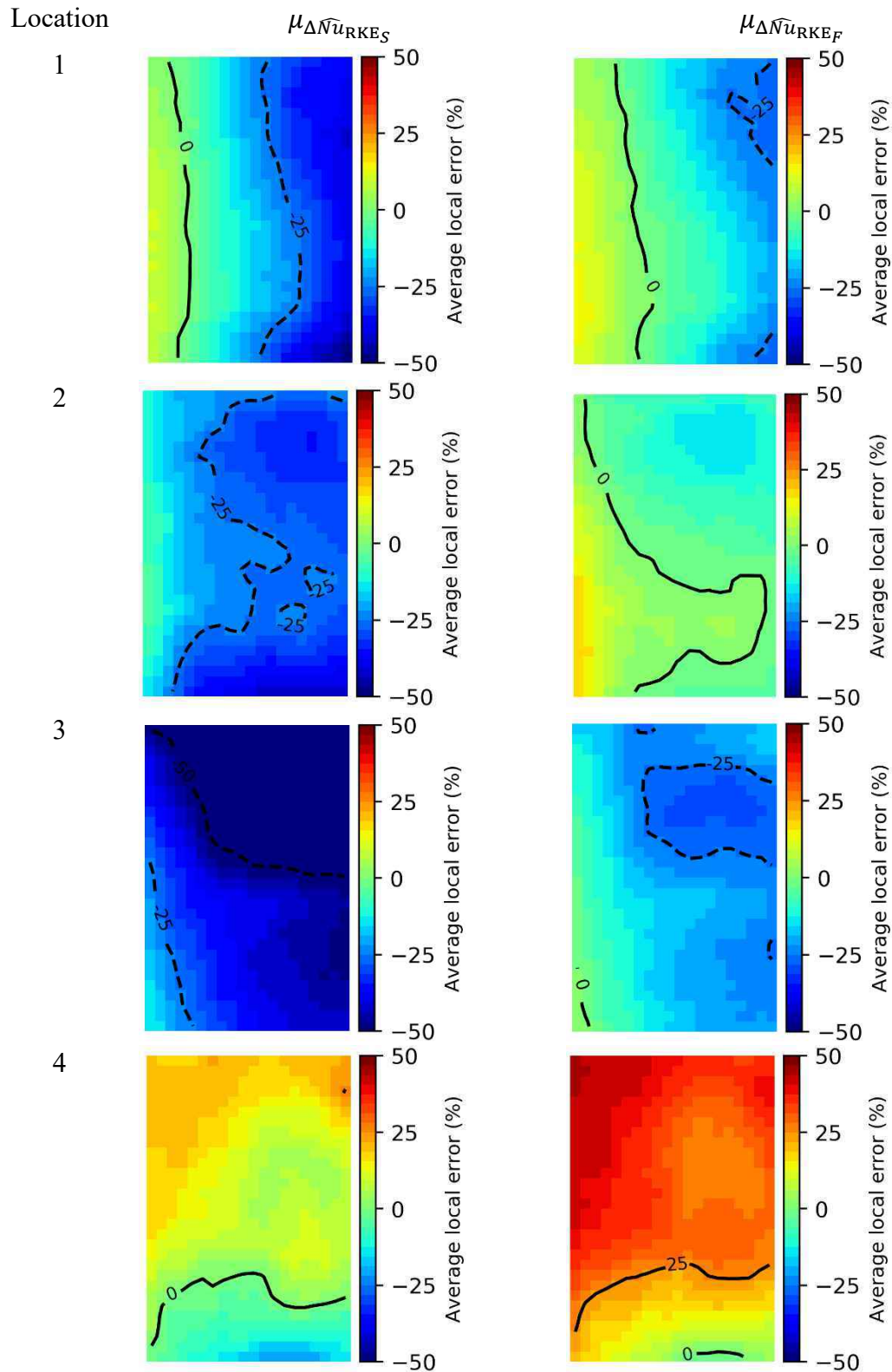


Figure 6.9: Average over the range $Re \in [10^5, 10^6]$ of the local relative error between \widehat{Nu}_{RKES} , \widehat{Nu}_{RKEF} and Nu_{EXP} .

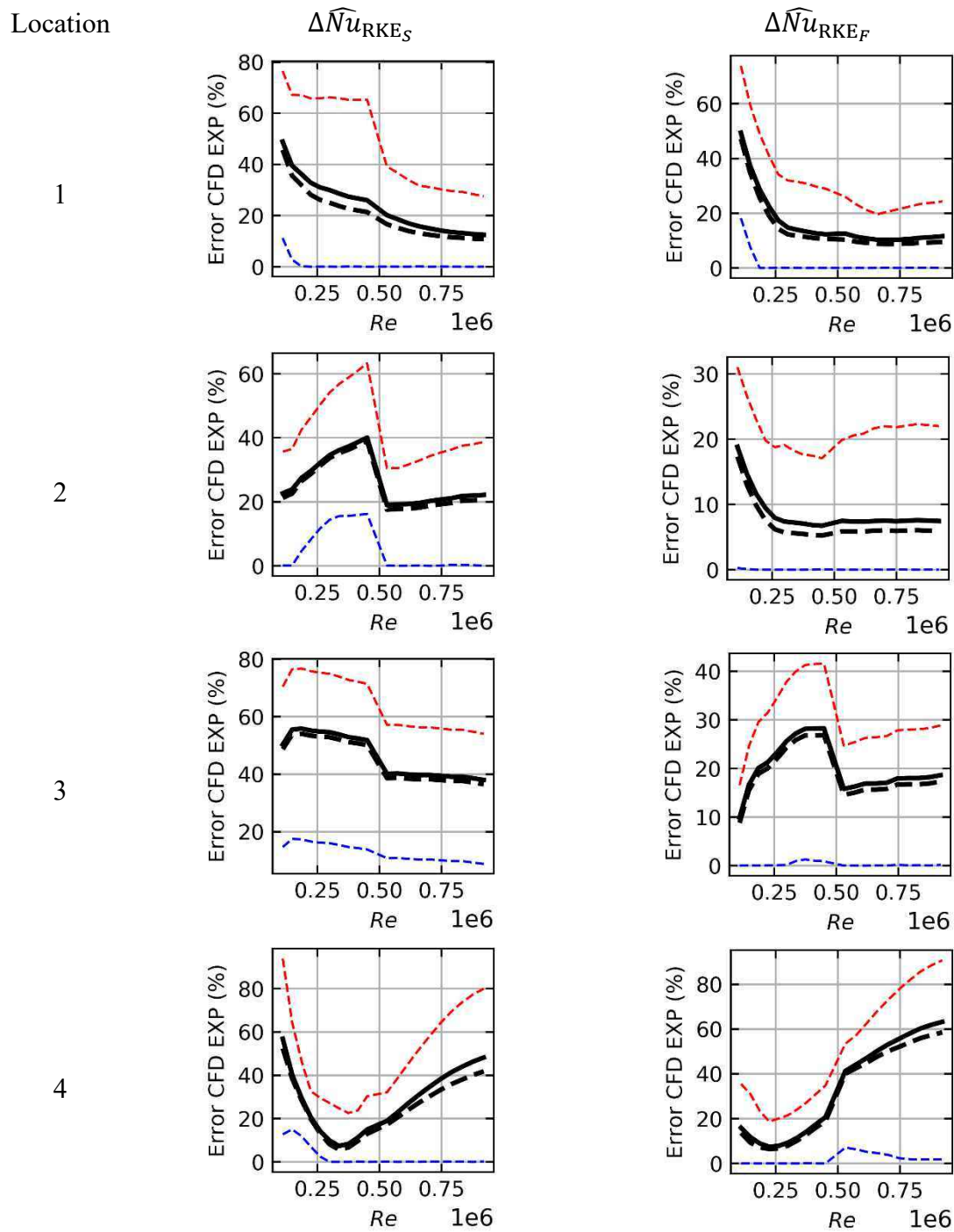


Figure 6.10: Evolution of the deviation between Nu_{CFD} and Nu_{EXP} . The MAE is given in black solid line, the min and max value of the absolute error over the surface are given in dotted line respectively in blue and red. The RMSE is given with solid dashed line.

The y^+ values in these zones are higher than those in location 1 and as such, they are more affected by the evolution of the surface distribution for increasing Reynolds number. In both cases, the evolution of the surface distribution induces a bias which is corrected when switching

grids. Finally, the Nusselt number's amplitude on location 4 is overestimated with CFD in both cases on the upper half of the samples in comparison to the experiments. On this location, the maximum values on the bottom half of the sample are well calculated with RKE_F and RKE_S giving an upper and lower bound of the experiments. However, the minimum value on the upper part is overestimated with both simulations.

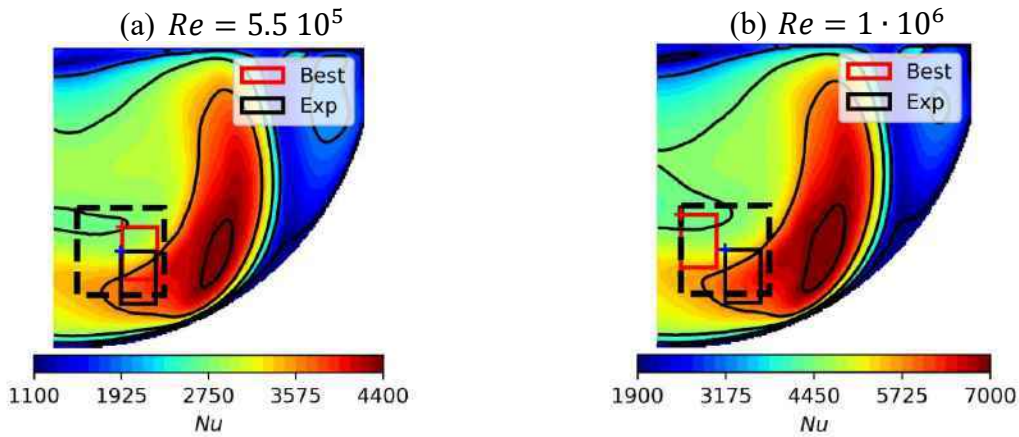


Figure 6.11: Example of minimum RMSE extraction on location 4 for RKE_S

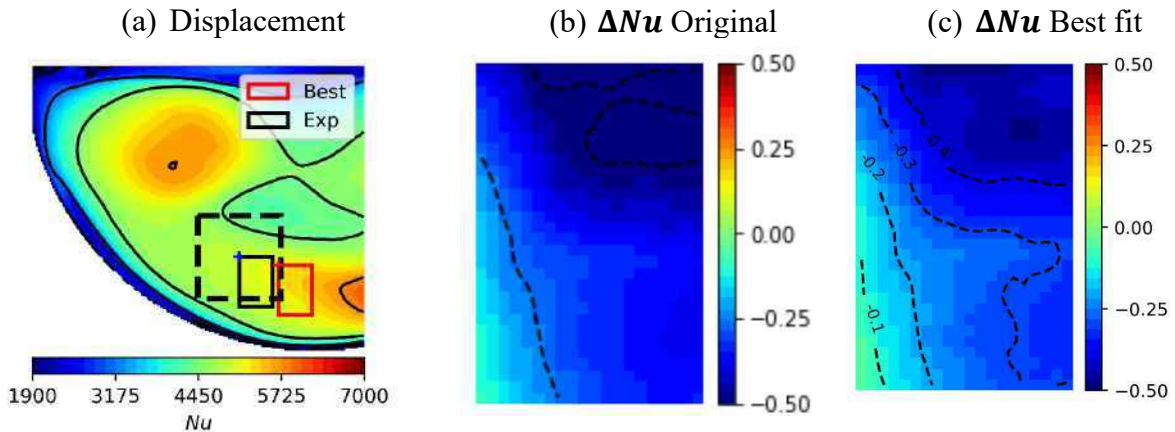


Figure 6.12: Comparison of ΔNu on location 3 for the original location and the moved window

The sensitivity of the gap between experiments and CFD to the location of the comparison window is investigated. The original comparison window (“Exp”) and the minimum RMSE comparison window (“Best”) for location 4 is given on Figure 6.11.. The comparison is done at two Reynolds number for the predictions with \widehat{Nu}_{RKE_S} on the thinner near wall mesh HRE. On this grid, the minimum of the RMSE follows the displacement of the central zone near the upper left of the plate. Similar behaviors have been observed for the other locations when computing with RKE_S model. For some of the locations, the window was too small reach a local minimum of the RMSE. In these cases, the best fit locations were found on the border of the window. An example is given for location 3 on Figure 6.12. It is likely that the banana shaped iso contour spreads further in reality than what is calculated with the RKE. The

evolution of the minimum RMSE is given on Figure 6.13 in comparison to the RMSE calculated at the measurement location.

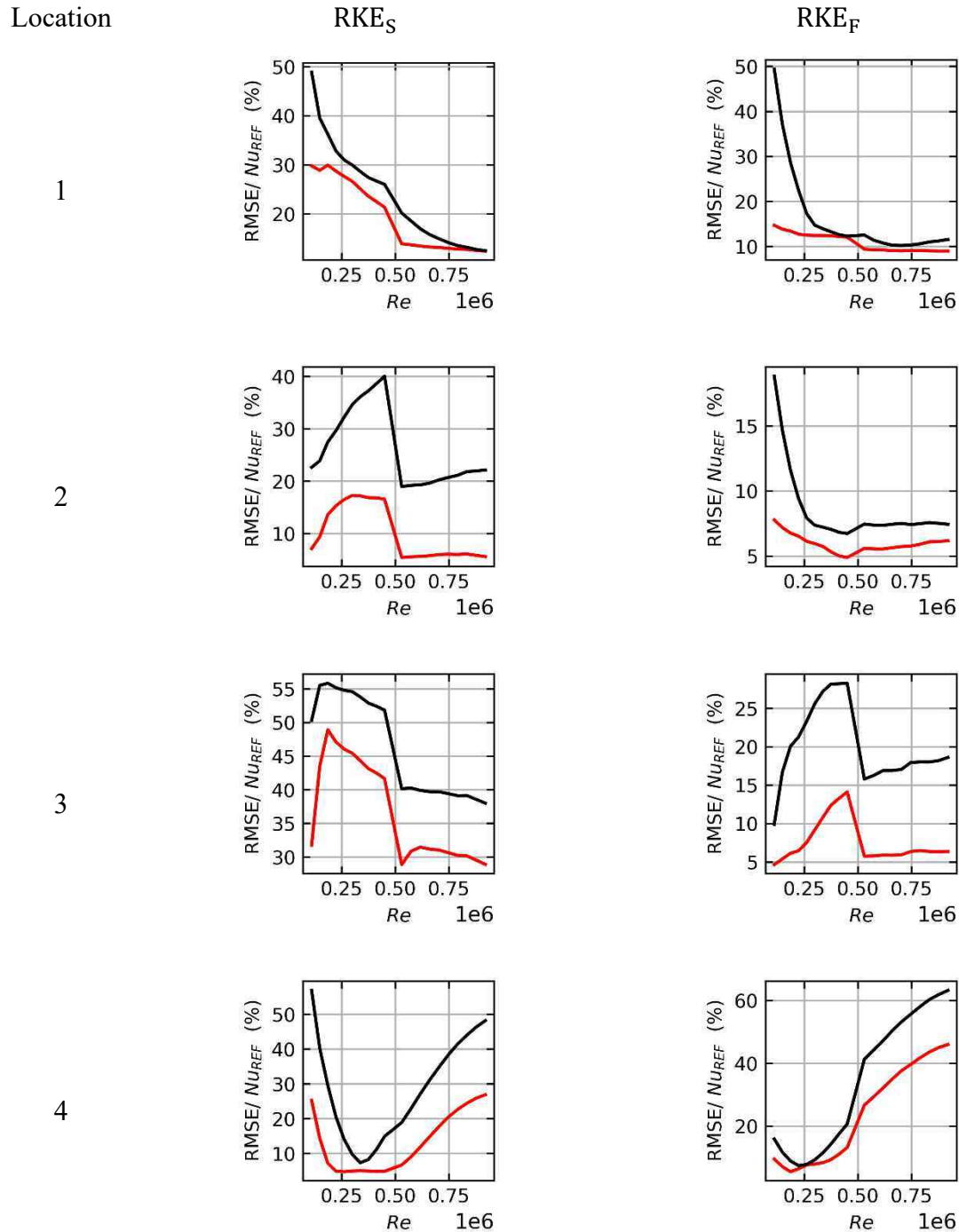


Figure 6.13: Evolution of the deviation between Nu_{CFD} and Nu_{EXP} with the windowed approach. The evolution of the minimum RMSE over the window is given in red. Its mean value in solid black line.

The minimum RMSE given in red decreases with the Reynolds number, except on location 4 where both RKE_S , RKE_F overestimate the Nusselt number.

It is noticeable that with the window approach, the difference between experiments and simulations decreases. It can be noticed that the RKE_F simulations are more accurate regarding the maximum heat transfer in comparison to RKE_S simulations which underestimates the Nusselt number's amplitude more importantly. The differences between these two models are mainly due to the grid which is different in both cases (tetrahedral vs. polyhedral cells) and to the solver's parameters which were different in both cases. When using equal grids and similar parameters in the solver, this difference is significantly reduced (cf. §Figure 5.9 and Figure 5.10).

In conclusion of the simulations performed with RKE_S and RKE_F models:

- The computations with the RKE model underestimate the Nusselt number amplitude on the partition plate when compared to the experimental data, except near the stagnation zone where the local minimum found experimentally is significantly overestimated with RKE_S and RKE_F simulations. The accuracy is better when comparing experiments and simulations on a translated window around the measurement position.
- Simulations using the tetrahedral grid was shown to be closer to the experimental Nusselt number obtained on the mock-up than the polyhedral grid on which the Nusselt number's amplitude was found lower.
- The deviation between CFD and experiments show important values at low Reynolds number, and then decreases around 20%-40% of the reference Nusselt value. The best performance are obtained on location 2 where the deviation with the experimental data is within 10% for the high Reynolds number simulations. On the other hand, the overestimation of the Nusselt number observed on location 4 reaches values at high Reynolds number around 30% to 60% depending on the model. On location 1, the performances are bad at low Reynolds numbers with important underestimations of the amplitude of the Nusselt number. At high Reynolds the accuracy is better (deviations around 15%-20%) and show smaller evolution.
- Translating the comparison window between experiments and CFD simulations affects importantly the results. The enhancement of the accuracy seems correlated to the displacement of the patterns visible on the Nusselt number distribution with the increase of the minimum y^+ values on the partition plate.
- The effect of near wall meshing of the fluid domain on the amplitude of the Nusselt number has been noticed on locations 2 and 3 when switching grids for simulations with intermediate Reynolds numbers. The deviation between CFD and experiment is significantly reduced for the mesh with the finer wall meshing. This might be because the wall functions used in the model cannot be used with too high values of the non-dimensional wall height y^+ of the cells adjacent to the walls. Additional tests can be done in the future to investigate the impact of the wall meshing on the simulation results.

6.5.2 $k - \omega$ SST and Scale Adaptive Simulation

The same process depicted in the previous section for the RKE turbulence model will be applied to the Nusselt number obtained with $\widehat{Nu}_{KOSST}, \widehat{Nu}_{SAS}$. The SAS model used in the simulations are based on the KOSST model (see §1.1.3.3.3) which has been reinterpreted as a $k - L$ model with L a turbulent length scale (Menter & Egorov, 2005). This explain the similarities that have been observed in the surface distribution of the Nusselt number with both models (see Figure 5.14 and Figure 5.15). It should be reminded that the deviation of the surrogate model \widehat{Nu}_{SAS} accuracy is significantly larger than \widehat{Nu}_{KOSST} , especially near location 1 on the upper left of the partition plate (see Figure 5.21). Moreover, it should also be reminded that the grid convergence has been done on the RKE. Some of the computations with the KOSST also seemed to be defective as undampened oscillations of the Nusselt number field have been observed during the convergence at the final state.

The evolution of the MAE and RMSE defined in (6.4) and (6.5) with the Reynolds number is given on Figure 6.14 on the four measurement locations. The average local error between Nu_{CFD} and Nu_{EXP} defined in (6.6) over the range $Re \in [10^5, 10^6]$ is given on Figure 6.15.

Different comments can be given on the comparison between the SAS, KOSST and experiments at the measurement locations:

- It is noticeable that both models underestimate importantly the Nusselt number on the different locations.
- The values of the Nusselt number computed by the KOSST and SAS models show important similarities as it can be seen on Figure 6.14, except on location 1. On this location, the deviation CFD-experiments calculated with the SAS model is more important. This coincides with the observation made on Figure 5.21: some of the results of the SAS model used for the comparison were not well converged on this specific location, leading to higher uncertainty in this zone which could explain the differences between both models.
- The deviation is significant for the lower Reynolds numbers, however, the surface average deviation given by the RMSE, and MAE also decreases significantly with respect to the Reynolds number increase.

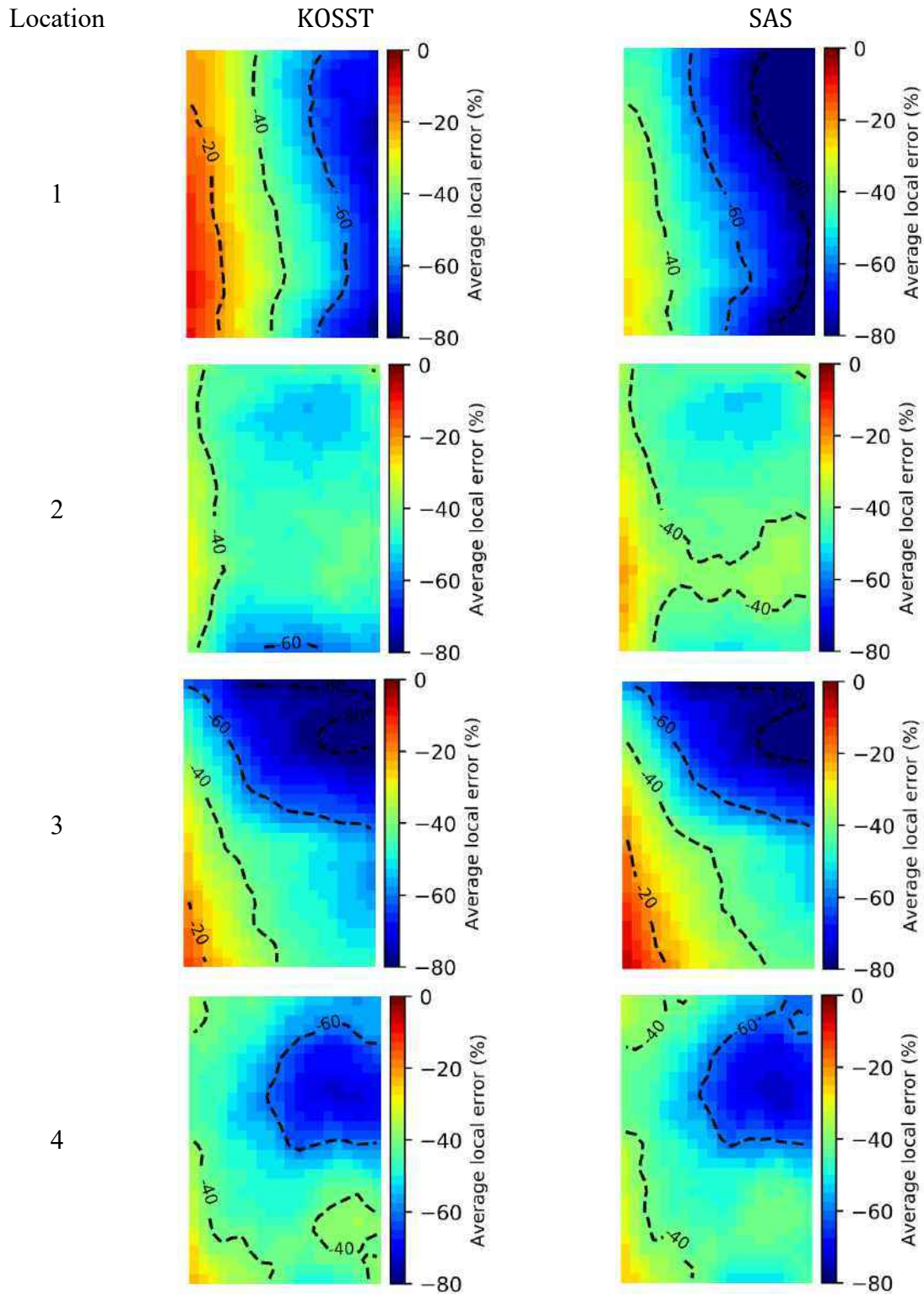


Figure 6.14: Average over the range $Re \in [10^5, 10^6]$ of the local relative error between \widehat{Nu}_{KOSST} , \widehat{Nu}_{SAS} and Nu_{EXP} .

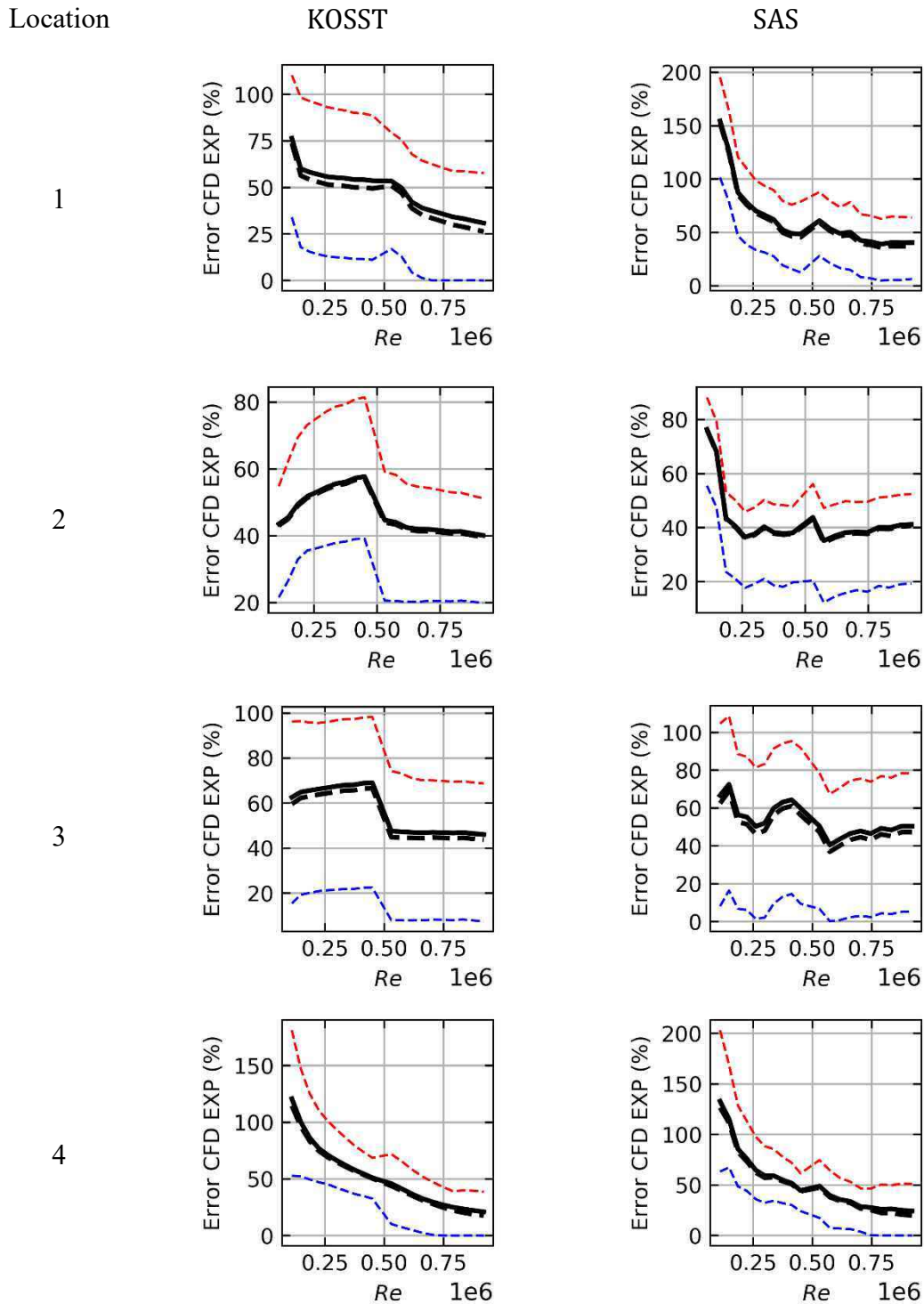


Figure 6.15: Evolution of the deviation between Nu_{CFD} and Nu_{EXP} for the KOSST and SAS models. The MAE is given in black solid line, the min and max value of the absolute error over the surface are given in dotted line respectively in blue and red. The RMSE is given with solid dashed line.

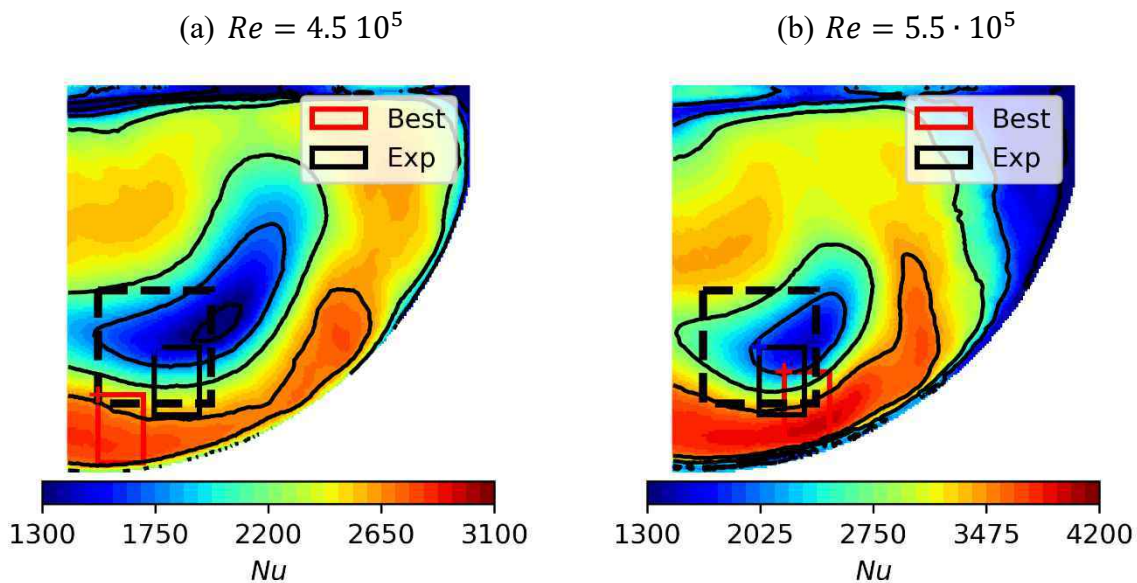


Figure 6.16: Example of displacement of the comparison with the SAS model for $Re = 4.5 \cdot 10^5$ and $Re = 5.5 \cdot 10^5$.

A sensitivity to the comparison window has also been tested with these models. The surface distribution of the KOSST and SAS were found to present the most fluctuations on the Reynolds range. Especially around location 4. An example is given for the SAS model on Figure 6.16 near $Re = 5 \cdot 10^5$ where the grid is switched in order to reduce the y^+ values on the partition plate. It is noticeable that for the high y^+ situation at $Re = 4.5 \cdot 10^5$, the comparison is best when displaced on the left of the window. The effect of the y^+ reduction is the repositioning of the patterns visible on the surface distribution. When the minimum y^+ values are closer to $y^+ = 30$ the minimum RMSE position is closer to the original position of the measurements. The minimum value of the RMSE on the window is given as a function of the Reynolds number on Figure 6.17 in comparison to the RMSE calculated at the measurement location.

For both cases, the surface distribution obtained at the minimum RMSE position shows better comparison to experimental values, especially for $Re > 5 \cdot 10^5$ where the effect of looking on a window reduces significantly the deviation. Finally, the results with the KOSST model were found to yield lower Nusselt number than the RKE model which was found to be closer to the experimental data. The SAS model results on the other hand were comparable to the RKE model of STAR-CCM+. Both SAS and KOSST model results on location 4 were found to be closer to experiments than the RKE model.

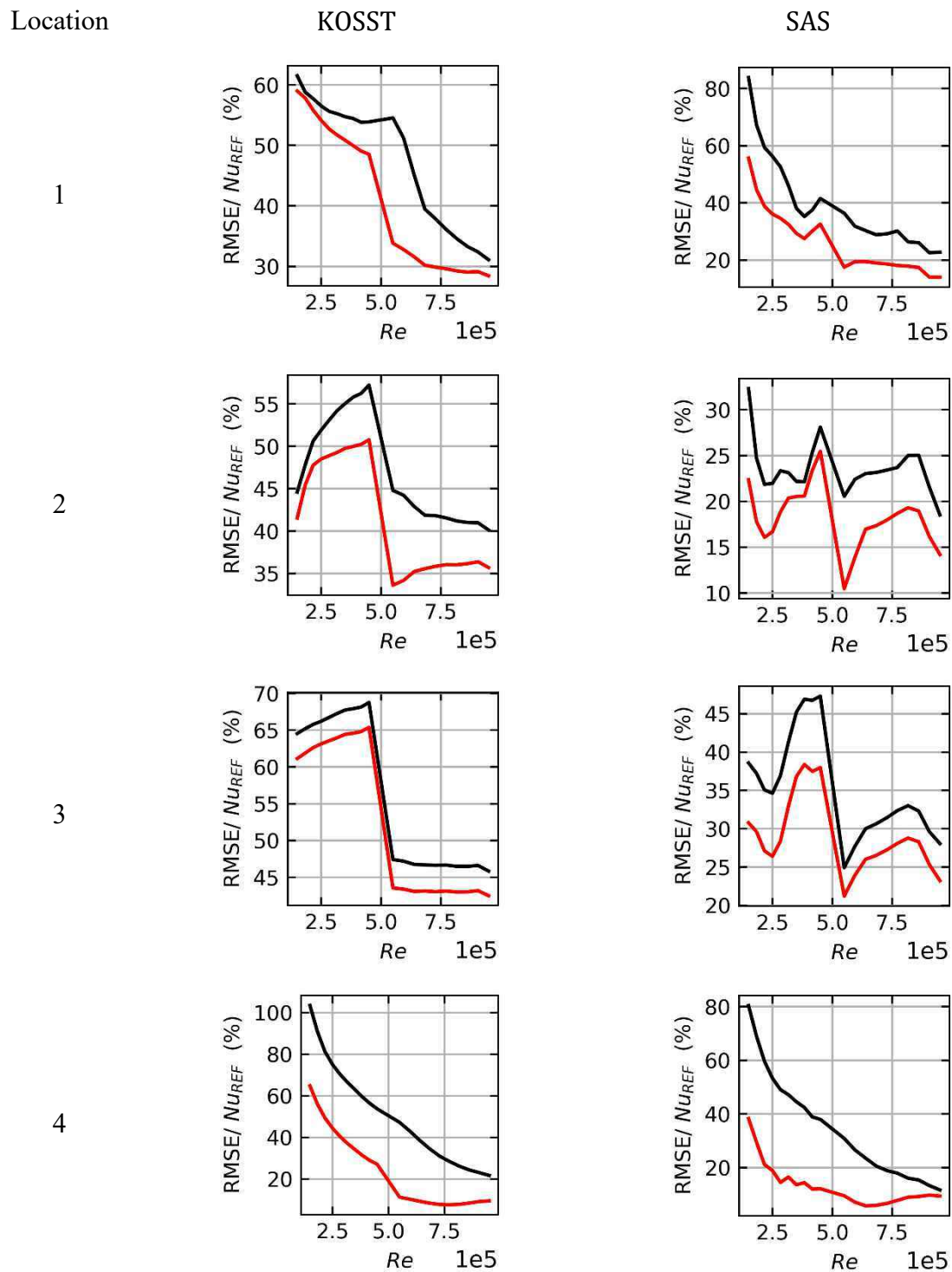


Figure 6.17: Evolution of the deviation between Nu_{CFD} and Nu_{EXP} for the KOSST and SAS models with the windowed approach. The evolution of the minimum RMSE over the window is given in red. Its mean value in solid black line, while a $\mu \pm 2\sigma$ interval is given in grey.

6.5.3 Conclusion

The comparison between CFD and experiments has been done for different turbulence models. The Realizable $k-\epsilon$, the $k-\omega$ SST and SAS models have been used with two grids and softwares. They have been used to generate the distribution of the Nusselt number on the partition plate of the mock-up and were compared to experiments. This comparison has been done by calculating the root mean square error between the Nusselt maps obtained experimentally and numerically for flows at Reynolds number in the range $[10^5, 10^6]$.

- The RKE model yields better estimation of the Nusselt number amplitude in wall jet regions far from the stagnation zone than the KOSST and SAS models. The RMSE decreases from high values at low Reynolds number simulations: maximum values of the RMSE around 60% in the worst case on location 3, to values around 20%-40% depending on the locations. Most of the locations show RMSE below 20% at high Reynolds number simulations. In the stagnation region, near location 4, the KOSST and SAS model are more accurate with RMSE around 20% at high Reynolds numbers. In comparison the RKE overestimates importantly the Nusselt number in this zone (RMSE around 50%)
- The simulation using the RKE model with tetrahedral cells provides results closer to experimental data than the polyhedral mesh simulation which underestimates the amplitude of the Nusselt number. The simulations using the KOSST and SAS models, were done respectively with the polyhedral grid and the tetrahedral grid. Differences of the same order of magnitude were found (around 20%).
- A sensitivity to the location of the comparison window where the RMSE between experiments and simulations is calculated has been done. This sensitivity has been done in order to estimate the effect of the variations of the Nusselt distribution for increasing Reynolds number. Some elements indicate that these variations were correlated to the increase of the y^+ value in the cells adjacent to the partition plate. (see §5.5.3.3). The high gradients region show a high sensitivity to the comparison window were small translations of the window could be used to reduce the deviation between experiments and simulations.
- The influence of the mesh refinement near walls has been observed for simulations at intermediate Reynolds number, where a switch between grids LRE and HRE has been done. The refinement of the near wall mesh reduces significantly the deviation between the experimental and numerical Nusselt number, which might indicate that this deviation can be contained by limiting the minimum y^+ values on the partition plate.

The deviation between CFD and experiments evolves on the Reynolds range: at low Reynolds, the accuracy provided by both models were bad, showing important deviations. The accuracy was found to be better at high Reynolds number. In addition, the variations of the deviation get lower with the increase of the Reynolds number.

Some elements still must be investigated to have a reliable estimation of the evolution of the error $E_{CFD/EXP}$ with the increase of the simulation's Reynolds number:

- The approach used to generate the experimental data impacts importantly the results of the comparisons, especially the transposition and the generation of the Nusselt distribution with POD. Additional work could be done to verify the sensitivity to the processing method.
- The influence of the wall meshing on the accuracy of the simulation has not been dissociated from the Reynolds number influence. Simulations could be done for different refinement of wall meshing in order to investigate the subject.

6.6 Model error

The model error combines the different sources of uncertainty calculated previously with the following formula:

$$\begin{aligned}\mu_{E_{model}} &= \mu_{E_{CFD/EXP}} + \mu_{U_{EXP}} - \mu_{U_{inputs,exp}} - \mu_{E_{NUM}} \\ \sigma_{E_{model}} &= \sqrt{\sigma_{E_{CFD/EXP}}^2 + \sigma_{U_{EXP}}^2 + \sigma_{U_{inputs,exp}}^2 + \sigma_{E_{NUM}}^2}\end{aligned}$$

The different sources of uncertainty have been quantified in the previous sections:

- The standard deviation $\sigma_{U_{EXP}}$ of the experimental uncertainty U_{EXP} on the Nusselt measurements is given on Figure 6.3 and is found to be in the range [7%, 15%] of the calculated Nusselt number on location 1, 2 and 3. On location 4, $\sigma_{U_{EXP}} \in [10\%, 20\%]$. The bias is estimated from the heat loss calculation in the measurement device described in §4.2.3.3. The correction is applied in order to have an unbiased measurement.
- The numerical error E_{NUM} has been quantified for the RKE model. The bias is found to take maximum local values of 2% of their mean with RKE_S on the range $Re \in [5 \cdot 10^5, 10^6]$. The standard deviation is approximately of the same order of magnitude. This bias has been assumed negligible in front of the error between CFD and experiment $E_{CFD/EXP}$. The standard deviation has also been assumed negligible in comparison of the experimental uncertainty standard deviation $\sigma_{U_{EXP}}$.
- The uncertainty when considering the simulation inputs uncertainty $U_{inputs,exp}$ has also been calculated and it has been shown that this uncertainty is negligible in comparison to $E_{CFD/EXP}$ and U_{EXP} with values of the bias below 1% and standard deviations around 5%.
- The deviation between CFD and experiments $E_{CFD/EXP}$ has been calculated for the different models. The standard deviation is assumed to be zero. The bias is given for a

moving comparison window, for which the minimum of the RMSE given (6.5) is obtained.

The importance of the experimental data is highlighted in this quantification of the model error where the only relevant uncertainties are both related to the experiments. The calculation of the model error is done at $Pr = 6$ which was the Prandtl number during the heat transfer coefficient measurements.

The evolutions of the bias and standard deviation with respect to the Reynolds number are given for the Realizable $k-\epsilon$ model (RKE) computations with STAR-CCM+ and Fluent on Figure 6.18. The calculation for the Scale Adaptive Simulation (SAS) model and $k-\omega$ SST (KOSST) model is given on Figure 6.19. The bias and standard deviation are given relatively to the mean Nusselt number on the partition plate.

It can be noticed that the evolution of the standard deviation of the model error $\sigma_{E_{model}}/Nu_{ref}$ decreases with respect to the Reynolds number for all the turbulence models. The values are larger than the ones indicated in $\sigma_{U_{EXP}}$ in §6.2 because the results were given relatively to the measurements. The mean Nusselt number over the plate is lower which has the effect of enlarging the relative values. The RKE models yield larger values of the Nusselt number which explains why the relative standard deviation is lower than the KOSST and SAS models.

The bias also seems to stabilize for increasing Reynolds, the value differs greatly between the different models and locations. It has been shown that switching to the tetrahedral cells makes the calculated Nusselt number grow in amplitude in (§5.5.2) explaining the differences obtained from Fluent and STAR-CCM+ simulations using the RKE model. These differences decrease with the Reynolds number for location 1 and 2. Also, the differences between code and grids were reduced importantly when comparing the SAS and the KOSST. It should be noticed that the calculations of the Nusselt number with the SAS and KOSST models on location 4 near the impingement zone are less sensitive to the Reynolds number evolution.

Finally, the bias is within the experimental uncertainty for all the models, except for location 4 with the RKE model.

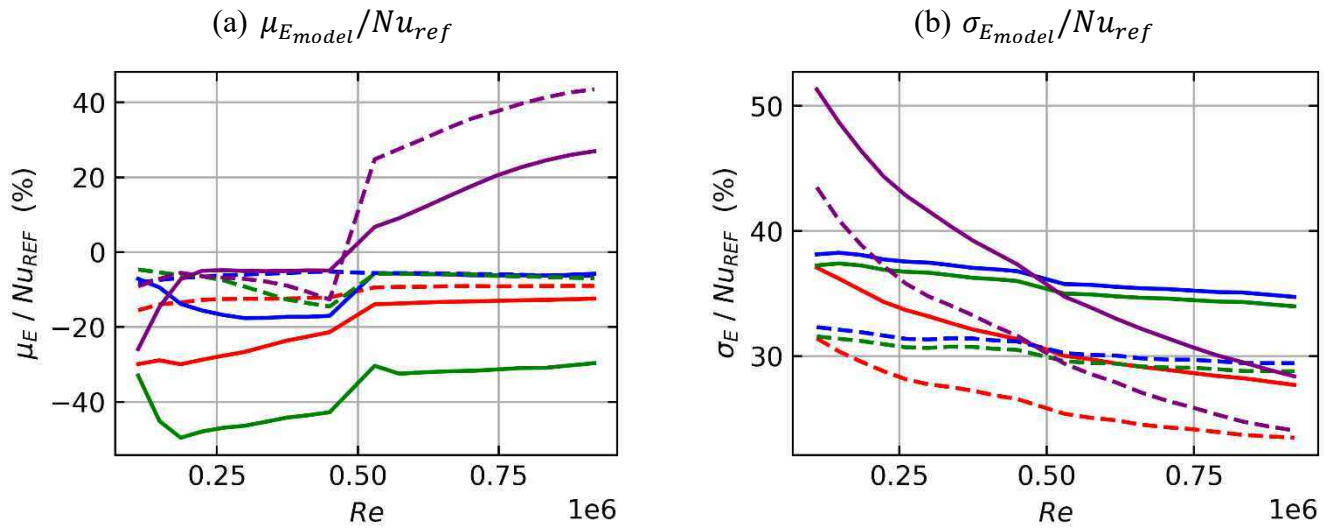


Figure 6.18: evolution of the mean value and standard deviation of the model error E_{model} of the RKE model relatively to the mean value over the partition plate. The model error is calculated on location 1 (red), 2 (blue), 3 (green) and 4 (purple). The computations with STAR-CCM+ are given in solid lines while the dashed lines are obtained from Fluent computations

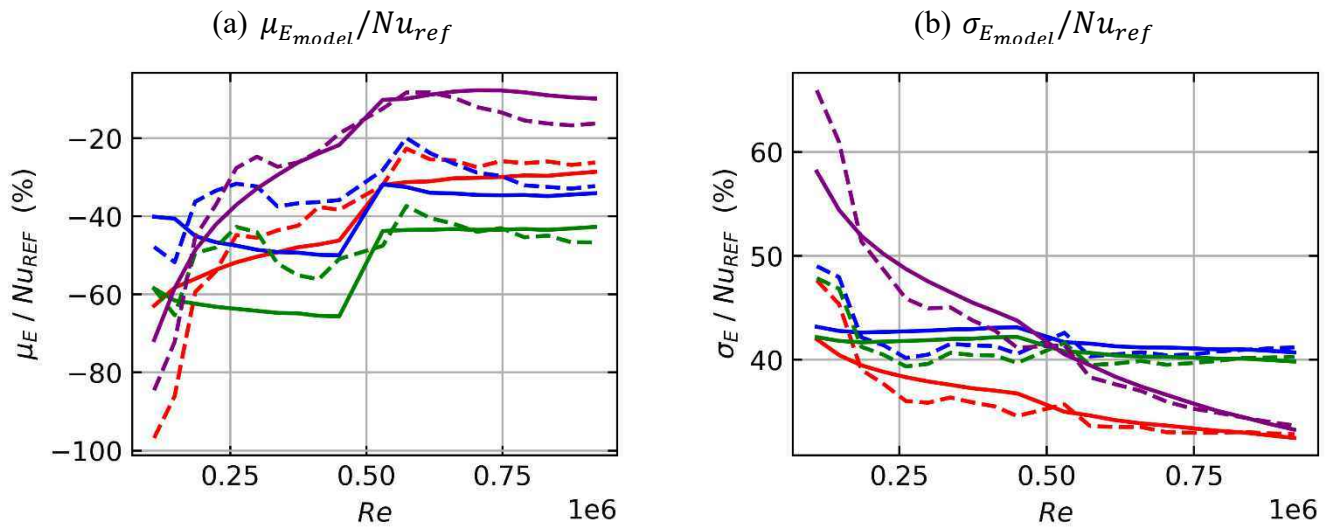


Figure 6.19: evolution of the mean value and standard deviation of the model error E_{model} of the SAS (dashed lines) and KOSST (solid lines) models relatively to the mean value over the partition plate. The model error is calculated on location 1 (red), 2 (blue), 3 (green) and 4 (purple).

6.7 Conclusion

The measurements and the computations of the heat transfer coefficient described in Chapter 4 and Chapter 5 were compared. An uncertainty quantification process has been applied to the Nusselt number calculated with CFD. The different sources of uncertainty have been identified and estimated.

It has been noticed that the numerical error E_{NUM} which is related to the grid resolution was negligible for RKE simulations. The grids that were used in §6.4 were shown to show small differences in their calculation of the Nusselt number. This error has not been estimated on the other turbulence model. It has been assumed that the numerical error was the same for the different turbulence models which is questionable in view of the increased deviation between CFD and experiments with the KOSST and SAS model.

The uncertainty arising from the simulation inputs uncertainty $U_{inputs,exp}$ has also been found to be negligible. The uncertainty of the Reynolds number and Prandtl number during the experiment have been propagated with Monte-Carlo method on a surrogate model. The resulting uncertainty has been found to differ whether the input parameters were defined with zero covariance or not. The bias and standard deviation have been found to be negligible when compared to the experimental uncertainty and to the gap between CFD and experiments.

An important aspect of this uncertainty quantification has been to find an appropriate methodology to generate experimental Nusselt number maps for given Reynolds and Prandtl numbers with reasonable experimental uncertainty U_{EXP} . This prediction has been done by combining the 2D maps obtained from Sherwood number measurements and surface average data obtained from Nusselt measurements. An analytical function is given for prediction of the experimental Nusselt number from the measurements. The uncertainty on the measurements has then been propagated through this analytical function with Monte Carlo method and yielded the most significant contribution to the model error's variance.

Finally, the error between CFD and experiments $E_{CFD/EXP}$ has been evaluated for the different turbulence models. It has been observed that the bias was affected by both the type of cells in the grid, the wall meshing and turbulence models. The computations with the RKE model with both softwares tested were found to provide more accurate results in view of the experimental data than the KOSST and SAS models. Moreover, the discrepancy between the Nusselt number's calculation by both softwares was found to be reduced when using identical grids. The results with the SAS and KOSST models were found to underestimate the experimental Nusselt number Nu_{EXP} more importantly, however, the surface distribution of the Nusselt number has been observed to be more accurate with these models near the stagnation region.

It should be noted that the non-dimensional near wall distance y^+ values on the partition plate have an impact on the accuracy of the computations:

- Larger values of y^+ decrease the amplitude of the maximum Nusselt number.
- The surface distribution is distorted when the y^+ values increase which leads to important differences between CFD and experiments when comparing on the measurement locations.

The model error E_{model} has been deduced from the different sources of error and uncertainty. $E_{CFD/EXP}$ and U_{EXP} were found to be dominant in front of the other sources $U_{inputs,exp}$ and E_{NUM} . The bias of the model error has been found to be bounded by the experimental uncertainty.

In the future, the impact of the y^+ on the calculation of the Nusselt number values should be explored. Clearly, when the Reynolds number is large, the effect of near wall meshing plays a lower role, nevertheless, confirmation must be given by comparing different wall meshing.

Conclusion and perspectives

The use of CFD softwares in the nuclear industry requires validation. The difficulty to obtain heat transfer data at the reactor scale led to a validation on reduced scale mock-ups, which present lower Reynolds numbers. The objective of this dissertation was to investigate the evolution of the model error for calculation of the heat transfer coefficient with RANS simulations according to the Reynolds number evolution in order to verify that its bias and standard deviation values do not increase between these two scales. The approach proposed in this dissertation was to:

- generate experimental heat transfer coefficient data on an extended range of Reynolds number
- reproduce the experiments with CFD simulation for identical flow configuration and boundary conditions
- proceed to the uncertainty quantification in order to obtain the evolution of the model error according to the Reynolds number.

The experimental aspect was certainly the most challenging as a new method relying on gypsum dissolution and on the heat and mass transfer analogy had to be developed. The method was first tested on the well-documented case of the rectangular channel flow. The work achieved on this flow configuration is presented in Chapter 2. During the experiments, it has been observed that the roughness which develops on the gypsum surface during the gypsum dissolution induced a bias for high Reynolds numbers. The correction of this bias was critical as the models that had to be tested in CFD provide smooth wall heat transfer coefficients. The enhancement of the mass transfer coefficient has been estimated with a transposition factor based on Gnielinski correlation of heat transfer which uses Darcy friction factor. The heat transfer data generated with this transposition factor was found to be in a good agreement with literature. Moreover, the test that have been carried out on the rectangular channel showed the importance of the preparation of the gypsum samples on the repeatability of the measurements.

The experimental data obtained was then used for the uncertainty quantification of two commercial CFD codes in Chapter 3. The work gave first insights on the importance of each source of error and uncertainty. Moreover, these simulations brought to light the differences between calculation with or without wall law with the Realizable $k - \epsilon$ turbulence model,

yielding significant differences regarding the establishment of the heat transfer coefficient, and smaller differences in the calculation of the heat transfer coefficient for an established thermal boundary layer. Differences between the heat transfer coefficient calculated with both codes were also noticed. Also, the uncertainty quantification process highlighted the relative importance of the experiments which are involved in the two main contributions of the model error being the experimental uncertainty U_{EXP} and the error between CFD and experiments $E_{CFD/EXP}$. In addition, two approaches were used in order to propagate the simulation inputs uncertainty through CFD simulations which yielded similar results. Finally, it has been found that the model error remains approximatively constant for increasing Reynolds numbers, with a difference between experiments and CFD remaining within the experimental uncertainty of the measurements.

Following this initial testing phase, the approach was reproduced on a reduced scale mock-up of a steam generator water box. The experimental measurements were presented in Chapter 4. The methodology used to transpose gypsum mass transfer data to the heat transfer domain had to be adapted, as the correlations on which the calculation relied in Chapter 2 were no longer appropriate for the flow configuration. In this case, the proposed approach was to make both heat and mass transfer measurements in order to estimate the surface distribution and amplitude of the heat transfer coefficient on the measurement locations. The heat transfer measurement device was designed to obtain two surface average values of the heat transfer coefficient which enabled the calculation of the transposition factor between mass transfer on rough walls and heat transfer on smooth walls. The surface distribution was obtained from gypsum dissolution measurements which were processed with the proper orthogonal decomposition. Partial comparison has been made between heat and mass transfer measurements which seemed to corroborate the heat and mass transfer analogy.

CFD calculations were then performed on the steam generator mock-up, which are presented in Chapter 5. The computations were performed with different turbulence models and different grids. The resulting values of the heat transfer coefficient on the plate opposing the jet were found to vary significantly for the different wall distance y^+ of the cells adjacent to the partition plate. The maximum heat transfer coefficient calculated has been found to decrease for increasing minimum y^+ values on the plate. Moreover, a translation of the patterns visible on the surface distribution of the heat transfer coefficient was observed. In addition, important differences were found between the turbulent models, the Realizable $k - \epsilon$ turbulence model calculations yielded higher values of the heat transfer coefficient compared to the $k - \omega$ SST model values. Differences between STAR-CCM+ and Fluent were observed for simulations using RKE model. These differences were shown to be significantly reduced when calculating on the same grids.

The comparison with experiments and the uncertainty quantification process was presented in Chapter 6. The numerical error was estimated with a grid convergence method for computations with the Realizable $k - \epsilon$ model. The values of the bias and standard deviation were found to be negligible with respect to other sources of error and uncertainties. The same conclusion was drawn for the uncertainty due to the simulation inputs uncertainty. The experimental uncertainty was estimated by combining the variability of the surface distribution observed with the gypsum measurements, and the uncertainty on the measured heat transfer coefficient due to the fluctuations of the operating conditions during the experiments. Finally, the error between CFD and experiments was evaluated for the computations presented in Chapter 5. The Realizable $k - \epsilon$ model was able to predict the most accurately the maximum heat transfer coefficient. In comparison, the $k - \omega$ SST model and the Scale Adaptive Simulation model gave better results regarding the surface distribution but both models underestimated more importantly the heat transfer on the measurement locations. However, these latter models were able to predict a local minimum of the heat transfer coefficient observed in the experiments which were not captured in the Realizable $k - \epsilon$ simulations. Moreover, a bias was induced on the comparison between experiments and CFD due to the evolution of the spatial distribution of the heat transfer coefficient for increasing Reynolds number. The y^+ value was not constant for all simulations, and its increase for a fixed mesh and larger Reynolds number has been found to modify the surface distribution. Thus, a method has been defined to estimate the bias by shifting the comparison around the measurement locations. The resulting model error was found to decrease for increasing Reynolds number for all the different simulations that were performed. Moreover, the bias between CFD and experiment was found to remain within the experimental uncertainty of the measurements. In addition, the deviation seems to be controlled by the mesh refinement near the walls. It has been observed in some cases that refining the mesh near wall boundaries in the fluid domain leads to a significant decrease of the deviation between experiments and simulations. The overall accuracy of the tested models (KOSST, SAS, RKE) at high Reynolds was found to be in the worst case around 40%. The precise determination of the “absolute” value of the model uncertainty of the investigated CFD codes was not the main target of this thesis. However, the order of magnitude of the uncertainty computed is found consistent with the margin usually taken in engineering analyses.

Following the last experimental and CFD results, perspectives can be drawn. From the experimental point of view, the impact of roughness on the mass transfer could be investigated further. Mass transfer data obtained with gypsum dissolution is available for experiments presenting difference in their roughness. This data might be sufficient to estimate a functional relation between the surface roughness and the enhancement of mass transfer. Otherwise, experiments could be done in order to obtain the mass transfer coefficient with different surface aspect by increasing or decreasing the exposition time of the gypsum samples in water. This functional relation could then be used in order to transpose the data to the heat transfer domain

without having to rely on heat transfer coefficient measurements. This would be particularly of interest for two other measurement locations in the steam generator mock-up which were not presented in this document. On these locations, only mass transfer data were available, the availability of a transposition factor in this case would enable the comparison of CFD simulation on two additional reference locations: the inlet nozzle of the jet, where the flow separates downstream a bend, and on the tubular plate which could give information on the repartition of the flowrate in the grid. Moreover, additional tests on roughness could be carried out, Framatome's experimental facility have the possibility to coat the surface of the heat transfer measurement device for it to display a rough surface. The dependency of the enhancement of heat and mass transfer with roughness with respect to the Prandtl number and Schmidt number could be investigated for different kinds of roughness and enable the comparison of wall laws for rough surfaces.

From the numerical point of view, the influence of the wall grid refinement on the surface distribution of the heat transfer coefficient affected the comparison between CFD and experiments. Additional simulations could be performed with more refined near wall meshes in order to have a more reliable estimation of the model error. Also, the grid convergence method could be applied to the models other than the Realizable $k - \epsilon$ model in order to verify that their results were not affected by non-converged grids.

Some differences were found between the turbulent quantities with the different models. A study of the effect of the jet turbulence and its correlation to the heat transfer coefficient surface distribution could be performed in order to explain the differences between the models.

Finally, the simulations could be done for higher Prandtl number approaching the Schmidt number during the experiments in order to verify the prediction abilities of RANS CFD in these cases.

In conclusion, it has been observed that the accuracy of the turbulence models used in commercial CFD softwares is not impaired for increasing Reynolds numbers in the range investigated, which is an element corroborating the fact that the validation carried out on reduced scale mock-ups for reactor scale applications do not induces an additional error due to the difference of turbulence scales.

References

- Allen, J. R. L., 1971. Bed forms due to mass transfer in turbulent flows: a kaleidoscope of phenomena. *Journal of Fluid Mechanics*, 65(4), pp. 49-63.
- Arolla, S. K. & Durbin, P. A., 2013. Modeling rotation and curvature effects within scalar eddy viscosity model framework. *International Journal of Heat and Fluid Flow*, Volume 39, pp. 78-89.
- Baldwin, B. & Lomax, H., 1978. *Thin-layer approximation and algebraic model for separated turbulentflows*. , 16th aerospace sciences meeting, p. 257.
- Barbier, A. et al., 2009. *Experimental characterization of hydraulics in the EPRTM lower plenum. Tests performed on the JULIETTE mock-up*. Tokyo,
- Bejan, A., 2013. *Convection heat transfer, Fourth edition*. :John wiley & sons.
- Belson, B. A., Tu, J. H. & Rowley, C. W., 2014. Algorithm 945: modred—a parallelized model reduction library. *ACM Transactions on Mathematical Software (TOMS)*, 40(4), pp. 1-23.
- Berger, F. P., Hau, K. -F. & Hau, F.-L., 1979. Local mass/heat transfer distribution on surfaces roughened with small square ribs. *International Journal of Heat and Mass Transfer*, 22(12), pp. 1645-1656.
- Bergmann, M., Cordier, L. & Brancher, J. P., 2005. Optimal rotary control of the cylinder wake using POD reduced order model. *Physics of Fluids, American Institute of Physics*, 17(09), p. 097101.
- Bergman, T. L., Incropera, F. P., DeWitt, D. P. & Lavine, A. S., 2011. *Fundamentals of heat and mass transfer*. :John Wiley & Sons.
- Berkooz, G., Holmes, P. & Lumley, J. L., 1993. The proper orthogonal decomposition in the analysis of turbulent flows. *Annual review of fluid mechanics*, 25(1), pp. 539-575.
- Blount, C. W. & Dickson, F. W., 1973. Gypsum-anhydrite equilibria in systems CaSO₄-H₂O and CaCO₄-NaCl-H₂O. *American Mineralogist: Journal of Earth and Planetary Materials*, Volume 58, pp. 323-331.
- Blumberg, P. N., 1970. *Flutes: a study of stable, periodic dissolution profiles resulting from the interaction of a soluble surface and an adjacent turbulent flows (Doctoral Dissertation, University of Michigan)*. :
- Blumberg, P. N. & Curl, R. L., 1974. Experimental and theoretical studies of dissolution roughness. *Journal of Fluid Mechanics*, 65(4), pp. 735-751.
- Boelter, L. M. K., Young, G. & Iversen, H. W., 1948. *An Investigation of Aircraft Heaters XXVII: Distribution of Heat-transfer Rate in the Entrance Section of a Circular Tube*,
- Brouillot, D., 2016. *Etude expérimentale de l'aérothermique et de la dynamique des jets impactants (Doctoral Dissertation, UT3 Paul Sabatier)*, Toulouse:

- Celik, I. et al., 2008. Procedure for Estimation and Reporting of Uncertainty Due to Discretization in CFD Applications. *Journal of fluids Engineering-Transactions of the ASME*, 130(7).
- Celik, I. & Karatekin, O., 1997. Numerical experiments on application of Richardson extrapolation with nonuniform grids. *ASME. J. Fluids Eng.* , 119(3), p. 584–590.
- Chaloner, K. & Verdinelli, I., 1995. Bayesian Experimental Design: A Review. *Statistical Science*, 10(3), pp. 273-304.
- Chang, S., Elkins, C., Eaton, J. K. & Monismith, S., 2013. Local mass transfer measurements for corals and other complex geometries using gypsum dissolution. *Experiments in fluids*, 54(7), p. 1563.
- Coleman, H. & Members, C., 2009. *ASME V&V 20-2009 Standard for Verification and Validation in Computational Fluid Dynamics and Heat Transfer.* :
- Coney, M. W. E., 1981. Erosion-Corrosion: the calculation of mass-transfer coefficients. *CEGB*.
- Cordier, L. & Bergmann, M., 2008. *Proper Orthogonal Decomposition: an overview. Lecture series 2002-04, 2003-4, 3 and 2008-01 on post-processing of experimental and numerical data.* Von Kármán Institute for Fluid Dynamics,
- Cressie, N., 1990. The Origins of Kriging. *Mathematical geology*, 22(3), pp. 239--252.
- Dawson, D. A. & Trass, O., 1972. Mass transfer at rough surfaces. *International Journal of Heat and Mass Transfer*, 15(7), pp. 1317-1336.
- Deissler, R. G., 1954. *Analysis of turbulent heat transfer, mass transfer, and friction in smooth tubes at high Prandtl and Schimidt numbers.* :
- Diamantaras, K. L. & Kung, S. Y., 1996. *Principal component neural networks: theory and applications.* :John Wiley & Sons, Inc..
- Dolleans, P., de Monplanet, C. & Fontes, J.-P., 2008. *EPR: Tests performed to confirm the mechanical and hydraulic design of the vessel internals.* ,
- Durbin, P., 1996. On the k-3 stagnation point anomaly. *Int. J. Heat and Fluid Flow*, Volume 17, pp. 89-90.
- Duvenaud, D., 2014. *Automatic model construction with Gaussian processes (Doctoral Dissertation, University of Cambridge).* :
- Ferson, S. et al., 2004. Summary from the epistemic uncertainty workshop: consensus amid diversity. *Reliability Engineering & System Safety*, Volume 85, pp. 355-369.
- Frank, M. W., 1999. Treatment of uncertainties in space nuclear risk assessment with examples from Cassini mission applications. *Reliability Engineering & System Safety*, 66(3), pp. 203-221.
- Gnielinski, V., 1967. New equations for heat and mass transfer in turbulent pipe and channel flow. *Int. Chem. Eng.*, 16(2), pp. 359-368.
- Goldstein, R. & Cho, H., 1995. A review of mass transfer measurement using naphtalène sublimation. *Experimental Thermal and Fluid Science*, 10(4), pp. 416-434.

-
- Goreaud, N., Nicaise, N. & Stoudt, R., 2004. *Evolution of the design methodologies for the next generation of RPV Extensive role of the thermal-hydraulics numerical tools.* ,
- Harris, C. R. et al., 2020. Array programming with NumPy. *Nature*, 585(7825), pp. 357-362.
- Hedberg, P. & Hessling, P., 2015. *Use of Deterministic Sampling for Uncertainty Quantification in CFD.* Chicago, Illinois,
- Hessling, P., 2013. *Deterministic Sampling for Propagating Model Covariance.* , , pp. 297-318.
- Holmes, P. J. et al., 1997. Low-dimensional models of coherent structures in turbulence. *Physics Reports*, 287(4), pp. 337-384.
- Hoogendoorn, C. J., 1977. The effect of turbulence on heat transfer at a stagnation point. *Internationnal Journal of Heat and Mass Transfer*, 20(12), pp. 1333-1338.
- Huber, M. L. et al., 2009. New International Formulation for the Viscosity of H₂O. *Journal of Physical and Chemical Reference Data*, 38(2), pp. 101-125.
- Jambunathan, K., Lai, E., Moss, M. A. & Button, B. L., 1992. A review of heat transfer data for single circular jet impingement. *International Journal of Heat and Fluid flow*, 13(2), pp. 106-115.
- Jayatilleke, C. L. V., 1966. *The influence of Prandtl number and surface roughness on the resistance of the laminar sub-layer to momentum and heat transfer (PhD thesis)*, : Imperial College London.
- Jischa, M. & Rieke, H. B., 1979. About the prediction of turbulent Prandtl and Schmidt numbers from modeled transport equations. *International Journal of Heat and Mass Transfer*, 22(11), pp. 1547-1555.
- Jones, W. P. & Launder, B. E., 1972. The prediction of Laminarization with a Two Equation Model of Turbulence. *International Journal of Heat and Mass Transfer*, Volume 15, pp. 301-314.
- Julier, S. J. & Uhlmann, J. K., 2004. Unscented filtering and nonlinear estimation. *Proceedings of the IEEE*, 92(3), pp. 401-422.
- Julier, S. J., Uhlmann, J. K. & Durrant-Whyte, H. F., 1995. A new approach for filtering nonlinear systems. *Proceedings of 1995 American Control Conference-ACC'95*, Volume 3, pp. 1628-1632.
- Kader, B. A., 1981. Temperature and concentration profiles in fully turbulent boundary layers. *International Journal of Heat and Mass Transfer*, 24(9), pp. 1541-1544.
- Kalpakli, A. & Örlü, R., 2013. Turbulent pipe flow downstream a 90° pipe bend with and without superimposed swirl. *International Journal of Heat and Fluid Flow*, Volume 41, pp. 103-111.
- Kays, W. M., 1994. Turbulent Prandtl number. Where are we?. *ASME Transactions Journal of Heat Transfer*, 116(2), pp. 284-295.
- Khayiguian, V. et al., 2020. *Mass transfer measurements in a rectangular channel.* Palaiseau, France, , pp. 936-949.

- Kleijnen, J. P. C., 2009. Kriging metamodeling in simulation: A review. *European Journal of Operational Research*, Volume 192, pp. 707-716.
- Kleijnen, J. P. C., 2017. Regression and Kriging metamodels with their experimental designs in simulation: A review. *European Journal of Operational Research*, 256(1), pp. 1-16.
- Kleijnen, J. P. C., 2018. *Design and Analysis of Simulation Experiments*. , Springer International Publishing.
- Klimchouk, A., 1996. The dissolution and conversion of gypsum and anhydrite. *International Journal of Speology*, Volume 25, pp. 21-36.
- Koeltzsch, K., 2000. The height dependence of the turbulent Schmidt number within the boundary layer. *Atmospheric Environment*, 34(7), pp. 1147-1151.
- Kulkarni, K. S., Madanan, U., Mittal, R. & Goldstein, R. J., 2017. experimental validation of heat/mass transfer analogy for two-dimensional laminar and turbulent boundary layers. *International Journal of Heat and Mass Transfer*, Volume 113, pp. 84-95.
- Lauder, B. E. & Sharma, B. I., 1974. Application of the Energy Dissipation Model of Turbulence to the Calculation of Flow Near a Spinning Disc. *Letter in Heat and Mass Transfer*, 1(2), pp. 131-138.
- Le, T., Ewing, D., Schefski, C. & Ching, C. Y., 2014. Mass transfer in back-to-back elbows arranged in an out of plane configuration. *Nuclear engineering and design*, Volume 270, pp. 209-216.
- Li, C. Y. & Garimella, S. V., 2001. Prandtl number effects and generalized correlations for confined and submerged jet. *International Journal of Heat and Mass Transfer*, 44(18), pp. 3471-3480.
- Lolja, S., 2005. Momentum and mass transfer on sandpaper-roughened surfaces in pipe flow. *International journal of heat and mass transfer*, 48(11), pp. 2209-2218.
- Loyd, J. R. et al., 2014. *How to build an automatic statistician*. [En ligne] Available at: <http://www.cs.toronto.edu/~duvenaud/courses/csc412/lectures/11-GPs.pdf>
- Lumley, J. L., 1967. The structure of inhomogeneous turbulent flows. *Atmospheric turbulence and radio wave propagation*, pp. 221-227.
- Ma, C. F. et al., 1997. Local characteristics of impingement heat transfer with oblique round free surface jets of large Prandtl number liquid. *International Journal of Heat and Mass Transfer*, 40(10), pp. 2249-2259.
- Manceau, R. & Hanjalic, K., 2002. Elliptic blending model: A near-wall-stress turbulence closure. *Physics of dfluids*, 14(2), pp. 744-754.
- Mannini, C., Šoda, A. & Schewe, G., 2010. Unsteady RANS modelling of flow past a rectangular cylinder: Investigation of Reynolds number effects. *Computers & fluids*, 39(9), pp. 1609-1624.
- Martinez, P. & Galpin, J., 2014. CFD modeling of the EPR primary circuit. *Nuclear Engineering and Design*, Volume 278, pp. 529-541.

- Matsumoto, M. & Nishimura, T., 1998. Mersenne twister: a 623-dimensionally equidistributed uniform pseudo-random number generator. *ACM Transactions on Modeling and Computer Simulation (TOMACS)*, 8(1), pp. 3-30.
- Mazhar, H., Ewing, D., Cotton, J. S. & Ching, C. Y., 2013. Experimental investigation of mass transfer in 90 pipe bends using a dissolvable wall technique. *International Journal of Heat and Mass Transfer*, Volume 65, pp. 280-288.
- Mazhar, H., Ewing, D., Cotton, J. S. & Ching, C. Y., 2014. Mass transfer in dual pipe bends arranged in an S-configuration. *International Journal of Heat and Mass Transfer*, Volume 71, pp. 747-757.
- Menter, F. & Egorov, Y., 2005. *A scale adaptive simulation model using two-equation models*. Reno, Nevada, 43rd AIAA Aerospace Sciences Meeting and Exhibit.
- Menter, F. R., 1994. Two-equation eddy-viscosity turbulence models for engineering applications. *AIAA Journal*, 32(8), pp. 1598-1605.
- Menter, F. R., Egorov & Y., 2004. *Revisiting the Turbulent Scale Equation*. Göttingen, IUTAM Symposium on One Hundred Years of Boundary Layer Research, pp. 279-290.
- Merz, B. & Thielen, A. H., 2005. Separating natural and epistemic uncertainty in flood frequency analysis. *Journal of Hydrology*, Volume 309, pp. 114-132.
- Miller, C. C., 1924. The Stokes-Einstein law for diffusion in solution. *Proceedings of the Royal Society of London. Series A, Containing Papers of a Mathematical and Physical Character*, 106(740), pp. 724-749.
- Mittal, R., Madanan, U. & Goldstein, R. J., 2017. The heat/mass transfer analogy for a backward facing step. *International Journal of Heat and Mass Transfer*, Volume 113, pp. 411-422.
- Mourgues, A., Houartané, V., Muller, T. & Caron-Charles, M., 2013. Boiling behaviors and critical heat flux on a horizontal and vertical plate in saturated pool boiling with and without ZnO nanofluids. *International Journal of Heat and Mass Transfer*, 57(2), pp. 595-607.
- Nikuradse, J., 1950. *Laws of flow in rough pipes*, : National Advisory Committee for Aeronautics Washington.
- Notter, R. H. & Sleicher, C. A., 1972. A solution to the turbulent Graetz problem—III Fully developed and entry region heat transfer rates. *Chemical Engineering Science*, 27(11), pp. 2073-2093.
- Ochoa, R. E., Gutiérrez, C. A., Rendón & Rodríguez, J. L., 2017. Effect of preparation variables of plaster molds for slip casting of sanitary ware. *Boletín de la Sociedad Española de Cerámica y Vidrio*, 56(6), pp. 263-272.
- Ochoa, R. et al., 2018. Effect of Water/Plaster Ratio on Preparing Molds for Slip Casting of Sanitaryware; Rheology of the Initial Plaster Slurry, Microstructure and Mold Properties. *Transactions of the Indian Ceramic society*, Volume 77, pp. 84-89.
- Patel, V. C., Rodi, W. & Scheuerer, G., 1985. Turbulence models for near wall and low Reynolds number flows: A review. *AIAA Journal*, 23(9), pp. 1308-1319.

- Pedregosa, F. V. G. G. A. M. V. T. B. G. O. .. & D. E., 2011. Scikit-learn: Machine learning in Python.. *the Journal of machine Learning research*, Volume 12, pp. 2825-2830.
- Podvin, B., 2011. *A POD-Based Model for the Turbulent Wall Layer*. Dordrecht, Springer Netherlands, pp. 309-316.
- Podvin, B. et al., 2020. Proper orthogonal decomposition analysis and modelling of the wake deviation behind a squareback Ahmed body. *Physical Review Fluids*, 5(6), p. 064612 .
- Pope, S. B., 2000. *Turbulent flows*. Cambridge: Cambridge University Press.
- Postlethwaite, J. & Lotz, U., 1988. Mass transfer at erosion-corrosion roughened surfaces. *The Canadian Journal of Chemical Engineering*, 66(1), pp. 75-78.
- Prandtl, L. & Weighardt, K., 1945. Uber ein neues Formelsystem dur die ausgebildete Tubulenz. *Nach. Akad. Wiss. Gottingen Math. Phis. Kl.*
- Rasmussen, C. E. & Williams, C. K., 2006. *Gaussian Processes for machine learning*. :The MIT Press.
- Reichardt, H., 1951. Vollständige Darstellung der turbulenten Geschwindigkeitsverteilung in glatten Leitungen. *ZAMM-Journal of Applied Mathematics and Mechanics/Zeitschrift für Angewandte Mathematik und Mechanik*, 31(7), pp. 208-219.
- Reynolds, A. J., 1975. The prediction of turbulent Prandtl and Schmidt numbers. *International Journal of heat and mass transfer*, 18(9), pp. 1055-1069.
- Reynolds, O., 1895. IV. On the dynamical theory of incompressible viscous fluids and the determination of the criterion. *Philosophical transactions of the royal society of london.(a.)*, Issue 186, pp. 123-164.
- Richardson, L. F., 1911. IX. The approximate arithmetical solution by finite differences of physical problems involving differential equations, with an application to the stresses in a masonry dam. *Philosophical Transactions of the Royal Society of London. Series A, Containing Papers of a Mathematical or Physical Characte*, Volume 210, pp. 307-357.
- Robinson, K. & Whelan, P. F., 2004. Efficient morphological reconstruction: a downhill filter. *Pattern Recognition Letters*, 25(15), pp. 1759-1767.
- Rodi, W., 1991. *Experience with Two-Layer Models Combining the k-e Model with a One-Equation Model Near the Wall*. , 29th Aerospace Sciences Meeting, p. 216.
- Ross, S. M., 1976. *A first course in probability*. New York: Prentice Hall.
- Rotta, J. C., 1972. *Turbulente Strömungen*. Stuttgart: Teubner Verlag.
- Sahlberg, A., 2016. *Ensemble for Deterministic Sampling with positive weights: Uncertainty quantification with deterministically chosen samples.*, :
- Sakakibara, J. & Machida, N., 2012. Measurement of turbulent flow upstream and downstream of a circular pipe bend. *Physics of Fluids*, 24(4), pp. 041702-.
- Sanitjai, S. & Goldstein, R., 2001. Effect of free stream turbulence on local mass transfer from a circular cylinder.. *Internationnal journal of heat and mass transfer*, Volume 44, p. 2863–2875.

- Sanitjai, S. & Goldstein, R., 2004. Heat transfer from a circular cylinder to mixtures of water and ethylene glycol.. *Internationnal journal of heat and mass transfer*, Volume 47, p. 4785–4794.
- Sarkar, S. & Balakrishnan, L., 1990. *Application of a Reynolds-stress turbulence model to the compressible shear layer.* , , p. 1465.
- Shih, T. et al., 1995. A new k- ϵ eddy viscosity model for high reynolds number turbulent flows. *Computers \& fluids*, 24(3), pp. 227-238.
- Simpson, J. & Carr, H. Y., 1958. Diffusion and nuclear spin relaxation in water. *Physical Review*, 111(5), p. 1201.
- Sirovich, L. & Kirby, M., 1987. Application of the Karhunen-Loeve procedure for the characterization of human faces. *Journal of the Optical Society of America A*, 4(3), pp. 519-524.
- Sleicher Jr, C. A., 1956. *Heat transfer in a pipe with turbulent flow and arbitrary wall-temperature distribution (PhD Thesis).* :University of Michigan.
- Smith, A. & Cebeci, T., 1967. *Numerical solution of the turbulent-boundary-layer equations*, Spalart, P. & Rumsey, C., 2007. Effective Inflow Conditions for Turbulence Models in Aerodynamic Calculations. *AIAA Journal*, 45(10), pp. 2544-2553.
- Sparrow, E. M., Hallman, T. M. & Siegel, R., 1957. Turbulent heat transfer in the thermal entrance region of a pipe with unigorm heat flux. *Applied Scientific Research, Section A*, 7(1), pp. 37-52.
- Sudo, K., Sumida, M. & Hibara, H., 1998. Experimental investigation on turbulent flow in a circular-sectioned 90-degree bend. *Experiments in Fluids*, 25(1), pp. 42-49.
- Van der Walt, S. et al., 2014. scikit-image: image processing in Python. *PeerJ*, Volume 2, p. e453.
- Van Meel, D., 1962. A method for the determination of local convective heat transfer from a cylinder placed normal to an air stream.. *Internationnal of heat and mass transfer* , 5(8), pp. 715-722.
- Villien, B., Zheng, Y. & Lister, D., 2005. Surface dissolution and the development of scallops. *Chem. Eng. Comm.* , 192(1), pp. 125-136.
- Virtanen, P. et al., 2020. SciPy 1.0: Fundamental Algorithms for Scientific Computing in Python. *Nature Methods*, Volume 17, pp. 261-272.
- Wang, D. & Ewing, D. ., C. C. Y., 2016. Time evolution of surface roughness in pipes due to mass transfer under different Reynolds number. *International Journal of Heat and Mass Transfer*, 103(11), pp. 661-671.
- Wang, D. & Ewing, D. ., C. C. Y., 2017. The effect of naturally developing roughness on the mass transfer in pipes under different Reynolds numbers. *Journal of Heat Transfer*, June.139(10).
- Wang, D. et al., 2015. On the non-destructive measurement of local mass transfer using X-ray computed tomography. *Internationnal Journal of Heat and mass transfer*, Volume 81, pp. 531-541.

-
- Wei, T. & Willmarth, W. W., 1989. Reynolds-number effects on the structure of a turbulent channel flow. *Journal of Fluid Mechanics*, Volume 204, pp. 57-95.
- Wilcox, D. C., 1988. Reassessment of the scale-determining equation for advanced turbulence models. *AIAA Journal*, 26(11), pp. 1299-1310.
- Wolfshtein, M., 1969. The velocity and temperature distribution in one-dimensional flow with turbulence augmentation and pressure gradient. *International Journal of Heat and Mass Transfer*, Volume 12, pp. 301-318.
- Zuckerman, N. & Lior, N., 2006. Jet impingement heat transfer: physics, correlations, and numerical modeling. *Advances in heat transfer*, Volume 39, pp. 565-631.

Appendix A Deterministic sample ensembles

Let \mathbf{X} be a multidimensional random variable of dimension p , $\mathbf{X} = (X_1, \dots, X_p)$ of known marginal moments $\langle \delta X_j^m \rangle$. The aim of Deterministic Sampling (DS) is to provide an ensemble of sigma points $\tilde{\mathbf{X}}$ which represents the random variable \mathbf{X} and respects most of its statistical moments. The approach presented in §1.2.4.2.2 relies also on the calculation of weights which can be placed in a vector \mathbf{W} .

$$\mathbf{W} = \begin{pmatrix} w_1 \\ \vdots \\ w_N \end{pmatrix}, \quad \tilde{\mathbf{X}} = \begin{pmatrix} \tilde{X}_{1,1} & \cdots & \tilde{X}_{1,p} \\ \vdots & \ddots & \vdots \\ \tilde{X}_{N,1} & \cdots & \tilde{X}_{N,p} \end{pmatrix}$$

The marginal moments are then be calculated with:

$$\boldsymbol{\mu}(\tilde{\mathbf{X}}) = {}^t \tilde{\mathbf{X}} \mathbf{W}, \quad \langle \delta^m \tilde{\mathbf{X}} \rangle = (({}^t \tilde{\mathbf{X}} - \mathbf{1}_{1 \times N} \otimes {}^t \tilde{\mathbf{X}} \mathbf{W})^{om}) \mathbf{W}$$

with, $\mathbf{1}_{1 \times N}$ a matrix of dimension $1 \times N$ full of 1, \otimes the symbol for Kronecker product between the matrixes $A = (a_{ij})_{i,j \in [1,m] \times [1,n]}$ and the matrix B :

$$A \otimes B = \begin{pmatrix} a_{11}B & \cdots & a_{1n}B \\ \vdots & \ddots & \vdots \\ a_{m1}B & \cdots & a_{mn}B \end{pmatrix}$$

with, \mathbf{A}^{om} the Hadamard power m of \mathbf{A} which is taking the power m of each element of the matrix \mathbf{A} .

The difficulty of DS resides in the calculation of $\tilde{\mathbf{X}}$ and \mathbf{W} in order to encode the known statistical moments $\langle \delta X_j^m \rangle$ or mixed moments. When no weights are used, satisfying the constraints on the statistical moments is equivalent to solve a nonlinear system of equations which can be hard to do, and which can even yield non real solutions. The linearization of the equations with the use of weights simplifies the process of encoding statistical moments but do not necessarily provides satisfactory results regarding propagation for any choice of weights (see for instance Appendix E (Sahlberg, 2016) where the weighted approach can yield a negative standard deviation). The method to find the ensembles and weight can be found in more detail in (Sahlberg, 2016). DS has been used in the nuclear industry for uncertainty propagation and comparisons have been done with other propagation methods such as polynomial chaos expansion or random sampling. The comparison showed that this method

can provide accurate results for very attractive costs. In this dissertation, the case of one uncertain parameter has been presented; however, the real advantage of this method is when the number of independent random variables gets higher as the cost of other methods to propagate uncertainty becomes prohibitive on industrial cases.

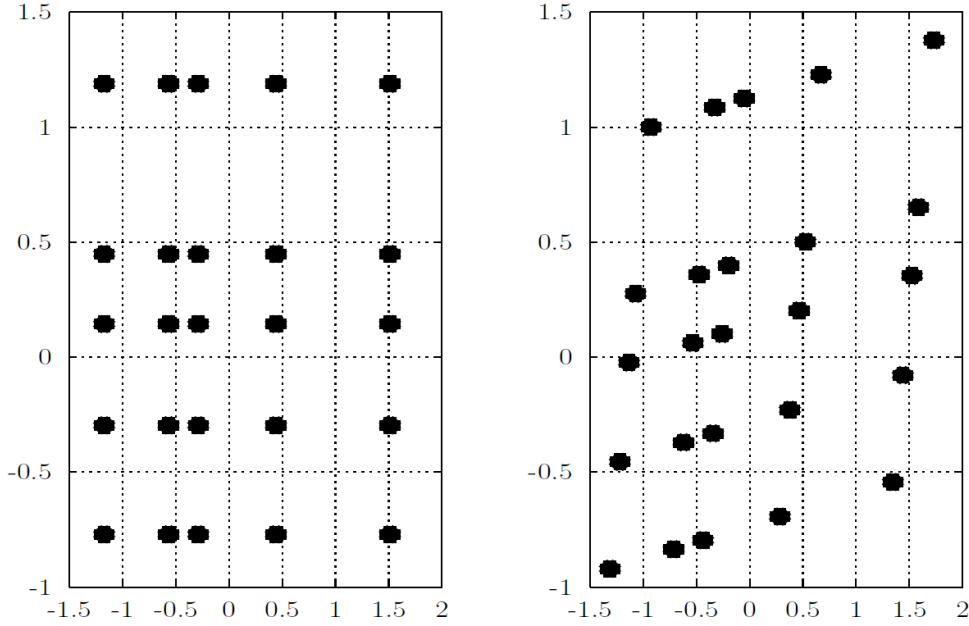


Figure A.1: ensembles of two parameters without any covariance (left) with positive covariance (right)

In this appendix, some excitation matrices (from (Sahlberg, 2016; Hessling, 2013)) used to design the ensemble $\tilde{\mathbf{X}}$ will be presented. The excitation matrices $\hat{\mathbf{V}}$ are general for any cases and depend only on the number of random parameters. These matrices are then scaled to the input random variables by introducing their covariance matrix \mathbf{C} and mean values $\langle \mathbf{X} \rangle = (\langle X_1 \rangle, \dots, \langle X_p \rangle)$ in order to obtain $\tilde{\mathbf{X}}$ (see (Hessling, 2013)):

$$\tilde{\mathbf{X}} = \langle \mathbf{X} \rangle \otimes \mathbf{1}_{1 \times N} + {}^t \mathbf{U} \mathbf{S} \mathbf{U} \hat{\mathbf{V}}$$

where, $\langle \mathbf{X} \rangle \otimes \mathbf{1}_{1 \times N}$ is a matrix containing the N same lines corresponding to the mean value of each unidimensional RV X_i :

$$\langle \mathbf{X} \rangle \otimes \mathbf{1}_{1 \times N} = \left(\begin{array}{ccc} \langle X_1 \rangle & \cdots & \langle X_p \rangle \\ \vdots & \ddots & \vdots \\ \langle X_1 \rangle & \cdots & \langle X_p \rangle \end{array} \right) \left. \vphantom{\begin{array}{ccc} \langle X_1 \rangle & \cdots & \langle X_p \rangle \\ \vdots & \ddots & \vdots \\ \langle X_1 \rangle & \cdots & \langle X_p \rangle \end{array}} \right\} N \text{ lines}$$

\mathbf{S} corresponds to a diagonal matrix containing the standard deviation in the principal directions of \mathbf{C} , and \mathbf{U} corresponds to a unitary matrix which accounts for the correlation between the parameters. In practice these two matrices are found by diagonalizing the matrix \mathbf{C} .

Then a set of weights \mathbf{W} can be calculated for this ensemble of sigma points. An algorithm is given in (Sahlberg, 2016) (§3.4 for unidimensional independent variables and in §3.5 for

multidimensional correlated variables). An example of ensemble for two independent random variables and correlated variables can be seen on Figure A.1.

In this appendix, the case of **independent variables with symmetrical distributions** will be considered in order to simplify the comprehension. In this case, the sigma points are found with $U = I$, where I is the identity matrix. The terms of the activation matrix are scaled by the standard deviation of each parameter and translated by the mean values. For instance, for two independent uncertain parameters X_1, X_2 of mean values μ_1, μ_2 and standard deviation σ_1, σ_2 , if the activation matrix is written:

$$V = \begin{pmatrix} -1 & 1 \\ 1 & -1 \end{pmatrix}$$

the sigma points matrix $\tilde{\mathbf{X}}$ is given by:

$$\tilde{\mathbf{X}} = \begin{pmatrix} \mu_1 - \sigma_1 & \mu_2 + \sigma_2 \\ \mu_1 + \sigma_1 & \mu_2 - \sigma_2 \end{pmatrix}$$

A.1 Standard

This excitation matrix contains $2p$ samples where p is the number of input random variables.

$$\hat{V}_{STD} = \sqrt{p} \begin{pmatrix} I_{p \times p} & -I_{p \times p} \end{pmatrix}$$

where, $I_{p \times p}$ is the identity matrix of dimension p .

This matrix is the one originally used in the Unscented Kalman Filtering (UKF) to propagate the covariance of random variables through functions. This ensemble has the advantage to be simple to evaluate, however, its use is often discouraged as the results become unsatisfactory for large values of p due to the scaling by \sqrt{p} (see (Hessling, 2013; Julier & Uhlmann, 2004)). The weights are equal for all the samples.

A.2 Hadamard

This matrix is defined only for orders which are power of 2 (see Appendix D (Sahlberg, 2016)):

$$H_{2^n} = \begin{cases} 1, & 2^n = 1 \\ \begin{pmatrix} H_{2^{n-1}} & H_{2^{n-1}} \\ H_{2^{n-1}} & -H_{2^{n-1}} \end{pmatrix}, & \text{for } 2^n > 1 \end{cases}$$

For instance, the three first Hadamard matrices defined for $p = 1$, $p = 2$, and $p = 4$ are:

$$H_1 = (1) \quad H_2 = \begin{pmatrix} 1 & 1 \\ 1 & -1 \end{pmatrix} \quad H_4 = \begin{pmatrix} 1 & 1 & 1 & 1 \\ 1 & -1 & 1 & -1 \\ 1 & 1 & -1 & -1 \\ 1 & -1 & -1 & 1 \end{pmatrix}$$

This matrix can be modified in order to be generalizable for any number of parameters p . The modified Hadamard matrix is denoted by letter M_p :

$$M_p = H_m(:, 2:p+1)$$

where, m is the smallest integer such as $m \geq p+1$ with m a power of 2. $H_m(:, 2:p+1)$ corresponds to the first p columns of the matrix H_m starting from the second column. The four first matrices are:

$$M_1 = \begin{pmatrix} 1 \\ -1 \end{pmatrix} \quad M_2 = \begin{pmatrix} 1 & 1 \\ -1 & 1 \\ 1 & -1 \\ -1 & -1 \end{pmatrix} \quad M_3 = \begin{pmatrix} 1 & 1 & 1 \\ -1 & 1 & -1 \\ 1 & -1 & -1 \\ -1 & -1 & 1 \end{pmatrix}$$

$$M_4 = \begin{pmatrix} 1 & 1 & 1 & 1 \\ -1 & 1 & -1 & 1 \\ 1 & -1 & -1 & 1 \\ -1 & -1 & 1 & 1 \\ 1 & 1 & 1 & -1 \\ -1 & 1 & -1 & -1 \\ 1 & -1 & -1 & -1 \\ -1 & -1 & 1 & -1 \end{pmatrix}$$

These two activation matrices are used with sets of equal weights.

A.3 Gauss Heavy Middle

This matrix is based on the modified Hadamard matrix by adding a row containing the centered test:

$$G_p = \sqrt{3} \begin{pmatrix} M_p \\ 0_{1 \times p} \end{pmatrix}$$

where, M_p is the modified Hadamard matrix of order p , and $0_{1 \times p}$ a row of p elements all set to zero.

The weights are calculated differently in this case in order to satisfy the four first moments of any **symmetric distribution with same shape**. The weights are equal for all the non-centered samples:

$$W = \frac{1}{k} \frac{\langle \delta^2 X \rangle^2}{\langle \delta^4 X \rangle}$$

where, k is the number of rows in the matrix G_p , $\langle \delta^2 X \rangle$ and $\langle \delta^4 X \rangle$ are the second and fourth moment of the random variables. For distribution with the same shape, the ratio $\frac{\langle \delta^2 X \rangle^2}{\langle \delta^4 X \rangle}$ are equal.

The weight of centered test is deduced from the other as following:

$$W_{centered} = 1 - \frac{\langle \delta^2 X \rangle^2}{\langle \delta^4 X \rangle}$$

Appendix B Detection of the adjacent flow direction.

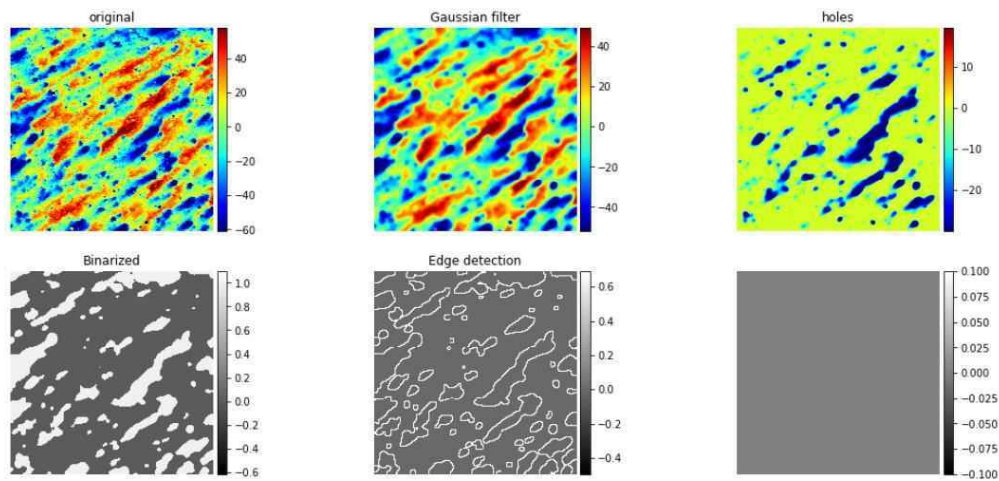


Figure B.1: example of steps for the extraction of the ridges angle.

An algorithm has been developed in order to estimate the direction of the flow in the near wall region adjacent to the gypsum sample. This algorithm is based on the fact that ridges are formed on the gypsum sample surface during dissolution, which direction seems to be colinear to the flow direction (see for instance (Villien, et al., 2005)).

The detection of the direction of the flow on the gypsum surface is done on smaller windows which size has been chosen in an empirical way by making trials. The roughness matrix e (see §0) is used. The steps for each window are as follows:

1. filtering of the image with a gaussian filter in order to have smooth contours
2. extracting the peaks or holes of the image with an algorithm from (Robinson & Whelan, 2004) implemented with the python library scikit-image (Van der Walt, et al., 2014)
3. thresholding the height of the matrix. The matrix is binarized (containing 0 or 1 with respect to their value compared to the threshold)
4. isolating the non-connected elements of the matrix which presents an elongated surface aspect

5. a linear regression is fitted on each of the isolated elements in order to calculate the angle of the line with the horizontal axis.
 6. calculation of the average value and standard deviation for all the isolated elements.
- The different steps can be found on Figure B.1.

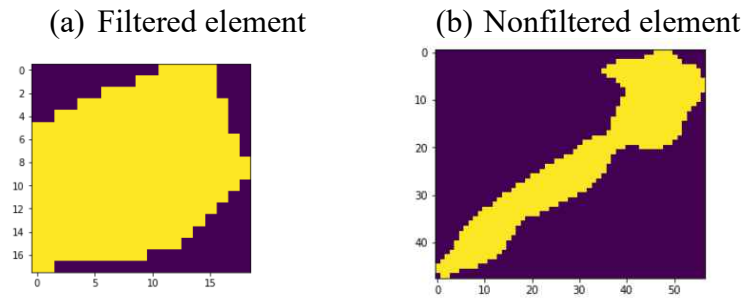


Figure B.2: example of non-connected elements. The element (a) is filtered due to a too important aspect ratio while element (b) combines an acceptable aspect ratio in regard to the maximum length and a low enough fractal dimension.

The step 4 which consists of isolating non-connected elements of the matrix with elongated surface aspect is done with the following methodology:

- A threshold size is given in order to keep only the biggest elements in the binarized matrix.
- the aspect ratio AR (Area/perimeter) is calculated for each element with the binarized matrix and the contours matrix.
- the maximum length separating two points of the elements l_{max} is calculated and a filtering is done in order to keep the elements with:

$$l_{max} > K \times AR$$

K is a calibrated constant.

- The fractal dimension of the element is calculated and an additional filtering on elements with too high values is performed. This process enables the filtering of elements with low aspect ratios which presents folded structures on which the extraction of a direction includes too much uncertainty.

Examples of a filtered element and of an element that has been kept are given on Figure B.2.

An example of the result of the algorithm for a sample exposed to the flow on location 2 (see §4.2) is given Figure B.3. It is noticeable that for some windows, a large standard deviation is calculated which indicates some limitation of the algorithm relating to the filtering of the non-connected elements of the binarized matrix. Nevertheless, satisfactory estimations of the flow directions could be done by combining the information retrieved for all the experiments.

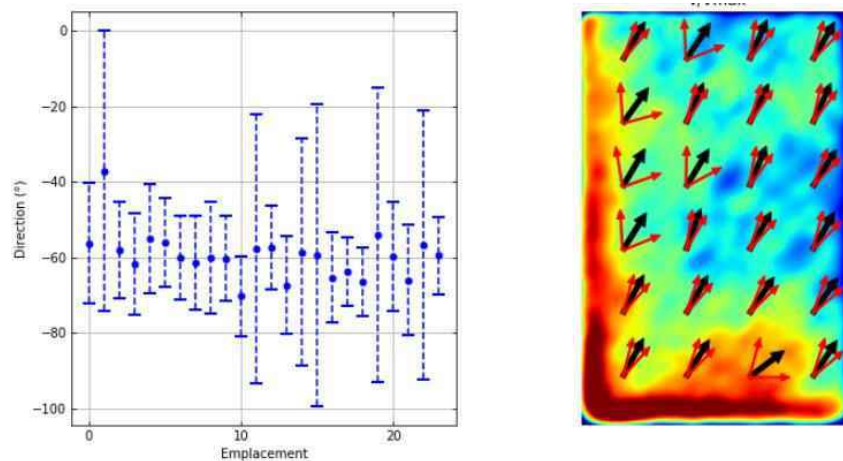


Figure B.3: Example of the calculation of the mean value and standard deviation of the flow direction with the algorithm presented on a sample exposed to the flow on location 2. On the left side, the mean value μ is given with blue filled circles while the standard deviation σ is given with the error bar indicating $\mu \pm 2\sigma$ intervals. On the right side, the heat map indicates the amplitude of the wear with red values relating to maximum values and blue to minimum values. The black arrows give the mean direction of the flow, and the red arrows give $\mu \pm 2\sigma$ intervals on the flow direction.

A $\pm 20^\circ$ interval is found for the flow direction on the sample by keeping the only the calculation with low standard deviation.

Appendix C Design of experiment for the CFD simulations

Design of experiments of Fluent simulations

BRE		HRE	
Re	Pr	Re	Pr
400265	1.84211	896682	1.84211
395728	8.57895	891280	8.57895
137095	4.78947	583384	4.78947
504627	7.73684	1020921	7.73684
477403	3.10526	745435	3.10526
540927	9	707622	5.21053
191544	6.47368	761639	1.84211
164319	3.52632	534768	6.05263
454716	4.36842	869673	6.47368
218768	2.26316	707622	3.94737
96258	6.05263	815656	9
255068	1	1069536	2.26316
341279	5.21053	648204	1.42105
363966	6.89474	977707	3.52632
463789	2.26316	945297	1
545464	5.21053	977707	2.26316
545464	2.26316	810255	4.78947
255068	4.36842	567178	1
522777	1.42105	761639	8.15789
400265	6.05263	1069536	6.05263
155245	7.73684	534768	3.10526
168857	1	993913	5.63158
418415	7.73684	1069536	3.52632
545464	6.89474	572581	6.89474
545464	3.94737	923690	5.21053
382116	3.52632	669811	8.15789
259605	8.15789	534768	9

96258	9	675212	2.26316
314054	6.05263	853469	3.94737
96258	3.94737	637401	9
227843	5.63158	540170	3.94737
182469	9	923690	7.31579
264143	6.89474	621195	5.63158
255068	3.10526	1037126	1.42105
354891	2.68421	545572	7.73684
96258	2.68421	729229	9
300442	9	1026323	4.78947
486477	6.05263	767042	6.47368
354891	1	540170	1.84211
304980	1.84211	929092	4.36842
445641	1	977707	9
96258	6.89474	966904	6.47368
327667	7.73684	788648	5.63158
359429	4.36842	1069536	9
96258	1.42105	837263	7.73684
454716	6.89474	659008	7.31579
96258	8.15789	831862	1
436566	5.21053	891280	3.10526
155245	1.84211	659008	6.47368
459253	9	729229	1

Design of experiments of STAR-CCM+ simulations

BRE		HRE	
Re	Pr	Re	Pr
349910	1.84211	783876	1.84211
345944	8.57895	779153	8.57895
119848	4.78947	509992	4.78947
441143	7.73684	892485	7.73684
417343	3.10526	651656	3.10526
472876	9	618601	5.21053
167447	6.47368	665822	1.84211
143647	3.52632	467492	6.05263
397511	4.36842	760265	6.47368
191246	2.26316	618601	3.94737
84149	6.05263	713044	9
222980	1	934985	2.26316
298345	5.21053	566658	1.42105
318178	6.89474	854708	3.52632

405443	2.26316	826375	1
476842	5.21053	854708	2.26316
476842	2.26316	708322	4.78947
222980	4.36842	495825	1
457009	1.42105	665822	8.15789
349910	6.05263	934985	6.05263
135715	7.73684	467492	3.10526
147614	1	868875	5.63158
365777	7.73684	934985	3.52632
476842	6.89474	500548	6.89474
476842	3.94737	807486	5.21053
334045	3.52632	585546	8.15789
226946	8.15789	467492	9
84149	9	590268	2.26316
274545	6.05263	746099	3.94737
84149	3.94737	557213	9
199180	5.63158	472215	3.94737
159514	9	807486	7.31579
230913	6.89474	543046	5.63158
222980	3.10526	906652	1.42105
310245	2.68421	476937	7.73684
84149	2.68421	637489	9
262646	9	897207	4.78947
425276	6.05263	670545	6.47368
310245	1	472215	1.84211
266613	1.84211	812209	4.36842
389577	1	854708	9
84149	6.89474	845263	6.47368
286446	7.73684	689433	5.63158
314212	4.36842	934985	9
84149	1.42105	731932	7.73684
397511	6.89474	576102	7.31579
84149	8.15789	727210	1
381644	5.21053	779153	3.10526
135715	1.84211	576102	6.47368
401477	9	637489	1

Appendix D POD on the Nusselt field over the partition plate.

The proper orthogonal decomposition (POD) has been applied to snapshots of the Nusselt number on the partition plate of the steam generator water box which have been calculated in Chapter 5 for different Reynolds and Prandtl numbers on the design of experiments given on Figure 5.4. The results for the Realizable $k - \epsilon$ (RKE) have been depicted in §5.5.3.3. This appendix gives the results for the other turbulence models including:

- The four first modes of the POD applied to snapshots obtained from simulation with the $k - \omega$ SST model (KOSST), simulations with the RKE model of Fluent and simulations with the SAS turbulence model.
- The evolution of the components $a_1(Re, Pr)$, $a_2(Re, Pr)$, $a_3(Re, Pr)$, and $a_4(Re, Pr)$.
- The mean absolute error MAE calculated between the original snapshots and the reconstructed surface distribution from the truncated POD with four modes.

$$MAE = \left\langle \frac{|Nu_{ORIGINAL} - Nu_{POD}|}{Nu_{ORIGINAL}} \right\rangle_S$$

where, $\langle \quad \rangle_S$ denotes the surface average value.

D.1 Modes calculated for the different turbulence models

The four first modes are given for:

- The KOSST simulations with STAR-CCM+ on grids LRE_{POLY} and HRE_{POLY} on Figure D.1 and Figure D.2.
- The SAS simulations with Fluent on grids LRE_{TET} and HRE_{TET} on Figure D.3 and Figure D.4.

- The RKE simulations with Fluent on grids LRE_{TET} and HRE_{TET} on Figure D.5 and Figure D.6.

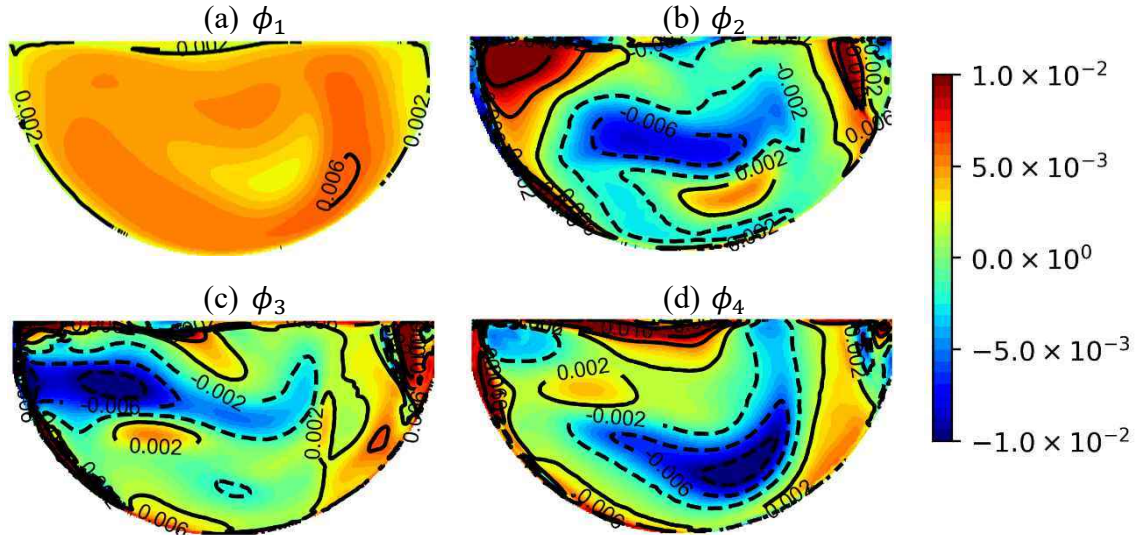


Figure D.1: surface distribution of the four first POD modes ϕ_1, ϕ_2, ϕ_3 and ϕ_4 obtained with snapshots of the Nusselt number calculated with the KOSST model on LRE_{POLY} .

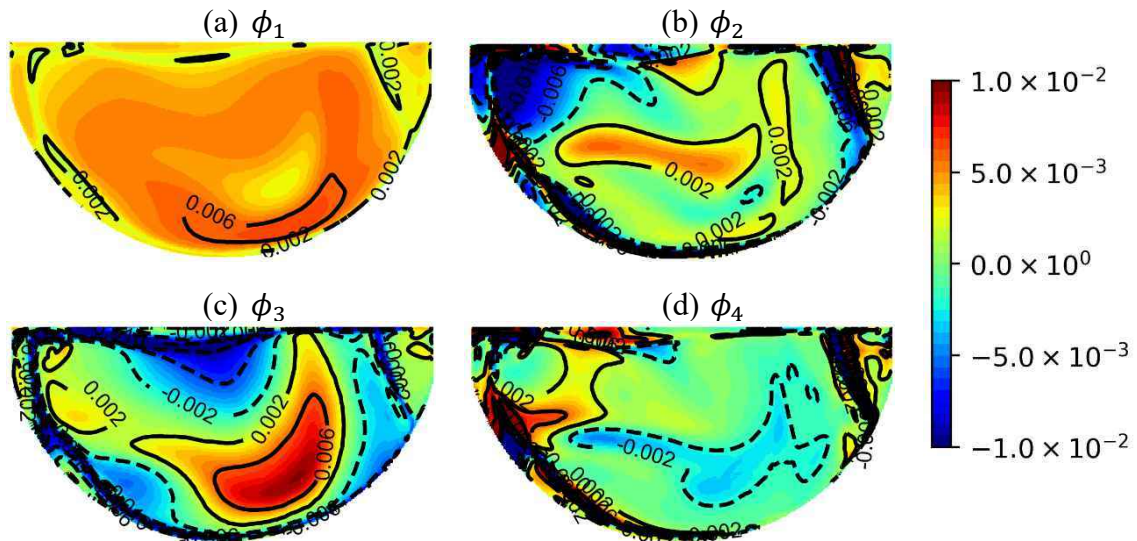


Figure D.2: surface distribution of the four first POD modes ϕ_1, ϕ_2, ϕ_3 and ϕ_4 obtained with snapshots of the Nusselt number calculated with the KOSST model on HRE_{POLY} .

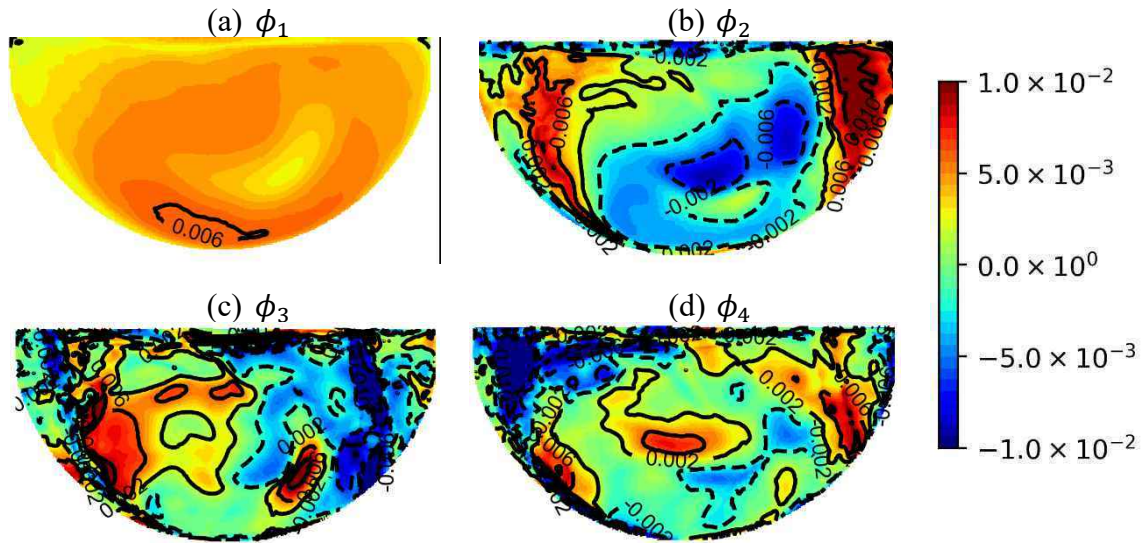


Figure D.3: surface distribution of the four first POD modes ϕ_1, ϕ_2, ϕ_3 and ϕ_4 obtained with snapshots of the Nusselt number calculated with the SAS model on LRE_{POLY}

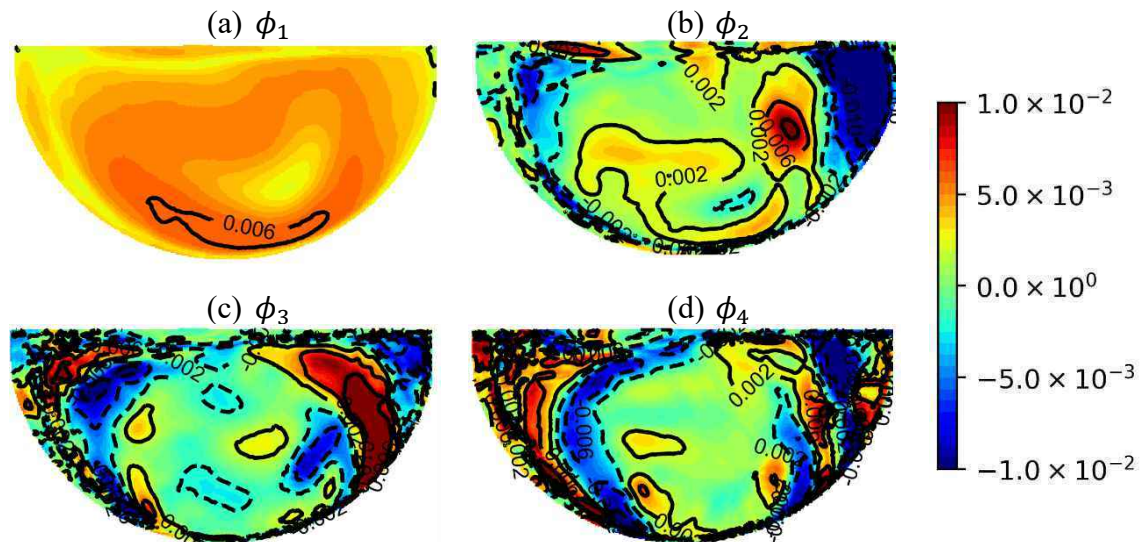


Figure D.4: surface distribution of the four first POD modes ϕ_1, ϕ_2, ϕ_3 and ϕ_4 obtained with snapshots of the Nusselt number calculated with the SAS model on HRE_{POLY}

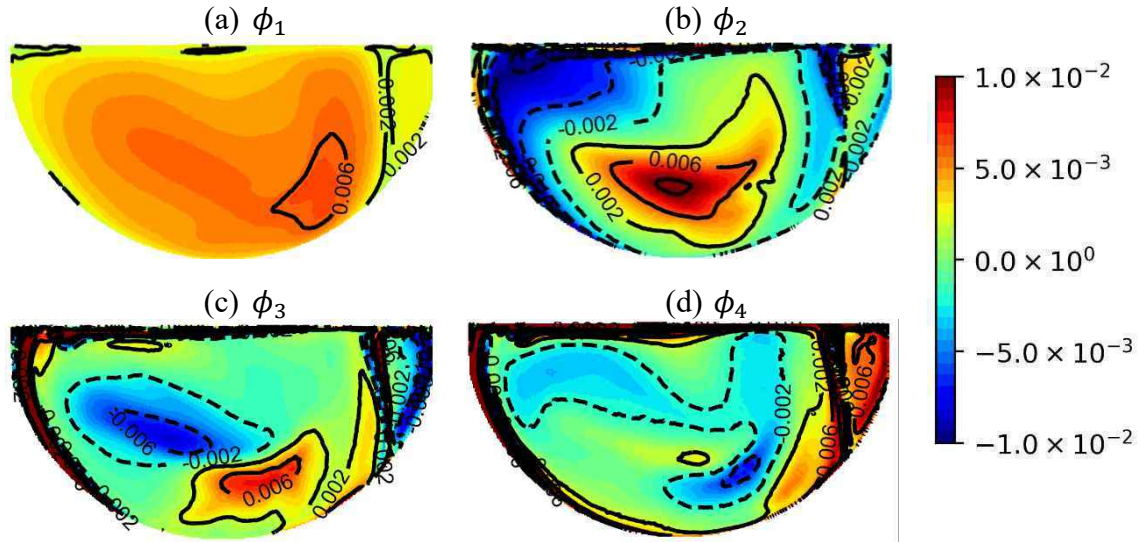


Figure D.5: surface distribution of the four first POD modes ϕ_1, ϕ_2, ϕ_3 and ϕ_4 obtained with snapshots of the Nusselt number calculated with the RKE model on LRE_{TET} .

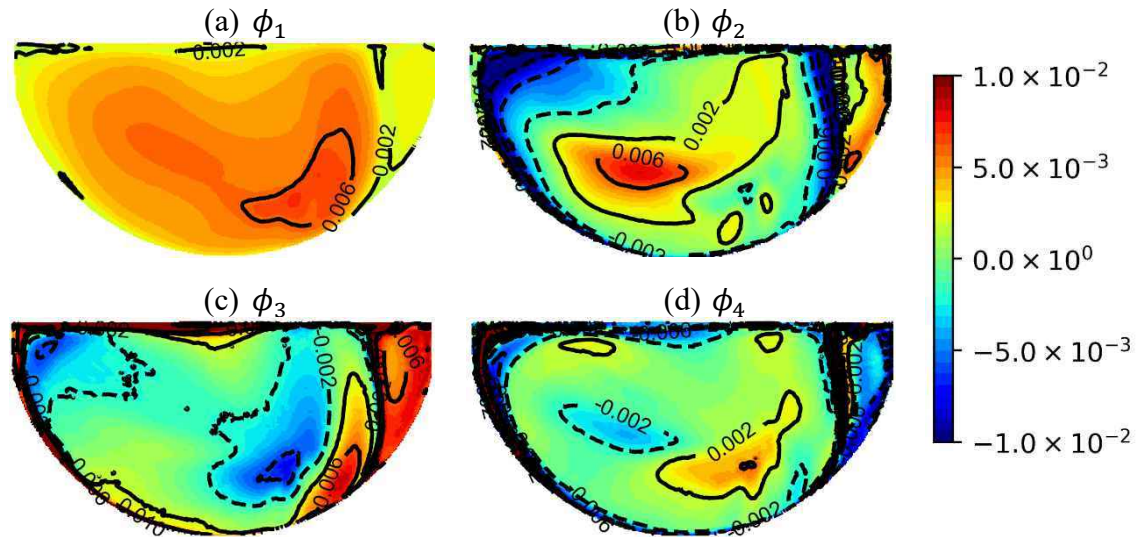


Figure D.6: surface distribution of the four first POD modes ϕ_1, ϕ_2, ϕ_3 and ϕ_4 obtained with snapshots of the Nusselt number calculated with the RKE model on HRE_{TET} .

Different comments can be given on the modes obtained:

- The first mode calculated with the SAS model and KOSST model show similar surface distribution with slight difference on the location of the iso contour $\phi_1 = 0.006$ and on the surface distribution on the upper left side of the plate.
- The modes ϕ_2 , ϕ_3 and ϕ_4 calculated for the SAS model seem to be more related to the noise present in the different calculated Nusselt number distribution, than to coherent structures evolving for the different Reynolds and Prandtl numbers.
- The importance of modes ϕ_3 and ϕ_4 for simulations with grid *LRE* and *HRE* seem to be reversed. This is the case for simulations with the KOSST turbulence model and the RKE turbulence model. Furthermore, it has been also observed for the simulations with STAR-CCM+ with the RKE turbulence model in §5.5.3.3.

D.2 MAE of the truncated POD

The MAE between the original snapshots and the truncated POD is calculated and its evolution with respect to the Reynolds number is depicted for the different turbulence models and grids. The results are summarized on Figure D.7. Comments on the results are given in §5.5.3.3.

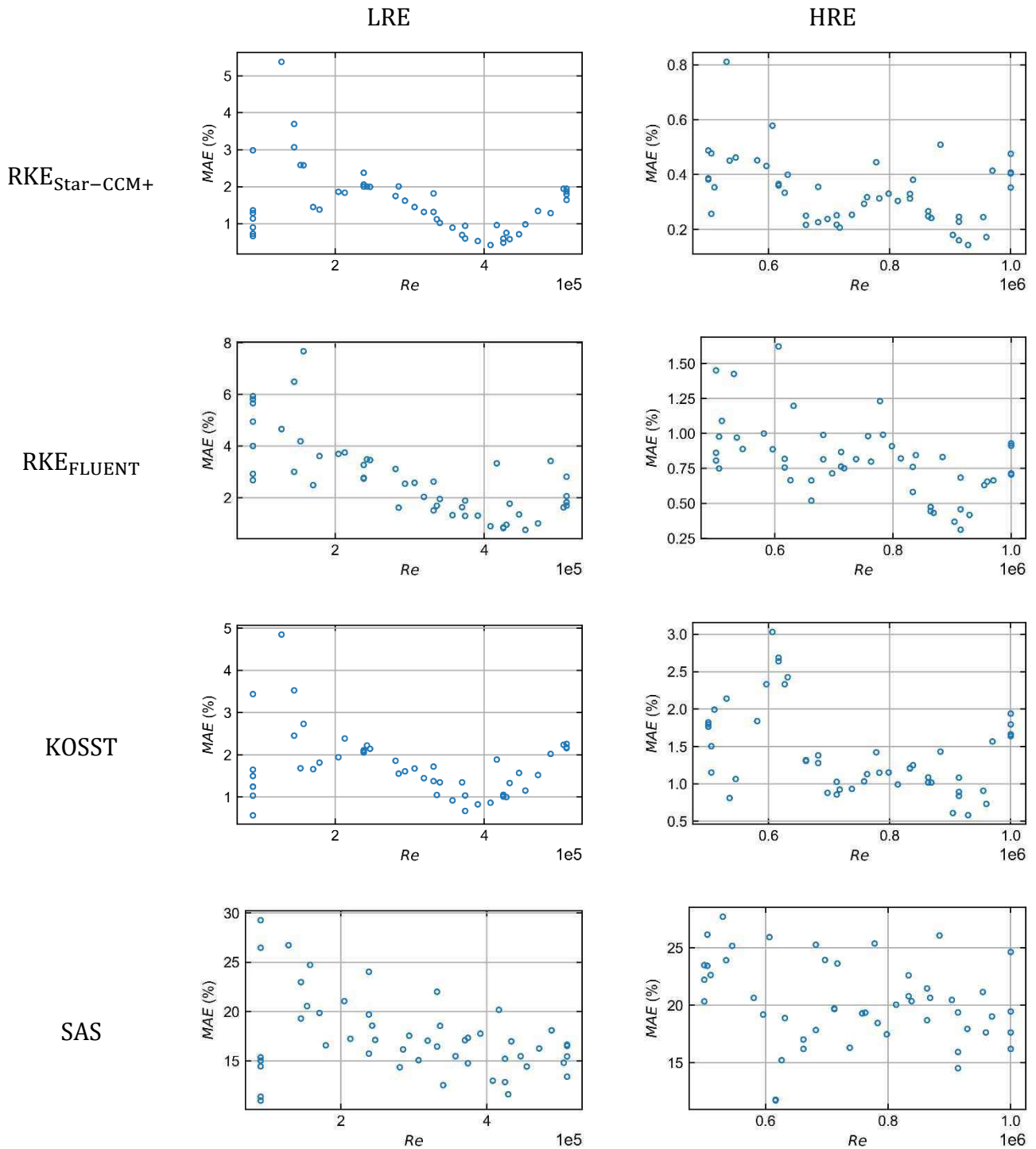


Figure D.7: MAE calculated between the truncated POD and the original snapshots with four modes.

D.3 Surrogate modelling of the components

The components $a_k(Re_j, Pr_j)$ of the snapshots Nu_j associated to the modes ϕ_k obtained with POD were used to design surrogate models \hat{a}_k . These were then used to predict the components on a much finer grid than the original design of experiment given Figure 5.4. The predictions of the components with $\hat{a}_1, \hat{a}_2, \hat{a}_3$ and \hat{a}_4 in the range $Re \in [10^5, 10^6]$ and $Pr \in [1, 9]$ is given for the Nusselt number obtained from the different turbulence models simulations. The surrogate models were designed separately for the range $Re \in [10^5, 5 \cdot 10^5]$ and $Re \in [5 \cdot 10^5, 10^6]$, as POD was applied separately on these respective intervals:

- the values of the components obtained from the surrogate models designed for KOSST simulations are given on Figure D.8
- the predictions of the components for the SAS model simulations are given on Figure D.9
- the surrogate models designed for the RKE turbulence model simulations carried out with Fluent are given on Figure D.10

The surrogate models were created with gaussian process and Bayesian statistics as depicted in §5.4. A squared exponential kernel has been chosen.

Different observations can be given regarding the results:

- First, the surrogate model created for the prediction of the components for the RKE model simulations with Fluent show significant similarities with the RKE simulations with STAR-CCM+ depicted in §5.5.3.3. Slight differences are visible on $\hat{a}_{3\text{HRE}}$ and $\hat{a}_{4\text{LRE}}$ where the surface distribution is wavier for the simulations with Fluent than with STAR-CCM+.
- The isocontours of the values predicted with the surrogate model created for the KOSST simulations show an increased waviness starting from the second mode. The location of these wavy isocontours corresponds to point where oscillatory convergence has been observed on the calculations. The simulations with HREb grid did not show these fluctuations.
- The values of the components calculated for the SAS model show a coherent behaviour for ϕ_1 . However, for higher order modes, the components were found to fluctuate more importantly than for the other simulations. The surrogate model calculated for mode ϕ_2 still shows a behaviour that seem correlated to the Reynolds and Prandtl evolution, but for ϕ_3 and ϕ_4 the large variability of the fluctuations impacted negatively the results of the prediction with the surrogate model.

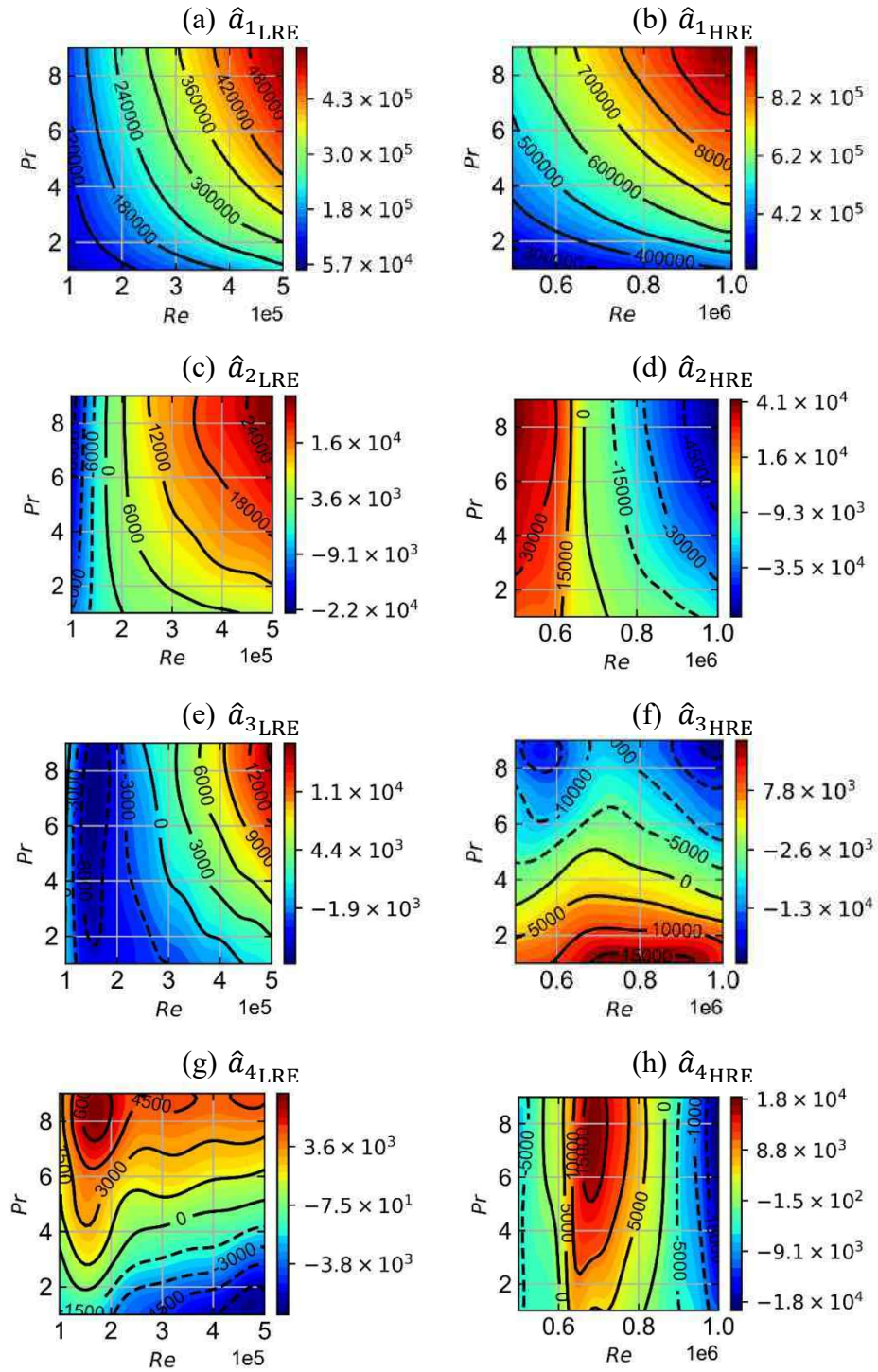


Figure D.8: predictions of the components associated to the modes obtained with the KOSST model on grids LRE_{POLY} and HRE_{POLY}. The predicted values are given with a heat map.

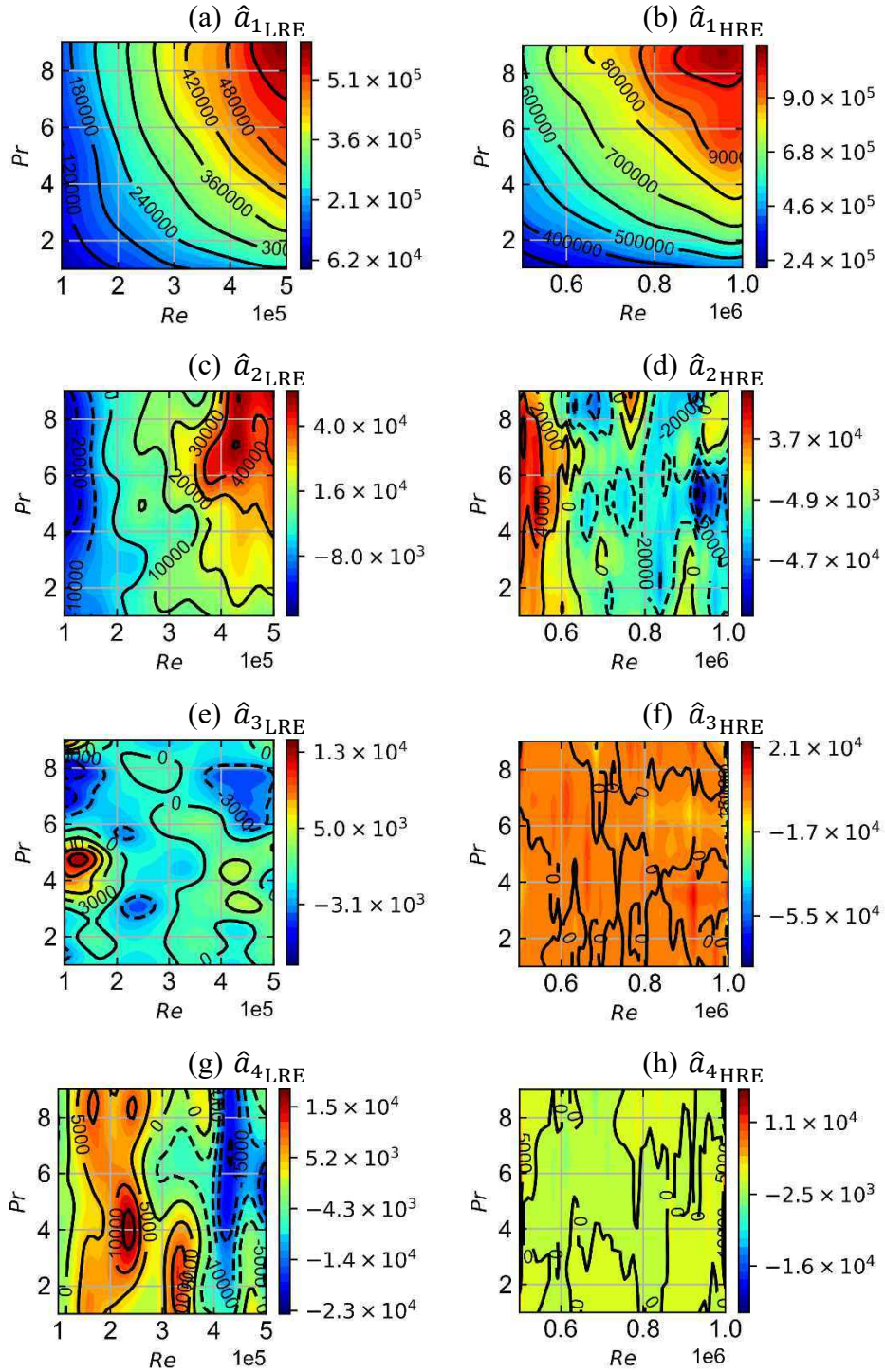


Figure D.9: predictions of the components associated to the modes obtained with the KOSST model on grids LRE_{POLY} and HRE_{POLY} . The predicted values are given with a heat map.

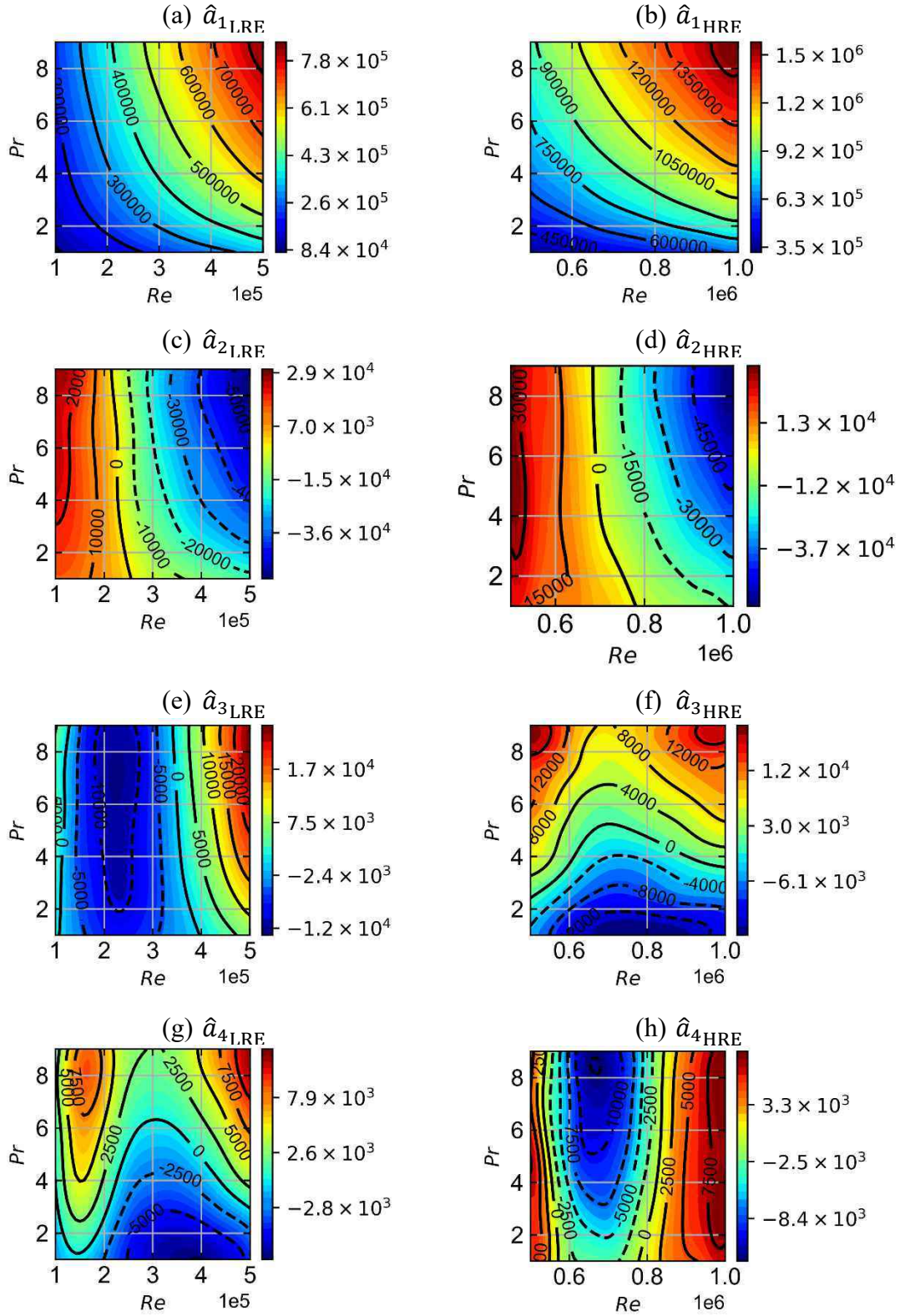


Figure D.10: predictions of the components associated to the modes obtained with the RKE model on grids LRE_{TET} and HRE_{TET}. The predicted values are given with a heat map.

